

Role of Structural Correlation with Lattice Dynamics in AFeO₃ (A= Pr, Ga) Multiferroic Materials

Ph.D. Thesis

**By
Anil Kumar**



**DISCIPLINE OF PHYSICS
INDIAN INSTITUTE OF TECHNOLOGY INDORE**

January 2021

Role of Structural Correlation with Lattice Dynamics in AFeO₃ (A= Pr, Ga) Multiferroic Materials

A THESIS

*Submitted in partial fulfillment of the
requirements for the award of the degree
of*
DOCTOR OF PHILOSOPHY

by

Anil Kumar



**DISCIPLINE OF PHYSICS
INDIAN INSTITUTE OF TECHNOLOGY INDORE
January 2021**



INDIAN INSTITUTE OF TECHNOLOGY INDORE

CANDIDATE'S DECLARATION

I hereby certify that the work which is being presented in the thesis entitled **Role of Structural Correlation with Lattice Dynamics in $A\text{FeO}_3$ ($A = \text{Pr, Ga}$) Multiferroic Materials** in the partial fulfillment of the requirements for the award of the degree of **Doctor of Philosophy** and submitted in the **Department of Physics, Indian Institute of Technology Indore**, is an authentic record of my own work carried out during the time period from July 2017 to December 2020 under the supervision of Dr. Pankaj R. Sagdeo, Associate Professor, Indian Institute of Technology Indore.

The matter presented in this thesis has not been submitted by me for the award of any other degree of this or any other institute.

Anil Kumar

Date- January 7, 2021

Signature of the student with date
(Anil Kumar)

This is to certify that the above statement made by the candidate is correct to the best of my/our knowledge.

P. R. Sagdeo
Dr. P. R. Sagdeo

Date- January 7, 2021

Signature of Thesis Supervisor with date
(Dr. Pankaj R Sagdeo)

Anil Kumar has successfully given his/her Ph.D. Oral Examination held on March 18, 2021.

Rupesh
Signature of Chairperson (OEB)
Date: 18/3/2021

[Signature]
Signature of External Examiner
Date: 18/3/2021

[Signature] 18/3/21
Signature(s) of Thesis Supervisor(s)
Date:

[Signature] 18/03/2021
Signature of RSPC Member #1
Date:

[Signature]
Signature of RSPC Member #2
Date: 18/3/21

[Signature] 18/02/21
Signature of Convener, DPGC
Date:

[Signature] 18/3/21
Signature of Head of Discipline
Date:

Dedicated to

My Parents

Acknowledgements

Uphill battle is not won by a single person; it requires a dedicated team which performs and guides in every step. During the last three and half years, I am privileged to have many such people who have provided me research supporting environment, and have helped in academics, teaching, and moral support to make this thesis possible. I hereby thank all of them.

*I would like to express my heartfelt gratitude to my thesis supervisor and Head of Department, **Dr. Pankaj R. Sagdeo** for giving me the opportunity to perform this work under his guidance and learning opportunities during this work. The constant scientific support and motivation by sir was essential for the completion of this thesis. I will be forever grateful to him for helping me to achieve this goal.*

*I would like to specially acknowledge my PSPC members, **Dr. Rajesh Kumar** and **Dr. Vipul Singh**, for their continuous support and constructive involvement throughout my PhD. Their evaluation, comments and suggestion helped me a lot to improve my research work. I feel a deep sense of gratitude for **Dr. Rajesh Kumar** and **Dr. Somaditya Sen**, who helped in developing a vision towards many good things that really matter in life.*

*I would like to express my gratitude to **Prof. Neelesh Kumar Jain**, acting director, IIT Indore. He always goes out of the way to help students of IIT Indore. His energy and enthusiasm toward research always motivated me.*

*I would like to thank all faculty members of the Department of Physics, IIT Indore. I am obliged to **Prof. Krushna R. Mavani** for providing the facility of vacuum furnace.*

*I was fortunate to collaborate with various external groups during the research work. I would like to sincerely thank **Dr A. K. Sinha**, **Dr. Archana Sagdeo**, **Mr. M. N. Singh** and **Mr. Anuj Upadhyay** from Indus Synchrotron Utilization Division, Raja Ramanna Centre for Advanced Technology Indore (RRCAT) (BL-12), India for their extending help during X-ray diffraction and XANES measurements.*

*I would like to express my deepest gratitude to **Dr. Soma Banik and Dr. Parasmani Rajput** from RRCAT Indore for continuous and fruitful discussion on x-ray absorption and VBS measurements. A special thank goes to **Dr. R. K. Sharma, Mr. Jaspreet Singh and Mr. U. K. Goutam** from RRCAT Indore (BL-14) for constructive discussion on XPS results.*

*Further, I wish to express my gratitude to the members of beamline-1, RRCAT Indore, **Dr. Mukul Gupta, Mr. Rakesh Kumar and Mr. R. P. Bhingade** for their extending help in XAS measurements.*

***Prof. Matthew, Prof. Adroja, Prof. Ivan da Silva and Prof. Svemir** from ISIS Neutron diffraction Centre are specially acknowledged for fruitful discussion on Compton scattering experiments.*

*I sincerely thank Sophisticated Instrumentation Center, IIT Indore, most specifically **Mr. Nitin Upadhyay and Mr. Kinny Pandey** for their support during XRD and SEM measurements respectively.*

*I would like to convey my special gratitude to not only my labmates but very good friends of mine, **Dr. Harimohan Rai, Dr. Vikash Mishra, Dr. M. Kamal Warshi, Dr. Aanchal sati, Nishchal, Omkar, Kailash, Ravikiran Late and Minal** for making environment work friendly in the lab.*

*I sincerely thank all the members of **Materials and Devices Lab** for their love, care and support. Also, I am very grateful to **Ravinder KC, Ekta Yadav, Ravindra Singh and Rameshwar** for their constant support and appreciation. This department has given me such incredible people in my life who have always been a support system for me.*

I wish to express my gratitude to my brothers and sisters, Sunil Kabira, Parveen, Anju, Aman, Jindu, Sandeep deepu, Ravi, Hardeep Shantu, Munna Canadian, Vipin and my sister in laws for their constant motivation, support, and all the sacrifices. I would like to share my happiness with the kids, Sharry Kamboj, Lavish, Kirat, Navu, Agampreet and Avish Kamboj for showering their love to me.

I would like to thank all my friends and siblings, Rajan, Sajjan, Harsh, Neetu Bhola, Sheenam, Poonam, Ankush Gaggi, Rinku Sararia, Bunty Canadian, Ravi Babbar, Ashish Kamboj and Sandeep Sippy for their tremendous support whenever I needed it. Moreover, several people

have knowingly and unknowingly helped me in successful completion of my thesis.

Last but not least, I would like to thank my parents for their constant motivation, support, and all the sacrifices they have made. I feel a deep sense of gratitude for my grandparents and my parents who have contributed to develop my vision and taught me the good things that really matter in life. Lastly, I want to thank the superpower/almighty, the creator and Guardian, and to whom I owe my existence.

Anil Kumar

List of Publications

List of publications from Ph.D. thesis work

1. **A. Kumar**, S. Umrao, P.R. Sagdeo, Orbital facilitated charge transfer originated phonon mode in Cr-substituted PrFeO₃: A brief Raman study, *J. Raman Spectrosc.* 10 (2020) 5894. <https://doi.org/10.1002/jrs.5894>. **(Impact Factor: 2.0)**
2. **A. Kumar**, M.K. Warshi, M. Gupta, P.R. Sagdeo, The magneto-elastic and optical properties of multiferroic GaFeO_{3-δ}, *J. Magn. Magn. Mater.* 514 (2020) 167210. <https://doi.org/10.1016/j.jmmm.2020.167210>. **(Impact Factor: 2.683)**
3. **A. Kumar**, V. Mishra, M.K. Warshi, A. Sati, A. Sagdeo, R. Kumar, P.R. Sagdeo, Strain induced disordered phonon modes in Cr-doped PrFeO₃, *J. Phys. Condens. Matter.* 31 (2019) 275602. <https://doi.org/10.1088/1361-648x/ab1195>. **(Impact Factor: 2.707)**
4. **A. Kumar**, M.K. Warshi, V. Mishra, A. Sati, S. Banik, A. Sagdeo, R. Kumar, P.R. Sagdeo, Optical spectroscopy: An effective tool to probe the origin of dielectric loss in Cr-doped PrFeO₃, *Ceram. Int.* 45 (2019) 8585–8592. <https://doi.org/10.1016/j.ceramint.2019.01.177>. **(Impact Factor: 3.830)**
5. **A. Kumar**, A. Sati, V. Mishra, M.K. Warshi, R. Kumar, P.R. Sagdeo, Charge neutral crystal field transitions: A measure of electron–phonon interaction, *J. Phys. Chem. Solids.* 135 (2019) 109102. <https://doi.org/10.1016/j.jpcs.2019.109102>. **(Impact Factor: 3.442)**
6. **A. Kumar**, V. Mishra, M.K. Warshi, A. Sati, A. Sagdeo, R. Kumar, P.R. Sagdeo, Possible evidence of delocalized excitons in Cr-doped PrFeO₃: An experimental and theoretical realization, *J. Phys. Chem. Solids.* 130 (2019) 230-235. <https://doi.org/10.1016/j.jpcs.2019.03.012>. **(Impact Factor: 3.442)**

7. **A. Kumar**, M.K. Warshi, V. Mishra, S.K. Saxena, R. Kumar, P.R. Sagdeo, Strain control of Urbach energy in Cr-doped PrFeO₃, Appl. Phys. A. 123 (2017) 576. <https://doi.org/10.1007/s00339-017-1186-9>. **(Impact Factor: 1.810)**

8. **Anil Kumar***, M. K. Warshi, **P. R. Sagdeo***, New route to estimate the Mott-Hubbard and charge transfer parameters using x-ray absorption and optical spectroscopy, Solid State Science 115 (2021) 106582. <https://doi.org/10.1016/j.solidstatesciences.2021.106582>.

(Impact Factor: 2.434).

9. **Anil Kumar**, Archna sagdeo and P. R. Sagdeo, Possibility of using ultraviolet radiation for disinfection of novel COVID-19, Photodiagnosis and Photodynamic Therapy, 34 (2021) 102234. <https://dx.doi.org/10.1016%2Fj.pdpdt.2021.102234>.

10. **Anil Kumar***, Omakr Rambadey and P. R. Sagdeo* An unorthodox approach to realize the correlation between electronic disorder and dielectric coefficient in Cr-doped PrFeO₃, The Journal of Physical Chemistry C (Accepted Manuscript). **(Impact Factor: 4.18).**

11. **A. Kumar***, M. K. Warshi, P. R. Sagdeo, Investigations on the electronic structure of strongly correlated electron system Cr-doped PrFeO₃, Solid State Sciences (under review). **(Impact Factor: 2.434).**

12. **A. Kumar* et al.**, Role of Pr atoms delocalization on the natural and magnetic field induced polar order in PrFe_{0.50}Cr_{0.50}O₃ (Under review).

List of publications as a contributing author:

1. M.K. Warshi, **A. Kumar**, A. Sati, S. Thota, K. Mukherjee, A. Sagdeo, P.R. Sagdeo, Cluster Glass Behavior in Orthorhombic SmFeO₃ Perovskite: Interplay between Spin Ordering and Lattice Dynamics, Chem. Mater. 32 (2020) 1250–1260. <https://doi.org/10.1021/acs.chemmater.9b04703>. **(Impact Factor: 9.567)**

2. M.K. Warshi, **A. Kumar**, P.R. Sagdeo, Design and development of a fully automated experimental setup for in-situ temperature dependent magneto-dielectric measurements, *Meas. Sci. Technol.* 30 (2019) 125901. <https://doi.org/10.1088/1361-6501/ab387e>. (**Impact Factor: 1.857**)
3. M.K. Warshi, **A. Kumar**, V. Mishra, A. Sati, A. Sagdeo, R. Kumar, P.R. Sagdeo, Effect of self-doping on the charge state of Fe ions and crystal field transitions in YFeO_3 : Experiments and theory, *J. Appl. Phys.* 125 (2019) 204101. <https://doi.org/10.1063/1.5092736>. (**Impact Factor: 2.328**)
4. V. Mishra, **A. Kumar**, A. Sagdeo, P.R. Sagdeo, Comparative structural and optical studies on pellet and powder samples of BaTiO_3 near phase transition temperature, *Ceram. Int.* 46 (2019) 3250-3256. <https://doi.org/10.1016/j.ceramint.2019.10.030>. (**Impact Factor: 3.830**)
5. A. Sati, **A. Kumar**, V. Mishra, K. Warshi, A. Sagdeo, S. Anwar, R. Kumar, P.R. Sagdeo, Direct correlation between the band gap and dielectric loss in Hf doped BaTiO_3 , *J. Mater. Sci. Mater. Electron.* 30, (2019) 8064–8070. <https://doi.org/10.1007/s10854-019-01128-z>. (**Impact Factor: 2.220**)
6. A. Sati, **A. Kumar**, V. Mishra, K. Warshi, P. Pokhriyal, A. Sagdeo, P.R. Sagdeo, Temperature-dependent dielectric loss in BaTiO_3 : Competition between tunnelling probability and electron-phonon interaction, *Mater. Chem. Phys.* 257 (2021) 123792. <https://doi.org/10.1016/j.matchemphys.2020.123792>. (**Impact Factor: 3.408**)
7. A. Sati, V. Mishra, **A. Kumar**, M.K. Warshi, A. Sagdeo, R. Kumar, P.R. Sagdeo, Effect of structural disorder on the electronic and phononic properties of Hf doped BaTiO_3 , *J. Mater. Sci. Mater. Electron.* 30 (2019) 9498–9506. <https://doi.org/10.1007/s10854-019-01281-5>. (**Impact Factor: 2.220**)
8. V. Mishra, M.K. Warshi, A. Sati, A. Kumar, V. Mishra, A. Sagdeo, R. Kumar, P.R. Sagdeo, Diffuse reflectance spectroscopy: An effective tool to probe the defect states in wide band gap semiconducting materials,

Mater. Sci. Semicond. Process. 86 (2018) 151–156.
<https://doi.org/10.1016/j.mssp.2018.06.025>. (**Impact Factor: 2.593**)

9. Vikash Mishra, M. Kamal Warshi, Aanchal Sati, **Anil Kumar**, Vinayak Mishra, Rajesh Kumar, P. R. Sagdeo, Investigation of temperature-dependent optical properties of TiO₂ using diffuse reflectance spectroscopy, SN Appl. Sci., 1, (2019) 241.
<https://doi.org/10.1007/s42452-019-0253-6>. (**Impact Factor: Not available**).

10. Minal Gupta, **Anil Kumar**, Archana Sagdeo and P. R. Sagdeo, Doping Induced Combined Fano and Phonon Confinement Effect in La Doped CeO₂: Raman Spectroscopy Analysis, The Journal of Physical Chemistry , 125 4, 2648-2658, <https://doi.org/10.1021/acs.jpcc.0c09133>. (**Impact Factor: 4.18**).

Table of Contents

Acknowledgement	i
List of Publications	iv
List of Figures	xiii
List of Table	xx
List of Abbreviations	xxii

Chapter 1: Introduction and origin of the problem

1.1 Introduction and origin of the problem	1
1.2 Multiferroics: a beautiful but challenging multi-polar world	4
1.3 Major challenges with the existing multipolar materials and Background	6
1.4 Perovskite-type Oxides	10
1.5 Rare-earth Orthoferrites	13
1.6 Magnetic interactions in rare earth orthoferrites	14
1.6.1 Antisymmetric Exchange Interaction	14
1.6.2 Zener Double Exchange Interaction	16
1.6.3 Antisymmetric Exchange Interaction	17
1.7 Possible signature of magnetism by Raman scattering	19
1.8 Crystal field splitting	20
1.9 The quantification of electron-phonon coupling by Fano model	23
1.10 The probing of electronic disorder by optical absorption spectroscopy	24

1.11 Aim of the present work	26
1.12 Organization of the thesis	33
Chapter 2: Experimental Techniques	
2.1 Material Synthesis technique Sol-Gel	
Method	37
2.2 Characterization techniques used	
2.2.1 X-Ray Diffraction	39
2.2.2 Williamson-Hall Plot	41
2.3 Diffuse Reflectance Spectroscopy	43
2.4 Raman Spectroscopy	46
2.5 Low Temperature Dielectric	
Experimental Setup	49
2.6 Magnetic Measurements	53
2.7 X-ray absorption spectroscopy	55
2.8 X-ray and ultraviolet photoelectron	
spectroscopy	59
2.9 Structural Characterization by synchrotron	61
x-ray diffraction	
Chapter 3: Structural, Optical and Dielectric	
Properties of $\text{PrFe}_{1-x}\text{Cr}_x\text{O}_3$ ($0 < x < 0.20$) Compounds	
65	
3.1 Introduction	65
3.2 Experimental Details	67
3.2.1 Synthesis of Rare-earth Orthoferrites	67
3.2.2 X-ray diffraction	67
3.2.3 Dielectric measurements	67
3.2.3 Diffuse reflectance spectroscopy	67
3.2.4 Valence band spectroscopy	67
3.3 Results and discussion	68
3.3.1 Optical absorption spectroscopy analysis	68

3.3.2 Dielectric measurements	71
3.3.3 Valence band spectroscopy	72
3.3.4 Direct correlation between dissipation factor and electronic disorder	73
3.4 Conclusion	75
Chapter 4: Strain induced disordered phonon modes in Cr-doped PrFeO ₃	77
4.1 Introduction	77
4.2 Experimental Details	79
4.2.1 Structural characterization	79
4.2.2 Diffuse Reflectance spectroscopy	79
4.2.3 Raman scattering experiments	79
4.3 Results and discussion	79
4.3.1 Structural studies	79
4.3.2 Raman spectral analysis	82
4.3.3 Systematic correlation between the structural disorder and Urbach energy	83
4.3.4 Discussion on cationic disorder	87
4.3.5 Some concluding remarks	88
4.4 Conclusion	94
Chapter 5: Orbital facilitated charge transfer originated phonon mode in Cr substituted PrFeO ₃ : A brief Raman study	97
5.1 Introduction	97
5.2 Experimental Details	79
5.2.1 Theoretical detail	100
5.3 Results and discussion	
5.3.1 Structural studies	100
5.3.2 Effect of Cr-substitution on Raman line shapes	100
5.3.3 Density functional theory, optical	103

absorption spectroscopy and valence band spectroscopy analysis	
5.3.4 Effect of vacuum annealing	106
5.3.5 Effect of excitation wavelength on Raman modes	109
5.4 Conclusion	111
Chapter 6: Role of Pr atoms delocalization on the natural and magnetic field induced polar order in $\text{PrFe}_{0.5}\text{Cr}_{0.5}\text{O}_3$	113
6.1 Introduction	113
6.2 Experimental Details	115
6.3 Results and discussion	116
6.3.1 Temperature dependent P-E measurements	117
6.3.2 Temperature dependent magnetization measurements	119
6.3.3 Temperature-dependent x-ray diffraction measurements	121
6.3.4 Temperature-dependent Raman Measurements	123
6.3.5 Effect of magnetic field on Raman line shapes	127
6.3.6 Possible origin of Pr atoms delocalization as a function of temperature	129
6.3.7 Inelastic and deep inelastic neutron scattering experiments	132
6.3.8 Temperature-dependent dielectric Measurements	138
6.4 Conclusion	140
Chapter 7: The magneto-elastic and optical properties of multiferroic $\text{GaFeO}_{3-\delta}$	141

7.1 Introduction	141
7.2 Experimental Details	144
7.3 Results and discussion	146
7.3.1 Structural studies	146
7.3.2 Temperature dependent magnetization measurements	147
7.3.3 Scanning electron Microscopy	148
7.3.4 X-ray absorption at Fe K-edge	149
7.3.5 Diffuse reflectance spectroscopy	151
7.5.6 Raman spectral analysis	155
7.5.7 Some concluding remarks on exciton line shap	163
7.4 Conclusion	167
Chapter 8: Conclusion and future Perspectives	
8.1 Conclusion	169
8.2 Future perspectives	171
References	172

List of Figures

- Figure-1.1: Relationship between ferroelectricity, magnetism, and ferroelasticity, their coupling and mutual control in multiferroics. 3
- Figure-1.2: The combination of ferroelectrics and magnetic properties in multiferroics. 5
- Figure-1.3: Variation of the remanent polarization as a function of temperature in orthorhombic LuFeO_3 . 7
- Figure-1.4: Magnetic field dependence of (a) magnetization and (b) electric polarization measured for CoCr_2O_4 above (27K) and below (18K) ferroelectric transition temperature ($T_S=26\text{K}$). 8
- Figure-1.5: Promotion and suppression of electric polarization by applying magnetic fields in NVO. 9
- Figure-1.6: Temperature-dependent spontaneous polarization along [010] as a function of temperature for SmFeO_3 . 9
- Figure 1.7: The ideal cubic $\text{Pm}\bar{3}\text{m}$ structure of ABO_3 perovskite oxides. A is a large 12-fold coordinated cation and B is a small 6-fold coordinated cation. 12
- Figure 1.8: Schematic Showing the DM vector and antisymmetric exchange interaction between two near-neighbour spins. 15
- Figure 1.9: An example of double exchange interaction in case of manganites. 17
- Figure 1.10: Illustration of the superexchange interaction in a magnetic oxide. 18
- Figure 1.11: The schematic representation for crystal field transitions and Jahn-Teller distortion in manganites. 21

Figure-1.12: The Raman spectra taken at room temperature for different $\text{La}_{0.70}\text{Sr}_{0.30}\text{Mn}_{1-x}\text{Fe}_x\text{O}_3$.	22
Figure 1.13: The Fano lineshape of the absorption cross near resonance energy E_r of a discrete state buried in the continuum for various values of q parameter.	24
Figure-1.14: The exponential variation of absorption coefficient near the band edge.	25
Figure-2.1: The schematic diagram of X-ray diffraction by a crystal.	40
Figure-2.2 Shows systematically representation of Williamson-Hall plots.	42
Figure-2.3: Schematic Diagram of Light Scattering from a powdered sample.	43
Figure-2.4: Experimental set up for diffuse reflectance measurement (a) Carry 60 UV-Vis spectrometer, (b) internal set up of 60 UV-Vis spectrometer (c) an integrating sphere attachment to detect diffuse reflectance.	45
Figure-2.5: The block diagram of the major components of Raman spectrometer set up.	48
Figure-2.6 Schematic diagram Low Temperature Dielectric Experimental Setup.	50
Figure-2.7: Schematic illustration of LCR circuit (middle panel) in association with the phase diagram between voltage and current individually for L, C and R (top and bottom panel).	51
Figure 2.9: A typical X-ray absorption spectrum showing XANES and EXAFS regions.	55
Figure 2.10: Schematic of x-ray absorption process of a core electron to continuum state.	56
Figure-2.11: The valence band and core level representations of energy diagrams for metals,	60

semiconductors and insulators.

Figure-2.12: The typical UPS spectrum for a 60 sample.

Figure-2.13: The SXRD data for Cr-doped PrFeO_3 61 series of samples.

Figure-2.14: The Rietveld refinements of prepared 62 series of samples by considering the space group *Pnma*.

Figure-3.1: (a) Optical absorption spectra for 69 $\text{PrFe}_{1-x}\text{Cr}_x\text{O}_3$ system, (b) the representative plot for Urbach energy, (c) Variation of Urbach energy and optical band gap with Cr content.

Figure-3.2: (a) Variation of dielectric loss for pure 71 and Cr doped samples respectively. The variation of dielectric loss ($\tan\delta$) at 10 MHz with Cr doping.

Figure-3.3: The valence band spectra of prepared 72 samples.

Figure-3.4: The estimated values and variation of 74 tunnelling probability as a function of Cr doping.

Figure-4.1: SXRD patterns of the prepared 80 samples.

Inset (a) FWHM of XRD peak with Cr concentration. Inset (b) shifting of XRD peaks with increase in Cr content.

Figure-4.1(b): The variation of octahedral tilt 81 angles

as a function of Cr doping.

Figure-4.1(c): The variation of crystallographic 81 strain as a function of Cr doping in PrFeO_3

Figure-4.2 (a): The Raman spectrum for prepared 83 series of samples.

Figure-4.2 (b): The systematic correlation between 84 Raman line width and Urbach energy with Cr

content.

Figure-4.3: The Raman spectrum for pure and 85
irradiated bulk PrFeO_3 . Inset (a) increase in
structural disorders after higher irradiation time.

Figure-4.4: The variation of disorder parameter (σ) 87
as a function of Cr content in PrFeO_3 .

Figure-4.5: The variation of soft mode of A_g 89
symmetry modes in magnified view.

Figure-4.6: Temperature dependent Raman spectra 92
for 20% Cr doped PrFeO_3 (a), the variation of
FWHM of Raman mode with temperature.

Figure-4.7: The variation of Urbach energy as a 93
function of temperature for 20% Cr doped PrFeO_3 .

Figure 5.1: The Synchrotron x-ray diffraction for 101
prepared series of samples (a). The variation of
tolerance factor and octahedral tilt angles as a
function of Cr content is depicted in figure-(b).

Figure 5.2: The Raman spectrum for prepared 103
series of samples by using laser having excitation
wavelength 633 nm.

Figure 5.3: The spin up (a) and spin up (b) total and 104
partial density of states for Cr substituted PrFeO_3 .

Figure-5.4 (a): The Franck-Condon picture for 106
mixed Fe-Cr systems. The orbital mediated charge
transfer from Cr^{3+} to Fe^{3+} after leaving them in Cr^{4+}
and Fe^{2+} state respectively is depicted in figure-(b).

Figure-5.5: The Raman spectrum for as prepared 108
and vacuum annealed PrFeO_3 (a) 30% Cr
substituted sample is represented in figure 6(b).

Figure-5.6: The resonance Raman spectrum for as 111
prepared PrFeO_3 (a) Cr substituted PrFeO_3 (b)
using different excitation wavelengths.

Figure-6.1: The variation of the remnant hysteresis 118

loops at 280 K (a) and 100 K (b).

Figure-6.2: Temperature dependence of the dc magnetization variation for polycrystalline $\text{PrFe}_{0.50}\text{Cr}_{0.50}\text{O}_3$. 119

Figure-6.3: (a) The temperature dependence of x-ray diffraction for $\text{PrFe}_{0.5}\text{Cr}_{0.5}\text{O}_3$, (b), (c) Rietveld refined x-ray diffraction data. (d) the variation of lattice constants as a function of temperature. 123

Figure-6.4: The temperature dependent Raman spectrum for $\text{PrFe}_{0.5}\text{Cr}_{0.5}\text{O}_3$ sample. 124

Figure-6.5 (a): The Raman shift for the B_{2g} (7) mode Figure-(b) variation of Raman line width for B_{2g} (1) mode fitted by Balkanski model. 125

Figure-6.6 (a): The variation of Raman spectra as a function of applied magnetic field in $\text{PrFe}_{0.5}\text{Cr}_{0.5}\text{O}_3$. (b) variation of Raman spectra as a function of applied magnetic field in PrFeO_3 . 128

Figure-6.7: Low temperature Raman spectra (a) and Fe atomic vibrations (b) with very small magnetic field (30 Gauss). (c&d) The variation of Raman shift as a function of temperature for B_{2g} (1) and A_g (7) modes with the application of magnetic field (e) The variation of Δw vs $\Delta \epsilon$. 131

Figure 6.8: Neutron Compton scattering spectrum for Cr- substituted PrFeO_3 (a) and PrFeO_3 (b). 133

Figure 6.8 (c) Inelastic neutron scattering spectra of Cr-substituted PrFeO_3 and PrFeO_3 . 137

Figure-6.9 (a): The temperature dependence of dielectric Inset of the figure represents the first derivative of dielectric constant with temperature. 139

Figure-6.9 (b): The linear variation between the $\Delta \epsilon$ and $M^2(T)$. 139

Figure-7.1: The refined x-ray diffraction for all 146

prepared series of samples.	
Figure-7.2: Temperature dependence of ac-susceptibility measurement results for prepared series of samples.	149
Figure-7.3: The scanning electron microscopy images for GaFeO ₃ sintered at 900°C (a), 1000°C (b), 1100°C (c), 1200°C (d).	150
Figure-7.4(a): The x-ray absorption spectra at Fe K-edge for GaFeO ₃ samples sintered at different temperatures 150, (b): The polynomial fitted plot of Fe oxidation state vs Fe K-edge energy for the standard samples.	151
Figure-7.5 (a): The optical absorption spectra for GaFeO ₃ at various sintering temperatures.	153
Schematic-1: Represents the illustration of spin allowed and forbidden transitions.	156
Figure-7.6: Room temperature Raman spectrum for the prepared series of samples (a). Figure-(b) represents the deviation from normal Lorentzian Raman line shapes.	157
Figure-7.7: The representative's temperature dependent Raman spectrum for GaFeO ₃ sintered at 1200°C.	158
Figure-7.8: The variation of Raman modes corresponding to 175 cm ⁻¹ for GFO-900 (a), GFO-1000 (b), GFO-1100 (c), GFO-1200 (d) as a function of temperature.	159
Figure-7.9: The defect induced localization of excitons due to increase in EPC with increasing the defects at different sites by laser irradiation.	164
Figure-7.10(a): The simulated optical spectra for PrFeO ₃ and Cr doped PrFeO ₃ by using full-potential linearized augmented plane wave (FP-LAPW)	165

method within the framework of density-functional theory.

Figure-7.11(c): Variation of $1/d^2E/dk^2$ (a quantity proportional to effective mass) for pure and Cr doped PrFeO_3 between R and Γ k points (near band gap region). 166

Figure-7.12: The estimated values of Urbach focus for pure PrFeO_3 (a) and 25% Cr doped PrFeO_3 (b). 167
The relatively lower value of Urbach focus (hw_F) than that of hw_{\max} is a signature of exciton localization (figure-2(a)) while vice-versa is true for delocalization (figure-7.12(b)).

List of Tables

Table 2.1: The variation of unit cell parameters as a function of Cr-doping in PrFeO_3 . The number in open bracket represents the last digit error bar.

Table 6.1: The widths (standard deviations), σ , of the Gaussian nuclear momentum distributions underlying the Doppler-broadened recoil peaks of individual nuclear species present in $\text{PrFe}_{0.5}\text{Cr}_{0.5}\text{O}_3$ and PrFeO_3 (see text for details).

Table 6.2: The values of the QE variable measuring the ‘quantumness’ of individual nuclear species present in $\text{PrFe}_{0.5}\text{Cr}_{0.5}\text{O}_3$ and PrFeO_3 .

Table-7.1: The variation of unit cell parameters as a function of sintering temperature for GaFeO_3 . The numbers in open bracket indicates the last digit error bar.

List of Abbreviations

Rare earth orthoferrites	RFeO ₃
Dzyaloshinskii-Moriya	DM
Density functional theory	DFT
X-ray diffraction	XRD
Diffuse reflectance spectroscopy	DRS
X-ray absorption near edge spectroscopy	XANES
Antiferromagnetic	AFM
Ferromagnetic	FM
Multiferroics	MF
Magneto-electrics	ME
Magneto-dielectrics	MD
Charge transfer	CT
Raman spectroscopy	RS
Full-Width Half Maxima	FWHM
Charge-coupled device	CCD
Kubelka-Munk Function	F(R)
Urbach Energy	E _u
Fermi energy	E _f
GaFeO ₃	GFO

Chapter 1

Introduction

1.1 Introduction and origin of the problem

This chapter gives a brief introduction to the field of Cr-substituted rare-earth orthoferrites and its importance in science and technology. The inclusion of different chemical elements at different sites results in distortion of the perovskite structure away from the ideal cubic structure. A review of Fe site substitution in orthoferrites is presented and a justification for the dopant and parent compounds, which have been selected for the present work, is given in this chapter.

In “Silicon Age,” silicon transistors form the core of much of the microelectronics and from the last few decades, the properties of silicon devices have been investigated to an astonishing extent, which enables the transformation of bulky old desktop computers into sleek smartphones[1–4]. But this revolution will soon be forced to come to culminate as the fundamental physical limits set by the size of the atoms that make up the silicon material. Therefore, the steady march toward smaller, faster, lighter products with more functionality can’t continue within our existing framework. The use of microelectronics is increasing worldwide so rapidly that may consume more than half of the world’s energy by information technologies within a couple of decades[1–3]. In order to improve and maintain the global standard of living, we need new multifunctional materials. Further, the demands of high-performance and multitasking micro-electronic devices that can store and share information in an easier and faster way motivate scientists for searching the new materials with multi-functional properties for reading, writing and data sharing processes[2,3]. The new emerging technology “Spintronics”, which explores the control of the magnetic (spin) state by electric fields and/or vice versa can solve this problem[2,3,5–7]. Such

approaches relies on exploiting the intrinsic spin of electron in addition to the electronic charge to encode the information[2,3,5–7]. The coexistence of magnetization and electric polarization may allow an additional degree of freedom for next-generation electronics devices such as solid-state transformers, high sensitively *dc* and *ac* magnetic field sensors, electrically tuneable microwave filters, and electromagnet-optic actuators[2,3,5–7].

As technology advances, the increasing need for data storage and advancement in miniaturization suggest an end to the era of conventional data storage techniques[8–10]. To overcome this upcoming crisis, modern technology is emerging as a solution these days. It is worth noting here that the efficiency of conversion of primary energy (coming from natural gas, burning coal or nuclear power plants) is around 35-40% and most of the (10-15%) primary energy is consumed by the electronic devices[11]. This consumption is expected to be growing exponentially in the next few years, putting more stress on our resources for energy production[11]. To overcome this issue, we need new materials or new emerging technology as an alternate solution to this problem[2,3,5–7]. The searches for new materials for various electronic applications have dominated the research worldwide particularly after the development of silicon-based tiny integrated circuits. The tiny as well as energy-efficient electronic devices are now dominating the research worldwide and replacing the conventional electronic circuit elements. The efforts are now being made to develop spin-based electronic devices and in these directions perovskite oxides are of great interest[3,5,6,12].

The perovskite type oxides are very popular and are being investigated due to their interesting underlying physics[13–16] as well as technological importance[17–20]. Indeed, the complex and unusual properties have been observed in these perovskite oxides due to the presence of strong coupling between the electric charge, spin, and lattice degrees of freedom. One of the intriguing properties shown by these transition metal oxides is their multiferroic (MF) behavior *i.e.* exhibit coexistence of at least two primary ferroic orders (amongst ferroelectric,

ferromagnetic and ferroelastic orderings) in a single-phase compound. These materials become attractive as they can have intrinsically combined magnetic, ferroelectric, and elastic properties. In MF, the magnetism and the ferroelectricity can occur independently or may have a strong coupling between these ferroic orders. Depending upon the said coupling multiferroics are divided into two groups, which can be categorized as type-I and type-II multiferroics. The type-I MF covers those materials in which magnetism and ferroelectricity have a different origin and appears independently of one another, though there may be a little (weak) coupling between them, while type-II multiferroics exhibit strong coupling between ferroelectric and magnetic orders[3]. The interaction between two ferroic orders in these materials would result into control of electric polarization with the application of applied magnetic field or in magnetization control of electric field[21]. Broadly, in type-I multiferroics, the transition temperature of ferroelectric ordering (T_{FE}) is generally higher as compared to that of the magnetic ordering (T_M) whereas T_{FE} and T_M are same in case of type-II MF's. There is a quest for searching the materials that exhibit such kind of coupling near to room temperature (RT), which further increases the possibility of scheming RT based novel MF devices[2,3].

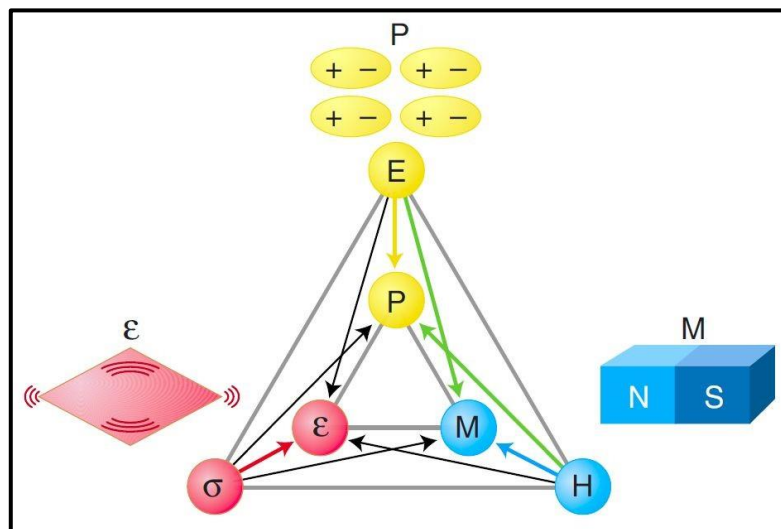


Figure-1.1: Relationship between ferroelectricity (polarization P and electric field E), magnetism (magnetization M and magnetic field H), and ferroelasticity (strain and stress), their coupling and mutual control in multiferroics[3].

1.2 Multiferroics: a beautiful but challenging multi-polar world

Aside from the potential applications, the fundamental physics of multiferroic materials is rich and fascinating[1,3,22]. It is well known that the conventional mechanism of ferroelectricity in perovskites requires the B site to have an empty d^0 orbital (such as Ti^{4+} , Ta^{5+} , W^{6+})[3], which is incompatible with ferroic orders (presence of partially filled electrons in the d -orbitals of transition metals, such as Cr^{3+} , Mn^{3+} , Fe^{3+})[3,5]. However, not all experimental and theoretical results support the argument that ferroelectricity and magnetism are incompatible, and integration of them seems to be possible. First, the well-known Maxwell equations which govern the dynamics of the magnetic field, electric field and electric charges, express that rather than being two independent phenomena, electric and magnetic fields are intrinsically and tightly coupled to each other. A varying magnetic field generates an electric field, whereas the motion of charge *i.e.* electric current produces a magnetic field. Second, the formal equivalence of the equations governing the electrostatics and magnetostatics in polarizable media; describes the similarities in the physics of ferromagnetism and ferroelectricity, such as their hysteresis behavior in response to the external field and anomalies (thermal, structural, mechanical, dielectric and magnetic) at the critical temperature[23]. These coupling phenomena or/and similarities in terms of the electric dipoles and spins endorse the integration of ferroelectricity and magnetism into single-phase materials and hence the possibility of MD/ME effect. This effect can be linear or/and non-linear with respect to the external fields, and can be described in terms of ME coupling coefficients which are given in the following equations. Thermodynamically, the ME effect can be understood in terms of expansion of free energy within the framework proposed in Landau-Devonshire theory[23];

$$\begin{aligned}
 F(E, H) = & F_0 - P_i^s E_i - M_i^s H_i - \frac{1}{2} \varepsilon'_{ij} \varepsilon'_{ij} E_i E_j - \frac{1}{2} \mu_0 \mu_{ij} H_i H_j - \alpha_{ij} E_i H_j \\
 & - \frac{\beta_{ijk}}{2} E_i H_j H_k - \frac{\gamma_{ijk}}{2} H_i E_j E_k + \dots
 \end{aligned} \tag{1.1}$$

here, F_0 is the ground state free energy, P_i^s and M_i^s are the components of spontaneous polarization P^s and magnetization M^s , subscripts (i, j, k) stand for three components of a variable in spatial coordinates, E_i and H_i are the components of electric field E and magnetic field H , respectively, μ_0 and ϵ_0 are magnetic and dielectric susceptibilities in vacuum, ϵ_{ij} and μ_{ij} are the second-order tensors of dielectric and magnetic susceptibilities whereas ϵ_{ijk} and μ_{ijk} are referred as the third-order tensor coefficients. Importantly, α_{ij} is the component of tensor α which is designated as linear ME coupling coefficient (or simply linear ME effect) and corresponds to the induction of magnetization by an electric field or polarization by a magnetic field.

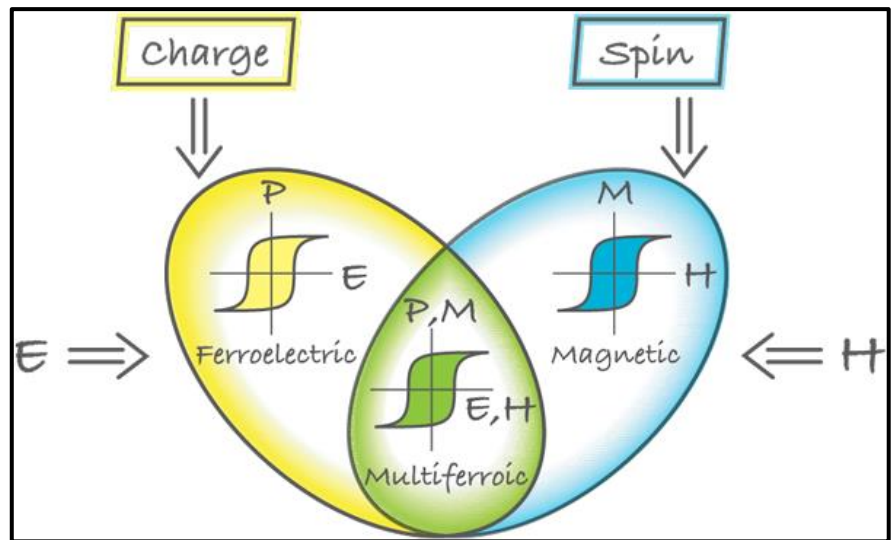


Figure-1.2: The combination of ferroelectrics and magnetic properties in multiferroics. Ideally, the electric polarization of ferroelectrics in an electric field displays the usual hysteresis (yellow), and magnetization has a similar response to applied magnetic field (blue). In multiferroics there is a simultaneously ferroelectric and ferromagnetic, then there is a electric response to applied magnetic field, or, vice versa[22].

The rest of the other such coupling coefficients in the preceding equation are corresponding to the high-order ME effects parameterized by tensors γ and β [2,23]. The partial differentiation of equation 1.1, w.r.t. H_i will lead to magnetization[23]

$$M_i(E, H) = -\frac{\partial F}{\partial H_i} = M_i^s + \mu_0 \mu_{ij} H_j + \alpha_{ij} E_j + \beta_{ijk} E_i H_j + \frac{\gamma_{ijk}}{2} E_j E_k + \dots (1.2)$$

whereas the differentiation of F w.r.t. E_i leads to polarization

$$P_i(E, H) = -\frac{\partial F}{\partial E_i} = P_i^s + \varepsilon'_0 \varepsilon'_{ij} E_j + \alpha_{ij} H_j + \frac{\beta_{ijk}}{2} H_j H_k + \gamma_{ijk} H_i E_j + \dots (1.3)$$

The above equations 1.1 to 1.3 are treated as the theoretical framework that describes ME coupling and provides the correlation between polarization (magnetization) and external magnetic (electric) field.

1.3 Major challenges with the existing multipolar materials and Background

The coexistence of magnetization and electric polarization may allow an additional degree of freedom for next-generation electronics devices[24–27]. The prerequisite is a simultaneous presence of ferromagnetic and ferroelectric orders well above room temperature. There are certain number of materials in which ferromagnetism and ferroelectricity coexists, but the coupling between these two properties is not always large enough at room temperature (RT)[2]. For bulk ceramics, combining the different ferroic orders is a tricky problem as such properties are exclusive in most materials. Distinctly, the controlling of magnetization (electric polarization) through external electric (magnetic) field *i.e.* the coupling between external magnetic (electric) field with electric dipoles (magnetization) is known as magneto-electric (ME) effect. Moreover, the magneto-electric effect is an independent phenomenon though it may coexist along with multiferroicity in specific compounds[2]. But, there are following major issues with existing literature of Magneto-dielectric (MD)/ME and multiferroic materials.

In multiferroics, the magnetism and the ferroelectricity can occur independently or may have a strong coupling between these ferroic orders[3]. On the other hand, the ferroelectricity can also be induced by the canting of magnetic spins or spin chirality[3]. It is interesting to note

that the origin of observed ferroelectric behavior in these MF materials is not attributed to the off-center displacement of small transition metal (TM) cation as in the case of BaTiO₃[5]. Such kind of ferroelectricity requires the *d* orbitals of the TM cation are formally unoccupied. In the case of LaFeO₃, it has been reported that the exchange striction between rare earth and Fe moments would result to ferroelectricity in these materials below magnetic ordering temperature (T_{N1}) as depicted in figure-1.3. Even though these materials exhibit fascinating properties, but the mechanism responsible for the appearance of MD/ME phenomenon and/or multiferroicity is still not very clear and no such generalized mechanism has been established till now. For example, the ME coupling in TbMnO₃, Ni₃V₂O₈, MnWO₄ and BaNiF₄[3,28–31,31] has been attributed to inverse Dzyaloshinski-Moriya (DM) effect, which works in systems with non-collinear spin structures (usually spiral magnetic structures; in which spins rotate around an axis perpendicular to the propagation vector of the spiral) and needs the direct action of the spin-orbit interaction[1,3,28–31,31,32].

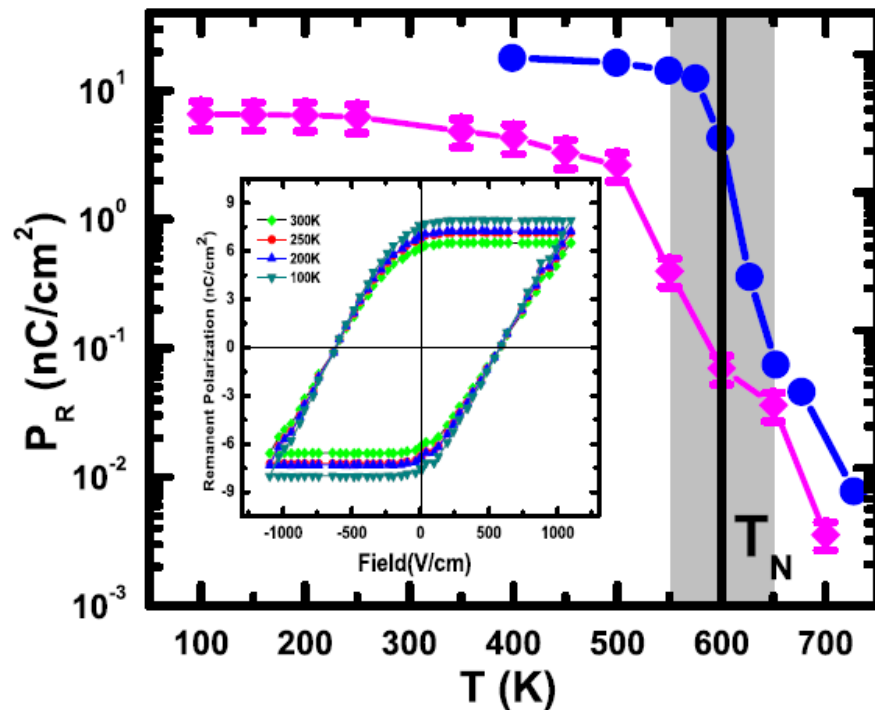


Figure-1.3: The variation of the remanent polarization as a function of temperature in orthorhombic LuFeO₃[33].

On the other hand, the MD/ME effect is generally witnessed with the application of high magnetic field of the order of several tesla and/or below room temperature (RT)[20,31,32] which inhibits low-field and RT applications of these materials. Magnetic reversal of ferroelectric polarization or dynamical and resonant coupling between magnetic and electric dipoles is reported in CoCr_2O_4 [34]. Both ferroelectric and magnetic order parameters were supposed to be changed simultaneously across these multiferroic domain walls (MFDWs). The multiferroic nature of CoCr_2O_4 is depicted in Figure 1.4 and it has been understood in terms of the dynamics of MFDWs and the electromagnon or electrically driven magnetic resonance. The ferroelectricity in particular, has been attributed to conical spin modulation for CoCr_2O_4 [34]. Further, simultaneous occurrence of long-range ferroelectric and incommensurate magnetic order has been observed across phase transition in $\text{Ni}_3\text{V}_2\text{O}_8$ [35] as shown in Figure 1.5.

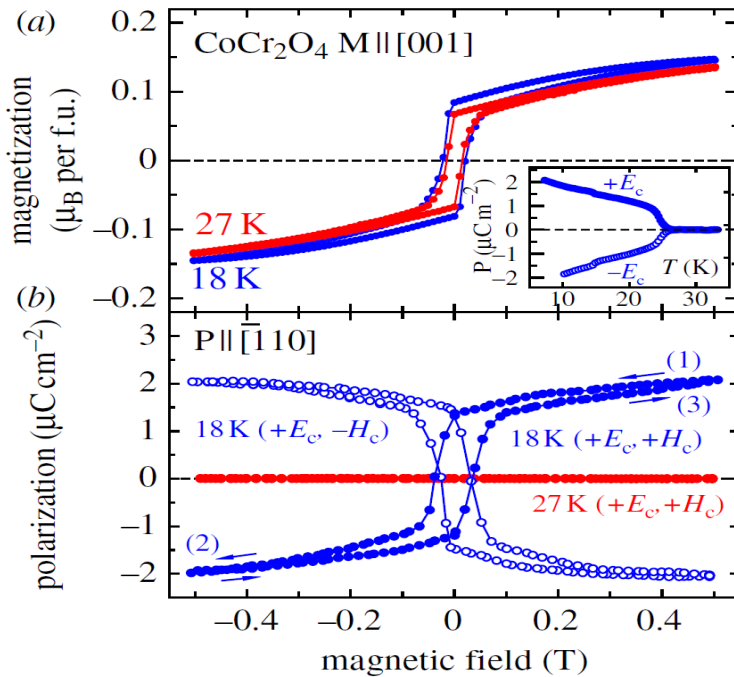


Figure-1.4: Magnetic field dependence of (a) magnetization and (b) electric polarization measured for CoCr_2O_4 above (27K) and below (18K) the ferroelectric transition temperature ($T_S=26\text{K}$). For measurements of polarization, the magnetic field was scanned between $+H_c$ and $-H_c$, for each magnetoelectrically cooled state prepared with (E_c, H_c) and $(E_c, -H_c)$, as represented by closed and open circles[34].

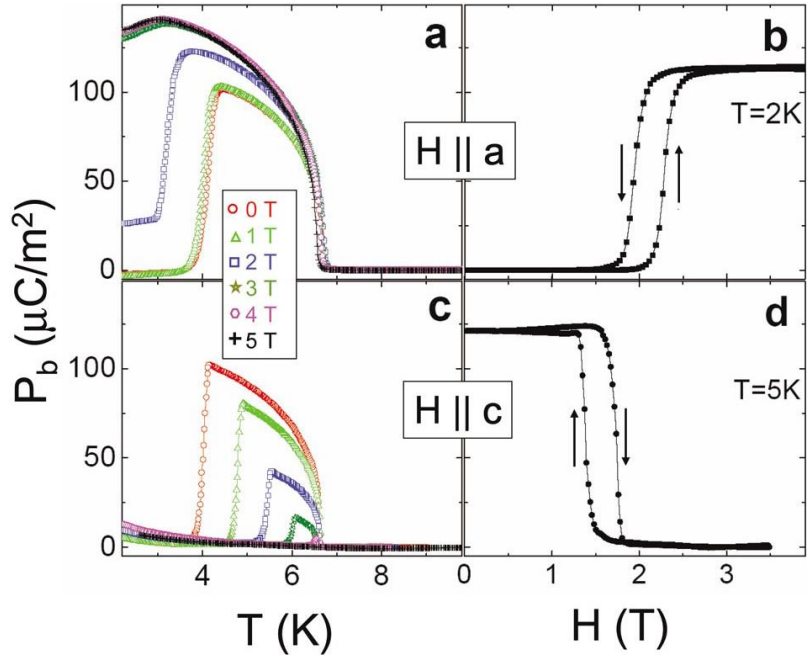


Figure-1.5: Promotion and suppression of electric polarization by applying magnetic fields in NVO. Temperature and magnetic-field dependence of electric polarization along the b axis for H along the a [frames (a) and (b)] and c [frames (c) and (d)] axes[35].

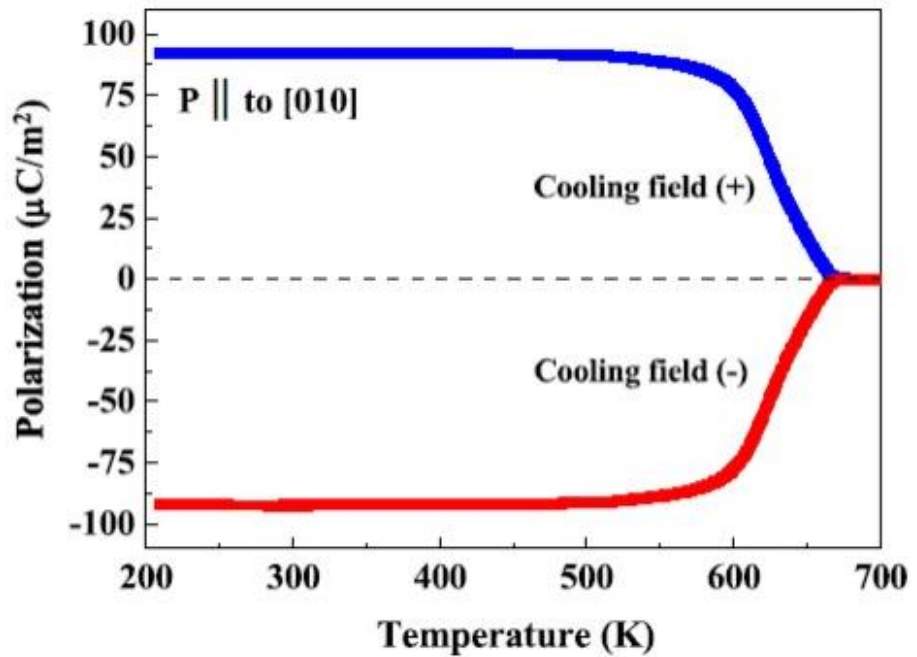


Figure-1.6: Temperature-dependent spontaneous polarization along [010] as a function of temperature for SmFeO₃[36].

The observed ferroelectricity was considered to be appeared only in the phase for which magnetic ordering breaks inversion symmetry and

hence assigned as magnetically driven. Recently in SmFeO_3 ferroelectric features (as shown in figure-1.6) has been reported below T_{N1} (670 K)[36], which is completely surprising due to the reason that R ion moments orders at very low temperatures (<15 K). Therefore, exchange striction mechanism cannot solely explain the cause of polarization observed at high temperatures. There has been an intense debate on the exact origin of multipolar order in these oxides[37–40]. Hence, the probing of local structure would be very important to understand the observed new class of multipolar order in these materials. Most importantly, these properties depend on the structural parameters such as octahedra tilts and distortions, various bond lengths, bond angles, and atomic displacements, *etc.* Therefore, in the present work, an attempt has been made to contribute to the field of multiferroic perovskite RFeO_3 in terms of their ferroelectric and magneto-dielectric properties.

1.4 Perovskite-type Oxides

The term perovskite is generally used for the class of compounds which have the crystal structure type of calcium titanate. The Ruddlesden-Popper phase (RPP) is the most general form of perovskite structure consist of two-dimensional perovskite slabs interleaved with cations[41]. The general form of RPP is $\text{A}_{n+1}\text{B}_n\text{X}_{3n+1}$, where A and B are cations and X is an anion (i.e. Oxygen), and n is the number of the layers of octahedra in the perovskite-like stack[41]. The RPP series of the form $\text{A}_{n+1}\text{B}_n\text{X}_{3n+1}$ are essentially made of n ABX_3 perovskite separated by a AO layer. Here, $n = \infty$, corresponds to the ABX_3 type perovskite type structure, while $n = 1$ and $n = 2$ correspond to K_2NiF_4 and $\text{Sr}_3\text{Ti}_2\text{O}_7$ type structure of RPP series respectively. The perovskite was first discovered by Gustav Rose and is named after Russian mineralogist L. A. Perovski. The general chemical formula of materials ($n = \infty$) crystallizes in the perovskite structure is ABX_3 [41,42]. In the case of perovskite-type oxides, the X site is occupied by oxygen O. Thus, the perovskite oxides usually represented with a general formula ABO_3 , where A site occupied with a larger ionic radius element such as rare-earth, alkali or alkaline

earth metal ions and B site is generally occupied by transition metals. A site atom is situated at the corner and B site atom remains at the centre of the unit cell forming three-dimensional BO_6 octahedra with six Oxygen atoms at the centre of each face[41,42]. An ideal perovskite structure adopts a cubic symmetry and crystalizes in the space group $\text{Pm}\bar{3}\text{m}$ as shown in Figure 1.7.

The perovskite structures have received great research interest because it can accommodate a large number of chemical elements into their structure. The doping of small chemical impurity introduces a significant amount of structural distortions and modifies the electronic structure of these materials to a large extent. Thus, the physical properties of perovskite oxides can be engineered.

The perovskite structure crystallizes in several different distorted lattices depending upon the structure flexibility of stabilization. The stability of the structure is defined in terms of Goldschmidt tolerance factor t based on the ionic radii of the A and B site cations and used as a figure of merit to characterize perovskites[43]. The tolerance factor t is calculated according to equation (1.4) using the radii of the ions for the general perovskite formula ABO_3 [43].

$$t = \frac{r_A + r_O}{r_B + r_O}, \quad (1.4)$$

where r_A , r_B and r_O are the ionic radii of A, B and Oxygen atoms respectively.

For an ideal cubic perovskite structure tolerance factor t considered to be unity[43]. In practice, the tolerance factors of cubic perovskites range from 0.8 to 1. The structural distortion in the lattices will increase with a deviation of t to either higher or lower values than *unity*. The distortion from the ideal perovskite structure can lead to a lower symmetry from cubic to orthorhombic, rhombohedral, tetragonal, monoclinic, or triclinic. The orthorhombic and rhombohedral lattices are the most common for the perovskites. The perovskite structure is assumed to be stable if the tolerance factor lies between 0.8 and 1.

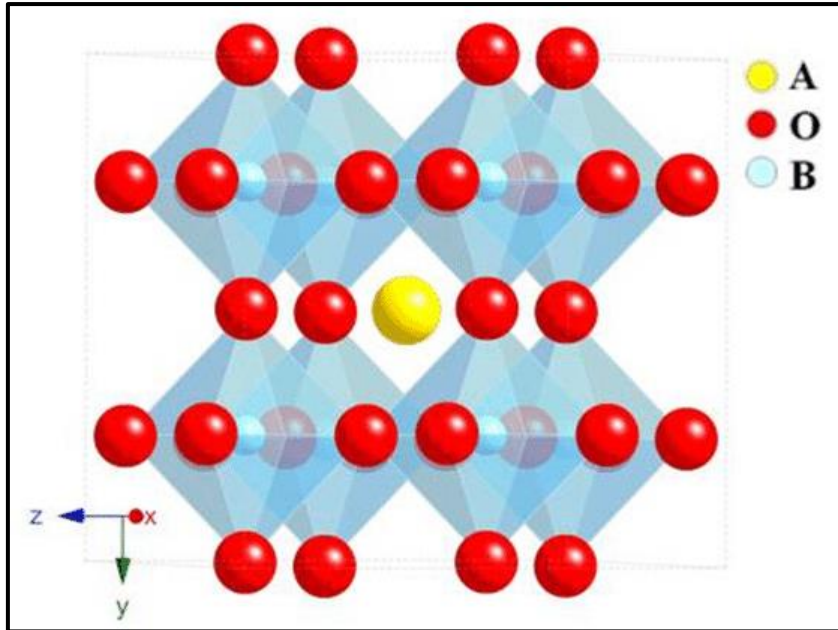


Figure 1.7: The ideal cubic $Pm\bar{3}m$ structure of ABO_3 perovskite oxides. A is a large 12-fold coordinated cation and B is a small 6-fold coordinated cation[41].

The incorporation and combination of different elements into the structure lead to distortions of the perovskites from the ideal cubic structure. A vast amount of work has been done to investigate the various types of distortions such as rotation or tilt of BO_6 octahedra, displacement of the cations and the distortion of the BO_6 octahedra and their consequence on the crystal symmetry[3,43–45]. The variety of the elements that can be incorporated into the perovskite system and the structural flexibility with respect to distortions lead to various properties such as metal-insulator transition, colossal magnetoresistance, multiferroic behavior *etc*[1–4]. The ABO_3 perovskite-type oxides which possess the more than one property at the same time can be potentially useful for technological applications and will be discussed in detail in the following section.

1.5 Rare-earth Orthoferrites

Recently, rare-earth orthoferrites (RFeO_3) perovskites have attracted the attention of scientific community worldwide due to the coexistence of electric and magnetic polarization in these materials. These compounds have been explored for novel applications in spintronic devices[45–47], high dielectric constants materials[48,49], ultrafast magneto-optical storage devices[50–52] and as magneto-dielectric devices[53–55] and fast lasting optical switches[53,54]. These materials also have much potential for photocatalytic activity, solid oxide fuel cells, gas sensors, detection of ozone in monitoring environment *etc.*[50–52]. All members of the RFeO_3 family are known to possess a canted antiferromagnetic structure arising from spins of the Fe^{3+} ions. The antiferromagnetic ordering of the iron ions occurs at Neel temperature (T_N) between 650K and 750K. Several orthoferrites have shown a spin reorientation at lower temperatures. The existence of electric polarization in RFeO_3 samples which possess a centrosymmetric space group ($Pbnm$) is an interesting phenomenon because it requires a space group with a non-centrosymmetric point of inversion. RFeO_3 is again retrieving the interest of researchers because of their fast spin dynamics, electric field control of magnetization and vice versa. Another interest is the possible application of these materials in devices because some of these compounds have recently shown to exhibit spontaneous electric polarization, which makes them multiferroic possibly due to their magnetic structure.

All the compounds of rare-earth orthoferrites group have been studied by using neutron diffraction and it was found that at room temperature the iron lattices are aligned antiferromagnetically and each iron ion having six anti ferromagnetic nearest neighbours[40]. On the other hand, the repeatability of the results of measurements of the weak ferromagnetism by the various groups suggests that it is an intrinsic property of these materials[40,51,56,57]. Dzyaloshinskii[56] and Moriya[58] have explained the origin of the weak ferromagnetism *via* antisymmetric exchange interaction and the detailed discussion on

magnetic exchange interactions will be elaborated in the following sections.

1.6 Magnetic interactions in rare earth orthoferrites:

1.6.1 Antisymmetric Exchange Interaction

It was shown by Dzyaloshinskii[56] and Moriya[58] “the combination of low symmetry and spin-orbit coupling give rise to an anisotropic exchange interaction” known as Dzyaloshinskii-Moriya (DM) interaction or antisymmetric exchange interaction. The presence of DM interaction favour’s a spin canting in magnetically ordered systems which leads to intrinsic weak ferromagnetism in an antiferromagnetic system like RFeO₃.

The DM interaction explains the contribution to the total magnetic moment due to exchange interaction between two neighboring magnetic spins S_i and S_j slightly canted with each other as shown in Figure 1.8. In DM interaction the Hamiltonian can be expressed according to equation (1.5) given below[56,58]

$$H_{DM} = \mathbf{D}_{ij} \cdot (\mathbf{S}_i * \mathbf{S}_j), \quad (1.5)$$

where \mathbf{D}_{ij} is a coupling constant and defined by the equation (1.6)

$$\mathbf{D}_{ij} \propto \mathbf{r}_i * \mathbf{r}_j, \quad (1.6)$$

The equation (1.6) implies that the direction of \mathbf{D}_{ij} is perpendicular to the plane of the triangle formed by the two neighbouring spins with a ligand as shown in figure 1.8. Here, \mathbf{r}_i and \mathbf{r}_j are the vectors connecting to the ligand from two neighboring spins S_i and S_j respectively. For RFeO₃ perovskite-type structure the direction vector of D_{ij} must be perpendicular to the Fe–O–Fe plane and the symmetry restriction. In more general terms, if we consider ABO₃ perovskite structure, the A and B sites substitutions lead to the oxygen octahedra tilt and distortion. This octahedral tilts and distortions move each oxygen ion of B-O-B configuration away from 180°

or from middle point, gives rise to a bent in B-O-B bond and break the axis rotation symmetry. The change in B-O-B bond angle will modify DM interaction as a relativistic correction to the super-exchange interaction between the B ions. This suggests that the antisymmetric B-B exchange interactions can be changed by changing structural tilts and (or) distortions in the ideal perovskites.

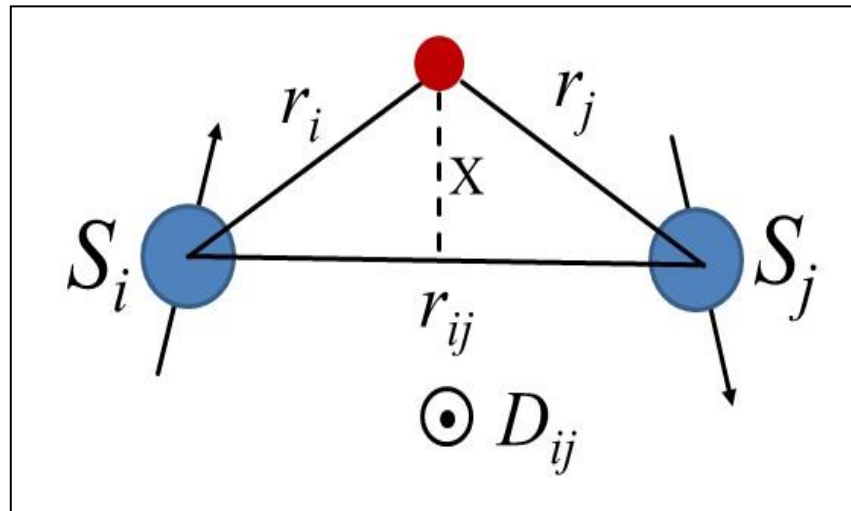


Figure 1.8: Schematic Showing the DM vector and antisymmetric exchange interaction between two near-neighbour spins[56,58].

The antisymmetric exchange interaction plays important role in understanding and the multiferroic behaviour of an antiferromagnetic system like $RFeO_3$. It explains not only the origin of the net ferromagnetic moment but also it is important for the understanding of magnetic field induced electric polarization in multiferroic materials.

The magnetic properties of any magnetic material depend on the strength of exchange interactions between the magnetic moments associated with the ions in it. The presence of two magnetic ions, rare earth (R^{3+}) and iron (Fe^{3+}) in the $RFeO_3$ samples would lead to the existence of complex magnetic interactions such as $R^{3+}-R^{3+}$, $Fe^{3+}-Fe^{3+}$, and $R^{3+}-Fe^{3+}$. According to Goodenough-Kanamori (GK) rule, the $Fe^{3+}-O-Fe^{3+}$ interactions are antiferromagnetic due to the reason that π -bonding formed by the three half-filled t_{2g} electrons and σ -bonding formed by two half-filled e_g electrons interacts through the super-exchange interactions, which follows the Hund's rule and are antiferromagnetic in nature. Particularly, Fe^{3+} moments in these orthoferrites exhibit a canted

antiferromagnetic (AFM) state and show a weak ferromagnetic moment below their magnetic ordering temperature. Therefore, the moments parallel to c-axis cancel out, whereas the moments perpendicular to c-axis gives rise to a weak spontaneous magnetization. It should be noted here that in RFeO₃, R-O-R and Fe-O-Fe interactions take place at <10 K and ~640K-750K respectively. Another distinctive magnetic transition observed in these materials is spin reorientation (SR) transition in which the direction of moments of Fe³⁺ sub lattice changes from one crystal axis to other. The spin reorientation transition in RFeO₃ takes place due to the domination of R³⁺-Fe³⁺ interactions over the antiferromagnetic Fe³⁺-Fe³⁺ interactions. The crystal symmetry of orthoferrites allows three magnetic configurations for the Fe³⁺ moments labeled as Γ_4 (G_x, A_y, F_z), Γ_2 (F_x, C_y, G_z) and Γ_1 (A_x, G_y, C_z). The SR transition observed in these samples is attributed to the transformation of high-temperature T₄ (G_x, A_y, F_z) phase to T₂ (F_x, C_y, G_z) phase observed at low temperatures[40]. Among the above-mentioned magnetic configurations, Γ_1 does not exhibit net magnetic moment, whereas the configurations Γ_2 and Γ_4 display weak ferromagnetic moments along x and z directions respectively.

1.6.2 Zener Double Exchange Interaction

The ferromagnetic behavior in mixed oxidation state perovskite systems such as in La_{1-x}Ca_x(Mn_{1-x}³⁺Mn_x⁴⁺)O₃ was first explained by Clarence Zener through Zener double exchange interaction. The spatial distribution and electron density of the Fe 3d and oxygen 2p orbitals strongly influence the strength and nature of the magnetic exchange interactions. Figure-1.9 represents the schematic of the double-exchange mechanism for La_{1-x}Ca_xMnO₃ system, where Mn ions remain in the mixed valence states of Mn³⁺ and Mn⁴⁺. When the oxygen p orbital overlaps with the empty orbital of Fe at one end and a half-filled orbital at another end, then the resulting magnetic coupling will be ferromagnetic and is known as double exchange interaction. Zener explained this phenomena in the following way: (1) intra-atomic exchange is strong so that the only important configurations are those

where the spins of each carrier is parallel to the local ionic spin (2) the carrier does not change their spin orientation when moving; accordingly they can hop from one ion to the next only if the two ionic spins are not antiparallel (3) when hopping is allowed the ground state energy is lowered because of strong Hund's rule coupling and results to lower energy for ferromagnetic configurations. The hopping of electrons has also a dependency on Mn-O-Mn bond angle. If the bond angle is 180° , the strong overlap between d-orbitals transition metal and p-orbitals of oxygen results to strong the interaction and vice-versa[59].

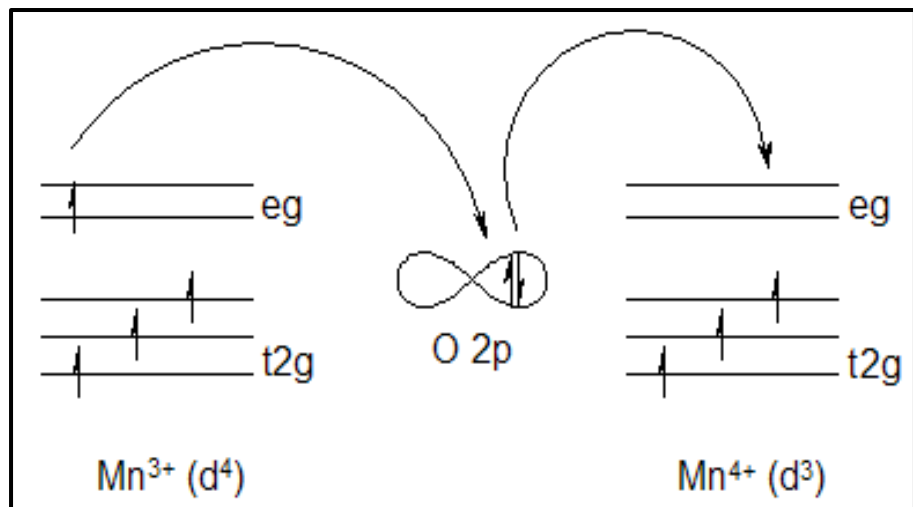


Figure 1.9: An example of double exchange interaction in case of manganite's[59].

1.6.3 Super exchange interactions

Super exchange interaction can be described as the interaction between the magnetic moments of two nearest neighboring ions mediated through a nonmagnetic ion. The idea that exchange can indeed proceed by means of an intermediate nonmagnetic atom was first pointed out by Kramers in 1934[60] and the theory was more formally developed by Anderson in 1950[61] and thereafter it was termed as Kramers-Anderson superexchange interaction. These interactions are of importance in ionic solids such as the transition metal oxides and fluorides, where the bonding orbitals are formed by the 3d electrons of TMO and the 2p valence electrons of the diamagnetic oxygen or fluorine atoms. Later in 1950, Goodenough[62] developed a set of semi-empirical rules to summarize the type of interactions, depending on the

type of orbitals (hybridized) that overlap with the oxygen 2p orbitals. These rules are based on the symmetry relations and the electron occupancy of the overlapping atomic orbitals, as illustrated for Mn atom in the Figure 1.10.

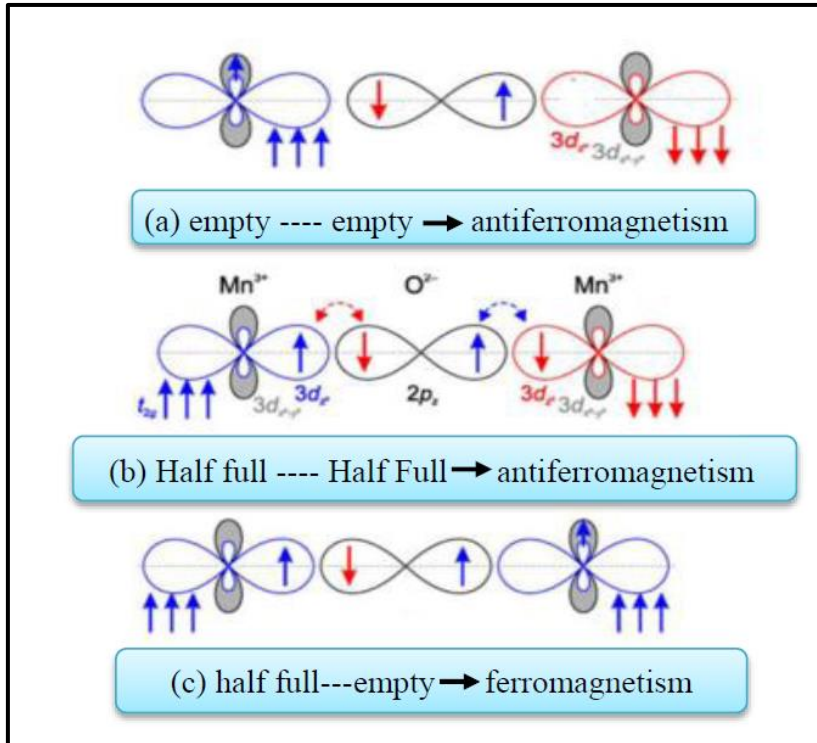


Figure 1.10: Illustration of the superexchange interaction in a magnetic oxide. The bonding involves symmetry adapted metal 3d and oxygen 2p orbitals. (a) and (b) show the spin configurations for an antiferromagnetic (AFM) ground state and (c) shows the spin configurations for a ferromagnetic (FM) ground state[62].

According to these rules:

(a) If both neighboring Mn ions point their empty orbitals toward O^{2-} , then the Mn-Mn separation is small and the exchange interaction between Mn ions is AFM, as shown in figure 1.10 (a).

(b) If both neighboring Mn^{3+} (half filled) ions points their filled atomic orbitals towards O^{2-} , then the Mn-O-Mn bond length will be large and the coupling between Mn ions is AFM, as shown in figure 1.10 (b).

(c) If one of the two neighboring Mn^{3+} ions (half filled) points its occupied orbital (atomic orbit) towards O^{2-} and the other points its unoccupied orbitals, then Mn-O-Mn separation will be large and the manganese ions will have FM coupling, as shown in figure 1.10 (c).

1.7 Possible signature of magnetism by Raman scattering

An important aspect of a real spin system is the interplay between the spin interactions on lattice dynamics commonly known as spin-phonon or magneto-elastic coupling. As discussed in the earlier sections, the strength of the magnetic interactions strongly depends on the bond length and bond angles and any variation in the local arrangement of the magnetic ions results into alteration in the exchange interactions, which hints that there exists a coupling between lattice and spin. Granado *et al.*[63] modeled the spin-phonon coupling in perovskite oxide $\text{La}_{1-x}\text{Mn}_x\text{O}_3$ by considering the superexchange interactions based on nearest neighbor $\text{Mn}_i\text{--Mn}_j$ spin Heisenberg Hamiltonian is given as:

$$H_{Spin} \approx -\Sigma J \langle S_i \cdot S_j \rangle \quad (1.7)$$

where J is the superexchange integral, $\langle S_i \cdot S_j \rangle$ is the scalar spin correlation function and the summation in j ($i, j > 0$) is over three nearest neighbors of the i^{th} Mn ion such that each pair is not considered twice. The anomalous behavior in the Raman shift around magnetic transition is related to the magnetic ordering induced renormalization of phonon modes and is proportional to spin-spin correlation function $\langle S_i \cdot S_j \rangle$ [63,64]. According to mean field theory, phonon renormalization function and magnetization is associated as follows[63,64]:

$$\Delta w(T) = w(T) - w_{anharmonic}(T) = \gamma \frac{M^2(T)}{M_{sat}^2(T)} \quad (1.8)$$

where, $M(T)$ is the temperature-dependent magnetization per Fe-site ions, $M_{sat}(T)$ indicates the saturation magnetization and γ epitomizes the spin-phonon coupling strength.

Raman spectroscopy (RS) is a widely used fast and non-destructive spectroscopic tool to explore the vibrational properties[65–67]. It is now well established that RS is one of the versatile technique, not only to investigate the local structural changes but also to study the orbital mediated charge transfer mechanism, presence of disorder and magnetic ordering temperature in perovskite systems[44,68,69]. However, the magnetic properties by RS can be investigated only if

spin-phonon coupling has a clear influence on phonon scattering. At magnetic ordering temperature, the alignment of spins encourages strain in the material by means of magnetostriction, which causes a distortion in the lattice and thus couples to the phonon system.

1.8 Crystal field splitting

Essentially, the crystal field is defined as the average electric field produced by neighboring ions in the crystal. The basic building block around which the physical properties of the orthoferrites and orthomanganites are the Fe/MnO₆ octahedron as depicted in figure-1.11, where a schematic of the perovskite structure is shown. In ferrite's, Fe ions are surrounded by six oxygen anions, which acts as an intermedator and due to the crystal field of oxygen ions, the five *d* levels split into lower triple t_{2g} (d_{xy}, d_{xz}, d_{yz}) and upper double e_g (d_{z2}, d_{x2-y2}) levels. This phenomenon occurs primarily due to electrostatic considerations between the *d* electrons and the surrounded oxygen anions. The energy of t_{2g} and e_g levels is decided by the directions of oxygen anions and *d* levels. The t_{2g} levels point in the directions between the ions, where the field are less and therefore stabilized at lower energy. The doubly degenerated e_g orbitals point directly at these ions and are shifted to higher energy. In perovskite containing trivalent Fe ions bonded with O, the energy of crystal field splitting is smaller than the paring energy of two electron, hence Fe ions in RFeO₃ always remains in the high spin state. An electron can be filled in d shell as per Hund's rule will occupy the lowest available orbitals compatible with the total spin associated with the metal ion. In case of orthoferrites, the orbital excitations take place within the 3d-orbital are basically transitions from (t_{2g})_{III} to (e_g)_{II} orbitals, so called *d-d* or crystal-field transitions and are well-known probes of the local electronic structure[70–72]. These crystal field transitions are highly sensitive to lattice distortions and contain crucial information about electron-lattice coupling (EPC)⁹. In the case of transition metal oxides, the width of *d-d* transition is believed to be governed by EPC[70–74], which further can be due to a change in density of states (DOS) near to the energy of *d-d* transitions[70,72]. The

changes in DOS ($\rho(E) \propto \sqrt{E - E_g}$ for $E > E_g$, else $\rho(E) = 0$)⁹ can be assumed a direct dependency on the spectral line width of such transitions and in EPC. The electron-phonon interaction is one of the fundamental interactions in semiconductors and this interaction between electronic and vibrational excitations plays an important role in optoelectronic properties, transport processes, linear or nonlinear optical absorption in semiconductors/insulators, *etc.*[75–77]. A systematic study on the strength of the EPC in semiconducting materials is important for practical applications and fundamental scientific understanding[78,79]. Keeping this in view, in the last part of the thesis, a detailed investigations on the effect of defects/non-stoichiometry generated on $d-d$ transitions have been studied experimentally as well as by density functional theory (DFT) implemented in WIEN2k package.

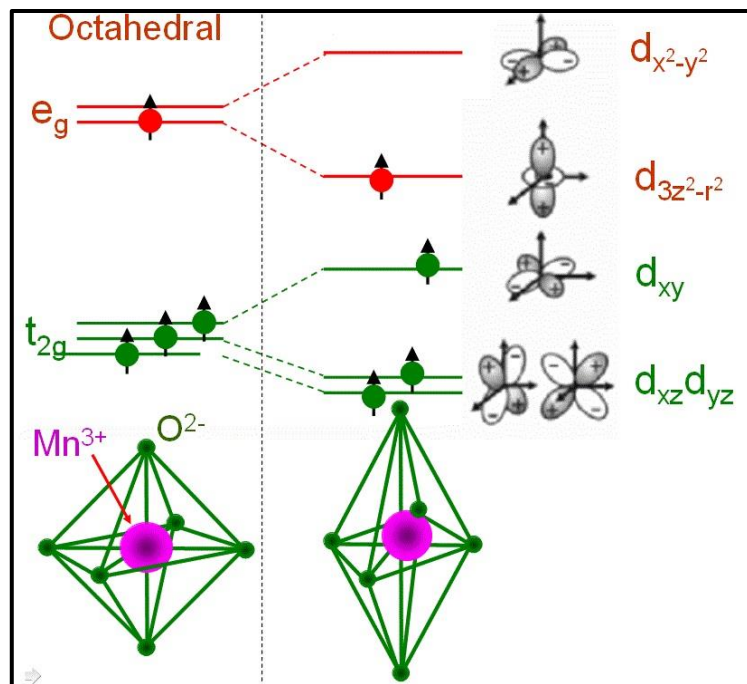


Figure 1.11: The schematic representation for crystal field transitions and Jahn-Teller distortion in manganites[80].

Further, Jahn and Teller have shown that if the electronic state of a nonlinear molecule is orbitally degenerate, then there is always at least one vibrational coordinate along which the molecule may distort, so as to lower its energy. For example, in case of $\text{Fe}^{4+}/\text{Mn}^{3+}$ ion, due to presence of a single electron in the double degenerate e_g levels can

distort the octahedron such as to lift the degeneracy of the levels. This is known as the Jahn-Teller distortion and is known to be crucial in stabilising various physical properties exhibited by the manganites.

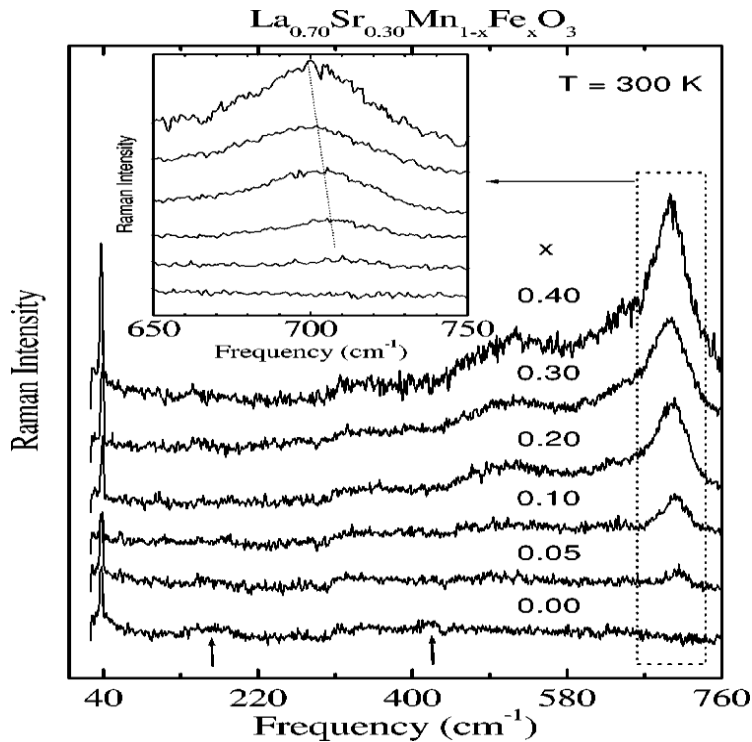


Figure-1.12: The Raman spectra taken at room temperature for different $La_{0.70}Sr_{0.30}Mn_{1-x}Fe_xO_3$ samples. The Raman mode arising around 710 cm^{-1} is attributed to the lattice rearrangement, which takes place by shining a photon having energy of the order of charge transfer in mixed oxidation state systems[83].

It is well known that in the case of manganite's, orbitons can be excited in Mn ions having JT configuration (d^4 electronic state)[81] through Jahn-Teller (JT) polaron hopping mechanism. The presence of JT distortion in Mn^{3+} results in the splitting of e_g orbital into states with lower energy which produces the potential to be minimum. The altering in the potential traps the electrons in that orbital, known as self-trapping, which increases the lifetime long enough for it to interact with lattice distortion[82] and results to generation of new Raman modes as depicted in figure-1.12. However, their consequences in the JT inactive materials have not been explored so far in detail. Therefore, in the present work, an attempt has been made to contribute in the orbital facilitated generation of Raman modes in JT inactive materials.

1.9 The quantification of electron-phonon coupling by Fano model

As discussed in the earlier section that the changes in the density of states (DOS) near to the energy of d-d transition affects the EPC and Raman spectroscopy is an effective tool to quantify the strength of EPC[84–86]. In a crystalline material, only transitions with $k \approx 0$ is allowed by the momentum selection rule of first-order Raman scattering[87,88]. However, disorder relaxes the Raman selection rule for $k \approx 0$, which allows first-order Raman scattering by phonons of larger k values and causes the asymmetric broadening of the phonon modes in the Raman spectra[89–91]. In crystalline materials a highly symmetric Raman spectrum with Lorentzian line shape is observed[4]. Any deviation from Lorentzian line shape can be due to various reasons associated with electron/exciton interactions, quantum confinement effects etc.[4]. The asymmetry (where asymmetry ratio is defined as γ_2/γ_1 , where γ_1 and γ_2 are the half widths on the lower and higher side of the Raman spectrum in the Raman line shape can be explained by the Fano model[4]:

$$I(\omega) = I_0 \frac{(q+y)^2}{1+y^2} \quad (1.9)$$

The term y is equal to $(\omega - \omega_p / \Gamma(\omega))$, ω_p is renormalized phonon frequency, and $\Gamma(\omega)$ is the width of Raman mode (line-width). The quantity $1/q$ (q =asymmetry parameter) is proportional to EPC[4] and its variation as a function of number of irradiated pulses (n) is illustrated in Table-1. Lesser the $|q|$ value, stronger is the interaction between continuum states and discrete phonons. The parameter $1/q$ is directly related to the number of free charge carriers in semiconductors[4] and disorder present in the system[92,93]. The schematic illustration of Fano interference is shown in figure-1.13.

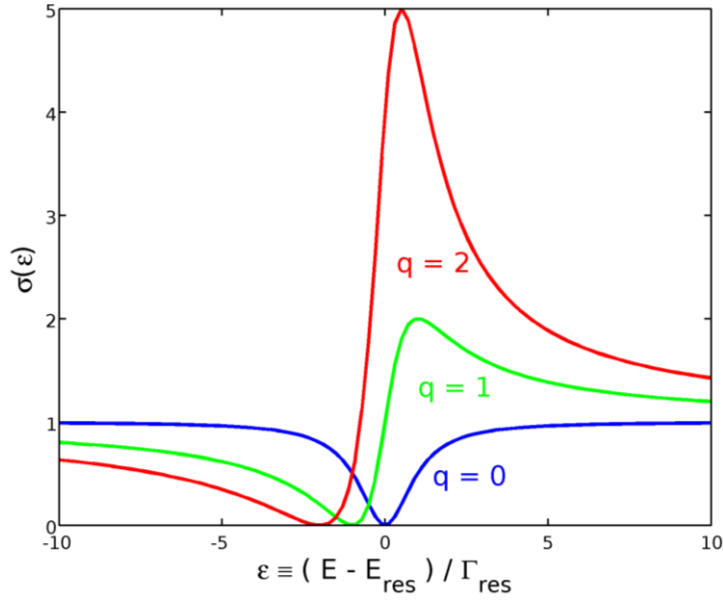


Figure 1.13: The Fano lineshape of the absorption cross near resonance energy E_r of a discrete state buried in the continuum for various values of the q parameter[94].

1.10 The probing of electronic disorder by optical absorption spectroscopy

The exponential variation of optical absorption near band edge (Urbach tail states/ Urbach energy) is one of the well-known feature of optical absorption spectra and the same has been observed in the optical spectra for almost all kinds of crystalline semiconductor materials, amorphous semiconductors and highly disordered non-metallic glassy systems [95–99]. The said tail states are very important from practical applications such as the improving electronic properties, improvement in absorption spectra in solar cells[100] and broadening of the emission spectra in light emitting devices etc.[101]. Generally, it is believed that Urbach energy (E_U) is a measure of total electronic disorder present in the system and scales with temperature and structural disorders (structural disorder induced by defects, vacancies, static strain fields, doping) etc.[99,102,103]. The character of the localized states observed in between the valance band and conduction band in optical spectroscopy for disordered semiconductors is a problem of importance with a history dating back to the fifties[103]. It has been understood earlier that band tail states in amorphous semiconductors arise due to the

thermal disorder[99]. The variation of absorption coefficient near the band edges was firstly observed by Urbach in 1953 in studying the optical properties of indirect band gap silver halides and described it in the following form[99]:

$$S = \frac{\partial(\ln(K))}{\partial(h\nu)} = -1/kT \quad (1.10)$$

where S is slope of exponent, K is absorption coefficient, $h\nu$ is photon energy and k is Boltzmann's constant. It was clear from equation given by Urbach that S has only temperature dependence and has no reliance on material properties. But experimentally it was observed that slope of exponent is a property of material as well as a function of temperature. Further Martienssen redefine the Urbach rule and wrote the same in following form [21]:

$$\alpha(E, T) = \alpha_0 \exp \left[\sigma \left(\frac{E - E_{00}}{kT} \right) \right] \quad (1.11)$$

Hence behavior of α is referred in literature as **Urbach-Martienssen's rule**. Where; α_0 and E_{00} are the constants determined by extrapolating linear region from $\ln(\alpha)$ versus E curves at a given temperature T.

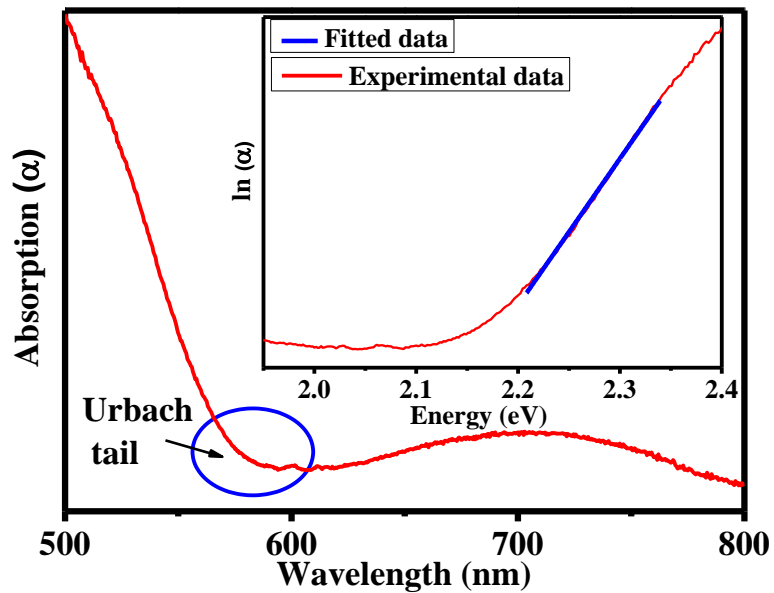


Figure-1.14: The exponential variation of absorption coefficient near the band edge. The inverse of linear fitting of logarithmic of (α) vs energy plot gives the Urbach energy as shown in the inset[44].

The quantity $E_u = \frac{kT}{\sigma}$ is termed as Urbach energy and can be approximated by linear fitting between logarithmic of (α) vs energy. The temperature and doping at different sites is expected to create the structural and on-site electronic disorder in the system. Such random potential fluctuations are known to create energy levels near band edge, which are termed as electronic disordered states and can be measured in the form of Urbach Energy[104,105].

1.11 Motivation and objectives

1.11.1 Selection of material and a brief modus operandi

Perovskite oxides have become the most versatile compounds in research of oxides[59,106,107]. Among these perovskites oxides, rare earth ortho-ferrites ($RFeO_3$) have gained enormous interests due to the possibility of its technological importance and interesting physics[108,109]. These oxides have been proposed for potential candidates in spintronic devices, chemical sensors[46,47], precession excitation induced by terahertz pulses, high dielectric constants materials[48,49], magneto-dielectric devices[110], ultrafast magneto-optical storage devices[50,52], magnetism induced ferroelectric devices *etc.* in last few years. The technological attention towards the renaissance of these materials was due to their potential in scheming microelectronic devices which consume lower energy[1]. In an unexpected complement to this original direction, these materials are now showing promise as materials for *harvesting* energy[1]. Also, astonishing progress has been done from the last few decades in exploring these materials for bio-medical applications such as enhanced scaffolds for tissue engineering and magnetically assisted *in vivo* targeted drug delivery[1]. The importance of these materials now enormously exceeds the applications envisaged at the start of the multiferroics rebirth at the turn of this century. This progress culminates in 2018 with the demonstration of a prototype *magnetoelectric spin-orbit logic* (MESO) device which consume substantively lower amount of energy than existing architectures[1,111]. The foremost challenge for the

multiferroics research community is to minimize the voltage needed to switch the ferroelectric state of the magnetoelectric component to around 100mV from the current value of approximately 5 V. In that case, for the MESO device to be competitive, the voltage output from the spin-orbit component should be increased to hundreds of mV from its current μV values[1,111].

It has been well explored that various fascinating properties can be achieved by applying the chemical pressure at Fe-site of orthoferrites materials[12,112–114]. The $\text{RFe}_{1-x}\text{Cr}_x\text{O}_3$ compounds have shown superior physical properties, with mixed Fe and Cr at B-site, relative to the end member RFeO_3 and RCrO_3 compounds[12,112–114]. According to Goodenough-Kanamori theory, Cr^{3+} could be the best choice to replace Fe^{3+} in order to achieve the superior magnetic properties[113]. The advantage of Cr^{3+} substitution at Fe^{3+} site is that the magnetic transition temperature (T_{NI}) can be tuned near to RT, which scales the possibility of magneto-electric coupling and possibility of scheming RT based novel magneto-dielectric devices[113,115]. This adds another possibility to the multiferroic materials, making $\text{RFe}_{1-x}\text{Cr}_x\text{O}_3$ ideal multifunctional materials for future-devices[12,112–114]. In addition to this, the importance of electron-phonon interactions has been epitomized so far in colossal magneto-resistance (CMR) observed in manganite's with Jahn-teller (JT) active ions[81,106]. However, the presence of said coupling would be very interesting and its consequence in the JT inactive materials has not been explored so far in detail. *Keeping this in view, in the present thesis work Cr-substituted RFeO_3 ($\text{R}=\text{Pr}$ in present case) samples were prepared with an expectation of aforementioned intriguing properties. Additionally, the optical and magneto-elastic properties of well-known multiferroic as well as magneto-electric material GaFeO_3 have been explored in detail in this work.*

1.11.2 Probing, quantification of electronic disorder and its correlation with dissipation factor

In the starting part of the thesis, the detailed analysis of structural, optical and electronic properties has been provided for $\text{PrFe}_{1-x}\text{Cr}_x\text{O}_3$ ($0 < x < 0.20$) system. The incorporation of Cr at Fe site appears to modify the local strain field and on-site Coulombic potential, possibly due to dissimilarity in the atomic number (Z) and ionic radii [77,105,116–118]. These two effects, collectively, result in an increment in the electronic disorder [77,105,116–118]. The major contributing factors that influence the values of electronic disorder arise due to presence of inhomogeneity caused by compositional fluctuation, structural disorder, thermal disorders and anharmonicity [99,102,119]. The contributing factors in the mentioned disorders can be modified by varying the rotation and distortion of the BO_6 octahedra (tilt angle disorder) and Fe-O bond lengths (structural disorder). In these ABO_3 perovskites, the tilts and distortions of BO_6 octahedra are the key to control various physical properties [120]. Hence, it is very important to explore the structural characteristics such as bond lengths, bond angles, octahedral distortion of $\text{PrFe}_x\text{Cr}_{1-x}\text{O}_3$ system with great accuracy to understand the physics and related properties of these samples. Therefore, this work has been started with the detailed structural characterization of Cr substituted PrFeO_3 samples using experimental and theoretical investigations.

Further for any practical applications, the dielectric loss ($\tan\delta$) must remain sufficiently small [121]. The mixed oxidation state of transition metal ions in these materials due to vacancies at various sites is believed to be responsible for the observed high values of dielectric loss in these materials [57,122]. Thus, in order to achieve real application of these materials, it is extremely important to have basic understanding of various contributing factors to the $\tan\delta$. For any dielectric material, it is believed that the dielectric loss consists of two parts (1) frequency dependent flipping of electrical dipole and (2) the leakage current. For samples having *Centro symmetric* crystal structure, it is believed that the hopping of electron possibly through disorder/defect states are

responsible for leakage current[123,124]. For semiconducting/insulating materials the leakage current is due to the defects/vacancy present²⁸ in the sample and is related to the band gap as; $\sigma = \sigma_0 \exp \exp \left(-\frac{E_g}{2kT} \right)$ (For Intrinsic case $E_a=E_g/2$)[121]. The random distribution of defects and doping at lattice sites, introduces potential fluctuations that creates energy levels within the forbidden energy gap or close to the valance/conduction band[104,105]. These energy levels are also termed as electronic disorders near the band edge and are measured in the form of Urbach Energy[104,105]. These statistical effects are known to distort the unperturbed density of states which are particularly important in determining the number of free carriers and hence, their contribution to the leakage current/dielectric loss[121]. Further, the disorder induced by Cr doping has been estimated by performing the optical absorption spectroscopy measurements. It is not easy to quantify these disorders exactly with the help of such absorption spectroscopy techniques alone³². In this regard, the Raman measurements have been carried out, which provides information associated with relative difference in the octahedral tilts and anharmonicity values through Raman modes. The main aim of this work was to develop a comprehensive understanding on the impact of $\text{PrFe}_{1-x}\text{Cr}_x\text{O}_3$ on the optical and also, phononic properties. The understanding of disorder created by Cr-substitution at Fe-site are very crucial for practical applications such as enlightening the electronic properties[121], broadening of the emission spectra in light emitting devices³⁵ and enhancement in absorption spectra of solar cells[100] *etc.*. Hence, the dependence of the electronic disordered term Urbach energy on temperature and doping is of scientific and technological interest³⁵. From last decades, various researchers have probed the electronic structure of various transition metal oxides with the help of optical spectroscopy and the said technique is known for its potential to probe electronic disorder (thermal, polar, chemical, structural and due to defects *etc.*) present in the sample[120]. The major contribution in Urbach energy is from various kinds of disorders present in the system and the said energy increases if disorder in the system increases[120].

Therefore, in the first part of the work, the structural optical and dielectric properties have been explored using experimental and theoretical investigations.

1.11.3 Strain and orbital mediated electron-phonon coupling induced new Raman modes in mixed Fe-Cr based orthoferrites

In the second part of thesis, the detailed investigations on the origin of strain induced disordered modes and orbital facilitated charge transfer originated Raman modes in $\text{PrFe}_{1-x}\text{Cr}_x\text{O}_3$ have been done. PrFeO_3 , in accordance with Raman selection rules, exhibits 24 first order Raman active modes and because of the presence of inversion symmetry, Fe does not contribute to scattering. Nevertheless, the inversion symmetry of FeO_6 octahedra can be destroyed by structural disorders induced by doping, which may result in formation of additional modes in Raman spectra as previously observed in case of centro-symmetric ionic crystals[125,126]. In the case of doped PrFeO_3 , new Raman modes have been observed and some experimental efforts have been made earlier by some research groups to understand the origin of these phonon modes[44,127,128]. For example the Raman mode around 510 cm^{-1} has been attributed to be due to strain induced structural disorder[120] and the mode at around 660 cm^{-1} predicted to be due to orbital mediated charge transfer between two transition metal ions[114] but there exist no unanimous consensus amongst the scientific community about the origin of the this Raman mode[12]. It is important here to note that the generation of new Raman mode in Raman spectra could be attributed to various factors such as orbital mediated EPC[129], symmetry breaking[44], strain induced structural disorder[44] *etc.* However, high-resolution synchrotron x-ray diffraction studies investigations on these samples suggest that there is no signature of change in the structural symmetry with Cr substitution[44]. Hence, the occurrence of new phonon modes cannot be due to the change in structural symmetry and strong evidence through rigorous experimental and theoretical

investigations is needed to establish the origin of the above-mentioned Raman modes. Hence, to explore the possible origin of orbital mediated charge transfer modes OAS, resonant and power dependent experiments along with the first principle density functional theory calculations were carried out and these discrepancies have been understood in terms of strain and orbital mediated EPC generated Raman modes in the present work. These analyses provide us a basic understanding of the interplay between the electron-lattice coupling and would prove useful for fundamental studies of the relation between global and local effects in correlated systems[130,131].

1.11.4 Role of spin-phonon coupling and Pr atoms displacement in natural and magnetic field induced polar order

Spin-phonon coupling has an important role in several intriguing phenomena related to transition metal oxides in the context of multiferroics and spintronics, and the coupling between lattice degrees of freedom and spin has been known to arise from the exchange interactions. It is now well accepted that the presence of unpaired transition metal *d*-electrons and rare earth *f*-electrons in these RFe/CrO₃ oxides spectacle many striking effects arises from the coupling between two magnetic sublattices[40]. It is reported that the exchange striction between rare earth and Fe/Cr moments would result in ferroelectricity in these materials below magnetic ordering temperature (T_{N1}). Recently in SmFeO₃, ferroelectric features have been reported below T_{N1} (670 K)[132], which is completely surprising due to the reason being R ion moments ordering at very low temperature (<15 K). Therefore, the exchange striction mechanism cannot solely explain the cause of polarization observed at high temperatures. The anisotropic interactions between R and Fe³⁺ ions may play an important role in inducing the net dipole moment in these oxides. Naveen *et al.*[133] explained the observed polar order in terms of distortion of R³⁺ ion due to R-Cr exchange field. Bhadram *et al.*[134] reported that the spin-phonon coupling encourages stabilization of the polar order in RFe/CrO₃ oxides.

Therefore, there has been an intense debate on the exact origin of ferroelectric order in these oxides. Hence, the probing of local structure would be very important to understand the electron–lattice dynamics and to observe a new class of ferro-electricity in these materials. To address this issue and its correlation with the observed ferro-electric behavior in detail, temperature and magnetic field dependent phonon spectra were studied to understand the possible origin of polar natural order in mixed Fe-Cr based orthoferrites. The basic physics of combined space-inversion symmetry and time-reversal breaking mean that these materials can be considered to be the model systems for realizing fundamental laws of nature that have analogous mathematical descriptions[1]. Further, attempts have been made to realize the magnetic field induced polar order in $\text{PrFe}_{0.50}\text{Cr}_{0.50}\text{O}_3$ at room temperature.

1.11.5 Defect induced d-d transitions and its correlation with electron (spin) lattice coupling in GaFeO_3

Another interesting feature of RFeO_3 (or GaFeO_3) compounds is the charge neutral crystal field $d-d$ transition, which appears due to the transition of t_{2g} electron to e_g level of same or near neighbor Fe atom[74,135,136]. In stoichiometric samples, Fe is having d^5 electronic configuration and such transitions are expectedly *spin* forbidden[6], moreover, it is well known that the high temperature sintered samples generally exhibit deviation from exact oxygen stoichiometry, which causes oxidation state of Fe to vary (*i.e.* Fe to be present in +2 or +4 oxidation state) [57]. Fe^{+4} and Fe^{+2} have electronic configurations d^6 and d^4 , respectively[108,127,137], and electron can be easily transported to the (e_g) level of the same or a nearby Fe atom[74,135,136], which intensifies crystal field $d-d$ transitions. In d^5 systems, $d-d$ transitions should be forbidden as per the electric dipole selection rule ($\Delta l = \pm 1$) and also, the spin selection rule ($\Delta S = 0$). It is seen that the strength of $d-d$ transitions is about a thousand times weaker than that of the dipole-allowed $p-d$ transitions ($\text{O}-2p$ and $\text{Fe}-3d$). In the present case, the intensity of such transitions is much higher; which strongly suggests the

possibility of spin permitted transitions[138]. As discussed in earlier section that these crystal field transitions are highly sensitive to lattice distortions and contain crucial information about EPC. The changes in DOS ($\rho(E) \propto \sqrt{E - E_g}$ for $E > E_g$, else $\rho(E) = 0$) can be assumed a direct dependency on the spectral line width of such transitions and in EPC[108,127,137]. A systematic study on the strength of the EPC in semiconducting materials is important for practical applications and fundamental scientific understanding[78,79]. Therefore, in the last part of this work, we have investigated the possible origins of *d-d* transitions and its correlation with EPC and magneto-elastic properties has been studied using optical absorption spectroscopy and Raman scattering experiments.

1.12 Organization of the Thesis

The present chapter covers a brief introduction to this work. The remaining chapters of the thesis are summarized as follows:

Chapter 2: Experimental Techniques used

This chapter gives a description of the characterization and synthesis techniques used during course of this work. The sol-gel synthesis method has been used to synthesize the samples and will be discussed in detail in this chapter. The important characterization techniques such as synchrotron x-ray diffraction (SXRD), diffuse reflectance spectroscopy (DRS), x-ray absorption spectroscopy (XAS) valence band and Raman spectroscopy techniques has been used for structural, optical electronic and vibrational properties characterizations *etc.*.

Chapter 3: Synthesis, Structural, electronic and optical Properties of Cr-doped PrFeO₃

In this chapter, the detailed analysis of structural, optical and electronic properties has been provided. The details about the synthesis and its structural properties in terms of Fe-O-Fe bond angles, Fe-O bond lengths, FeO₆ octahedra distortions, *etc.* have been provided in this chapter. The optical and electronic properties in correlated materials are strongly controlled by these parameters. The optical properties such as optical band gap and electronic disorder term (Urbach energy) of

prepared series of samples have been examined in detail. Further, OAS has been used to probe the origin of dielectric loss in prepared series of samples.

Chapter 4: Strain induced disordered phonon modes in Cr-doped PrFeO₃

The present chapter has been devoted to exploring the origin of octahedral distorted new Raman modes around 510 cm⁻¹ in PrFe_{1-x}Cr_xO₃. In order to further confirm the appearance of this Raman mode, FeO₆ octahedra has been distorted by KrF Excimer laser irradiation, which in turn result to formation of additional mode at 510 cm⁻¹. Further, a systematic correlation between crystallographic strain, Raman line width, disordered parameter (σ) and Urbach energy is also provided in this chapter.

Chapter 5: Orbital mediated charge transfers originated Raman modes: A brief experimental and theoretical investigations

In this chapter, the possible origin of orbital facilitated new Raman mode in orthorhombic perovskite PrFe_{1-x}Cr_xO₃ has been investigated using resonance Raman spectroscopy and first principle DFT calculations.

Chapter 6: Origin of spin reorientation, strong magneto-elastic coupling and observed polar order in PrFe_{1-x}Cr_xO₃

In this chapter, a lot of fascinating properties such as; spin reorientation, strong magneto-elastic coupling, intrinsic and magnetic field induced polar order in PrFe_{1-x}Cr_xO₃ has been examined in detail by using temperature and magnetic field dependent Raman measurements, neutron gamma Dopplerimetry experiments, and dc magnetization measurements.

Chapter 7: Origin of charge neutral *d-d* Transitions in Pr/GaFeO₃ (3d⁵) Systems: Experiments and Theory

This chapter includes the possible origin of charge neutral crystal field (d-d) transitions in the optical absorption spectra of R/GaFeO₃ (3d⁵) samples. Our experimental and theoretical analysis suggests that the non-stoichiometry present in samples is the main origin of *d-d*

transitions peak in the optical spectra of R/GaFeO₃ ($3d^5$) samples and so does in d^5 systems. Further, charge neutral crystal field ($d-d$) transitions and its possible correlation with coupling between continuum states above the optical band gap in pure and laser irradiated PrFeO₃ has been examined in detail in this chapter.

Chapter 8: Conclusions and future perspectives

This chapter summarizes the results of the present research work with concluding remarks. The possible future scope of present study has also been discussed.

Chapter 2

Experimental Detail

In this chapter, the detail about synthesis and various experimental techniques relevant to this thesis have been provided. The $\text{PrFe}_{1-x}\text{Cr}_x\text{O}_3$ ($0 < x < 1$) samples were synthesized using wet chemical/sol-gel method. The structural characterization of the prepared samples was performed using synchrotron x-ray diffraction (SXRD) and Raman scattering experiments. Optical properties were studied using UV-Vis-NIR spectroscopy. Further, the important characterization techniques such as x-ray absorption near edge spectroscopy (XANES), x-ray absorption spectroscopy (XAS) and valence band spectroscopy were used for investigations of electronic properties.

2.2 Experimental details

2.2.1 Material Synthesis technique Sol-Gel Method

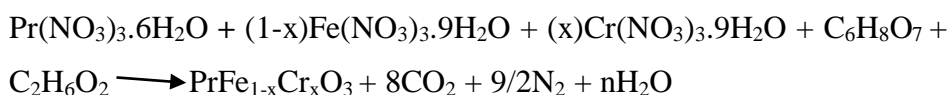
Wet chemical method is one of the well-established sample synthesis methods to prepare novel oxide ceramic and metal oxide nanoparticles. This synthesis method has a potential to control over the surface and textural properties of the materials. The sol is a molecular suspension or colloidal (according to IUPAC) solution of solid particles, whereas gel is a semi-rigid mass which remains after the evaporation of sol. Generally, metal nitrates are used as the precursor's materials in this method. The obtained gel is densified through thermal annealing. It is possible to fabricate ultra-fine ceramic powders, glassy, aerogel materials using this method. The details about the sample synthesis technique for samples under investigation are given below:

In this method, the stoichiometric amount of metal nitrates such as; $\text{Pr}(\text{NO}_3)_3 \cdot 6\text{H}_2\text{O}$, $\text{Fe}(\text{NO}_3)_3 \cdot 9\text{H}_2\text{O}$ + $\text{Cr}(\text{NO}_3)_3 \cdot 9\text{H}_2\text{O}$ were mixed in

excess of water to form stable metal chelate. Then an equimolar amount of ethylene glycol and citric acid per mole of metals ions has been added to the solution. In the synthesis process, citric acid acts as a chelating/complexing agent and ethylene glycol fulfills the process of hydrolysis and gelation¹. The resulting sol was constantly stirred and heated at 90°C until a gel like network is formed. The prepared gel was further calcinated in a furnace for 6h at 400°C and a final treatment was done at 12h at 700°C. The obtained powder was grinded and pelletized at the pressure of 10 tons to make the pellet.

It is to be noted that particularly for dielectric measurements pellets with very high density (i.e., low porosity) are needed. Hence, in order to further enhancing the intimate bonding between crystallites (i.e. minimizing the porosity), the pure phase powder is pressed in the form of a circular pellet by means of a hydraulic press and a suitable die set. Then the pellet is again heated/sintered at high temperature (well above to calcination temperature), but, below the melting point. This post-calcination sintering (below melting point), helps in (i) improving the crystal quality by minimizing defects, (ii) enhancing grain growth by reducing the total area of grain boundary (GB), and (iii) attaining the maximum possible density. Moreover, as far as present research work is concerned, the pure phase powder samples have been pelletized to form circular discs of 1 mm thickness and 12 mm diameter by applying a pressure of 15 ton. These pellets were allowed to sinter in air at 1200 °C for 24 hours. Further, these pellets were coated with silver paint and were fired at 300° C for 30 min. These pellets are then used for, almost, rest of all the measurements carried out under present research work.

The chemical reaction may be written in the following form



The main advantages of the sol-gel process are

- Lower formation temperature,
- High homogeneity,
- Precise composition control of multi-component compounds
- Synthesis with low-cost apparatus.

2.3 Characterization techniques used

2.3.1 X-Ray Diffraction

X-ray diffraction (XRD) is the most reliable, suitable and non-destructive tool to probe the structure and chemical composition of a material[44,139,140]. As the x-rays have wavelengths of order of the interatomic distances, they are more suitable to probe the structural arrangement of atoms. In XRD, an X-ray falls on the material at some incidence angle, gets diffracted through different set of atomic planes present in the crystal structure. When, both, d (spacing between successive atomic planes; also called as d -spacing) and θ (the angle of incidence of X-ray), satisfies the Bragg relation $2d\sin\theta=n\lambda$ (here, d is the inter-planer distance, λ is wavelength of incident X-ray and n is an integer), a constructive interference takes place between the diffracted waves³. The Bragg condition *i.e.*, the basic of XRD can be understood with help of a schematic ray diagram depicted in Figure 2.1. According to Bragg's law of x-ray diffraction, a radiation having a particular wavelength will constructively interfere if it is reflected between crystal planes with a path difference equal to an integral multiple of the wavelength[140].

$$\text{Path difference } (\Delta) = 2d\sin\theta = n\lambda$$

where d is the interplanar distance, θ is the angle made by incident x-rays with planes of reflection, and λ is the wavelength of x-rays and n is an integer. In this way, with the satisfaction of Bragg's condition, a peak, across the corresponding θ value appears in the intensity versus angle (2θ) curve. There are sets of planes of lattices which are indexed using Miller indices hkl and the interplanar distances d could also be written as d_{hkl} . In this way, with the satisfaction of Bragg's condition, a

peak, across the corresponding θ value appears in the intensity versus 2θ curve. The XRD pattern of each element/material is unique and can be considered as a signature of its structural phase. This uniqueness enables the XRD to identify and validate the purity of a structural phase for a given material. It is worth noting here that the intensity provides the information of the total scattering from each plane, which can be expressed as[140]:

$$I_{hkl} = K \frac{1+\cos^2\theta}{4\sin^2\theta\cos\theta} |F_{hkl}|^2 \quad (2.1)$$

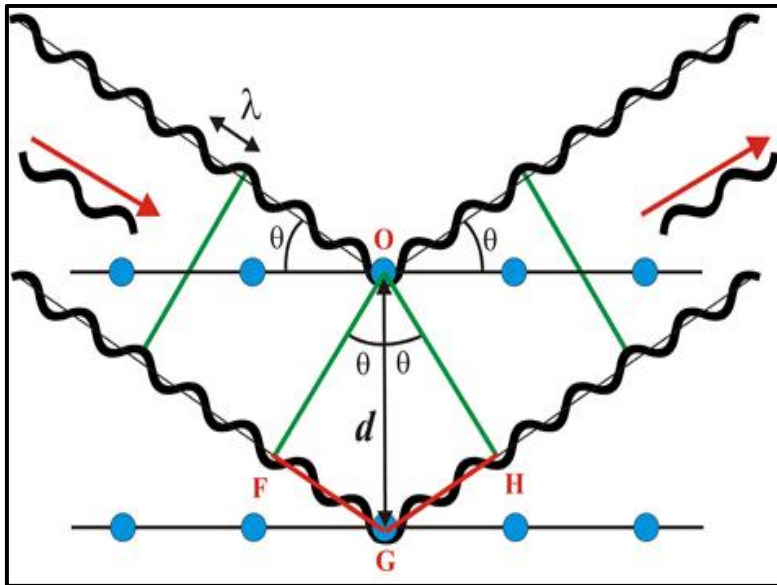


Figure-2.1: The schematic diagram of X-ray diffraction by a crystal (Reproduced from, https://commons.wikimedia.org/wiki/File:Bragg_legea.jpg).

where, K is a constant and F_{hkl} is the structure factor, which can be ascribed as:

$$F_{hkl} = \sum f_i \exp[2\pi j(hx_i + ky_i + lz)] \quad (2.2)$$

where x_i, y_i, z_i are the coordinates of i^{th} atom, f_i is the atomic scattering factor.

In the present work, primary phase-purity of the samples has been checked with the help of lab source XRD experiments on a Rigaku smart Lab diffractometer, wherein $\text{Cu K}\alpha$ ($\lambda = 1.54 \text{ \AA}$) radiation was

employed and operated at an applied voltage of 45 kV. For the calculations of structural parameters with great accuracy, synchrotron powder x-ray diffraction experiments were performed at Indian synchrotron radiation source (Indus-II), at Raja Ramanna Center for Advanced Technology Indore, India. The phase purity of synthesized samples was checked by matching the experimental data with the Joint Committee on Powder Diffraction Standards (JCPDS) database followed by Rietveld refinements. The details on the refined parameters will be discussed in Chapter 3.

2.3.2 Williamson-Hall Plot

In ideal and perfectly ordered crystals, there is a periodic arrangement of all atoms and when the Bragg condition is satisfied, corresponding diffraction peaks will be observed. These Bragg peaks would be very narrow or ideally, point like. But practically, the crystals grown in laboratory are not perfect due to **Mosaic effect** (Mosaic effect states that a crystal always consists of mosaic blocks which are misaligned relative to the idealized lattice by typically 0.3 degrees) and various kinds of disorders (dislocation, vacancy *etc.*) present in the sample, which results in broadening of XRD peaks[140]. This mosaicity is responsible for the instrumental broadening of diffraction peaks. Also, the incorporation of doping during the growth of the crystals gives significant contribution in the XRD peak broadening, which will produce the micro strain in the host lattice. Instead to these entire effects, this broadening is also a function of crystallite size. For large sized grains diffraction peaks are very sharp and vice versa. Williamson-Hall Plot is based on the idea that the broadening of the diffraction peaks has a contribution from the size broadening (β') and strain broadening (β_e).

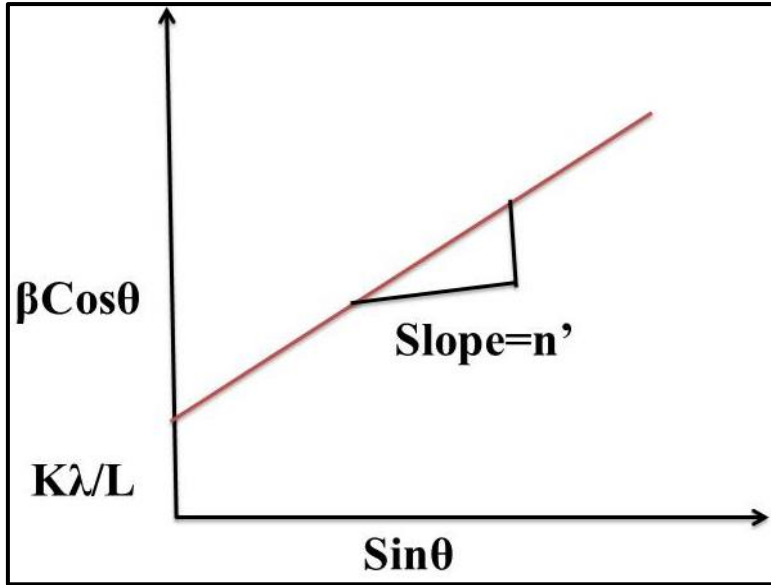


Figure-2.2 Shows systematically representation of Williamson-Hall plots.

The relation between the broadening of the x-ray peak β' is related to the size of the crystallite L is given in eq. (2.3) [139,140].

$$\beta' = \frac{K\lambda}{L\cos\theta} \quad (2.3)$$

Whereas, the Strain broadening is given by eq. (2.4)

$$\beta e = n' \tan\theta \quad (2.4)$$

Williamson and Hall assumed that if both the contributions in broadening are present then by convolution total broadening is a simple sum of these two broadenings, then we get:

$$\beta = \beta e + \beta' = \frac{K\lambda}{L\cos\theta} + n' \tan\theta \quad (2.5)$$

where β is total broadening due to strain and crystallite size contribution

Now on multiplying the eq. (2.3) by $\cos\theta$ then we get:

$$\beta\cos\theta = \frac{K\lambda}{L\cos\theta} + n'\sin\theta \quad (2.6)$$

on comparing the eq. (2.4) to general equation of straight line, we can easily obtain strain component from plot of $\beta\cos\theta$ versus $\sin\theta$ and crystallite size component from the intercept ($K\lambda/L$). The schematic representation of Williamson-Hall plot is given in figure 2.2.

2.4 Diffuse Reflectance Spectroscopy (DRS)

Diffuse reflectance spectroscopy (DRS) is a spectroscopy in which we study the light absorbed in UV and visible regions of the electromagnetic spectrum [139,141–143]. It is a well-known non-destructive technique used for the quantitative and qualitative analysis of optical properties. The advantage of DRS is that there is no need for difficult sample preparation, powder/pellet samples could be used for the purpose. It is based on the principle of diffused reflection. When light falls on the surface of a sample, it is reflected in specular and non-specular directions through multiple scattering; as shown in figure-2.3.

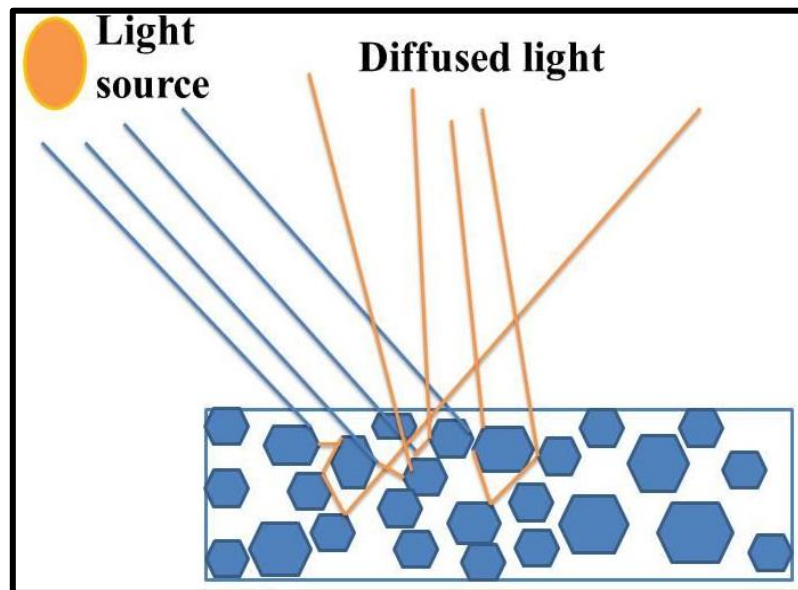


Figure-2.3: Schematic Diagram of Light Scattering from a powdered sample.

Some part of the light undergoes multiple scattering inside the sample and fraction of this part is emitted back into the detector. Since the light cannot penetrate the solid samples and is reflected from the sample

surface. As displayed in the figure, incident light scattered in different directions independent of the angle of incidence is called "diffuse reflection"[143]. When the UV-Visible light shines on the sample surface, the incident light either gets absorbed or reflected (transmission is negligible). Due to the finite absorption coefficient of the sample, as the diffuse reflected light is reflected becomes weaker i.e. loses its intensity and this loss of intensity is a function of absorption coefficient of sample which is function of λ of incident beam. This diffused reflected light is detected by the detector and give a corresponding DRS spectrum. Although various models exist but the Kubelka-Munk model is the most usual approach to interpret the DRS spectra. The Kubelka-Munk formula considers that light passing through a diffused reflecting surface can be divided into two components: (i) light flux traveling into the medium and (ii) returning to the surface. Each component loses intensity by scattering and absorption and each also adds up the intensity via scattering of its partner. For the powder or infinitely thick layered samples the Kubelka-Munk equation may be written as[121,143]:

$$F(R_{\infty}) = \frac{K}{S} = \frac{(1-R_{\infty})^2}{2R_{\infty}} \quad (2.7)$$

$R_{\infty} = R_{\text{Sample}}/R_{\text{Standard}}$. Where, R_{Sample} and R_{Standard} denote, respectively, the diffuse reflectance for the sample and for the standard (as BaSO_4 or white paper). K and S , respectively, are the Kubelka–Munk absorption and scattering functions. Since, powder samples have been used for diffuse reflectance measurements, hence, the assumption that the reflected light being scattered in a perfectly diffused manner holds true. For such cases, the scattering function S is nearly constant with wavelength and the Kubelka–Munk function can be related to the absorption coefficient (α) as:

$$F(R_{\infty}) \propto \alpha \propto \frac{(h\nu - E_g)^{1/n}}{h\nu} \quad (2.8)$$

where, $n = 2$ would correspond to direct band gap transitions, whereas $n = 1/2$ for an indirect transition ^[20].

Therefore, a plot of $[F(R_{\infty}) \times h\nu]^n$ versus $h\nu$ gives a straight line whose intercept, on energy axis, yields the value of the band gap.

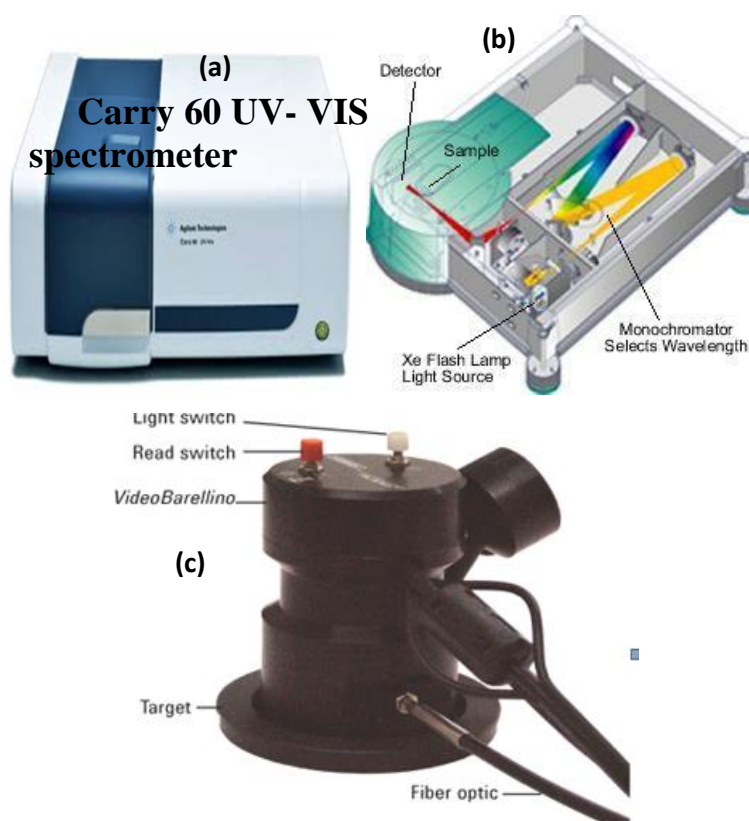


Figure-2.4: Experimental set up for diffuse reflectance measurement (a) Carry 60 UV-Vis spectrometer, (b) internal set up of 60 UV-Vis spectrometer (c) an integrating sphere attachment to detect diffuse reflectance.

We have measured DRS spectra in the present investigations using a commercial spectrometer Carry 60 from Agilent Technology, displayed in figure 2.4(a). Figure 2.4 (b) shows its internal ray diagram. In DRS measurement, a broad spectrum of UV-Vis-NIR radiation is made to fall on a rough bulk sample through an optical fiber coupled with source and the diffusely reflected light through the sample are collected using ellipsoidal lens and guided to the detector (shown in figure 2.4 (c)). From this radiation, a spectrum is obtained containing the information about the optical properties of target samples. The DRS setup available in the lab can measure the band gap with an accuracy of 0.001 eV and the detail about the data processing and the calculation of optical band gap and electronic disordered term Urbach energy will be discussed in chapter 3.

2.5 Raman spectroscopy

Raman spectroscopy is based on the scattering phenomenon wherein a monochromatic beam of radiation, incident on a sample is scattered from it[144]. When the scattering occurs with no energy loss, the frequency of the scattered beam is same as that of incident beam. This is known as Rayleigh scattering (Elastic scattering), whereas when the energy of radiation changes during the scattering process, such kind of scattering is known as Raman scattering (Inelastic scattering) [144] and was first discovered by C.V. Raman and his collaborator K.S. Krishnan in 1928[144]. Raman effect is an inelastic scattering of light from the atomic vibrations (phonons), which measures how atoms vibrate about their equilibrium positions and provides valuable information about microstructural properties like crystal structure, chemical composition and the nature of chemical bonds[44,138,144].

Raman scattering is a consequence of inelastic scattering of the incident photons, where energy is either received from or transferred to the sample. as a result of change in the vibrational and rotational modes of the sample, causing a change in the energy and therefore, the frequency of the scattered light[144]. The changes in the energy are observed in the form of discrete lines in the scattered light above and below the Rayleigh line called Stokes and anti-Stokes lines, respectively. An even smaller fraction of the scattered photons (approximately 1 in 10 million) can be scattered *inelastically*, with the scattered photons having an energy different (usually lower) from those of the incident photons, these are Raman scattered photons. Because of conservation of energy, the material either gains or loses energy in the process. When the incident photon transfers energy to the sample, the phonon excites to the higher vibrational energy level, then the change (Raman shift) in the energy (frequency) of phonons is red shifted and is known as Stokes shift. Alternatively, if a molecule is previously in an excited state, an incident photon may lead to the de-excitation of lattice phonon to lower vibrational energy level, and the corresponding scattered photon is termed as anti-Stokes shift[144].

In the present thesis, room temperature Raman spectra were recorded by using the Jobin-Yvon Horiba Raman micro spectrometer attached to two air-cooled solid-state laser kits, at 532 nm, at 785 nm and a He-Neon gas laser having excitation wavelength 633 nm[44] and with a power of less than 10 mW. For temperature dependent Raman measurements, THMS600 stage from Linkam having accuracy of 0.1 K was used. The other major components of the Raman Spectrometers are:

1. Plasma line filter: This filter is used to cut the plasma lines generated by gas laser due to formation of plasma. These plasma lines are very intense and can interfere in the Raman spectra of the specimen therefore it needs to be cut to accomplish good Raman spectra.

2. Edge Filter: An edge filter is used to exclude the Rayleigh lines as the intensity of the elastically scattered Rayleigh lines are 106 times higher than the Raman lines and it can overshadow the Raman lines therefore it needs to be removed. The edge filter ensures that only Raman Stokes lines are transmitted. The edge filter has a very narrow width of transition which allows it to measure even the smallest Raman shifts.

3. Microscope: The present system is equipped with three objective lenses 100x, 50x and 10x for the collection Raman scattered radiation. All these lenses are different by their working distance, numerical aperture and resolution. In the present work, mostly 50x objective lens is used for the low temperature measurements as in this case long working distance is required because of the height of the stage used for taking the sample to low temperature.

4. Grating: It acts as a dispersive element and separates the scattered photons on the basis of wavelength before they enter the detector. The Raman set up is equipped with the two gratings, 600grooves/mm and 1800grooves/mm. The spectral range covered by the spectrograph in one shot depends on the grating and wavelength used for the excitation.

5. CCD Detector: The output of the spectrograph is detected by the charge coupled device (CCD). It collects the scattered photons and gives an electrical signal to the computer, where the software (Labspec6.0) processes the signal by subtracting the energy of the scattered photon

from the incident photon and generates the pattern of intensity vs. Raman shift (cm^{-1}) with reference to the zero set energy of incident photon.

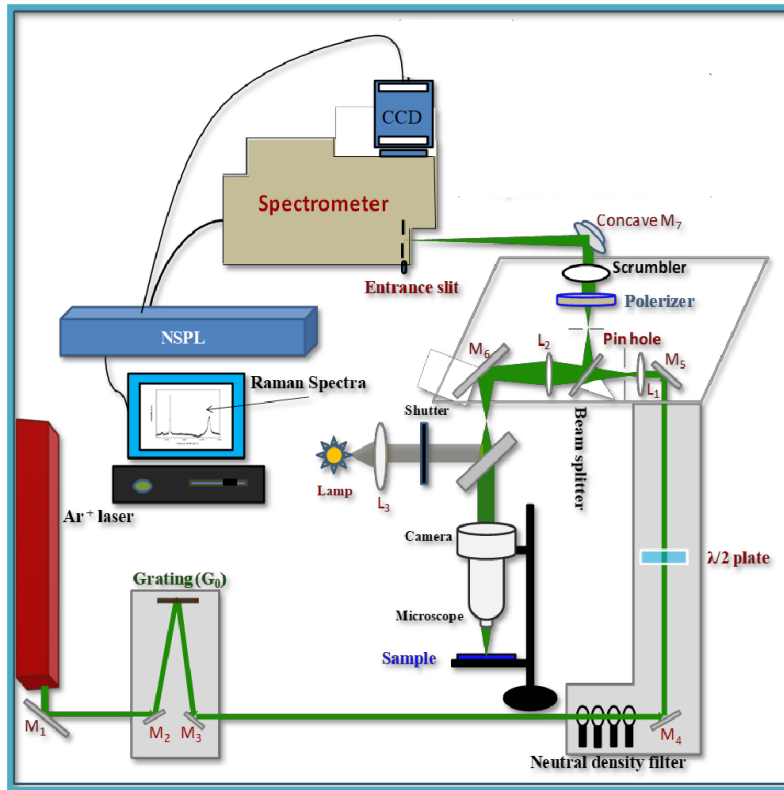


Figure-2.5: The block diagram of the major components of Raman spectrometer set up.

2.6 Dielectric properties

The dielectric materials are electrical insulators that can be polarized by the application of electric field[145]. These materials allow the passage of an electric field or flux which leads to slightly shift of electric charges from their equilibrium position and would results to the formation of electric dipoles. The mean electric dipole moment developed per unit volume of the sample is termed as polarization of the sample, which is dependent on the applied field frequency. The dielectric susceptibility χ , of a material is correlated to the polarization by $dP/dE = \epsilon' \cdot \chi$, (where $\epsilon' = 1 + \chi$). Therefore, the slope of a plot of Polarization vs Electric field depends directly on the dielectric constant

or capacitance of the material. In case of a dielectric material, the capacitance in parallel-plate geometry is defined as[146,147]:

$$C = \varepsilon_0 \varepsilon' (A/d) \quad (2.9)$$

where ε_0 , ε' , A and d stand for permittivity of free space, dielectric constant, area of the contact plates and thickness of the sample, respectively.

2.6.1 Sample Preparation for the Dielectric Measurements

For the measurement of the dielectric properties, generally disc shaped specimens (pellets) are used. The samples were properly polished to remove the roughness on the surface during sintering. After measuring the thickness and diameter of the pellets, their two parallel opposite faces were coated with silver paste to form parallel plate capacitor geometry with the material (prepared samples) as the dielectric medium.

2.6.2 Low Temperature Dielectric Experimental Setup

A homemade (designed in our own laboratory) sample-holding assembly (see Figure 2.6) with the provision of cooling up to liquid nitrogen temperatures and vacuum upto 10^{-3} mbar (or even lower), was used to place the sample[148]. The more detail about the experimental set up is given in our recently published article[148]. Figure-2.6 Shows the Schematic diagram of Low Temperature Dielectric Experimental Setup. For low temperature dielectric measurements sample is cooled up to 78 K in liquid nitrogen gas. A sensor is connected to the heater (which provides heat to the samples) which is further connected to the temperature controller to get the sample temperature. By using the lab view based user interface dielectric properties of the samples at various temperatures and frequencies is measured. In addition to above mentioned parts/equipments, a data acquisition unit, a liquid N₂ (nitrogen) container and a turbo Vacuum pump (Pfeiffer vacuum company), were also used for recording RT and temperature dependent dielectric response. We have measured the dielectric loss and dielectric

constant at different-2 temperatures for frequencies range 20 Hz to 10MHz frequencies and results are discussed in chapter 1 and chapter 6.



Figure-2.6 Schematic diagram Low Temperature Dielectric Experimental Setup.

2.6.3. Working

When a dielectric material is placed in an alternating electric field and its dielectric response is recorded through a LCR meter, a phase lag or lead may appear between the applied field (voltage) and the response (current) of the system depending upon the type of component (*capacitor* or *inductor*). It is to be noted that unlike capacitive or inductive counterparts, a *resistor*, does not induce any phase shift between the applied voltage and measured current as illustrated (for ideal L, C, and R elements) in the top and bottom panel of Figure 2.7. However, when an unknown element/material is kept in an alternating electric field, an arbitrary/unknown phase shift can be expected. For present research work, the sample is kept in parallel plate geometry with a difference that all the sample were circular in shape and hence the electrode plates on both the sides were also circular in shape as they were just coating of silver paint on both the faces of circular pellet. Note that in an impedance analyzer (LCR meter) the capacitance (indirectly ϵ')/impedance is recorded by measuring the above discussed phase shift.

The basic theoretical formulation for these measurements is given below.

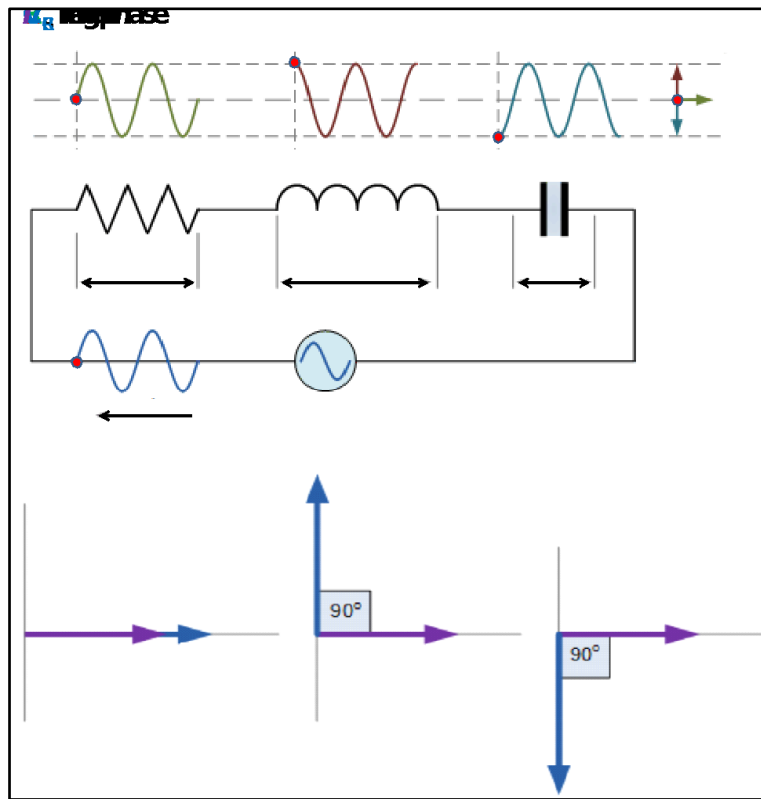


Figure-2.7: Schematic illustration of LCR circuit (middle panel) in association with the phase diagram between voltage and current individually for L, C and R (top and bottom panel).

The impedance is defined as quotient of voltage vector and current vector calculated from a small single sinusoidal measurement. The impedance of the system obeys Ohm's law, when an *ac* signal is fed to it, as ratio of voltage to current in the time domain[147].

$$V(t) = V_0 \exp(j\omega t) \quad (2.10)$$

$$I(t) = I_0 \exp(j\omega t - \phi) \quad (2.11)$$

The impedance is a complex quantity, which has both magnitude $|Z|$ & phase angle (ϕ) and expressed as

$$Z(\omega) = |Z| \exp(-j\phi) \quad (2.12)$$

$$Z(\omega) = |Z| \cos \phi - j|Z| \sin \phi \quad (2.13)$$

$$Z^* = Z' - jZ'' \quad (2.14)$$

where Z' is the real and Z'' is an imaginary part of complex impedance, whereas $j=\sqrt{-1}$. In impedance technique, both the real and imaginary quantities of impedance, for the specimen, are simultaneously measured as a function of frequency. The impedance data so obtained can be converted in the three other forms using following conversion relations

$$\varepsilon^* = \varepsilon' - j\varepsilon'' = \frac{1}{jC_0Z^*} \quad (2.15)$$

$$Y^* = Y' + jY'' = \frac{1}{Z^*} \quad (2.16)$$

$$M^* = M' + jM'' = jC_0Z^* \quad (2.17)$$

where ε^* , Y^* and M^* are complex permittivity, complex admittance and complex modulus respectively. ε' is the real or relative permittivity, also known as dielectric constant, ε'' is the imaginary equivalent or dielectric loss. Similarly, remaining quantities with a single prime are real whereas double primed ones are corresponding imaginary counterparts. C_0 is the vacuum capacitance (or capacitance of free space) and $\omega= 2\pi f$ is the angular frequency. In present investigations, all the dielectric measurements were carried out with the help of a precision impedance analyzer (LCR meter)-6500B of Wayne Kerr company with a measurement accuracy of $\pm 0.05\%$. For TD dielectric measurements a cryogenic temperature controller- CTC100 of SRS (stanford research systems) company was used to record the temperature dependent dielectric response in the present investigations.

2.7 Magnetic measurements

For present research work, the temperature dependent magnetic state of the sample i.e. magnetization versus temperature (M - T) data as well as field dependent magnetic response (M - H) at a fixed temperature has been recorded using superconducting quantum interference device (SQUID) vibrating sample magnetometer (VSM) of Quantum Design. Working principle of a SQUID VSM is briefly described below.

SQUID VSM: A conventional VSM is based on the Faraday's laws of induction to measure the magnetic moment of a sample. In VSM, a magnetic sample vibrates inside a detection coil under a magnetic field. Consequently, due to the change in flux through the coil the voltage of the coil changes[149]. This change in voltage is proportional to the magnetic moment of the sample. Schematic of VSM is shown in Figure 2.8. On the other hand, the principle of SQUID is based on the change in the persistence current in a superconducting detection circuit due to change in flux in the detection coil by magnetic moment of the sample[149]. This change results in voltage variation in the SQUID output which is proportional to the moment of the sample. The SQUID is a very sensitive magnetometer and it can detect magnetic moments as low as 10^{-7} emu[149]. Interestingly, a SQUID VSM combines the high sensitivity of conventional SQUID magnetometer and fast scan speed of a VSM. The major components of a SQUID VSM are:

Superconducting Magnet: The magnet is in the form of a solenoid and constructed in the form of a close superconductor loop. Once the loop is charged up to a critical current the magnet can be used in a persistent mode without the need of external power source[149].

Superconducting detection unit: This is the most important and sensitive part of the magnetometer. It consists of a single superconducting wire which is wound in a second order gradiometer geometry containing three sets of coils.

Sample space and Temperature controller: The sample space is a tube of 9 mm inner diameter. The temperature is controlled precisely by means of a temperature controller in association with a heater and two thermocouples placed at the bottom of the sample space. The SQUID VSM can be operated from 2K to 450 K. However, high temperature susceptibility measurements up to 1100 K can be performed by using a VSM oven option[149]. In present research work, following magnetic measurements were performed on the bulk samples.

2.7.1 Temperature dependent Magnetization (*M-T* measurements)

M-T measurements are important for observation of different magnetic phase transitions and for finding the corresponding transition temperature. These measurements can be performed in two modes. (i) Zero Field Cooled (ZFC) measurement; in this mode, the specimen is cooled to the lowest permissible temperature and the magnetic moment is measured in presence of a low magnetic field (like 100 Oe) while heating the sample. (ii) Field Cooled (FC) measurement; in this mode, the specimen is subjected to cooling to the lowest temperature under a fixed magnetic field and the moment is measured under heating cycle again in the same field.

2.8 X-ray absorption spectroscopy (XAS)

XAS is a widely used technique that provides information of electronic structure of a material[150]. The experiments are generally performed at synchrotron radiation source, which provides tunable and intense X-ray beam[138,151,152]. X-rays are ionizing radiation with wavelengths ranging from $\sim 25 \text{ \AA}$ to 0.25 \AA or energies ranging from $\sim 500 \text{ eV}$ to 500 keV and thus, have potential to eject an electron from a core level of an atom[153,154]. When a substance is scanned for x-ray energies across the binding energy of a core level, an abrupt increment in absorption cross-section takes place, which gives rise to an absorption edge in the absorption versus photon energy plot. When an x-ray enters a material, its intensity decreases due to the absorption of x-ray photons in that material. This phenomenon is described by Lambert-Beer's law, given by equation below[155]:

$$I_f = I_i e^{-\mu d}, \quad (2.18)$$

where I_i and I_f are the incident and transmitted intensities measured before and after the absorption of x-ray photons by the absorber with thickness d and linear absorption coefficient μ . The equation (2.4) may be written as:

$$\mu = \frac{1}{d} \ln \left(\frac{I_i}{I_f} \right), \quad (2.19)$$

The probability that an x-ray photon is absorbed by the material is given by this absorption coefficient μ described in equation (2.5). As shown in figure 2.9, it can be noticed that when the x-ray energies equal to the bonding energies of a core-electron of an element in the material, μ increases sharply and this step-like feature in an absorption spectrum are called *absorption edge*[155]. The absorption edge energy depends on the binding energy of a core level. The absorption edges for an atom can be termed as per the principal quantum number associated with that electron, that is, K for n=1, L for n=2, M for n=3, *etc.*

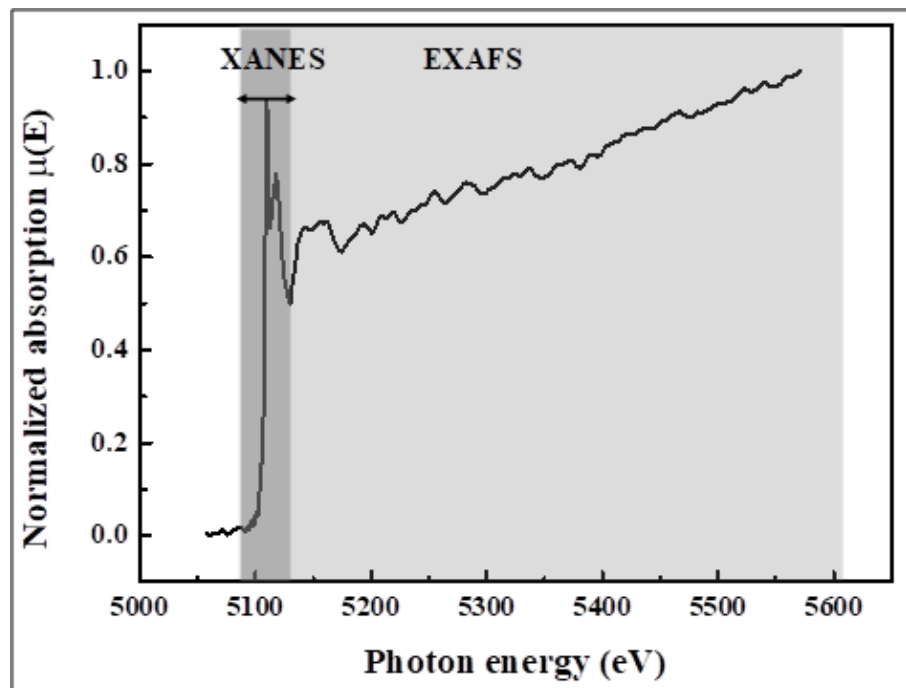


Figure 2.9: A typical X-ray absorption spectrum showing XANES and EXAFS regions[156].

The XAS spectra acquired of a material shows oscillations just above the absorption edge and these oscillations are called x-ray absorption fine structure[153,154]. Thus, the spectrum can be cleaved into two portions: the x-ray absorption near edge structure (XANES) up to 50 eV above the absorption edge and the extended x-ray absorption fine structure (EXAFS) - region from 50 eV to 1000 eV above

absorption edge (as shown in figure 2.10)[156,157]. In this work we will focus on XANES spectroscopy.

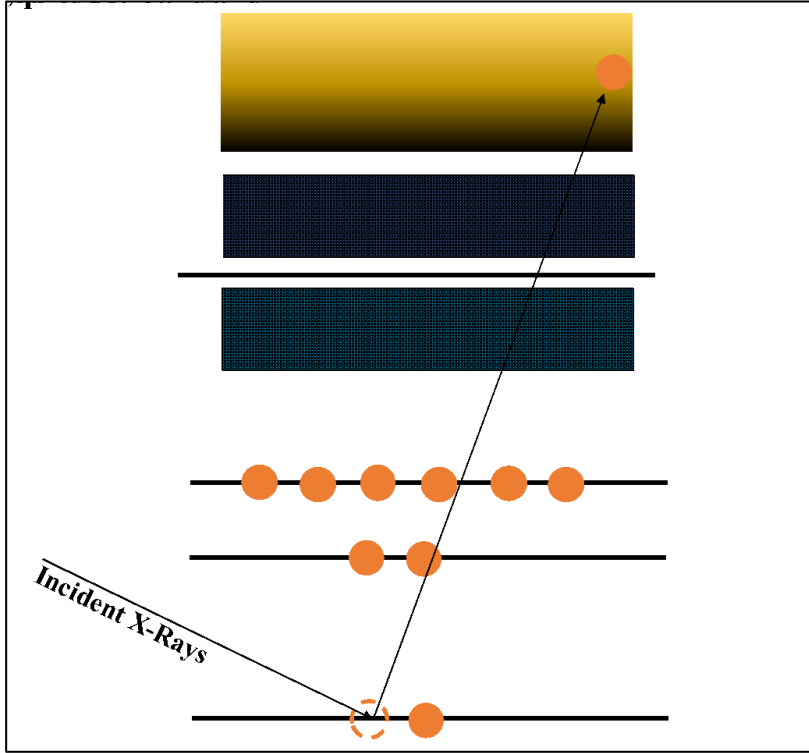


Figure 2.10: Schematic of x-ray absorption process of a core electron to continuum state[157].

XANES spectroscopy is a well-established technique to get information about the electronic structure of a material. In XANES, an X-ray photon is absorbed, leading to excitement of an electron from a core state to a higher unoccupied state. XANES basically measures the change in the absorption of the x-rays due the photoelectric effect and the intensity of the XANES spectra described with the Fermi-Golden rule, which can be written as[153,154]:

$$I_{XANES} \propto |\langle \Phi_f | \hat{e}_q \cdot r | \Phi_i \rangle|^2 \delta_{E_f - E_i - \hbar\omega}, \quad (2.20)$$

where, $\hat{e}_q \cdot r$ is the dipole matrix operator coupling initial state (Φ_i) and final state (Φ_f). given, δ is the delta function that takes care of the energy conservation.

In the final state, a core electron has been excited and can be defined as the initial state with a continuum electron (ϵ) added and a core electron

is removed, *i.e.* $\Phi_f = c\epsilon\Phi_i$. Therefore, the intensity of XANES spectra can be written as[153,154]:

$$I_{XANES} \propto |\langle c\epsilon\Phi_i | \hat{\epsilon}_q \cdot r | \Phi_i \rangle|^2 \delta_{E_f - E_i - \hbar\omega}, \quad (2.21)$$

All electron rearrangements taking place on excitement of a core hole to a continuum electron are neglected, the delta functions may be replaced by the density of states (ρ) and the XANES spectral intensity becomes

$$I_{XANES} \propto |\langle \epsilon | \hat{\epsilon}_q \cdot r | c \rangle|^2 \rho, \quad (2.22)$$

The dipole matrix element dictates that the density of states has an orbital moment that differs by 1 from the core state *i.e.* $\Delta l = \pm 1$, while the spin is conserved *i.e.* $\Delta S = 0$. The quadrupole transition is ~ 100 times weaker than the dipole transitions and may be neglected in broad sense. But, in the case of the metal K edges, the quadrupole transition is important as the 3d density of states is much larger than the 4p density of states and the quadrupole peaks occur in the pre-edge region where no 4p density of states is there[138,153].

Transition metal K edge (1s) XANES spectroscopy is an important technique to investigate local coordination environment and electronic structure depending on sample composition, and structure. The K edge transition of 3d transition metal has energies ranging from about ~ 4 keV to ~ 9 keV[153,154]. The shift of metal 1s XANES spectra edge energy towards higher energies with higher valency is generally used to determine the valence of 3d transition metals[138,153,154]. The metal 1s XANES spectra are often interpreted with the help of molecular orbital approach[153,154]. In this work, the Fe K edge XANES spectra of RFeO_3 having orthorhombic structure has been investigated. The Fe K edge XANES spectra were acquired at Indian synchrotron radiation center, Raja Ramanna centre for Advanced Technology Indore, India, Indus-II, BL-12[138]. The measurements were performed in fluorescence mode using an energy dispersive detector (VERTEX-EX).

The spectra were normalized to the incident photon current, measured by an ionization chamber. For the photon energy calibration, the absorption edge energies of Fe foil, FeO and Fe₂O₃ samples were used as standard[138]. The low-energy pre-peak region observed in the Fe K edge spectra is a representative of quadrupole 1s to 3d excitations. In the present work, Fe K edge XANES measurements were taken in the transmission mode to determine the oxidation states of Fe atoms. The experiments were performed at Indian synchrotron radiation center BL-12, Indus-II, Raja Ramanna Center for Advanced Technology Indore, India.

2.9 X-ray and ultraviolet photoelectron spectroscopy

X-ray photoelectron spectroscopy (XPS) is a surface-sensitive spectroscopic technique, which is based on the principle of photoelectric effect and it can quantitative identify the elemental composition existing in a material[154,158,159]. XPS is a non-destructive experimental technique, which gives not only the information related to elements present in the sample, but also gives the information of what other elements they are bonded to. The XPS spectra are obtained by irradiating the x-rays beam on the material and by measuring the kinetic energy (KE) of the ejected electron material properties can be investigated. High vacuum ($p \sim 10^{-6}$ Pa) or ultra-high vacuum ($p < 10^{-7}$ Pa) condition is maintained by using vacuum pumps before performing the XPS measurements, although ambient-pressure XPS is a current area of development in which samples are analysed at pressures of a few tens of millibar. On the other hand, the basic principle of Ultraviolet Photoelectron Spectroscopy (UPS) is same as that of XPS, and the difference is that the incident radiations have energies of ~ 10 eV which instigate the photoelectric effect, whereas in case of XPS the incident radiations have energy greater than 1keV[154]. The valence band and core level representations of energy diagrams for metals, semiconductors and insulators are depicted in figure-2.11. In the UPS measurements, UV photons are created by means of a gas discharge lamp, which is usually filled with helium (He) gas, though other gases like Neon (Ne) and

Argon (Ar) can also be used[154,158,159]. The photons emitted by the lamp filled with He gas have energies of 21.2eV (He I) and 40.8eV. Due to this small energy of photons, core level photoelectrons are out of reach using UPS and hence spectral acquisition is only limited to the valence band region. UPS and XPS, both together, could be very important tools to investigate the valence band as the ionisation cross section of an orbital has a strong dependency on the energy of incident photons, therefore, by using different photon energies, different electronic transitions and states can be probed. Thus, using the photoelectric effect equation, the binding energy (BE) of an emitted electron can be estimated as given in equation-2.23[154,158,159]:

$$E_{\text{Binding}} = E_{\text{Photon}} - (E_{\text{Kinetic energy}} + \phi) \quad (2.23)$$

Here, E_{Binding} , E_{Photon} , $E_{\text{Kinetic energy}}$ and ϕ , respectively, denote BE of the electron, energy of the incident x-ray photons, the KE of the photoelectron and the work function for the specific sample. Hence, by counting the photo-electron over a range of kinetic energies a spectrum is recorded, which provides crucial information related to electronic work function. The typical UPS spectrum for a sample is given in figure-2.12.

In the present investigations, the effect of Cr doping on the density of states near Fermi level have been investigated using UPS measurements. Excitation of monochromatic He-1 line from SPECS (UVS 300) source has been used to study the valence band of the prepared samples at the experimental station of angle resolved photoelectron spectroscopy (ARPES) *beamline* BL-10 at Indus-2 synchrotron source. Polycrystalline pellets were cleaned in-situ by sputtering with Argon ions at 1.5 keV for 10 min. Valence band spectra have been recorded with a SPECS Phoibos 150 electron energy analyser. The base vacuum during the measurement was $\sim 7 \times 10^{-11}$ mbar[121].

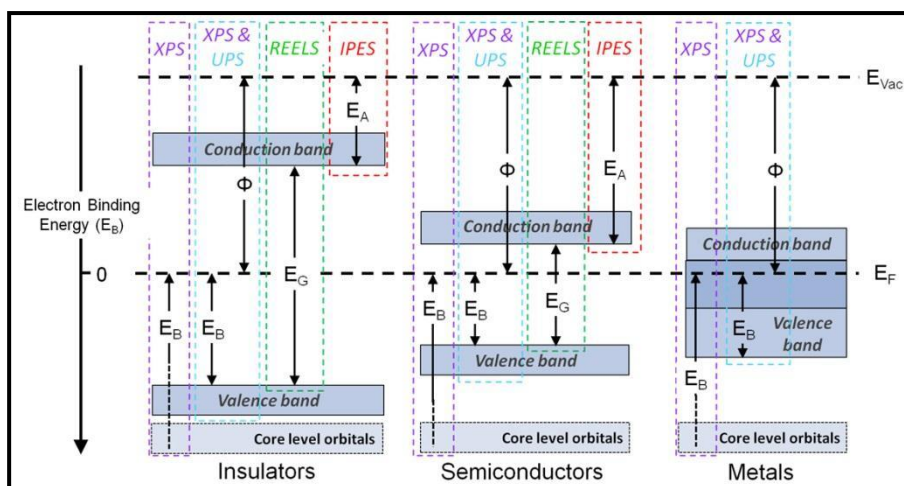


Figure-2.11: The valence band and core level representations of energy diagrams for metals, semiconductors and insulators (<https://xpssimplified.com/UPS.php>).

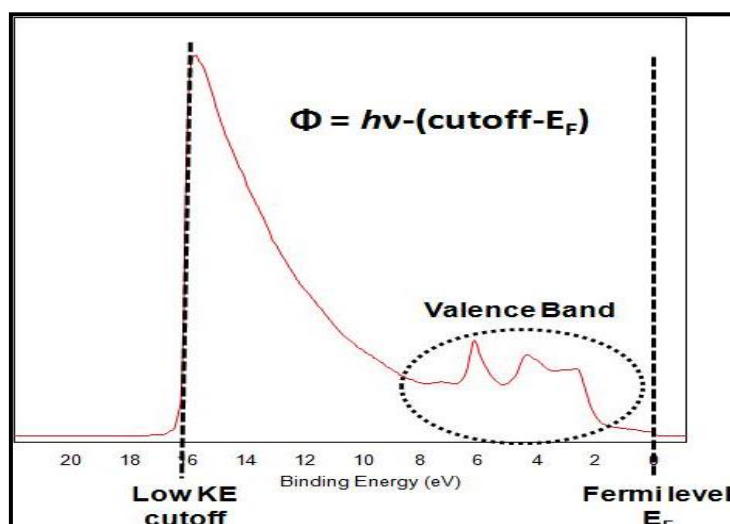


Figure-2.12: The typical UPS spectrum for a sample (<https://xpssimplified.com/UPS.php>).

2.10 Structural Characterization by synchrotron x-ray diffraction

In Figure 2.13 the SXRD pattern of the as-synthesized Cr-substituted PrFeO_3 samples have been shown. SPXRD patterns reveal that these samples were synthesized in pure phase and there is no impurity present in these samples. Rietveld refinements of SXRD data of all samples (depicted in figure-2.14) have been done to calculate the structural parameters like lattice constants, bond lengths, bond angles,

etc.. The x-ray diffraction data has been refined considering orthorhombic space group $Pnma$. The structural parameters like lattice constants, cell volumes, Fe-O bond lengths and Fe-O-Fe bond angles were extracted from the Rietveld refinements of XRD data of the prepared series of samples and their evolutions with Cr-substitution is given in the Table-1. It has been observed (Table-1) that lattice constants (a, b and c) and cell volume decreases systematically with Cr doping in PrFeO_3 . The decrease in the value of lattice constants has been understood in terms of slightly different ionic radii of Cr^{3+} (0.615 Å) than that of Fe^{3+} (0.645 Å) ion in high spin states of Fe [160–164]. The variation in the lattice constants with Cr doping is well consistent with earlier reports[160–169]. The systematic scaling in the Fe-O-Fe bond angles and reduction in the Fe-O bond length (as shown in Table-1) enhances the overlapping of Fe-3d and O-2p orbitals which strongly affects the optical properties. In recent years, optical absorption spectroscopy has been widely used to probe the electronic structure of similar ferrites and the said electronic structure is believed to be responsible for various physical properties of these materials. Thus, the following section is devoted to exploring the effect of Cr-substitution on the optical and electronic properties of PrFeO_3 .

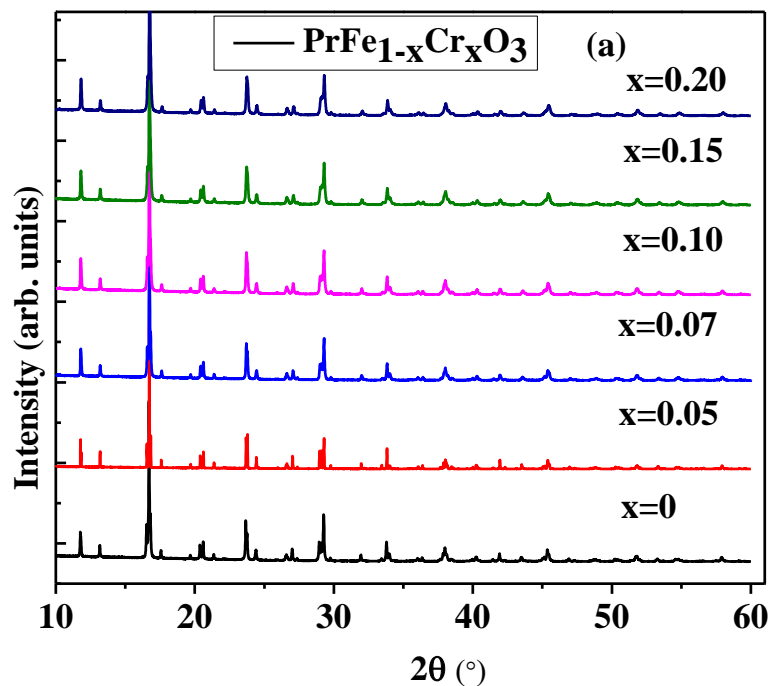


Figure-2.13: The SXRD data for Cr-doped PrFeO_3 series of samples.

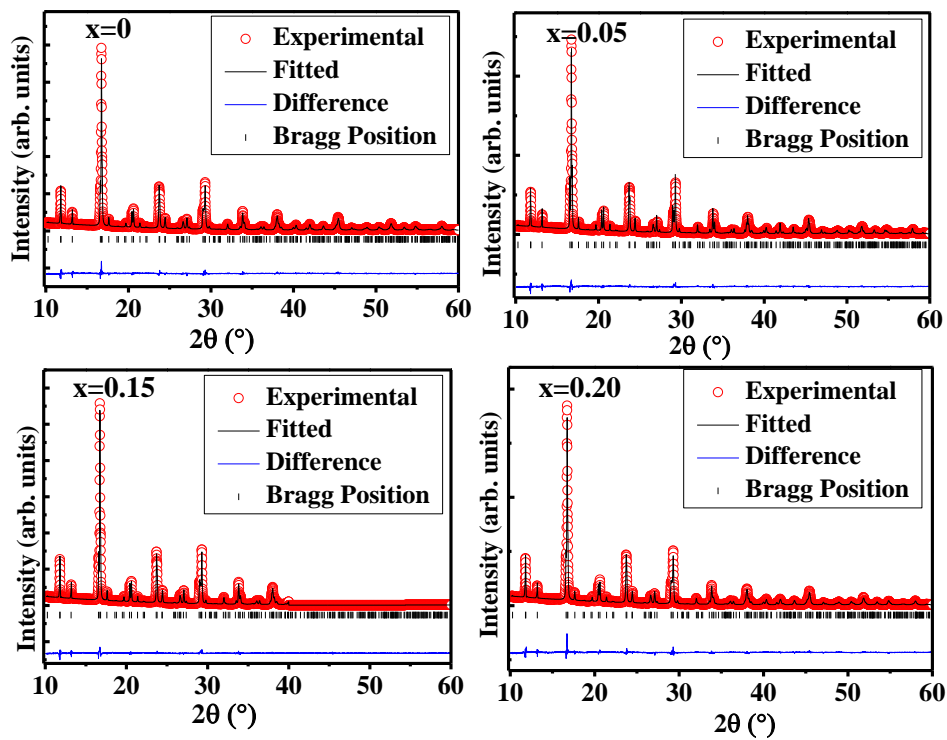


Figure-2.14: The Rietveld refinements of prepared series of samples by considering the space group $Pnma$.

Table-1: The variation of unit cell parameters as a function of Cr-doping in PrFeO₃. The number in open bracket represents the last digit error bar.

Cr% (x)	a (Å)	b (Å)	c (Å)	Fe-O1 (Å)	Fe-O1 (Å)	Fe-O2 (Å)	Fe-O1-Fe (°) Degrees	Fe-O2-Fe (°) Degrees
0	5.477(9)	5.5649(5)	7.7755(9)	2.013(7)	2.011(7)	2.005(9)	153(4)	152(5)
0.01	5.475(10)	5.5636(4)	7.7744(6)	2.000(6)	2.001(6)	2.002(9)	153(4)	152.4(5)
0.02	5.4741(7)	5.5601(8)	7.7731(5)	2.013(5)	2.001(7)	2.001(8)	153.2(5)	152.5(6)
0.03	5.4737(1)	5.5596(7)	7.7723(3)	2.009 (4)	1.998(5)	1.998(5)	153.5 (7)	153.1(6)
0.05	5.4736(7)	5.5581(5)	7.7714(7)	2.007(7)	1.998(7)	1.995(2)	153.8(4)	153.7(5)
0.07	5.4731(5)	5.5531(8)	7.7704(8)	2.023(7)	1.995(7)	1.998(3)	153.2(4)	153.2(5)
0.10	5.4721(6)	5.5507(7)	7.7658(5)	2.012(6)	1.993(6)	1.997(8)	153.5(4)	153.6(5)
0.13	5.4712(7)	5.54639(5)	7.7658(5)	2.023(7)	1.989(7)	1.994(3)	153.5(5)	153.6(6)
0.15	5.4709(8)	5.5464(4)	7.7647(4)	1.999(7)	1.981(7)	1.991(3)	153.6(6)	154.2(6)
0.18	5.4706(9)	5.5425(6)	7.7633(7)	1.992(8)	2.015(9)	1.991(3)	152.7(5)	154.1(7)
0.20	5.4694(3)	5.5421(7)	7.7614(8)	2.012(7)	1.991(7)	1.992(3)	153(5)	154.2(6)

Chapter 3

Structural, Optical and Dielectric Properties of $\text{PrFe}_{1-x}\text{Cr}_x\text{O}_3$ ($0 < x < 0.20$) Compounds

The detailed analysis about the structural, optical and dielectric properties has been provided in this chapter. The optical properties such as optical band gap and electronic disorder term Urbach energy have been examined. After rewriting the conductivity equation $\sigma = \sigma_0 \exp\left(-\frac{E_g}{2kT}\right)$, a completely new way has been established in order to understand the possible correlation between these terms in the form of tunnelling probability. As a final remark, systematic variations between dissipation factor and tunnelling probability have been discussed in detail. The importance of these investigations lies in the fact that optical absorption spectroscopy could be used as an alternative tool to probe the origin of dielectric loss in prepared series of samples. Results in this chapter have been published in the literature.*

*Kumar *et al.* Ceram. Int. 45 (2019) 8585–8592.
<https://doi.org/10.1016/j.ceramint.2019.01.177>.

3.1 Introduction

As discussed in chapter-1, for any practical applications, the dielectric loss in the sample must remain sufficiently small[122].The mixed oxidation state of transition metal ions in these materials due to vacancies at various sites is believed to be responsible for the observed high values of dielectric loss in these materials[57,122].Thus, in order to achieve real application of these materials, it is extremely important to have basic understanding of various contributing factors for observed

high value of $\tan\delta$. In case of dielectric materials, the dielectric loss consists of two parts (1) frequency dependent flipping of electrical dipole and (2) the leakage current. For samples having *Centro symmetric* crystal structure, the hopping of electron possibly through disorder/defect states is responsible for leakage current [123,124]. For semiconducting/insulating materials the leakage current is due to the defects/vacancy present [123] in the sample and is related to the band gap as; $\sigma = \sigma_0 \exp\left(-\frac{E_g}{2kT}\right)$ (For Intrinsic case $E_a=E_g/2$) [170]. The random distribution of defects and doping at lattice sites, introduces potential fluctuations that creates energy levels within the forbidden energy gap or close to the valance/conduction band[104,105]. These energy levels are also termed as electronic disorders near band edge and are measured in the form of Urbach Energy[104,105]. These statistical effects are known to distort the unperturbed density of states, which are particularly important in determining the number of free carriers and hence contributes to the leakage current/dielectric loss[105]. In order to understand the correlation between electronic disorder term Urbach energy and dissipation factor $\tan\delta$ in details, optical absorption spectroscopy in diffuse reflectance mode and dielectric measurements have been carried out on prepared series of samples.

Keeping this in view, the possible origin of dielectric loss in pure and Cr doped PrFeO_3 and its correlation with that of the electronic disorder have been demonstrated in this part of thesis work. Inclusion of Cr at Fe site seems to modify local strain field, possibly due to difference in the ionic radii of Fe and Cr. Further, it is natural to expect that random distribution of Cr also leads to the change in the on-site potential due to difference in the ionic radii as well as atomic number (Z). These two effects lead to an overall increase in the electronic disorder. Hence, polycrystalline samples of Cr doped PrFeO_3 have been prepared and composition dependent optical absorption as well as dielectric measurements have been carried out on these samples.

3.2 Experimental detail

3.2.1 Sample preparation

Polycrystalline samples of $\text{PrFe}_{1-x}\text{Cr}_x\text{O}_3$ have been prepared via sol-gel method[102,171]. Citric acid has been used as a chelating agent and ethylene glycol as a fuel. The details of sample preparation methodology have already been discussed in the chapter-2.

3.2.2 Structural studies

SXRD experiments were carried out at BL-12 ADXRD beamline at Indus-2, Synchrotron Radiation Source (Raja Ramanna Centre for advanced Technology Indore). The energy of the incident x-ray beam was 15 keV. The diffraction pattern recorded in the 2θ range of $10-50^\circ$ with the step size of 0.01° using Huber six-circle diffractometer (model: 5020). All obtained diffraction patterns have been analyzed by using the FullProf suite and VESTA software was used for visualization of the crystal structure of the refined pattern. The details analysis of SXRD data have been discussed in the chapter-2.

3.2.3 Dielectric Measurements

Precision impedance analyzer (Wynne Kerr 65120B) having oscillator voltage of ± 1 volt has been used to perform dielectric measurements. For this purpose the obtained powdered samples have been pelletized at high pressure of ~ 20 ton to make ~ 1 mm thick and ~ 13 mm diameter circular pellets, these pellets have been sintered in air at 1100°C for 24 hours and then coated with silver paint on both sides followed by heating at 200°C to make parallel plate capacitor[9].

3.2.4 Diffuse Reflectance Measurements

Room temperature variations of optical band gap and electronic disorder in terms of EU of prepared samples have been estimated using diffuse reflectivity measurements. These measurements have been performed, in the wavelength range 190 nm to 800 nm, using Cary-60 UV-VIZ-NIR spectrophotometer having Harrick Video-Barrelino diffuse reflectance probe[99].

3.2.5 Valence band spectroscopy measurements

In order to investigate the effect of Cr doping on the density of states near Fermi level, valence band spectroscopy measurements have been carried out. Excitation of monochromatic He-1 line from SPECS (UVS 300) source has been used to study the valence band of the prepared samples at the experimental station of angle resolved photoelectron spectroscopy (ARPES) *beamline* BL-10 at Indus-2 synchrotron source. Polycrystalline pellets were cleaned in-situ by sputtering with Argon ions at 1.5 keV for 10 min. Valence band spectra have been recorded with a SPECS Phoibos 150 electron energy analyser. The base vacuum during the measurement was $\sim 7 \times 10^{-11}$ mbar[121].

3.3. Results and discussion

This section is divided into four subsections. The variation of optical properties such as optical band gap and Urbach energy are discussed in the first segment. Further in second subsection, the dissipation factors as a function of frequencies have been analyzed. The impact of Cr doping near Fermi level have been examined using valence band spectroscopy experiments in third subsection. In last subsection, a direct correlation between the dissipation factor and tunneling probability will be elaborated in detail.

3.3.1 Optical absorption spectroscopy analysis

It is well known that the optical spectroscopy could be an effective tool to estimate the value of electronic disorder, present near the band edge in the form of Urbach energy. The doping of different atomic species *i.e.* Cr at Fe site in the present case is expected to create the structural and on-site electronic disorder in the system. Further, such random potential fluctuations are known to create energy levels within the forbidden energy gap near band edge[121]. These states are also termed as electronic disorders near band edge and can be measured in the form of Urbach Energy[104,105]. Hence, in order to understand the possible correlation between dielectric loss, band gap and width of electronic disorder near band edge, the optical absorption spectroscopy (OAS) experiments have been carried out. In figure-3.1(a), absorption

spectra of all prepared series of samples have been shown as a function of energy. It is clear from the figure that many features dominate in absorption spectra for the prepared samples. Strong absorptions have been observed around 2.1 eV in all samples, generally, it is called p-d transition, and this is recognized as the main absorption peak which decides the band gap of these materials. The interesting feature centred around 1.7 eV is attributed to crystal field $d-d$ transitions[172], the linear region around 2.1 eV corresponds to optical band gap region and another interesting feature related to this spectrum is the exciton line shapes[173].

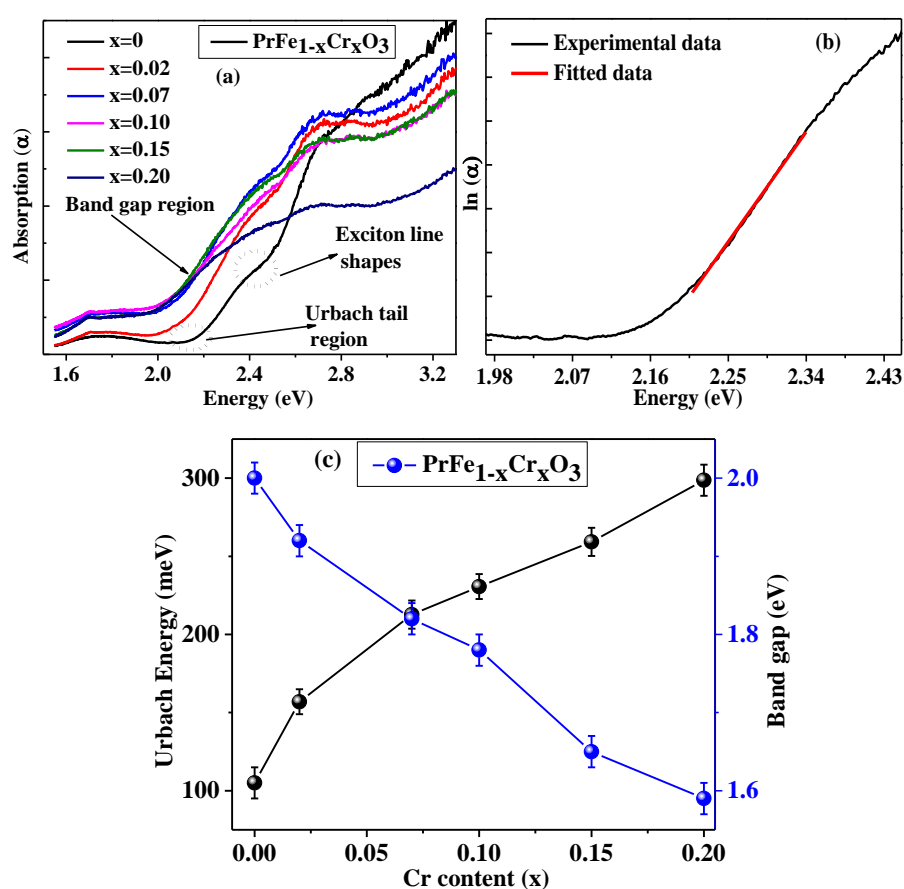


Figure-3.1: The optical absorption spectra for $\text{PrFe}_{1-x}\text{Cr}_x\text{O}_3$ system (a), whereas the representative plot for Urbach energy is depicted in figure-(b). The Variation of Urbach energy (E_U) and optical band gap with Cr content is given in figure-(c).

In order to estimate the optical band gap, the obtained DRS spectra have been converted into equivalent absorption spectra using Kubelka–Munk equation[141].

$$F(R_{\infty}) = \frac{K}{S} = \frac{(1-R_{\infty})^2}{2R_{\infty}}. \quad (3.1)$$

Where, $F(R_{\infty})$ is Kubelka- Munk function, K and S are the Kubelka–Munk absorption and scattering functions respectively and $R_{\infty} = R_{(\text{Sample})}/R_{(\text{Standard})} \cdot R_{(\text{Sample})}$ and $R_{(\text{Standard})}$ are the diffuse reflectance of the sample and standard white reference. E_g can be calculated by fitting straight line of $[F(R_{\infty})hv]^n$ after converting the Kubelka- Munk function into Tauc equation[102,174]. Here ‘n’ can take two values *i.e.* $n = 2$ for direct band gap transition and $n = 1/2$ (in present case) for indirect band gap transition. Here we have used $n = 1/2$ as our DFT studies on the similar ferrites suggest that these samples have an indirect band gap.

In order to estimate the value of Urbach energy (E_u), optical absorption α has been plotted as a function of energy E. This optical absorption α is related to energy as[104,175];

$$\alpha(E, T) = \alpha_0 \exp \left[\sigma \left(\frac{E - E_{00}}{kT} \right) \right] \quad (3.2)$$

Where; α_0 and E_{00} are the constants determined by extrapolating linear region from $\ln(\alpha)$ versus E curves at a given temperature T. The quantity $E_u = \frac{kT}{\sigma}$ is termed as Urbach energy. The quantity σ is called steepness parameter. This implies that logarithm of α plotted as a function of $E = hv$ can be approximated by a straight line in energies just below the fundamental absorption edge and the linear fitting can be used to estimate the value of Urbach energy as depicted in figure-3.1 (b).

The variation of band gap and Urbach energy is depicted in figure-3.1 (c). It can be clearly seen from the figure that E_u increases systematically with inclusion of Cr doping. It is now well accepted that E_u is a measure of total “electronic disorder” present in the system and has contributions due to thermal disorder (arises due to random vibrations of atoms with temperature) as well as disorder which gets further induced due to difference in lattice mismatch or defects present in the system[174]. In the present case, the contribution due to thermally induced disorder may be considered as constant[103], since all the measurements have been carried out at room temperature. Hence, major contribution in Urbach energy is due to temperature independent term

i.e. structural disorder induced by Cr doping[105]. However, optical band gap systematically decreases with Cr doping, which is attributed to the formation of Cr states near Fermi level.

3.3.2 Dielectric Measurements

The obtained dielectric data for pure and Cr doped PrFeO_3 as a function of frequency has been shown in figure-3.2 (a).

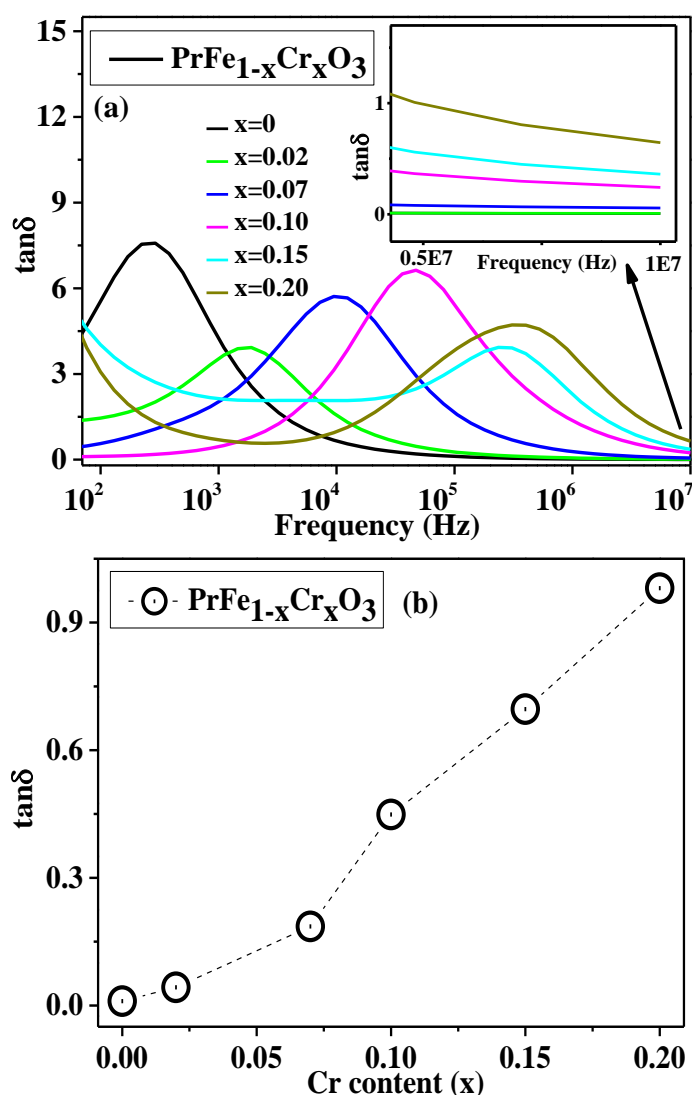


Figure-3.2: Variation of dielectric loss at different frequencies for pure and Cr doped samples respectively. The inset of figure (a) clearly suggests the increase in value of dielectric loss with increasing the Cr concentration in PrFeO_3 at higher frequencies. The variation of dielectric loss ($\tan\delta$) at 10 MHz with Cr doping is depicted in figure-(b).

The dielectric relaxation[176] in the dielectric measurements is clearly evident from the figure. At this juncture, it is important to note that at low frequency region the dielectric measurements have contribution due to the space charge regions *i.e.* due to the contact between metallic electrodes or grain boundaries[124]. Hence, in order to examine only the grain contribution, the data have been collected at much higher frequency *i.e.* up to 10MHz. The variation of dielectric loss ($\tan\delta$) at 10 MHz as a function of Cr doping has been shown in figure-3.2 (b), which clearly indicates the systematic scaling of dielectric loss with Cr doping.

3.3.3 Valence band Spectroscopy Analysis

As in semiconductors/insulating materials, the density of states is predicated to be scale with the electronic disorder[105,116], hence in order to investigate the effect of Cr doping on the density of states, valence band spectroscopy measurements have been carried out. The valence spectra of the prepared samples have been shown in figure-3.3. From the figure, it is clear that the intensity of the feature near Fermi level E_f , as indicated by arrow, systematically increases with Cr doping. This may possibly be due to increase in random statistical fluctuation in the potential due to Cr doping.

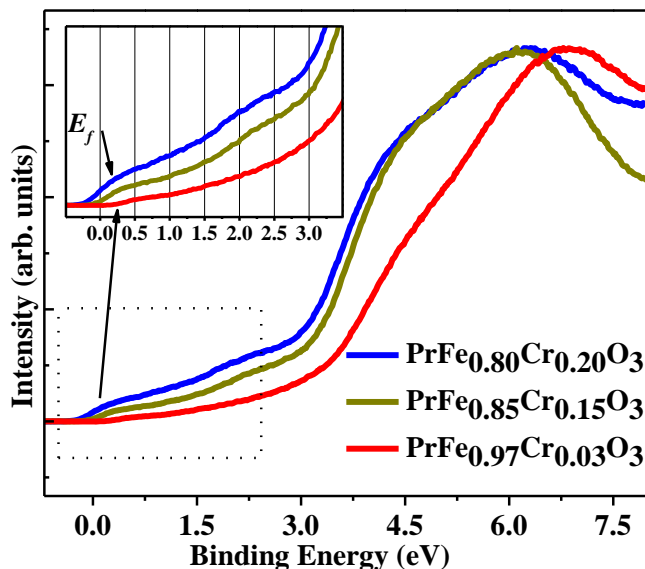


Figure-3.3: The valence band spectra for some of prepared samples. Inset of figure suggests increase in the value of the intensity of the feature near Fermi level E_f (as indicated by arrow) with Cr doping.

Additional features at 4.5 eV and 6.5 eV in the valance band spectra is related to the Fe 3d (t_{2g}) states and the Fe 3d- O 2p bonding states respectively. The positions of both the features tend to decrease in energy with the inclusion of Cr and same could be responsible for the decrease in the band gap with incorporation of Cr to PrFeO₃. It should be noted that the spectral feature near Fermi level E_f as indicated by arrow (2.25 eV) has been assigned to Cr-3d states related to PrCrO₃ whereas feature at 4.5 eV is primarily related to the Fe 3d states of PrFeO₃-like local compositions. Thus, it appears that Cr-3d states hybridize weakly with O-2p states, thereby gaining less binding energy compared to Fe 3d states in PrFeO₃. Hence, Fe 3d states lies deeper in energy with respect to Cr-3d states which could be responsible for decrease in the band gap with Cr doping.

3.3.4 Direct correlation between dissipation factor and electronic disorder

As discussed in earlier sections that the dielectric loss (in MHz frequency range) and Urbach energy increases systematically with the inclusion of Cr doping as illustrated in figure-3.1. In this section, the correlations of above-mentioned results have been presented. As discussed earlier, the dielectric loss of a material essentially consists of two parts (i) frequency dependent flipping of electric dipoles and (ii) leakage current. In the absence of net dipole moment in the sample *i.e.* for centro symmetric crystal structure; the leakage current which is due to thermally activated hopping of charge carriers and electronic disorder/defect states, plays a crucial role in dictating the value of dielectric loss[124,177–179]. The probing of such disordered states is possible by using optical spectroscopy in the form of Urbach tails and these disordered states/defects are the major contributing factor in the dielectric loss. Hence, there should be a direct correlation between dissipation factor and electronic disorder *i.e.* Urbach energy. Keeping this in view, equation $\sigma = \sigma_0 \exp\left(-\frac{E_g}{2kT}\right)$ can be written in completely new way in the form of tunnelling probability given as:

$$T_{ij} = C \exp \left[-\left(\frac{E_g - 2E_u}{kT} \right) \right] \quad (3.3)$$

Here T_{ij} is tunnelling probability and C is constant. As discussed in the introduction, the value of dielectric loss (leakage current) is critically controlled by the band gap and electronic disorder, hence, it is expected that with decrease in the band gap and increase in the electronic disorder dielectric loss increases, which, further could be due to increase in tunnelling probability or escape probability (T_{ij}) of an electron from the localized states as given in equation-3.1. As all the experiments have been performed at room temperature, hence kT is constant for all the samples. Using obtained values of E_g and E_u , values of T_{ij} have been estimated and plotted in figure-3.4. From figure, it is clear that estimated variation of T_{ij} as a function of Cr inclusion, shows a similar functional form as that of dielectric loss as shown in Figure-3.2 (b).

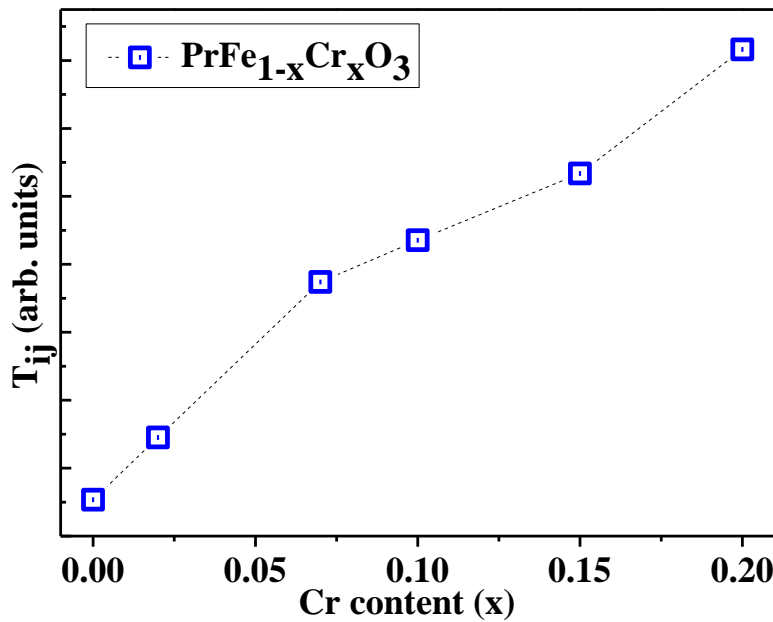


Figure-3.4: The estimated values and variation of tunnelling probability as a function of Cr doping.

Thus, with decrease in the band gap and increase in the Urbach energy, the effective value of tunneling probability systematically increases and appears to be responsible for observed value of dielectric loss. Therefore, it seems that using the combined dielectric and optical spectroscopy, we have demonstrated a new way to understand the origin of dielectric loss in correlated electron system.

3.4 Conclusion

The optical absorption spectroscopy has been used to probe the origin of dielectric loss in Cr doped PrFeO₃. Present investigations strongly suggest that there should be a direct correlation between dissipation factor and electronic disordered term *i.e.* Urbach energy. After rewriting the conductivity equation $\sigma = \sigma_0 \exp\left(-\frac{E_g}{2kT}\right)$, a completely new way has been established in order to understand the possible correlation between these terms in the form of tunnelling probability. In present study, it has been observed that with inclusion of Cr doping optical band gap systematically decreases, whereas, electronic disorder increases systematically. These factors lead to overall increase in the tunnelling probability of electron from localized states and said tunnelling is responsible for systematic scaling of dielectric loss. Present studies leads to a new way to analyse the origin of dielectric loss in highly correlated electron systems.

Chapter 4: Strain induced disordered phonon modes in Cr-doped PrFeO₃

The dissipation factor and its relationship with Urbach energy and optical band gap have been presented in previous chapter. Here, in this chapter attempts have been made to realize the systematic correlation between crystallographic strain, Raman line width, disordered parameter (σ) and Urbach energy. Further, the origin of octahedral distorted new Raman modes around 510 cm^{-1} in $\text{PrFe}_{1-x}\text{Cr}_x\text{O}_3$ is also provided in this chapter. Results presented in this chapter are published in peer reviewed journal.*

*Kumar *et al.* J. Phys. Condens. Matter. 31 (2019) 275602.
<https://doi.org/10.1088/1361-648x/ab1195>.

4.1 Introduction

The exponential variation of optical absorption near band edge is one of the well-known feature of optical absorption spectra and the same has been observed in the optical spectra for almost all kinds of crystalline semiconductor materials, amorphous semiconductors and highly disordered non-metallic glassy systems[95–99]. Generally, it is believed that Urbach energy (E_U) is a measure of total electronic disorder present in the system and scales with temperature and structural disorders (structural disorder induced by defects, vacancies, static strain fields, doping) *etc.*[103]. Earlier, various efforts have been made by many research groups in order to explain the behaviour of E_U , its functional form as a function of temperature (T) and structural disorder (X) [95,98,180,181]. The said tail states are very important from practical applications such as the improving electronic properties, improvement in absorption spectra in solar cells[100] and broadening of the emission spectra in light emitting devices *etc.*[101]. The major contributing factors which influence the values of Urbach energy arises from

presence of structural disorder, inhomogeneity due to compositional fluctuation, thermal disorders and anharmonicity[99,102,119]. The contribution due to thermal disorder can be considered as very small and could be treated as constant at given temperature in the case of doping dependent measurements. In addition to thermal disorder the anharmonic terms do not have significant involvement at room temperature[120].

Apart from this, in case of orthoferrites the octahedral breathing mode disorder is expected to modulates mainly the asymmetric Fe-O-Fe stretching frequencies through the variable M-O bond distance[82]. However, the tilt angle disorder arises due to change in the octahedral tilt angles also affects the total disorder present in the system. Thus, it is clear that the structural, compositional, chemical and thermal disorder contributes to the tail part of the optical absorption spectra and affects the total value of Urbach energy. Raman spectroscopy (RS) is a widely used fast, effective and non-destructive spectroscopic tool to explore the crystal structure as well as phononic disorder[120]. The exact quantification of these disorders is not easy only by using such optical absorption spectroscopy techniques. For this purpose the combined synchrotron x-ray diffraction (SXRD) and Raman measurements could be useful, as these data have information on the relative change in the value of octahedral tilts and anharmonicity in Raman modes.

Thus, keeping in view of the potentials of these experimental techniques to probe the crystal structure and total disorder, a comparative study have been presented here. One of the major outcomes of the present work is the broadening in the Raman line shapes is mainly due to temperature independent term structural disorder. Moreover, a systematic correlation between crystallographic strain, Raman line width, disordered parameter (σ) and Urbach energy has been observed, which implies that structural disorder affects phononic as well as electronic states of the system. To the best of our knowledge, such correlation between structural disorders, phonon disorder and Urbach energy E_U was not available in the literature. Present study would be useful to understand the variation of electronic disorder and phononic disorder with structural strain and density of disordered phonons.

4.2 Experimental detail

4.2.1 Structural characterizations

The structural phase purity of the prepared samples has been investigated by SXRD technique using ADXRD beamline BL-12, at Indus-2, the Indian synchrotron source. All the experiments were performed in angle-dispersive mode using a Huber 5020 diffractometer and with beam energy of 15 keV [152,182].

4.2.2 Diffuse Reflectance Measurements

Room temperature and temperature dependent variation of electronic disorder in terms of E_U of prepared samples has been estimated using diffuse reflectivity measurements. These measurements have been performed in the 190 nm to 800 nm wavelength range using Cary-60 UV-VIZ-NIR spectrophotometer having Harrick Video-Barreliino diffuse reflectance probe[120].

4.2.3 Raman measurements

The Raman measurements were carried out on prepared pellets samples by using LABRAM HR dispersive spectrometer equipped with a 633 nm excitation laser source and a CCD detector in backscattered mode. For temperature dependent Raman measurements THMS600 stage from Linkam having accuracy 0.1 K was used[120].

4.3 Results and discussion

This section is divided into five subsections. The variation of structural parameters has been discussed in detail in the first subsection. Further in second subsection, the room temperature Raman scattering results has been analyzed. In the last three subsections, a systematic correlation between the Raman line width, Urbach energy, compressive strain and disorder parameter have been demonstrated.

4.3.1 Structural studies

Figure-4.1(a) shows the SXRD pattern of all synthesized polycrystalline Cr-doped PrFeO_3 samples. The obtained x-ray diffraction data has been refined considering orthorhombic structure having space group $Pnma$ [102,171]. A comparison of experimental & the calculated

diffraction data and the absence of any extra peak in the diffraction data confirm the structural phase purity of the prepared samples. It is clear from the inset of figure-4.1 (a) that the peaks shift towards higher 2θ values with increase in Cr content, indicating the decrease in lattice parameters/compressive strain with inclusion of Cr doping. In order to understand the effect of Cr doping on the structural distortions particularly in terms of octahedra tilts, the lattice constants were used to find the distortions along (100) and (001) axes of basic cubic perovskite structure based on the formalism reported by Warshi *et al.*[183]. In Glazer's notation the octahedra tilt of $Pbnm$ system is expressed as $a^-a^-c^+$ or in pseudocubic settings it is known as rotations by angles θ , ϕ , and Φ around the (110), (001), and (111) axes, respectively. In order to probe the said tilt angles SXRD data has been carefully analyzed. The tilt angles θ [110] and ϕ [001] are related to the lattice parameters as[183,184]:

$$\theta = \cos^{-1}(a/b), \phi = \cos^{-1}(\sqrt{2}a/c), \quad (4.1)$$

where a, b and c are the lattice constants of orthorhombic unit cell.

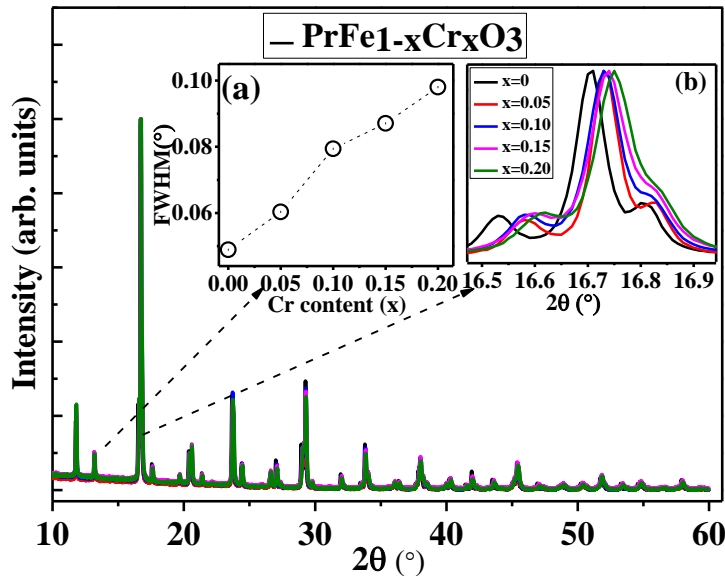


Figure-4.1: SXRD patterns of the prepared series of samples. Inset (a) illustrates the increase in FWHM of XRD peak with Cr concentration. Inset (b) shows the shifting of XRD peaks towards higher 2θ values with increase in Cr content, indicating the decrease in lattice parameters with inclusion of Cr doping.

From systematic variation of lattice parameters octahedral tilt angles θ and ϕ has been estimated and are provided in figure-4.1 (b). It can be seen from the figure that the average tilt angle decreases with the inclusion of Cr, which could be attributed to the increase in the stability and tendency towards the more symmetric structure. These results are in excellent agreement with the reported literature[44,82].

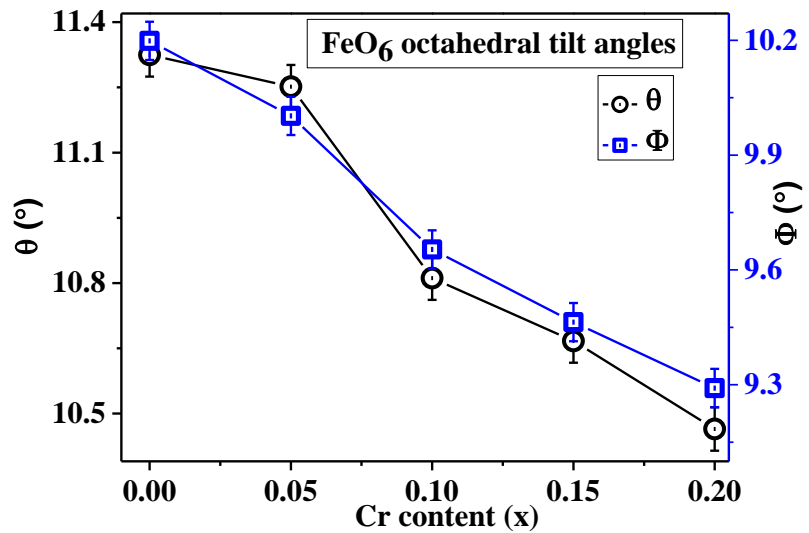


Figure-4.1(b): The variation of octahedral tilt angles as a function of Cr doping.

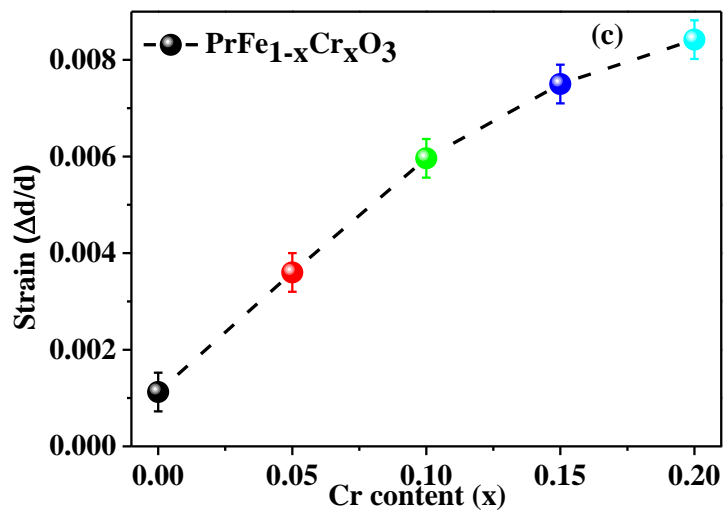


Figure-4.1(c): The variation of crystallographic strain as a function of Cr doping in PrFeO₃ estimated by using William son hall method.

The variation of lattice parameters and Fe-O bond lengths is already discussed in the Table-1 of chapter-2. A systematic decrease in lattice parameters (see Table-1) is consistent with the fact that the ionic radii of Cr^{3+} (0.61 Å) is smaller than Fe^{3+} (0.64 Å)[169,171]. The systematic decrease in the values of Fe-O bond lengths clearly suggest the compressive strain induced with inclusion of Cr doping which has been further quantified by Williamson-Hall plot as shown in figure-4.1(c).

4.3.2 Raman spectral Analysis

PrFeO_3 has orthorhombic distorted structure having 24 Raman-active modes which decompose into ($7A_g + 7B_{1g} + 5 B_{2g} + 5B_{3g}$), 25 infrared-active modes ($7 B_{1u} + 9 B_{2u} + 9 B_{3u}$), 8 inactive modes ($8 A_u$) and 3 acoustic translational modes ($1 B_{1u} + 1 B_{2u} + 1 B_{3u}$)[185,186]. The Raman spectra for prepared series of samples are shown in figure-4.2 (a). An increase in the overall Raman line width (corresponding to phonon mode $\sim 340 \text{ cm}^{-1}$) has been observed with inclusion of Cr clearly indicating the scaling of Cr induced structural disorder with Cr concentration. Further, the generation of a new phonon mode at $\sim 510 \text{ cm}^{-1}$ is clearly evident from figure-4.2 (a), which could be either due to structural phase transition with doping or Cr induced structural disorder [186–189]. The variation in the FWHM of phonon mode corresponding to 340 cm^{-1} is shown in figure-4.2 (b).

It is well known that in AFeO_3 type of systems, the observed Raman spectrum is basically dominated by FeO_6 octahedral vibration modes [186,190]. The spectral features are clearly evident in figure-4.2 (a). The modes between or around $400\text{-}500\text{cm}^{-1}$ and 600cm^{-1} are assigned to bending/Asymmetric stretching (AS) and symmetric stretching (SS) of FeO_6 octahedral Raman modes respectively [190,191]. It should be noted here that Raman mode that appears around 620 cm^{-1} in AFeO_3 type of systems is assigned to SS of FeO_6 octahedral Raman modes and becomes harder with doping [190,191]. Therefore, its appearance at higher wave number is quite reasonable due to Cr substitution at Fe site. Raman spectrum for prepared series of samples is shown in figure-4.2 (a). It is clear from the figure that in Cr doped

samples Raman peaks shifts to higher wave number region, clearly indicating the blue shift/compressive strain/hardening behaviour. Here, it should be noted that symmetric broadening of Raman peaks is essentially controlled by crystallographic strain[185,186]. However, anti-symmetric broadening of Raman line shapes could be due to interaction of electrons/excitons with phonons[192]. In the present case, symmetric broadening (Raman line shape having single mode of vibration i.e. 340 cm^{-1}) in Raman line shapes has been observed with Cr doping which clearly indicates the increase in crystallographic strain after inclusion of Cr^{3+} ions at Fe site.

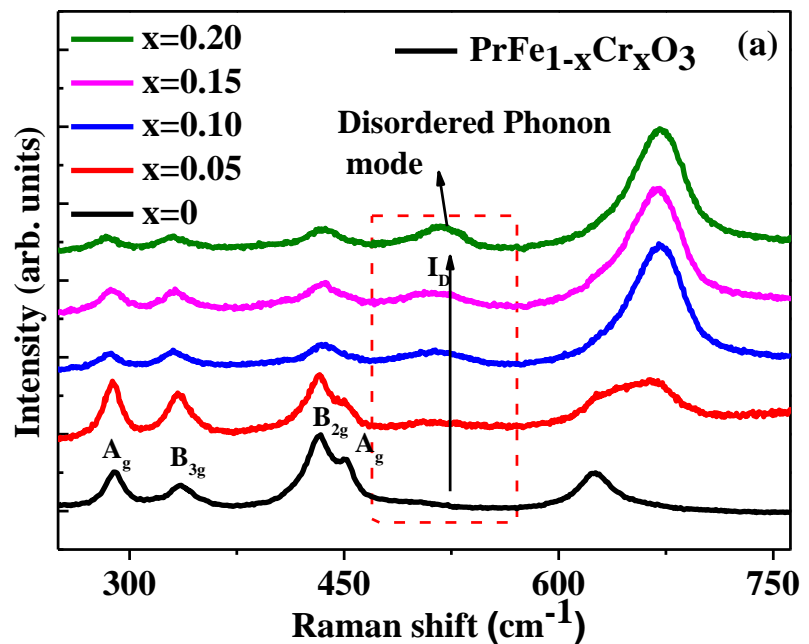


Figure-4.2 (a): The Raman spectrum for prepared series of samples. An additional band generated at around 510 cm^{-1} whose intensity goes on increasing with increasing the Cr content is a direct indication of increase in structural disorder with incorporation of Cr doping.

4.3.3 Systematic correlation between the structural disorder and Urbach energy

Now, if we recall the variation of Urbach energy in chapter-2, there is a scaling of Urbach energy with Cr-substitution. Apart from this, the systematic broadening in Raman line width and FWHM of x-ray diffraction peak follow the similar trend with Cr-substitution, which

suggest that SXRD/Raman line width and Urbach energy are dominated by a common factor. Hence, it might be possible to separate the effects of structural, compositional disorders from those of anharmonic effects, which will be discussed later. These results suggest that the crystallographic disorder affects phonons as well as electronic states of the system. In order to understand the physical significance of the various broadening contributions discussed above, it is useful to make a comparative study between electronic disorder term E_U and Raman line width. Such comparative study allows us to find the correlation between densities of tail states, structural disorders and anharmonic effects probed by Raman spectroscopy.

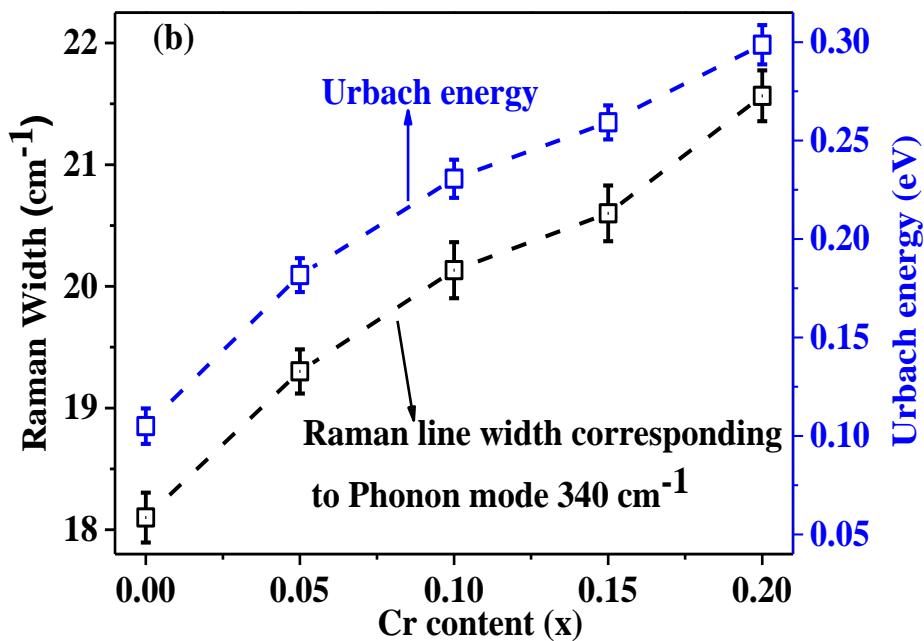


Figure-4.2 (b): The systematic correlation between Raman line width (Raman mode having single mode of vibration 340 cm^{-1}) and Urbach energy as a function of Cr content.

It is important here to note that both PrFeO_3 and PrCrO_3 have orthorhombic structure and have 24 Raman active modes[185,186]; hence, from Raman spectrum it's not easily possible to differentiate the orthorhombic and any other space group. However, any change in the spectrum with incorporation of doping is expected to be either due to a structural phase transition or it can also be treated as disordered phonon

modes [187–189,193]. It is clear from the figure-4.2 (a) that with Cr doping an additional mode is generated at around 510 cm^{-1} and intensity of this mode increases with increasing the Cr doping.

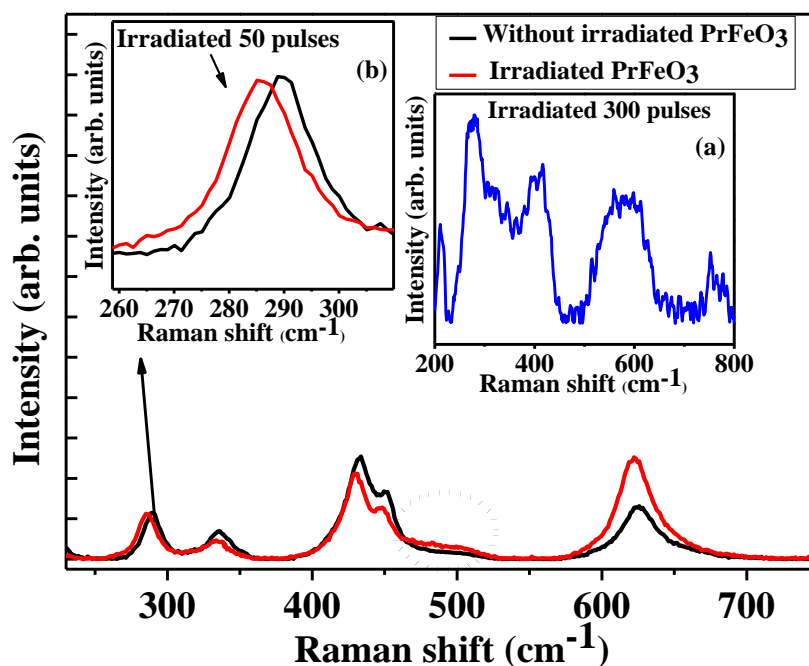


Figure-4.3: The Raman spectrum for pure and irradiated bulk PrFeO_3 . The scaling of Raman line width with irradiation of Laser pulses clearly indicates the locally induced structural disorder. Inset (a) of figure clearly signifies the increase in the structural disorders after higher irradiation/exposed time. The shifting of Raman modes (inset (b)) to lower wave-number side signifies the expansion of material due to irradiation.

As discussed in earlier section, the generation of new mode in Raman spectra with Cr doping can be due to structural disorder [187,188] or due to symmetry breaking [189,193], SXR studies do not show any new peak due to symmetry breaking as no new peak in the diffraction pattern appears or existing peak disappears even at much higher values of 2θ where the resolution of the system is much higher. Hence, it appears that the formation of new Raman mode in the Raman spectra is possibly due to structural disorder [118,187,188]. Present results are in well agreement with earlier reports [187,193–196]. In order to further confirm the appearance of Raman mode around 510 cm^{-1} is due to the structural disorder; laser irradiation has been carried out on pure PrFeO_3 samples.

The used laser parameters are listed in the Table:

Laser	KrF Excimer
Wavelength	248 <i>nm</i>
Energy density	2J/cm ²
Rep rate	2 Hz

It is important here to note that various researchers have used laser and irradiation to produce the structural disorder[118,187,188,197]. Figure-4.3 shows the effect of laser irradiation on the Raman spectra of pure PrFeO₃. Interestingly the relative intensity ratio of disorder peak (around 510cm⁻¹) increases after laser irradiation. Further change in the relative intensity of *AS* and *SS* mode (as indicated in figure-4.3) indicates that the bending or asymmetric stretching of FeO₆ octahedral modes are highly sensitive to structural disorder which is consistent with earlier studies[118,190,195,198]. From the inset (a) of figure-4.3 it is clearly evident that further laser irradiation leads to huge structural disorder as evident from increase in the intensity of disorder peak at 510cm⁻¹. Additionally, scaling of Raman line width with irradiation of Laser pulses clearly indicates the locally induced structural disorder, which further leads to change in relative intensity ratio of *AS* and *SS* FeO₆ octahedral modes similar to Cr doping. A significant red shift due to irradiation is clearly visible from inset (b) of figure-4.3. This shifting of Raman modes to lower wave-number side signifies softening of *AS/SS* FeO₆ octahedral modes, indicates expansion of material (or tensile strain) due to irradiation. At this point it should be noted that according to Raman selection rules, PrFeO₃ exhibit 24 first order Raman active modes and Fe does not contribute in scattering due to presence of inversion symmetry. However, structural disorders (defects and impurities) can destroy the inversion symmetry of FeO₆ octahedra which in turn may result to formation of additional mode at 510cm⁻¹. Similar phenomena was previously observed in case of centro-symmetric NaCl, KI and KCl crystals[125,126]. From this discussion, it can be concluded

that the generation of new Raman mode at around 510cm^{-1} with Cr doping is due to structural disorder and represents the disordered phonon mode and not a symmetry/structure change.

4.3.4 Discussion on cationic disorder:

Additionally cationic disorder has been studied and estimated value of disorder parameter σ [189,199] is shown in figure-4.4. It is well known that disorder due to ionic size mismatch between various ions at the same crystallographic site influences the transport properties of materials[199]. Average cation size and cation disorder are known to affect the electronic as well as magnetic properties of highly correlated oxides[200].

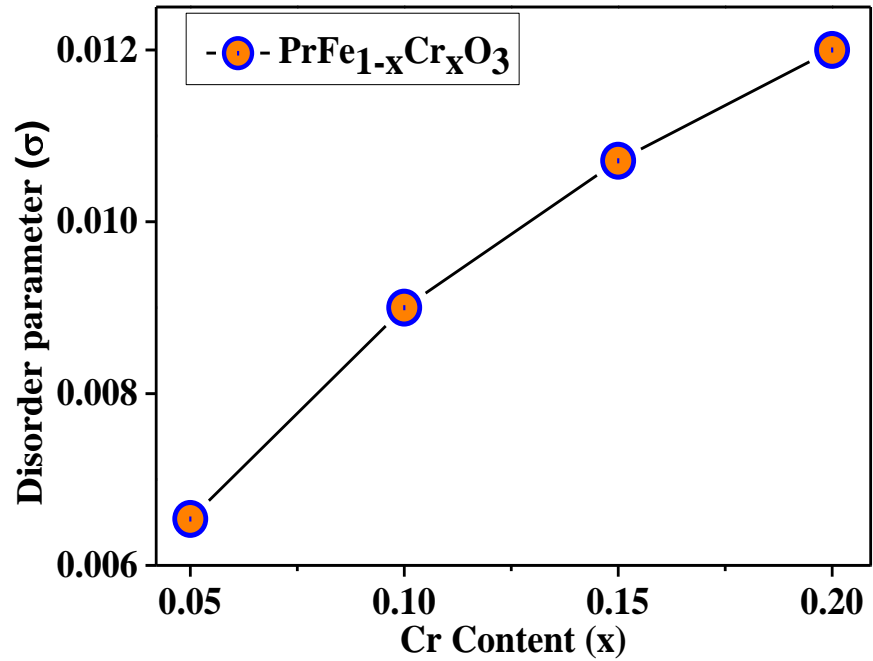


Figure-4.4: The variation of disorder parameter (σ) as a function of Cr content in PrFeO_3 .

Cation disorder at B-site (σ^2) in this ABO_3 system can be calculated by standard deviation of the average ionic radii[199,200].

$$(\sigma^2 = \langle r_B^2 \rangle - \langle r_B \rangle^2) \quad (4.2)$$

Here in case of Cr-doped PrFeO_3 , The cation disorder parameter σ scales with the Cr content as illustrated in figure-4.4 and has been understood

in terms of modification of strain and on-site potential fluctuations due to difference in the ionic radii and atomic numbers of Fe and Cr.

4.3.5 Some Additional Remarks and Quantification of different kind of disorders

As discussed in the earlier sections optical absorption spectroscopy have a potential to probe the total disorder present the system. However, in order to quantify the different kind of disorders (structural, thermal, compositional, chemical etc.) are not possible only through the optical absorption spectroscopy techniques. The octahedral breathing mode disorder modulates mainly the asymmetric M-O-M (Fe-O-Fe) stretching frequencies through the variable M-O (Fe-O) bond distance[82] and the corresponding changes can be reflected in Raman Spectroscopy. Similarly the change in the tilt angle and the corresponding tilt disorder, however, affects the lower frequency FeO₆ liberation-type modes of A_g symmetry[45]. In order to probe the said tilt angles SXRD data has been carefully analysed. The tilt angles θ [110] and φ [001] are related to the lattice parameters as[183,184]:

$$\theta = \cos^{-1}(a/b), \varphi = \cos^{-1}(\sqrt{2}a/c),$$

where a, b and c are the lattice constants of orthorhombic unit cell.

From systematic variation of lattice parameters (which is consistent with the fact that the ionic radii of Cr³⁺(0.61 Å) is smaller than Fe³⁺ (0.64 Å)) octahedral tilt angles θ and φ has been estimated and are provided in figure-4.1(b). It is clear from the figure that with increase in Cr doping θ and φ decreases systematically, which is well conformance with earlier report on similar ferrite system[82]. The disorder due to variation in tilt angle disorder affects the lower frequency soft modes of A_g symmetry. Figure-4.5 represents the low frequency mode of A_g symmetry in magnified view. It is clear from the figure that with inclusion of Cr doping corresponding mode shifts slightly to lower wave number region. The detail analysis of this mode suggests that the FWHM of this peak also increases which could be responsible for tilt angle disorder, in the present case the percentage change in the FWHM

(with respect to the pure PrFeO_3 samples) is found to be increasing with Cr doping.

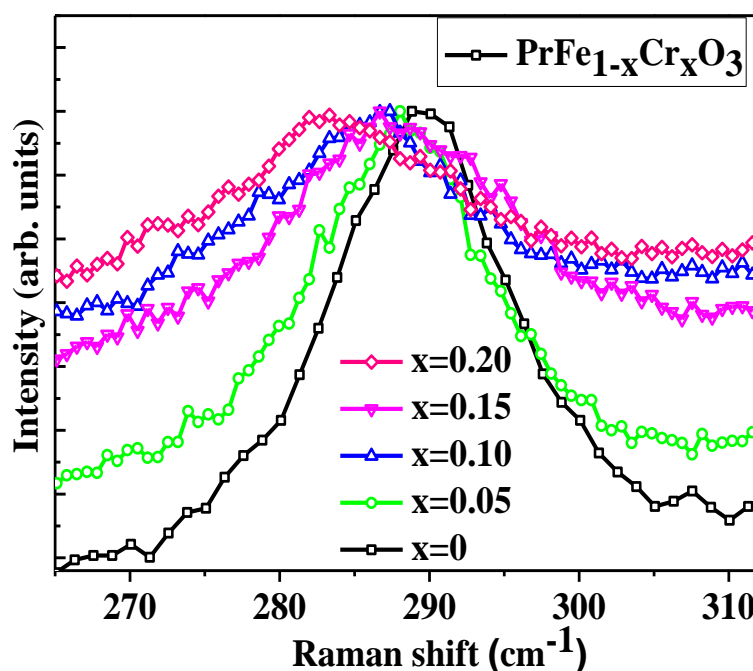


Figure-4.5: The variation of soft mode of A_g symmetry modes in magnified view.

The evaluation of results shows the linear relation between the vibrational frequencies of soft A_g modes and the octahedral tilt angles. However, direct probing of tilt angles are chronically not easy to probe directly, because it requires in depth synchrotron radiation diffraction experiments or neutron diffraction experiments. Our results clearly suggest the linear relation of tilt angles with soft A_g modes; hence, it seems that Raman spectroscopy could be an appropriate tool to probe the lattice distortions and slight changes in octahedral rotations.

However, disorder in octahedral breathing modes modulates mainly the asymmetric Fe-O-Fe stretching frequencies through the variable Fe-O bond distance. A systematic decrease in Fe-O bond length has been observed, whereas Fe-O-Fe bond angles increases with Cr doping. The variation of Fe-O bond length and Fe-O-Fe bond angles is consistent with earlier reports[120,171]. These parameters affect the asymmetric M-O-M stretching mode (AS) as illustrated in figure-4.2 (a). It seems that AS mode shifts towards higher wave number, which could

be due to compressive strain induced with Cr doping (due to decrease in Fe-O bond lengths). Hence, it seems that Raman spectroscopy could be an effective tool to quantify the different types of disorders.

In order to quantify the weightage of octahedral/polyhedral tilt angle disorder and octahedral breathing mode disorder (*i.e.* disorder due to the presence of two different M-O bond lengths) (*i.e.* Cr-O and Fe-O bond length) percentage change in FWHM for corresponding Raman modes has been estimated. The percentage change in Raman mode (B_{3g}) around 340 cm^{-1} is found to be 27% with respect to PrFeO_3 which could be the involvement due to the presence of two different Cr-O and Fe-O bond length. However, the percentage change in Raman mode corresponding to soft A_g mode/octahedral tilt angles is found to be 7% with respect to parent sample which could be considered as the involvement due to tilt angle disorder. The values of said disorders have also been estimated from the corresponding shifts in the peak positions. It has been observed that the contribution due of octahedral breathing mode disorder is ~4 times larger than that that of the tilt disorder. Hence the value of the total Urbach energy will have involvement from the said disorders accordingly (assuming the linear contributions from each disorder).

In order to estimate the possible impact of anharmonic terms, temperature dependent (TD) Raman spectroscopy measurements were carried out on 20% Cr doped PrFeO_3 sample. Figure-4.6 (a) illustrates the temperature dependence of Raman shift in temperature range 120K to 300K. A significant red shift to lower wave-number side is clearly visible, signifies expansion of material (or tensile strain) due to temperature. In order to estimate the effect of anharmonic terms variation of Raman FWHM (corresponding to Raman mode at 340 cm^{-1}) as a function of temperature is fitted with Balkanski model expressed as[120,201]:

$$T(T) = T(0) + A \left[1 + \sum \frac{1}{\exp\left(\frac{h\omega_i}{2\pi kT}\right) - 1} \right] \quad (4.3)$$

where term $T(0)$ in the model is corresponding to temperature independent terms such as compositional fluctuations, structural defects, inhomogeneity contribution etc. A is related to the anharmonic coefficients for three phonon processes.

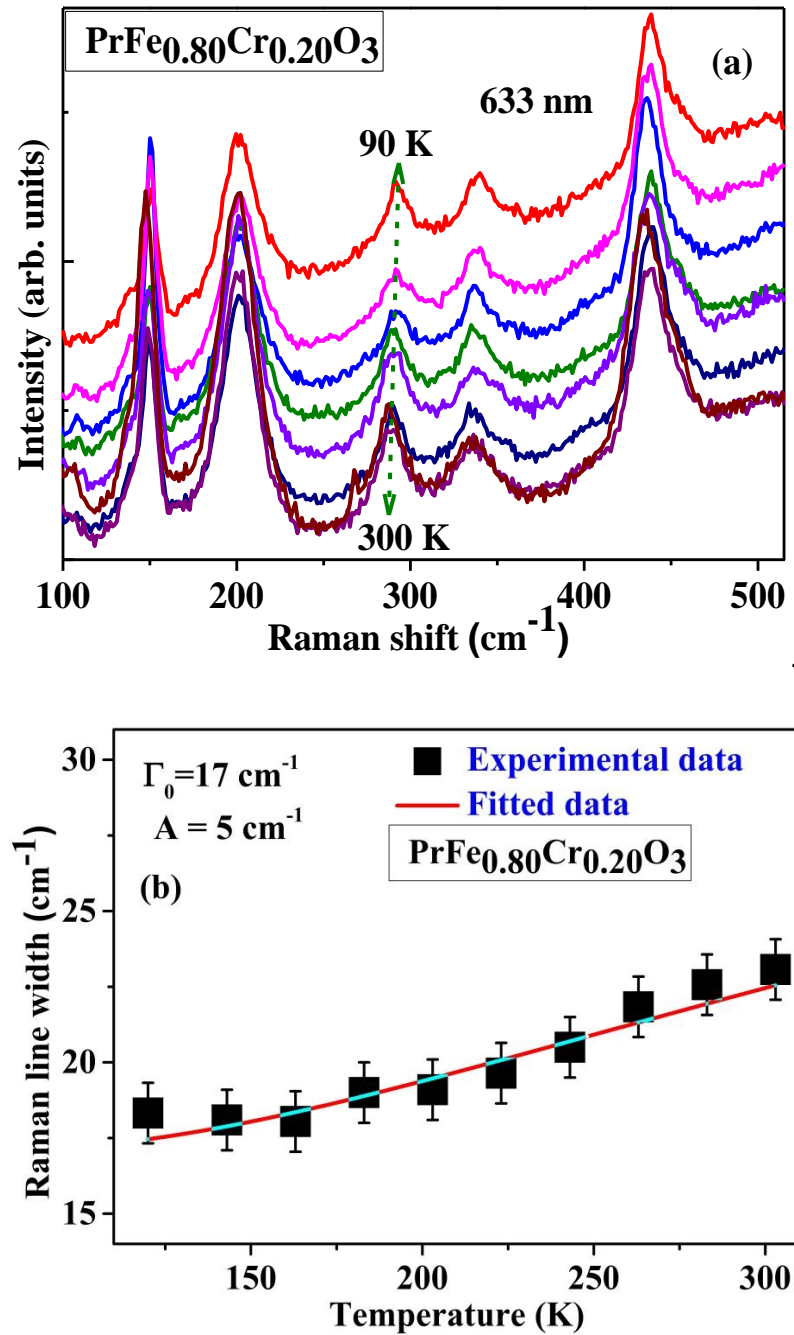


Figure-4.6: Temperature dependent Raman spectra for 20% Cr doped PrFeO_3 (a), whereas the variation of FWHM of Raman mode at 340 cm^{-1} as a function of temperature is depicted in figure-(b).

Here, in the present study we have not considered the four phonon process due to the reason that the involvement of anharmonic terms is small even at room temperature and becomes less significant at low temperatures.

Figure-4.6 (b) presents the variation of Raman line width as a function of temperature with fits to Balkanski model. The term $T(0)$ ($=17.01 \text{ cm}^{-1}$) is temperature independent term (attributed to structural disorders) have significant contribution, whereas, ΔT (6 cm^{-1}) and anharmonic involvement is considered as negligible. These results are well conformance with the earlier reports[119,202].

As discussed in earlier sections that all E_U measurements have been carried out at 300K, hence it can be assumed that thermal disorder is approximately constant. This statement seems meaningful since the weightage of anharmonic terms is almost constant up to room temperature. In addition to this this statement appears to be justified as there exists no substantial variation in Debye temperature even with 20% Ni doping in similar ortho-ferrite LaFeO_3 [203,204]. Thus, the contribution due to thermal disorder may be treated as constant. Hence, it can be concluded that the systematic scaling of Urbach energy, broadening in Raman line width and $FWHM$ of x-ray diffraction peak are dominated by a common factor *i.e.* structural disorder.

From this discussion, it is clear that at room temperature the major contributing factor in Urbach energy is due to structural disorders. In order to understand this context in details high temperature optical absorption spectroscopy and Raman measurements were carried out. Here, it should be noted that increase in random vibrations of atoms with temperature would leads to create thermal disorder as clear from OAS analysis (depicted in figure-4.7).

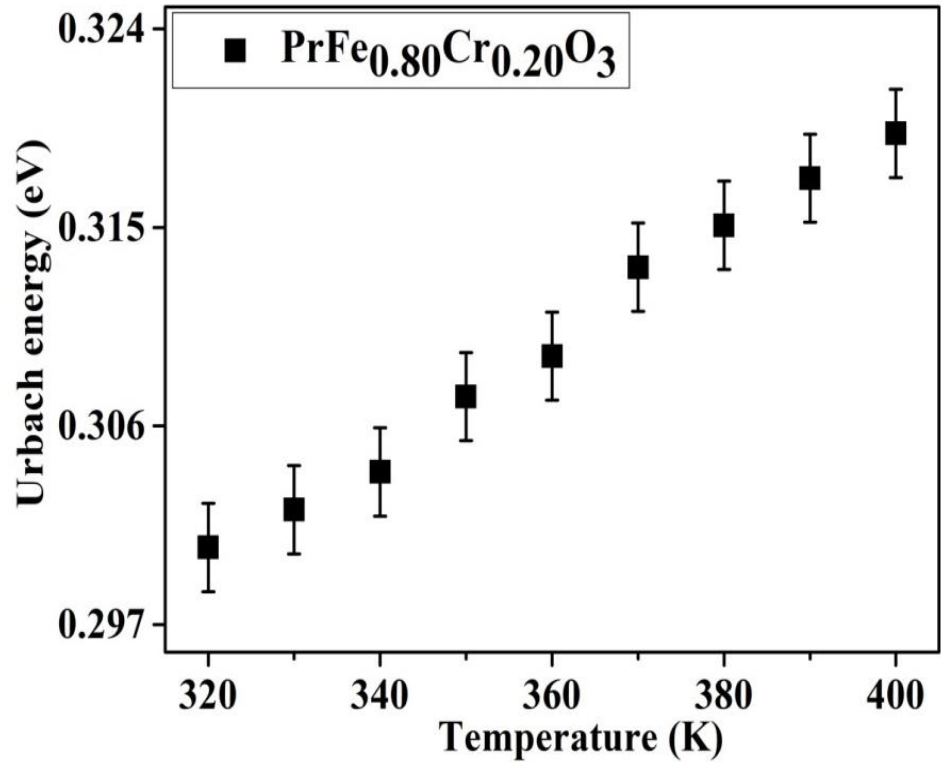


Figure-4.7: The variation of Urbach energy as a function of temperature for 20% Cr doped PrFeO_3 .

Since Raman spectroscopy is a powerful technique to probe the thermal/structural disorders and possible signature of such disorders is essentially lies in spectral width of Raman line shapes. The increase in Raman line width with temperature is depicted in Figure-4.6 (b). It is clear from the figure that E_U varies in similar trend as the Raman line width increase, clearly indicating the affection of temperature on phonons dynamics as well as on electronic states of the system. The scaling of FWHM of Raman line width and Urbach energy follows the same trend, *i.e.* the systematic variation with temperature is dominated by a common factor. However, at high temperatures anharmonic influence significantly contributes to the both terms. The similar variation of electronic disorder term and Raman FWHM is due to increase in random vibrations of atoms with temperature as discussed in earlier literature brief[99,194,201,202].

In additional, Raman spectra (shown in figure-4.2 (a)) the mode around 660 cm^{-1} consists very less intensity in the parent PrFeO_3 ,

whereas this peak gains intensity in mixed combination of both Fe and Cr at the B-site, could be due to enhancement in orbital mediated electron–phonon coupling (EPC) with inclusion of Cr doping[82,129,205]. However, due to lack of such coupling in PrFeO₃, the mode around 660 cm⁻¹ gains very less intensity. This mode is attributed to be due to in phase Fe-O stretching/breathing vibrations[82,129,206,207]. The possible origin of enhancement in intensity of such stretched modes is the charge transfer between the Fe³⁺ (d⁵) and Cr³⁺ (d³) through an orbital facilitated e-ph interaction mechanism[82,129,205]. At this juncture, it should be noted that d⁵ and d³ electronic configurations does not support such orbital mediated EPC due to absence of highly interacted half-filled e_g levels in both transition metal ions. However, when a photon having energy equal to or greater than charge transfer (CT) energy gap between transition metals ions (i.e. Fe³⁺ and Cr³⁺ in present case), an electronic transition takes place from Fe³⁺ to Cr³⁺ ions leaving them in a highly coupled configuration (d⁴-d⁴). The increase in such super exchange interactions with inclusion of Cr doping clearly suggests the enhancement in the magnetic interactions[82,129,205]. From this discussion, it seems that Raman spectroscopy could be used as an alternate characterization technique for predicting the magnetic properties and small variation in the octahedral tilt angles, this need to be further investigated. Also, the evaluation of these results suggests that these samples can be used as a model compound to understand the electron-phonon coupling in detail.

4.4 Conclusion

In conclusion, extent of electronic disorder E_U is quantified in terms of octahedral breathing mode disorder, tilt angle disorder, thermal and contributions due to anharmonic terms. Present results clearly suggest the linear relationship of tilt angles and soft A_g modes. Hence, it seems that Raman spectroscopy could be an appropriate tool to probe the lattice distortions, slight changes in octahedral rotations etc. An additional band observed in Raman spectra around 510 cm⁻¹ has been

understood in terms of structural disorder produce by Cr doping. Moreover, a systematic correlation between crystallographic strain, Raman line width, disordered parameter, and Urbach energy has been observed, which implies that structural disorder affects phonons as well as electronic states of the system.

Chapter 5

Orbital facilitated charge transfer originated phonon mode in Cr substituted PrFeO₃: A brief Raman study

In recent years, Raman spectroscopy has been widely used to probe the vibrational properties of mixed Fe-Cr based RFeO₃ systems and the properties is believed to be responsible for various physical properties of these materials. The origin of strain induced disordered Raman modes have been discussed in the previous chapter. Here, the present chapter the origin of orbital facilitated new Raman mode in orthorhombic perovskite PrFe_{1-x}Cr_xO₃ has been investigated using resonance Raman spectroscopy and first principle DFT calculations. Results reported here are published in the literature.*

*Kumar *et. al.* J. Raman Spectrosc. 10 (2020) 5894.
<https://doi.org/10.1002/jrs.5894>

5.1 Introduction

The importance of electron-phonon interaction has been epitomized in colossal magneto-resistance (CMR) observed in manganite's with Jahn-teller (JT) active ions[81,106]. It is well known that in the case of manganite's, orbitons can be excited in Mn ions having JT configuration (d⁴ electronic state)[81] through JT polaron hopping mechanism. The presence of JT distortion in Mn³⁺ results in the splitting of e_g orbital into states with lower energy which produces the potential to be minimum. The altering in the potential traps the electrons in that orbital, known as self-trapping, which increases the lifetime long enough for it to interact with lattice distortion[82]. However, the presence of said coupling and its consequence in the JT inactive materials has not been explored so far in detail. Electron-lattice dynamics plays a very important role to realize the phenomenon of CMR

in rare earth-transition metal oxides[106] and the correlation between the structural, magnetic and orbital ordering is very important to realize the orbital facilitated charge transfer (CT) mechanism, which is the base for the EPC[82,106].

In the case of doped PrFeO_3 , new Raman modes have been observed and some experimental efforts have been made earlier by some research groups to understand the origin of these phonon modes[44,127,128]. For example the Raman mode around 550 cm^{-1} has been attributed to be due to strain induced structural disorder[44] and the mode at around 660 cm^{-1} predicated to be due to orbital mediated charge transfer between two transition metal ions[129] but there exist no unanimous consensus amongst the scientific community about the origin of the this Raman mode. It is important here to note that the generation of new Raman mode in Raman spectra could be attributed to various factors such as orbital mediated EPC[129], symmetry breaking[44], strain induced structural disorder[44] *etc.* However, high-resolution synchrotron x-ray diffraction studies investigations on these samples suggest that there is no signature of change in the structural symmetry with Cr substitution[44]. Hence, the occurrence of new phonon mode at around 660 cm^{-1} cannot be due to the change in structural symmetry. In addition to this, the generation of the said new phonon mode in distorted perovskites has been discussed in detail based on the orbital mediated charge transfer and Franck-Condon principle[208,209]. It is important here to note that the generation of this Raman mode due to orbital mediated lattice rearrangement is not allowed for the atomic arrangement having orthorhombic symmetry as per the selection rules of group theory for orthorhombic system[210]. Recently, J. Andreasson *et al.*[208,209] studied the Franck-Condon higher-order lattice excitations in $\text{LaFe}_{1-x}\text{Cr}_x\text{O}_3$ system and attributed the possible origin of Raman mode around 660 cm^{-1} to orbital mediated Fe to Cr charge transfer effects. However, strong evidence through rigorous experimental and theoretical investigations is needed to be established and to prove the origin of the above-mentioned Raman mode.

Keeping the above in mind, the present study is aimed to

understand the origin of Raman mode arising around 620 cm^{-1} (in PrFeO_3) and 660cm^{-1} (in Cr-substituted PrFeO_3). To the best of our knowledge, Jahn-teller (JT) compounds such as manganite's are known to exhibit electron-phonon coupling mechanism through JT polaron hopping mechanism[106,150]. However, the presence of above-mentioned coupling in JT inactive compounds would be very interesting to explore. Therefore, Cr-substituted PrFeO_3 has been prepared by the wet chemical method[171,211] and the interplay between the electron dynamics and lattice has been studied in the same. One of the important outcomes of the present investigations is that both Fe^{3+} and Cr^{3+} ions are JT inactive and no JT coupling is expected in parent compounds. However, in the samples having mixed Fe and Cr ions, it seems that the lattice rearrangement takes place through the orbital mediated electron transfer from Cr^{3+} to Fe^{3+} ions with the shining of a photon with energy equal to charge transfer gap, which is further supported by first-principle calculations, experimental resonance Raman spectral analysis, optical absorption and valence band spectroscopy measurements[171] carried out on as prepared and vacuum annealed samples. Thus, by using the different techniques, a possible mechanism for orbital mediated electro-phonon coupling in $\text{PrFe}_{1-x}\text{Cr}_x\text{O}_3$ system is provided here.

5.2 Experimental details

The synthesis of $\text{PrFe}_{1-x}\text{Cr}_x\text{O}_3$ samples has been achieved by the citric acid route method. The details of the synthesis method had been discussed in chapter-2. The crystalline phases of the prepared samples were identified by synchrotron x-ray diffraction (SXR) at BL-12 using the Indus-2 synchrotron source[44,171]. The Horiba Raman micro spectrometer is attached to two air-cooled solid-state laser kits, at 532 nm, 785 nm and a He-Neon gas laser having excitation wavelength 633 nm was used to probe the vibrational properties of prepared samples[44]. The optical properties have been studied by optical absorption spectroscopy (OAS) experiments in the wavelength range 200–800 nm[65,66,212,213]. Valence band spectroscopy measurements were carried out to investigate the effect of Cr substitution on the density of

states near the Fermi level. Excitation of monochromatic He-1 line from SPECS (UVS 300) source has been used to study the valence band of the prepared samples at the experimental station of angle-resolved photoelectron spectroscopy (ARPES) beamline BL-10 with a SPECS Phoibos 150 electron energy analyser with base vacuum $\sim 7 \times 10^{-11}$ mbar at Indus-2 synchrotron source [171].

5.2.1 Theoretical details

In the present study, first-principle calculations were carried for 25% Cr-substituted PrFeO₃ sample by using a full-potential linearized augmented plane wave (FP-LAPW) method within the framework of density-functional theory as implemented in WIEN2k package [127,214–216]. The experimental values of lattice parameters and Wyckoff positions extracted from the refinement of x-ray diffraction data have been used for first-principle calculations with strong Coulomb interaction (GGA+U) U= 3 eV for Fe and U= 2 eV for Cr was taken into consideration to simulate the density of states (DOS). A super-cell of size 2×1×1 containing 40 atoms was used to generate the DOS for the present system.

5.3. Results and discussion

This section is divided into five parts; first part presents the structural characterizations using synchrotron x-ray diffraction experiments. In the next four parts, a detailed investigations on the orbital mediated charge transfer originated Raman modes have been presented using Raman scattering, valence band spectroscopy and first principle calculations.

5.3.1 Structural studies

The structural phase purity of the prepared samples has been examined using synchrotron x-ray diffraction (SXRD) measurements and the details of various structural parameters are provided in the Table-1. Further, the values of Goldschmidt structural tolerance factor defined as: $t = \frac{R_{A-O}}{\sqrt{2}R_{B-O}}$ (where; R_{A-O} and R_{B-O} are the average Pr-O and Fe-O bond length respectively) has been estimated to understand the

structural parameters in detail. For this purpose, the SXRD data have been refined considering the $Pnma$ space group.

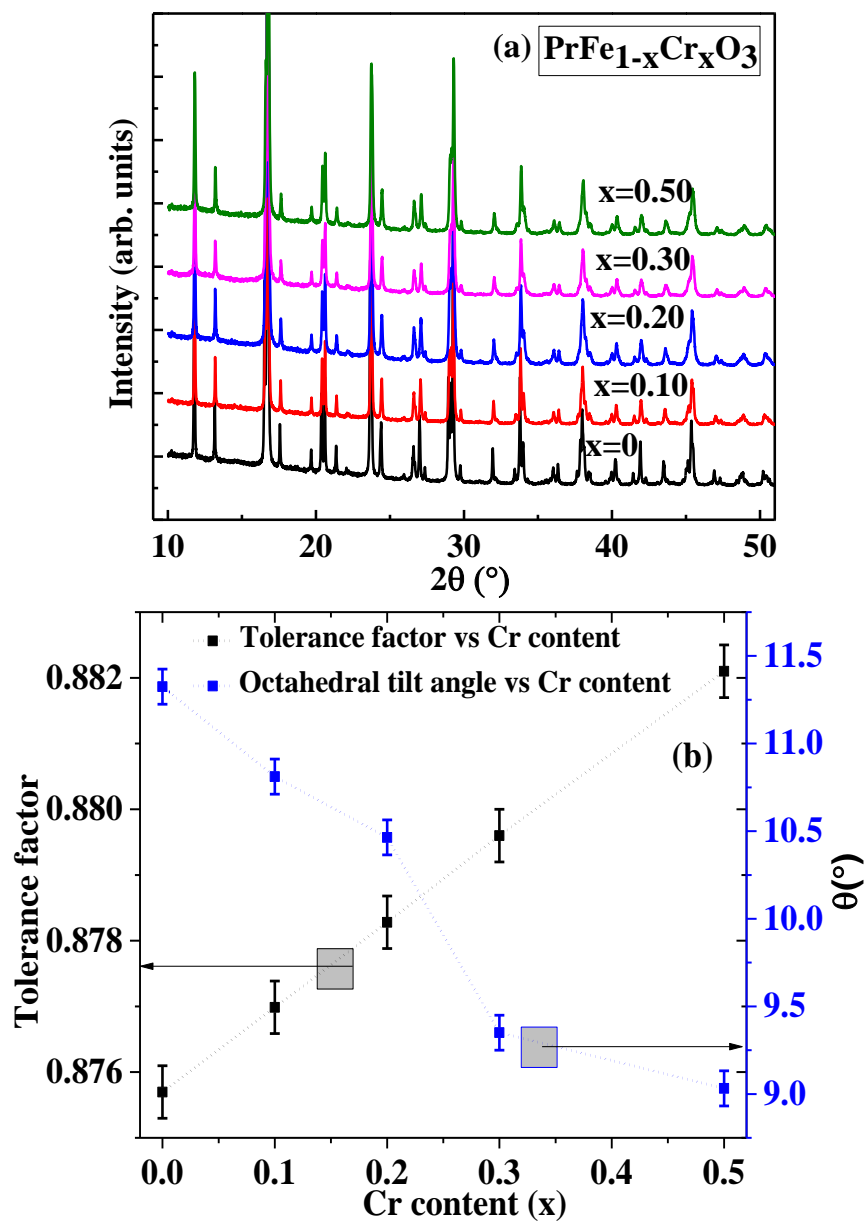


Figure 5.1: The Synchrotron x-ray diffraction for prepared series of samples (a). The variation of tolerance factor and octahedral tilt angles as a function of Cr content is depicted in figure-(b).

Figure-5.1 represents the estimated values of Goldschmidt structural tolerance factor, which scale systematically with Cr content, indicating the increase in the stability and tendency towards the more symmetric structure *i.e.* the values of Goldschmidt structural tolerance factor is approaching towards 1 and Fe-O-Fe bond angles towards 180° with Cr

substitution. Apart from this, the average tilt angle has been estimated[183,184] from the variation of unit cell parameters. It can be seen from the figure-5.1 that the average tilt angle decreases with the inclusion of Cr, which could be attributed to the increase in the stability and tendency towards the more symmetric structure. These results are in excellent agreement with the reported literature[44,82].

5.3.2 Effect of Cr-substitution on Raman line shapes

Figure-5.2 represents the Raman spectra using 633 *nm* excitation laser acquired at room temperature. It is now well accepted that the samples experiencing compressive strain undergo a blue shift of Raman mode and the same is clearly visible in the present case, as shown by the blue rectangle in figure-5.2. This systematic blue shift is attributed to the decrease in the Fe-O bond length with increasing the Cr content, which is in good agreement with the variation of Fe-O bond length as shown in Table 1. At this point, it should be noted that the Raman mode (arising around 660 cm^{-1}) shifts towards higher wavenumber (as shown by the blue rectangle in figure-5.2), whereas, the soft A_g modes (as shown by the black rectangle) show the redshift with Cr substitution. As discussed by Weber *et al.*[186], soft A_g modes at lower wavenumber are governed by the variation in the octahedral tilts and the red shift with Cr substitution could be attributed to the reduction in the orthorhombic distortion. The possible reason for orthorhombic distortion present in these $R\text{FeO}_3$ oxides is ascribed in terms of the difference in the size of rare-earth ions and transition metal ions. These effects further distort the FeO_6 octahedra in terms of tilting and rotation in order to fulfil the extra space present around R ion[82,217]. It is interesting to note that the increase in the values of Fe-O-Fe bond angle parameters (see Table 6.1 in chapter-2) with Cr content suggests the decrease in deviation from the ideal value of 180° and the systematic reduction in the octahedral tilt angle with doping is in excellent agreement with the linear relationship between the soft A_g Raman modes and tilt angle. In addition to this, two new phonon modes are visible at $\sim 510 \text{ cm}^{-1}$ and $\sim 660 \text{ cm}^{-1}$. The generation of new phonon mode arising around 510 cm^{-1} has been

understood in terms of strain-induced structural disorder due to Cr substitution[44].

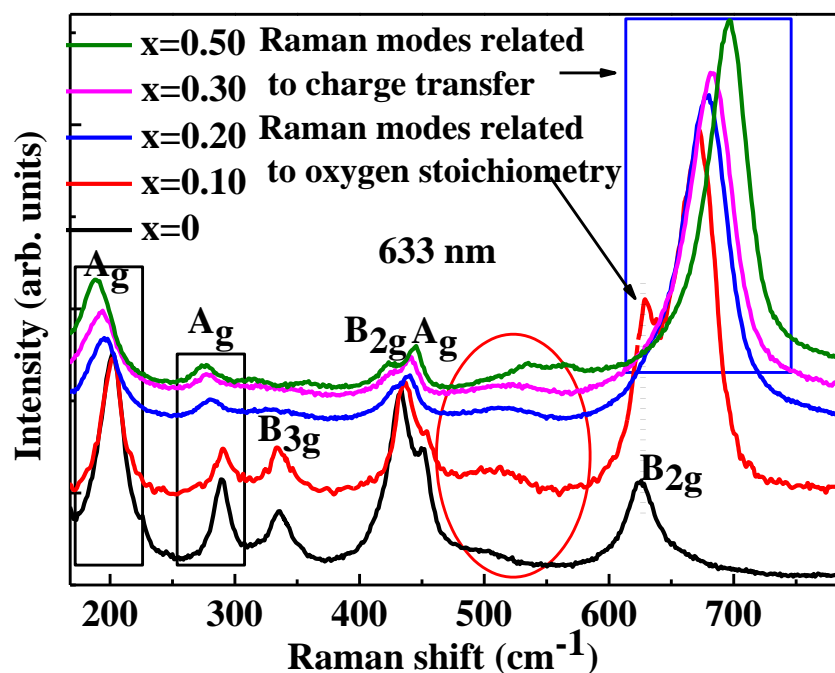


Figure 5.2: The Raman spectrum for prepared series of samples by using laser having excitation wavelength 633 nm. Dark black rectangles represent the red shift in soft A_g modes, whereas dark blue rectangles show the blue shift with doping.

Also, the origin of Raman mode around 620 cm^{-1} in PrFeO_3 is related to the oxygen defects. However, with strong experimental and theoretical evidences the origin of 620 cm^{-1} in PrFeO_3 and 660 cm^{-1} in mixed Fe-Cr systems has not been done so far in available literature. To understand this in detail, first principle calculations, OAS and valence band spectroscopy measurements have been done on the prepared series of samples and will be elaborated in detail in the next sections.

5.3.3 Density functional theory, optical absorption spectroscopy and valence band spectroscopy analysis

To deeply understand the origin of Raman mode arises around 620 cm^{-1} in PrFeO_3 and 660 cm^{-1} in mixed Fe-Cr system, the first-principle calculations on 25% Cr substituted PrFeO_3 sample were carried out and corresponding partial dos is depicted in figure-5.3. It is well

known that metal-3d states and O-2p states generally contribute to the band gap in these ABO₃ type transition metal oxides^[22,34]. The overlapping between these states gives rise to the separation of energy bands.

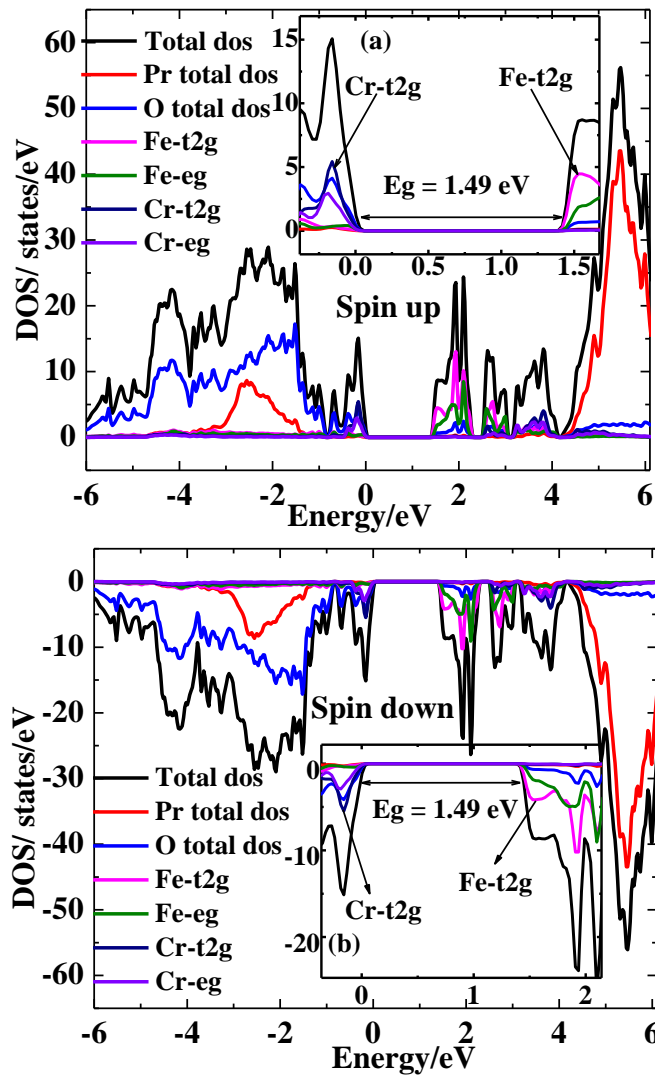


Figure 5.3: The spin up (a) and spin up (b) total and partial density of states for Cr substituted PrFeO₃.

From the figure-5.3, the band gap of 1.49 eV can be clearly seen, which separates the occupied density of states (DOS) of Cr close to Fermi level and unoccupied DOS of Fe atoms centred around 2 eV. Apart from this, it can be evident from the inset of figure-5.3 that, Cr-t_{2g} states contribute near the Fermi level in PrFe_{1-x}Cr_xO₃. The energy difference of centre of Cr-t_{2g} band from the Fe-t_{2g} band is about ~2.1 eV

and the probability of electronic transition between these bands is maximum, which is in excellent agreement with the formation of exciton line shape in optical absorption spectra as shown in detail in chapter-3 (figure-3.5). Hence, the observed mechanism can be realized in terms of charge transfer from Cr- t_{2g} band to Fe- t_{2g} band with the absorption of a photon having energy of the order of ~ 2 eV. It is evident from the inset of figure-5.3 that, Cr states contribute near the Fermi level in $\text{PrFe}_{1-x}\text{Cr}_x\text{O}_3$.

The formation of Cr states near Fermi level has been further confirmed experimentally by performing the Valence band spectroscopy measurements on some of the prepared series of samples. The detail about the Valence band spectroscopy has already been discussed in chapter-3. In the case of semiconducting oxides, the intensity at the Fermi level is negligible, which is consistent with the present results. However, the systematic increase in the intensity of feature near E_f (as shown in the inset of figure-3.5 of chapter-3) suggests that Cr states dominate near the Fermi level in $\text{PrFe}_{1-x}\text{Cr}_x\text{O}_3$.

From this discussion, it can be concluded that Cr states are formed about 0.1 eV below the valence band maxima and the density of these states systematically scales with Cr concentration as clear from experimental VBS results. Therefore, the probability of CT from $\text{Cr}^{3+}\text{-O}^{2-}\text{-Fe}^{3+}$ is maximum instead of $\text{Fe}^{3+}\text{-O}^{2-}\text{-Cr}^{3+}$ transition with shining a photon of energy ~ 2 eV. Hence, the origin of aforesaid Raman mode could be related to the transfer of charge from $\text{Cr}^{3+}\text{-O}^{2-}\text{-Fe}^{3+}$. The mechanism for the generation of Raman mode around 660 cm^{-1} could be related to the orbital mediated lattice rearrangement due to excitation of electrons from Cr^{3+} to Fe^{3+} and leaving them in $d^2\text{-}d^6$ ($\text{Cr}^{4+}\text{-O}^{2-}\text{-Fe}^{2+}$) configuration. The interactions of these configurations are different from $\text{Cr}^{3+}/\text{Fe}^{3+}$, which further couples with the intrinsic breathing mode and activates the Raman mode[219]. The schematic representation of orbital mediated Franck-Condon (FC) scattering is shown in figure-5.4 (a&b).

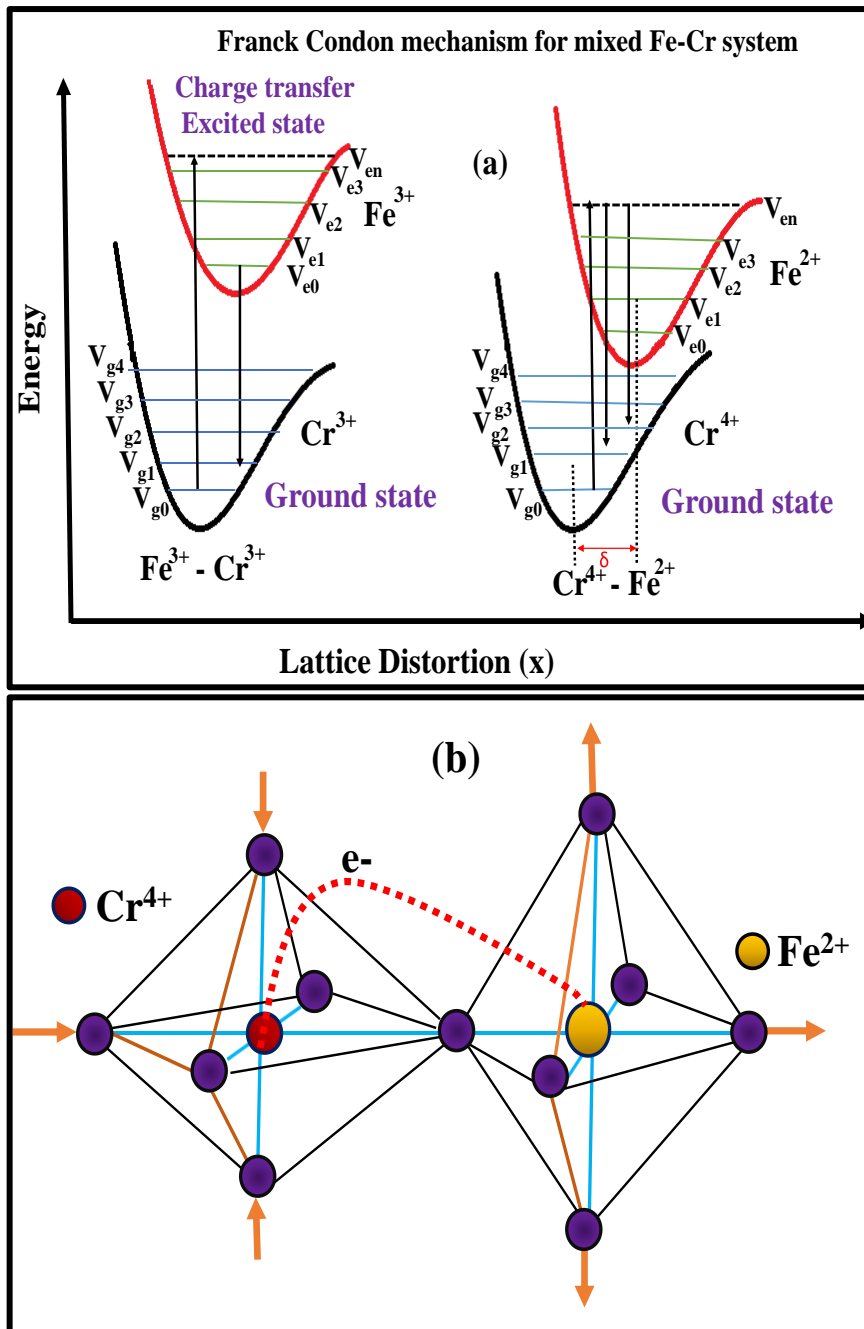


Figure-5.4 (a): The Franck-Condon picture for mixed Fe-Cr systems. The orbital mediated charge transfer from Cr^{3+} to Fe^{3+} after leaving them in Cr^{4+} and Fe^{2+} state respectively is depicted in figure-(b).

It is based on the idea that when electrons are promoted to an excited state having very short-life time, atomic nuclei do not change its position during this short interval as clear from figure-5 (a). When the electronic excited state has a lifetime analogous to the atomic vibration period, then the nuclei can readjust its positions to achieve a new total

energy minimum so-called lattice relaxation. The orbital mediated FC scattering principle applies to a case, where light excites an electron to the excited state and could have a sufficiently long lifetime for a lattice relaxation[220]. It is interesting to note that the electric field component of light acts as a perturbation within the context of quantum mechanical perturbation theory in this scattering. If the lattice distortion is sufficiently large, then this should result in generation of new modes in the Raman spectrum. The relative intensities of new originated Raman modes contain the crucial information of lattice distortion and permit these modes to be distinguished from other modes having different origins.

5.3.4 Effect of vacuum annealing

As discussed in earlier sections, the present investigations are aimed to understand the possible origin of Raman mode arising around 620 cm^{-1} in PrFeO_3 and 660 cm^{-1} in mixed Fe and Cr system. The generation of these Raman modes are not allowed for the normal *Pnma* space group as per the selection rules of group theory[210]. The evaluation of results infers that the intensity of this Raman mode in PrFeO_3 has a direct relationship with the presence of oxygen stoichiometry, the extent of disorder/local lattice imperfection *etc.*, which might be responsible for the presence of strongly interacting e_g electrons and Raman mode around 620cm^{-1} in PrFeO_3 [82,215]. To deeply understand the origin of this mode in PrFeO_3 , the samples have been annealed in vacuum for 10 hours at 1000°C . Figure 5.5 (a) and (b) represent the compared Raman spectra for polycrystalline vacuum annealed PrFeO_3 and $\text{PrFe}_{0.70}\text{Cr}_{0.30}\text{O}_3$ samples recorded at room temperature respectively.

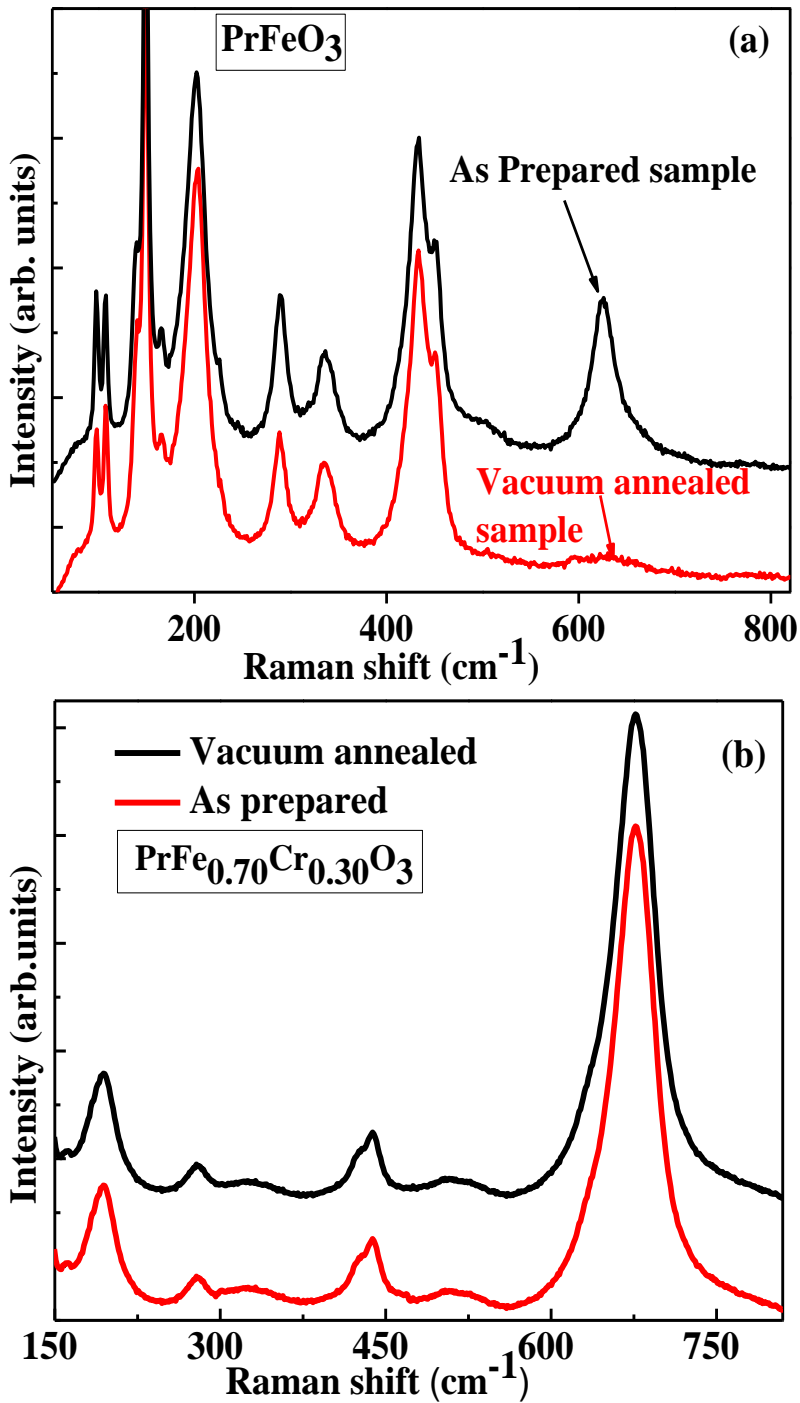


Figure-5.5: The Raman spectrum for as prepared and vacuum annealed PrFeO_3 by using laser excitation wavelength 633 nm. The disappearance of Raman mode around 620cm^{-1} after vacuum annealing suggests the origin of this mode is related to oxygen Stoichiometry (a). No observable changes have been observed for 30% Cr substituted sample as represented in figure 6(b).

Interestingly, the absolute intensity, positions and Raman line width of Raman modes below 600 cm^{-1} remain similar after annealing in vacuum, while these properties for the Raman mode at around 620 cm^{-1} change drastically after annealing in vacuum for PrFeO_3 . Hence, it seems that this mode does not relate to the normal Raman modes of orthorhombic structure having space group $Pnma$. The evolution of results seems meaningful because of the reason that normal space group modes are insensitive to external conditions such as annealing temperature. For transition metal oxides, it is well known that self-trapping of electronic excitations would result in the instigation of Franck Condon scattering. Generally, the self-trapping is facilitated by hybridization between the metal- $3d$ and O- $2p$ orbitals and d^4 configuration seems to be necessary for the appearance of Franck Condon scattering in these oxides[219]. Therefore, the presence of Raman mode around 620 cm^{-1} in PrFeO_3 could be attributed to variation in oxygen stoichiometry/ d^4 configuration. However, for $\text{PrFe}_{0.70}\text{Cr}_{0.30}\text{O}_3$, no significant changes have been observed after vacuum annealing, which strongly reveals that the origin of Raman mode around 660 cm^{-1} is not related to the above-mentioned lattice imperfection or oxygen defects. The detailed analysis of the aforesaid mode will be elaborated in the following sections.

5.3.5 Effect of excitation wavelength on Raman modes

Further, to shed more light on the orbital mediated charge transfer mechanism, resonant Raman scattering experiments were performed on pure and Cr-doped samples. Raman spectra for vacuum annealed PrFeO_3 and Cr-substituted PrFeO_3 sample using different excitation wavelength sources (532 nm , 633 nm and 785 nm) strongly support the CT speculation and the representative data is given in figure-6.6 (a) and (b) respectively. The wavelengths 532 nm and 633 nm are in the range of optical band gap and $d-d$ transitions[129,209], where resonance can be expected[44,82,129]. The presence of oxygen defects, the extent of disorder/local lattice imperfection *etc.*, in as prepared PrFeO_3 would results to self-trapping of electrons, which increases the

lifetime long enough for electrons to interact with lattice distortion and results to formation of Raman mode around 620 cm^{-1} in those samples having laser excitation energy is comparable to CT gap. Apart from this, the lattice rearrangement through photon irradiation can take place by CT from $\text{Cr}^{3+} (d^3)$ to $\text{Fe}^{3+} (d^5)$ ions and leaving them in $d^2-d^6 (\text{Cr}^{4+}-\text{O}^{2-}-\text{Fe}^{2+})$ configuration[129]. The Coulomb interactions of this configuration are different from $\text{Cr}^{3+}/\text{Fe}^{3+}$, which further couples with the intrinsic breathing mode and activates the new Raman mode. This can be understood as follows: In the case of semiconducting materials, the transition of electron from valence to the conduction band is modeled as follows[221,222]:

$$\eta_{(V \rightarrow C)} = C_{V \rightarrow C} \rho(\omega) \rho(V_B) \quad (5.1)$$

where $\eta_{(V \rightarrow C)}$ is a rate of transition of electron from valence to conduction band, $C_{V \rightarrow C}$ is a constant of proportionality (for given energy ω), $\rho(\omega)$ is the density of photon having frequency ω and $\rho(V_B)$ represents the density of electron in top of the valence band. The absorption coefficient (C_{VC}) is ideally zero for photon energy; $E < E_g$ (E_g is charge transfer gap), which scales with the photon energy E [108,215]. From the equation-1, it is clear that with increase in the energy ($C_{V \rightarrow C}$) and density of photon ($\rho(\omega)$), the rate of electronic transition scales systematically. It is interesting to note that by exciting a particular Raman mode, electron–phonon interactions even induce metal–insulator transitions and changes in the magnetic order[130], which makes these phenomena’s further very interesting. At this point, it is important here to note that with changing the laser excitation energy penetration depth also changes, which contributes to the change in the relative intensity of phonon modes. The intensity of modes related to the normal $Pnma$ space group is stronger for 785 nm and 633 nm excitation than 532 nm , which is in good conformance with the weaker optical absorption at higher wavelengths and large penetration depth. However, relative intensity (of Raman mode around 660 cm^{-1} and A_g mode around 300 cm^{-1}) is scaling with the Cr concentration, which strongly suggests the dominating factor

is the distortion/lattice rearrangement related to the CT and effect of penetration depth can be ruled out.

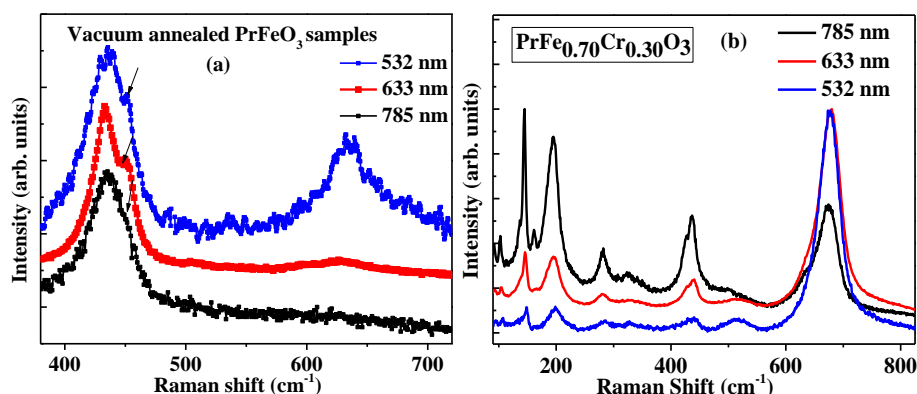


Figure-5.6: The resonance Raman spectrum for as prepared PrFeO₃ (a) Cr substituted PrFeO₃ (b) by using different excitation wavelengths.

From this discussion, it can be concluded that the origin of Raman mode around 620 cm⁻¹ in the vacuum annealed PrFeO₃ is attributed to the oxygen defects, the extent of disorder/local lattice imperfection *etc.* However, in the case of mixed Fe-Cr samples, the fundamental excitation is generated by strong orbital facilitated electron-phonon interactions activated according to the Franck Condon picture by a photon-induced transfer of an electron from an Cr to an adjacent Fe ion. Present results demonstrate the case of selective phonon mode excitation and the magnitude of the observed Franck Condon scattering should prove useful for fundamental studies of the relation between global and local effects in correlated systems in general and electron-phonon interactions in particular, as well as for the study of transient phenomena such as electron-phonon interactions induced metal-insulator transitions, changes in the magnetic interactions *etc*[130,131].

5.4 Conclusion

A detailed investigation on the origin of orbital facilitated electron-phonon coupling has been done in orthorhombic perovskite PrFe_{1-x}Cr_xO₃. The presence of mixed Fe-Cr ions would instigate the orbital mediated electron-phonon coupling mechanism due to transfer of

charge from Cr^{3+} to Fe^{3+} ions. The systematic increase in the absolute intensity of Raman mode arising around 660cm^{-1} suggest that the probability of charge transfer is maximum for the highest Cr substituted sample, which is in conformance with the Resonance Raman scattering results. Another important and intriguing aspect of present work is the absence of e_g electrons seems to be responsible for the non-presence of Raman mode around 620 cm^{-1} in vacuum annealed PrFeO_3 . The presence of strongly interacted e_g electrons in as prepared PrFeO_3 would results to self-trapping of electrons, which increases the lifetime long enough for electrons to interact with lattice distortion.

Chapter 6

Role of Pr atoms delocalization on the natural and magnetic field induced polar order in $\text{PrFe}_{0.5}\text{Cr}_{0.5}\text{O}_3$

The controversial discovery of ferroelectricity in RFeO_3 [Kuo et al., Phys. Rev. Lett. 113, 217203 (2014)] and mixed Fe-Cr based orthorhombic (Pnma) perovskites, [Yang et al., Physical Review B 101, 014415 (2020)] inspire further investigations on these strongly correlated systems. Here, in this chapter, we studied the possible origin of natural and magnetic field induced polar order near room temperature in $\text{PrFe}_{0.5}\text{Cr}_{0.5}\text{O}_3$ using temperature-dependent synchrotron x-ray diffraction, P-E measurements, Raman spectroscopy and Compton scattering experiments. The present results show a significant contribution in understanding the ferroelectric polarization and progress in search for new room temperature magneto-dielectric materials.

6.1 Introduction

As discussed in the earlier chapters that the search for new materials that exhibit magneto-electric coupling has become the need of the day, which increases the possibility of scheming RT based novel devices. The development of silicon-based tiny integrated circuits has open new avenue for research in the direction of exploring new materials for various electronic applications [5–8]. Nowadays, research is focused on developing new tiny as well as energy- efficient electronic devices and replacing the conventional electronic circuit elements. The efforts are now being made to develop spin-based electronic devices and in these directions perovskite oxides are of great interest[3,5,6,12].

In this work, we focus on the $\text{PrFe}_{0.5}\text{Cr}_{0.5}\text{O}_3$ ceramic, and its end members *i.e.* both PrFeO_3 and PrCrO_3 crystallize in orthorhombic structure along with the space group $Pnma$ [12,223–225]. Earlier, astonishing efforts have been made by various research groups to understand the multi-ferroic properties of these compounds[33,39,226,227]; however, the origin of natural and magnetic field-induced polar order in these materials is not clear so far in the available literature[14,15]. It is now well accepted that the presence of unpaired transition metal d -electrons and rare earth f -electrons in these RFe/CrO_3 oxides is responsible for the existence of the coupling between two magnetic sublattices[40]. It is reported that the exchange striction between rare earth and Fe/Cr moments would result in ferroelectricity in these materials below magnetic ordering temperature (T_{N1}). Recently in SmFeO_3 , ferroelectric features have been reported below T_{N1} (670 K)[36], which is completely surprising as it would require R ion moments ordering at very low temperature (<15 K). Therefore, the exchange striction mechanism cannot solely explain the cause of polarization observed at high temperatures. The anisotropic interactions between R and Fe^{3+} ions may play important role in inducing the net dipole moment in these oxides. Bhadram *et al.*[37] reported that the spin-phonon coupling plays an important role in stabilizing the polar order in RFe/CrO_3 oxides. Therefore, there has been an intense debate on the exact origin of ferroelectric order in these oxides. Hence, the probing of local structure would be very important to understand the observed new class of ferroelectricity in these materials.

It is worth noting that the magnetic ordering temperature in these orthoferrite oxides can be tuned to room temperature and the strength of magneto-dielectric coupling is maximum around transition temperature[138,228]. The magnetic ordering temperature (T_{N1}) for the parent PrFeO_3 sample is 700 K and for $\text{PrFe}_{0.5}\text{Cr}_{0.5}\text{O}_3$, T_{N1} is near room temperature[32]. Therefore, it could be possible to tune the orientations of spins by applying very small magnetic field by means of magnetostriction. Further, the demands of high-performance and multitasking

micro-electronic devices that can store, share information in an easier and faster way motivate scientists for searching the new materials with multi-functional properties for reading, writing and data sharing processes[2,3].

Keeping the above in view, temperature-dependent (TD) Raman, synchrotron x-ray diffraction, neutron Compton scattering experiments and dc magnetization measurements were performed to investigate the origin of the natural and magnetic field-induced polar order in $\text{PrFe}_{0.5}\text{Cr}_{0.5}\text{O}_3$. The careful analysis of neutron Compton scattering data, TD and magnetic field dependent Raman data strongly demonstrates an increased magnitude of delocalization of Pr^{3+} ions in the presence of the Cr in the lattice at room temperature which seems to be one of the important contributing factors for the observed ferroelectric behavior in $\text{PrFe}_{0.5}\text{Cr}_{0.5}\text{O}_3$. The present investigations suggest that Cr^{3+} substitution at Fe^{3+} site in ortho-ferrites would scale the possibility of magneto-dielectric coupling for scheming RT based novel devices.

6.2 Sample characterization techniques used

6.2.1 Structural characterization

The structural phase purity of the prepared sample has been confirmed by performing the synchrotron x-ray diffraction (SXRD) facility at Indus-2 Indian synchrotron radiation source at beamline (BL-12) using Huber 5020 diffractometer. The beam energy used for the measurements was 15keV. A resistive heater was used for heating the sample. Measurements were performed in θ - 2θ mode. The x-ray wavelength used in the present study is 0.756 Å and was accurately calibrated by measuring the XRD pattern of NIST LaB_6 standard sample. The SXRD data has been refined by considering the space group $Pnma$ [223,229]. The one to one fit of experimental data with the fitted data clearly suggests the prepared sample is in single phase.

6.2.2 P-E experiments

The TD polarization vs electric field measurements have been carried out using the ferroelectric loop tracer system of Radiant Technologies (Precision multiferroic test system). In order to perform the dielectric measurements, the obtained powdered samples were pelletized to circular pellets at high pressure of ~20 ton. These pellets were sintered in air at 1200 °C for 24 hours and then coated with silver paint on both sides to make a parallel plate capacitor.

6.2.3 Magnetic Measurements

To understand the magnetic ordering temperature and spin reorientation temperature in $\text{PrFe}_{0.5}\text{Cr}_{0.5}\text{O}_3$, temperature-dependent dc magnetization measurements have been performed using a magnetic property measurement system (MPMS, Quantum Design, U.S.A.) in 500 Oe magnetic field and temperature ranging from 5 K to 310 K[230].

6.2.4 Temperature-dependent Dielectric measurement

The temperature-dependent (TD) dielectric experiment has been performed by using precision impedance analyzer (Wynne Kerr 65120B) with oscillator voltage of ± 1 volt[21].

6.2.5 Temperature and magnetic field dependent Raman experiments

The temperature and magnetic field dependent vibrational properties of prepared samples have been studied by using LABRAM HR dispersive spectrometer equipped with 633 nm excitation laser source[66,212,229,231–233]. The TD Raman measurements have been carried out using THMS600 stage from Linkam having accuracy of the order of 0.1 K[229].

6.2.6 Inelastic and deep inelastic (Compton) neutron scattering experiments

Neutron Compton scattering (NCS) and inelastic neutron scattering experiments were performed at VESUVIO[234–237] and

TOSCA[238–243] inverted geometry spectrometers, both located at the ISIS neutron and muon spallation source at the STFC Rutherford Appleton Laboratory in Harwell, Oxfordshire, UK. The VESUVIO measurements of PrCrO_3 and $\text{PrFe}_{0.5}\text{Cr}_{0.5}\text{O}_3$ samples were carried out at $T=300\text{K}$ and at $T=10\text{K}$, whereas the TOSCA measurements at $T=10\text{K}$. The powder samples were placed into flat aluminum cells. The cells were assembled out of two flat (one front and one backside) walls, each of cross-section of 64 square centimeters, fully exposed to the incident VESUVIO neutron beam when placed perpendicular to its direction. The general setup of VESUVIO was described elsewhere [234–237]. The raw NCS data were corrected for multiple scattering effects in a self-consistent manner according to the established and widely used protocol[237]. During all subsequent steps of the NCS data correction protocol the technique of ‘stoichiometric fixing’ was applied, whereby the ratios of the integral scattering intensities of peaks present in the NCS spectra recorded in the TOF domain were constrained to be equal to the ratios of the products of the total bound scattering cross sections and the number of moles of the respective nuclei per formula unit of the compound under consideration[237].

6.3 Results and discussion

6.3.1 Temperature dependent PE measurements

An important goal of the present study is to understand the origin of natural and magnetic field-induced polar order in $\text{PrFe}_{0.5}\text{Cr}_{0.5}\text{O}_3$. To explore this in detail, temperature-dependent PE measurements were carried out and the representative PE plots at different temperatures are displayed in figure-6.1. A discernible hysteresis loop has been observed below 280 K in $\text{PrFe}_{0.5}\text{Cr}_{0.5}\text{O}_3$, which might be due to the presence of net dipole moment in the sample. The observed values of polarization are very small but exactly similar loop for these samples have been reported to be due to ferroelectricity in literature[10,11,27,38]. It is important here to note that the observed natural PE may have extrinsic origin but keeping in view the various reports published [9,10,11,27,38], we

presumed that the observed hysteresis is attributed to the intrinsic ferroelectricity. Naveen *et al.*[244] explained the observed polar order in terms of distortion of R^{3+} ion due to R-Cr exchange field. Bhadram *et al.*[27] reported that the presence of spin-lattice coupling plays a critical role in persuading the ferro-electric polarization. Hence, probing of the local structure of these compounds would be very important to understand the observed new class of ferroelectricity in these materials. The SXRD experiments (see figure-6.3) carried out on the prepared samples is best fitted by centro-symmetric $Pnma$ space group, which is not compatible with the emergence of natural ferroelectricity in this sample and the observed polar order cannot be explained in terms of displacement of Fe/Cr ions or non-centrosymmetric structure as in the case of classical ferroelectric materials[9]. It is reported in the literature that this observed polar may have a magnetic origin[38,40]. Therefore, to get more insight into this phenomenon, TD magnetization measurements have been performed and will be elaborated in detail in the next sections.

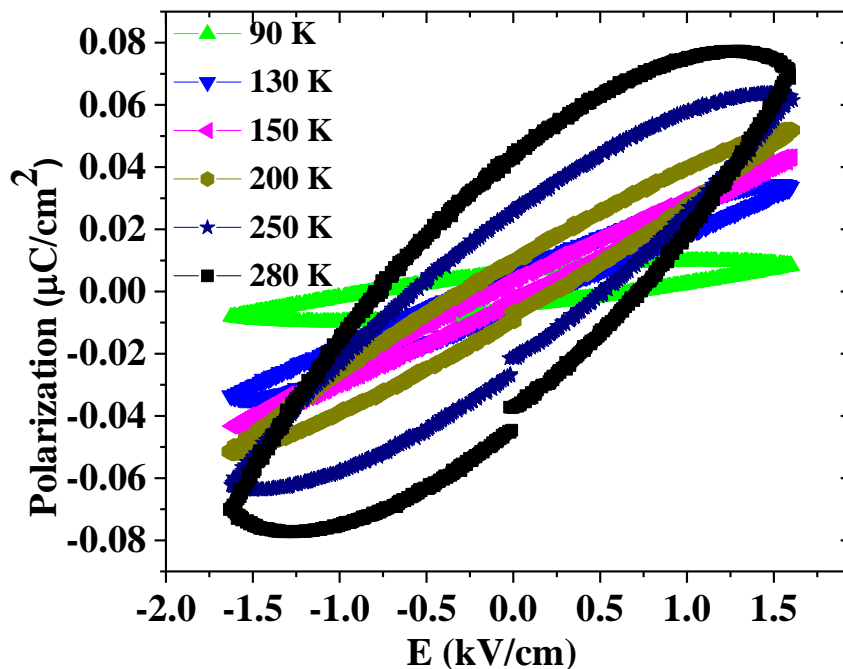


Figure-6.1: The variation of the remnant hysteresis loops at 280 K (a) and 100 K (b). The ferroelectric loop was absent at 300 K and emergence of loop around 280 K may have a magnetic origin.

6.3.2 Temperature dependent Magnetization measurements

Figure-6.2 represents the TD magnetization under the FC (field cooled) and ZFC (zero-field cooling) mode with $H = 500$ Oe. It can be seen from the figure that $\text{PrFe}_{0.5}\text{Cr}_{0.5}\text{O}_3$ exhibits three obvious magnetic transitions at temperatures; $T_{N1}=280$ K, $T_{N2}=140$ K, $T_{N3}=10$ K. The possible origin of these magnetic transitions may arise due to the presence of several magnetic interactions like Pr-O-(Fe/Cr), Pr-O-Pr, Fe-O-Cr, Cr-O-Cr, Fe-O-Fe. It should be noted here that in PrCrO_3 , Pr-O-Pr and Cr-O-Cr interactions take place at <10 K and 140 K respectively, whereas in PrFeO_3 , Fe-O-Fe and Pr-O-Pr interactions take place at 700 K and <10 K respectively[115]. Here in this section, the possible reasons for the increase in the magnetization values at 280 K followed by spin reorientation (160 K) will be discussed in detail.

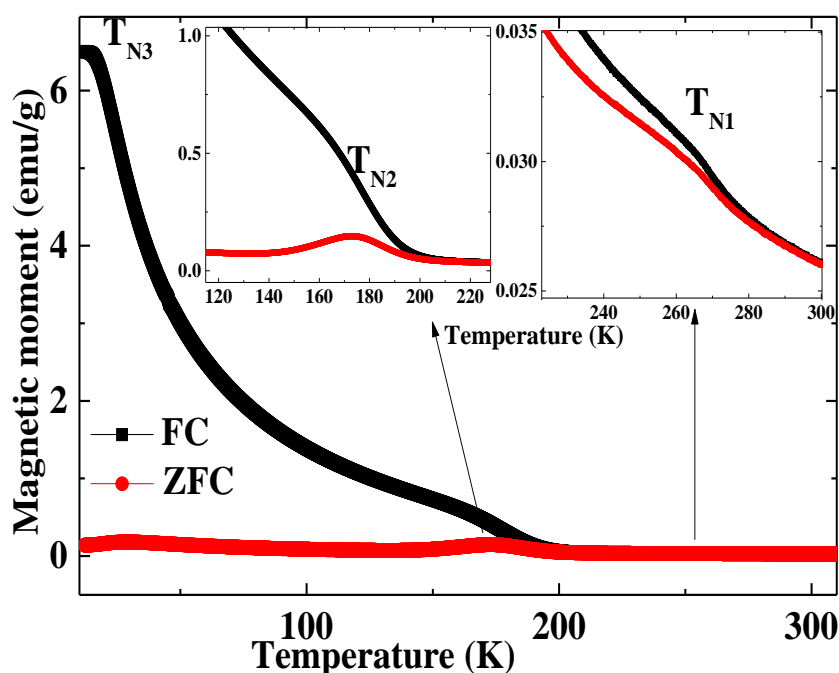


Figure-6.2: Temperature dependence of the dc magnetization variation for polycrystalline $\text{PrFe}_{0.5}\text{Cr}_{0.5}\text{O}_3$. Inset corresponding to T_{N1} and T_{N2} represents the magnetic transition and spin reorientation temperature. At low temperature ascribed as T_{N3} is attributed to the ordering of Pr^{3+} ions.

The two possible reasons for the alteration in the values of T_{N1} are (i) structural distortion induced by the inclusion of Cr doping (ii) dilution of the Fe/Cr-O-Fe/Cr antiferromagnetic exchange interactions. The structural distortion arises due to the difference in ionic radii of Fe^{3+} (0.645 Å) and Cr^{3+} (0.615 Å), which may affect the super-exchange interactions and results in systematic altering in the values of T_{N1} . Apart from this, the weakening of Fe/Cr-O-Fe/Cr super-exchange interactions with the inclusion of Cr^{3+} ions could be better described by Good - Kanamori (GK) rule[245] in the terms of interactions between two adjacent transition metal ions with virtual charge transfer.

According to GK rule, the Fe^{3+} -O- Fe^{3+} interactions are antiferromagnetic due to the reason that π -bonding formed by the three half-filled t_{2g} electrons and σ -bonding formed by two half-filled e_g electrons interacts through the super-exchange interactions, which follows the Hund's rule and are antiferromagnetic in nature[113,115]. However, the incorporation of Cr at Fe site would result in a ferromagnetic component apart from the antiferromagnetic interactions in filled t_{2g} orbitals. The interplay between the ferromagnetic and antiferromagnetic interactions in $PrFe_{0.5}Cr_{0.5}O_3$ may result to altering in the values of T_{N1} . In addition to this, the observed variation in T_{N1} is consistent with the molecular field theory. According to this theory, the correlation between T_N and J is defined as[246]:

$$\frac{J}{k} = \frac{3T_N}{2zS(S+1)} \quad (6.1)$$

where, k is Boltzmann's constant, z is the nearest neighbor's number *i.e.* = 6 for $RFeO_3$, J is the strength of super-exchange interaction between nearest-neighbor ions, $S=5/2$ and $3/2$ for Fe^{3+} and Cr^{3+} ions respectively. The calculated values of J for $PrFeO_3$ (18.42 K) is greater than $PrCrO_3$ (9.43 K), which indicates the dilution of strength of super-exchange interaction with the inclusions of Cr doping and results in the decrement of the values of T_{N1} . It can be mentioned here that the antiferromagnetic ordering temperature for $PrFeO_3$ is around 700 K[115] and with the incorporation of 50% Cr doping, T_{N1} reaches to near room

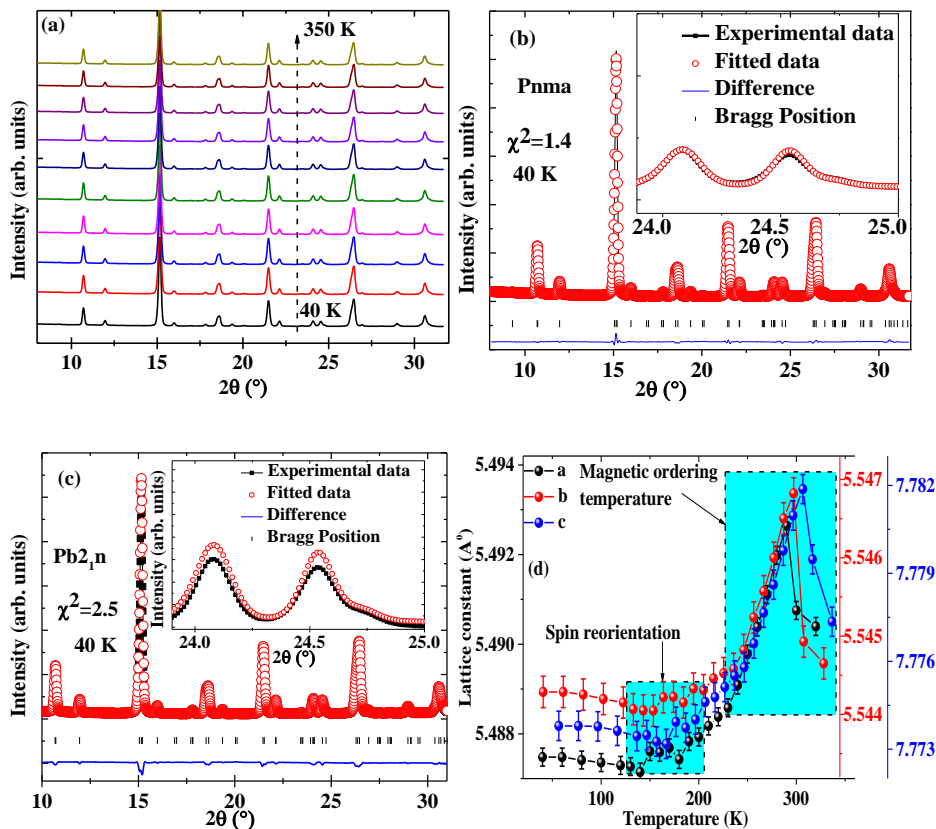
temperature (RT). Hence, Cr^{3+} could be the best choice to replace Fe^{3+} in order to achieve superior magnetic properties. The advantage of Cr^{3+} substitution at Fe^{3+} site is that the T_{N1} can be achieved near RT, which scales the possibility of magneto-electric coupling and developing RT based novel magneto-dielectric devices[113,115].

Apart from T_{N1} , there is a peak in M-T data assigned as T_{N2} , which corresponds to the spin reorientation (SR) transition. Such transitions in $\text{RFe}_{1-x}\text{Cr}_x\text{O}_3$ (R= rare-earth atom) system arises due to complex exchange interactions between R^{3+} and $\text{Fe}^{3+}/\text{Cr}^{3+}$ ions[115]. It is worth noting here that the T_{N2} for parent RFeO_3 is of the order of 50 K, however with the inclusion of Cr-doping[115], it systematically scales up to 150 K. The SR transition observed in these samples is attributed to transformation of high-temperature T_4 ($\text{G}_x\text{A}_y\text{F}_z$) phase to T_2 ($\text{F}_x\text{C}_y\text{G}_z$) phase observed at low temperatures[40]. The spin reorientation transition in PrFeO_3 takes place due to the domination of Pr^{3+} - Fe^{3+} interactions over the antiferromagnetic Fe^{3+} - Fe^{3+} interactions. The inclusion of Cr^{3+} ions at Fe^{3+} site dilutes the Fe^{3+} - Fe^{3+} interactions and Pr^{3+} - $\text{Fe}^{3+}/\text{Cr}^{3+}$ interaction enhances, which may result to increase in T_{N2} for Cr substituted samples [40]. The transition T_{N3} is basically attributed to the magnetic ordering of rare-earth atoms. It is well accepted that around the magnetic transitions region, the alignment of spins produces strain in the material by means of magneto-striction, which causes a distortion in the lattice and thus magnetic ordering couples to phonon modes[113,115]. In order to confirm the same, TD Raman scattering experiments were carried out and will be elaborated on in detail in the following sections.

6.3.3 Temperature dependent x-ray diffraction measurements

The Synchrotron x-ray diffraction data (SXRD) is depicted in figure-6.3 followed by Rietveld refinements. The coexistence of PE hysteresis and spin-lattice coupling (SPC) around 280 K strongly reveals that SPC could be a crucial factor, which may have a connection with the observed polar order as discussed in the earlier sections. To further

confirm the centrosymmetric/non-centrosymmetric structure, temperature-dependent x-ray diffraction experiments were carried out for the $\text{PrFe}_{0.5}\text{Cr}_{0.5}\text{O}_3$ sample in the temperature window of 40–350 K followed by the Rietveld refinement. The x-ray diffraction data is best fitted by centrosymmetric $Pnma$ space group (see figure-6.3(b.)) in the given temperature range, which strongly reveals that the observed ferroelectricity is not attributed to the displacement of Fe/Cr ions as in the case of well-known classical ferroelectric BaTiO_3 . Hence, it seems impossible to probe the non-centrosymmetry experimentally might be due to a small deviation from the centrosymmetric structure. Further, from the refinements, the lattice parameters and average Fe-O bond lengths have been estimated as shown in figure-6.3(c) &(d) respectively. The lattice parameters and average Fe-O bond lengths systematically scales with the temperature, which is related to the inherent anharmonicity of the bonds. Also, an unusual cusp-type anomaly in the lattice constant and Fe–O bond lengths around the spin reorientation (150 K) and magnetic transition temperature (280 K) have been observed which, could be attributed to the presence of strong SPC.



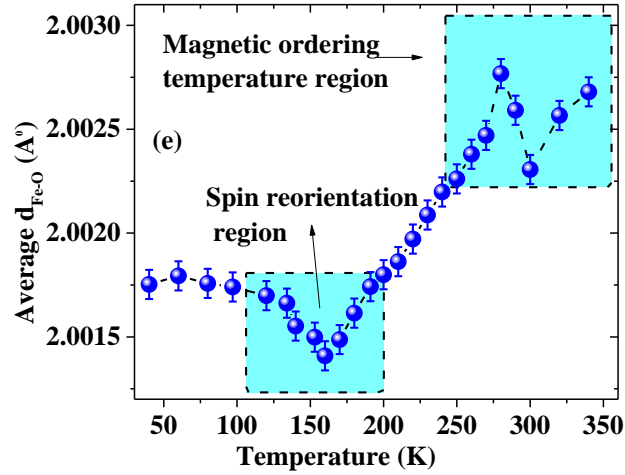


Figure-6.3: The temperature dependence of x-ray diffraction for $\text{PrFe}_{0.5}\text{Cr}_{0.5}\text{O}_3$ (a), Figure-(b) and (c) represents the representative Rietveld refined x-ray diffraction data by considering the $Pnma$ and $Pb2_1n$ space group at 40 K respectively. Inset in the figure represents the quality of fitting. Figure-(d) shows the variation of lattice constants as a function of temperature. The anomalies corresponding to spin-reorientation and magnetic ordering temperature region suggest the presence of strong spin-lattice coupling. Figure-(e) represents the variation of average Fe-O bond lengths as a function of temperature.

6.3.4 Temperature dependent Raman measurements

It is well established that Raman spectroscopy (RS) can be employed as a microscopic tool to examine the changes in the structure, EPC, spin-phonon coupling, presence of defects, orbital mediated charge transfer. *etc.*[17, 24–26]. The group theory analysis for the $Pnma$ space group suggests the 24 Raman active modes with four formula unit per unit cell ascribed as:

$$7A_g + 5B_{1g} + 7B_{2g} + 5B_{3g}$$

The Raman spectrum pertinent to $\text{PrFe}_{0.5}\text{Cr}_{0.5}\text{O}_3$ as a function of temperature is depicted in figure-6.4.

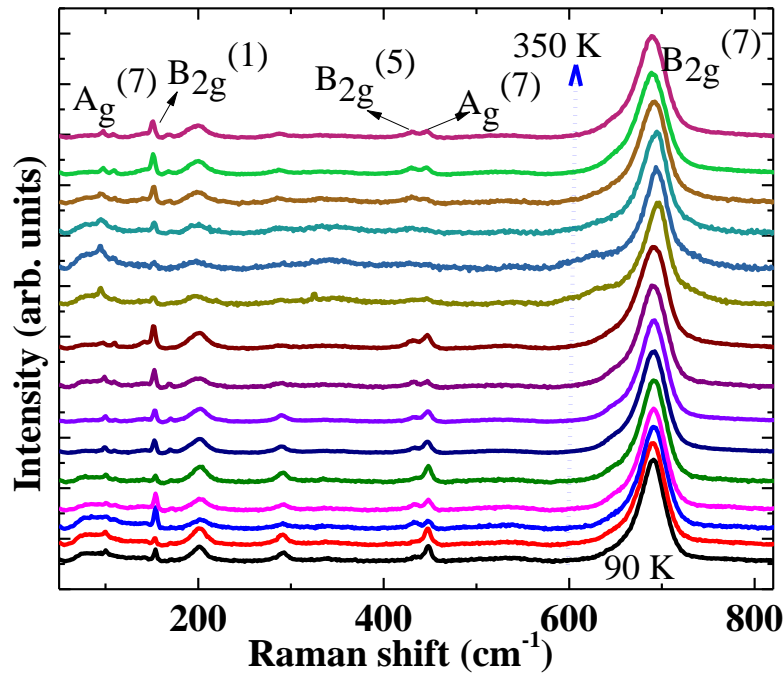


Figure-6.4: The temperature dependent Raman spectrum for $PrFe_{0.5}Cr_{0.5}O_3$ sample.

The detailed analysis of the Raman modes has been done in earlier chapters and is not discussed here. It is now well accepted that RS has a potential to investigate the structural changes and magnetic ordering with temperature[12,138]. The non-appearance/disappearance of any Raman mode in TD Raman spectra indicates the absence of any structural symmetry in the temperature range 90-300 K. Further, to get more insight about the effect of magnetic ordering temperature and spin-reorientation temperature on the phonon modes, Raman shift and full width at half maxima (F.W.H.M.) have been plotted and is depicted in figure-6.5(a&b). The anomalous behavior in Raman mode position and F.W.H.M. around the T_{N1} and T_{N2} have been observed, which could be attributed to the presence of very high SPC across these temperatures.

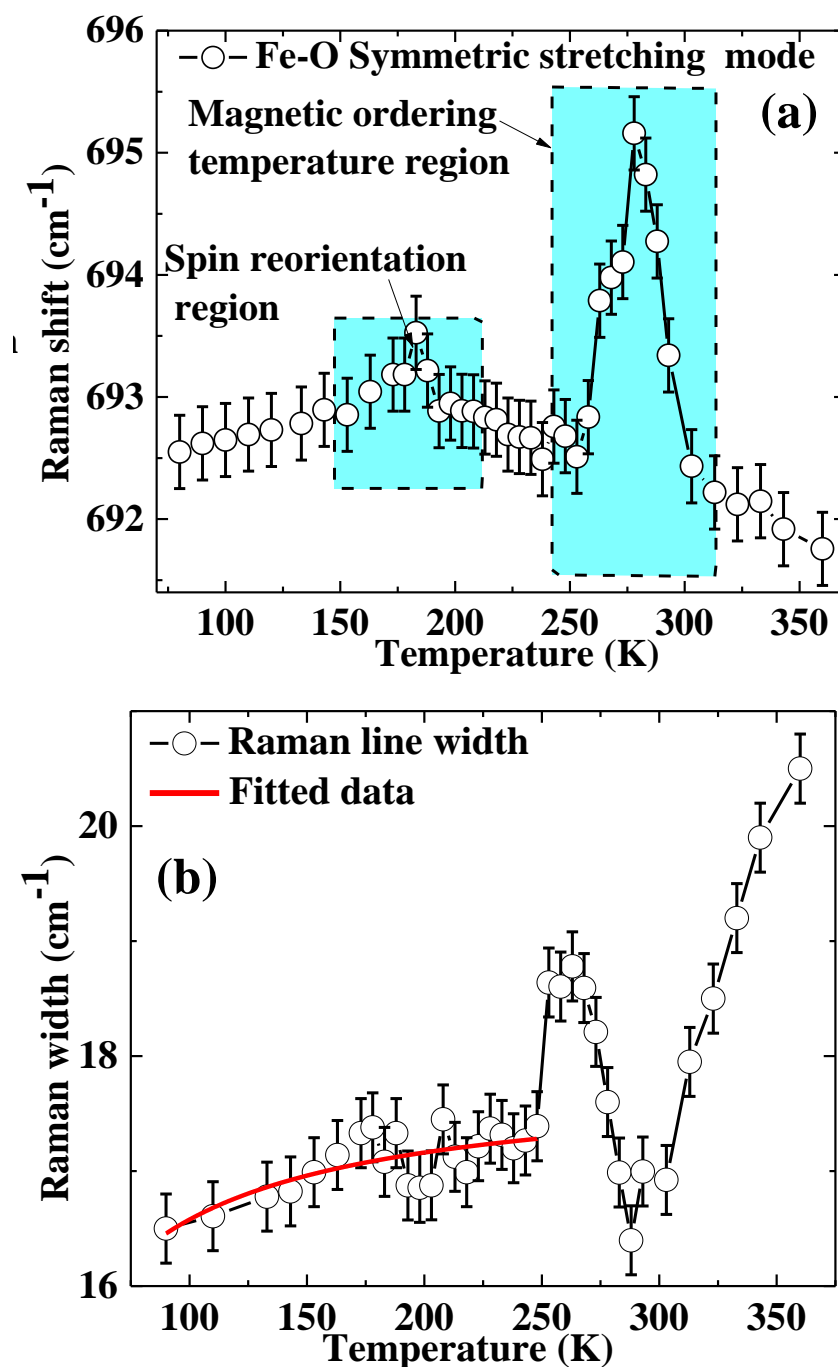


Figure-6.5 (a): The Raman shift for the B_{2g} (7) mode and Fe-O symmetric stretching Raman mode as a function of temperature. Figure-(b) represent the variation of Raman line width for B_{2g} (1) mode fitted by Balkanski model.

Kumar et al.[138] discussed the variation of Raman shift with temperature and the aforementioned shift is attributed to these factors ascribed below:

$$w(T) - w(0) = \Delta w_{lattice} + \Delta w_{sp-ph} + \Delta w_{anharmonic}$$

where $w(0)$ corresponds to the Raman shift at 0° K, $\Delta w_{lattice}$ gives the involvement of lattice volume contribution, Δw_{sp-ph} is the SPC contribution and $\Delta w_{anharmonic}$ represents the anharmonic terms contribution respectively. The term $\Delta w_{lattice}$ represents the volume contribution and can be considered as negligible[138]. Therefore, the observed changes in Raman modes with temperature may arise due to a combination of anharmonic terms and SPC contribution.

Further, the anharmonic term contribution has been estimated by Balkanski model expressed as[138,229]:

$$T(T) = T(0) + A \left[1 + \Sigma \frac{1}{\exp\left(\frac{h\omega_i}{2\pi kT}\right) - 1} \right] \quad (6.2)$$

Where, $T(0)$ is the Raman F.W.H.M. at 0° K, A (anharmonic coefficient) represents the contribution due to higher-order terms for three phonon processes. The dependence of Raman line width with temperature has been fitted by using the Balkanski model and from the estimated values of A (6 cm^{-1}) below 280 K, it can be concluded that the anharmonic terms contribution is negligible, which is consistent with the earlier reported literature[138,229]. The deviation of Raman F.W.H.M. of B_{2g} (1) with temperature can be seen from figure-6.5 (b), which suggests the presence of strong SPC around the magnetic transition temperature regions. Apart from this, the deviation of experimental data by fitted Balkanski model[247] data below T_{N1} indicates the presence of another dominating factor than anharmonicity. Hence, it seems that the main contributing factor for the anomalies observed in TD Raman shift and F.W.H.M. is due to the presence of SPC, which may have direct correlation with the observed magneto-dielectric coupling near room temperature and will be elaborated in detail in the following sections.

6.3.5 Effect of Magnetic field on Raman line shapes at 290 K

To understand the intrinsic origin of magneto-dielectric coupling, magnetic field dependent Raman measurements has been carried out at 290 K. The detailed analysis of phonon modes for orthorhombic structure with space group $Pnma$ was presented in our recent publications[12,127]. It is now well accepted that the samples which experience tensile strain undergo a red shift of Raman modes, which, in the case of the system under investigation, is further attributed to the increase in the Fe/Cr-O bond length. The Raman mode arising around 690 cm^{-1} is related to symmetric stretching of the Fe/Cr-O bonds, whereas the soft A_g modes at lower wavenumber have a direct connection with the octahedral tilting. Figure-6.6 (a) represents the magnetic field dependent Raman spectra. It can be clearly seen that Raman spectra for $\text{PrFe}_{0.5}\text{Cr}_{0.5}\text{O}_3$ are highly affected by the applied small magnetic field. However, no significant changes have been observed for the parent PrFeO_3 sample (see figure-6.6 (b)), which reveals that SPC plays a crucial role for the observed magneto-dielectric coupling. The Raman mode attributed to symmetric stretching vibrations of FeO_6 octahedra (690 cm^{-1} mode) shows the softening behavior or magneto-expansion with field, which reveals that Fe/Cr-O bond length is strongly affected by the magnetic field. The soft A_g modes at lower wavenumber also show a similar behavior, which could be attributed to the variation in the octahedral tilts with magnetic field as suggested by Kumar *et al.*[12]. In addition to this, the enhancement in intensity of symmetric stretching vibrational mode (690 cm^{-1} mode) can be seen from the figure-6.6 (a), which could be explained in terms of enhancement in the super-exchange magnetic interactions by charge transfer from Cr^{3+} (d^3) to Fe^{3+} (d^5) ions[12]. It is reported in literature that the contribution of SPC in polarization (P) can be given as, $P = \Delta Z * M(T) / \omega(T)^2$, where ω is the frequency of the phonon mode, M is the magnetization and ΔZ is the effective charge[33]. This term arises due to the significant contribution of SPC effect to the polarization.

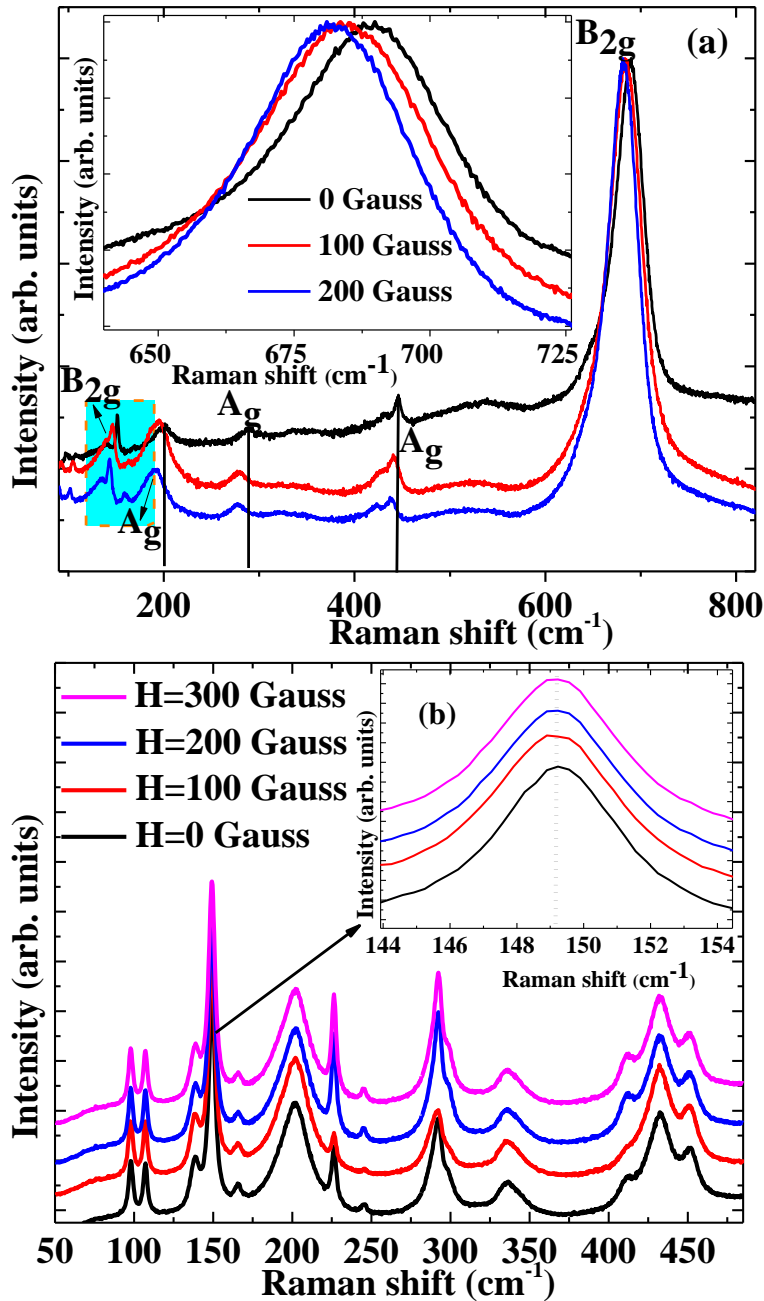


Figure-6.6 (a): The variation of Raman spectra as a function of applied magnetic field in $\text{PrFe}_{0.5}\text{Cr}_{0.5}\text{O}_3$. Inset of the figure represents the spin-phonon coupling induced magneto-expansion effect with the application of magnetic field. **Figure-6.6 (b)** represents the variation of Raman spectra as a function of applied magnetic field in PrFeO_3 .

Therefore, the variation in Raman shift with applied magnetic field could have a direct connection with the induced polarization. Apart from this, the B_{2g} (1) Raman mode arising around 160 cm^{-1} is related to the displacement of Pr^{3+} ions [113]. It is clear from the figure-6.6 (a) that a Raman spectrum for $\text{PrFe}_{0.5}\text{Cr}_{0.5}\text{O}_3$ is highly affected by the applied

small magnetic field (100-300 Gauss), which is an indirect signature of magneto-electric coupling even at room temperature. It should be noted here that the signature of magneto-electric coupling is completely missed in PrFeO_3 as depicted in figure-6.6 (b). Hence, it can be concluded that Pr^{3+} ions in PrFeO_3 are highly localized, whereas, with the inclusion of Cr substitution, Pr^{3+} ions get delocalized and would contribute significantly to magneto-electric coupling. The distortion of Pr^{3+} ion due to Pr-Fe/Cr exchange field seems to be responsible for the displacement of Pr^{3+} ion *i.e.* the polyhedron formed around Pr^{3+} ion is no more centrosymmetric and results to produce a local dipole.

6.3.6 Possible origin of Pr atoms delocalization as a function of temperature and its role in natural and field induced polar order

To understand the possible origin of delocalization of Pr atoms and its role in the natural and magnetic field induced polar order, the magnetic field dependent Raman scattering experiments as a function of temperature have been performed by applying a very small magnetic field (30 Gauss). It is worth mentioning here that the applied magnetic field was so small that it does not lead to any change in the Raman spectra at RT. The corresponding Raman spectrum at 90 K with the application of magnetic field is depicted in figure-6.7 (a&b). It can be seen from the figure that the visible Raman shift of the order of 2 cm^{-1} in the low wavenumber Raman mode (160 cm^{-1}) has been observed at 90 K, whereas no significant changes in all other Raman modes corresponding to Fe ($>400 \text{ cm}^{-1}$) vibrations have been observed as clear from the figure-6.7 (b). It is important to note here that the Raman modes below 400 cm^{-1} are attributed to the heavier Pr atom vibrations and the deviation of only these modes with applied magnetic field reveals that the large values of $\Delta\epsilon$ (a detailed discussion is given in section 3.9) at low temperatures have a direct relationship with the displacement of Pr atoms. Importantly in this context, the polarization (P) is proportional to the displacement of soft $B_{2g}(1)$ mode[51] (*i.e.* $P = T w_{160}$, T is a constant of proportionality and w_{160} is the Raman shift of the particular mode). This qualitative relation would lead to the

following simplified expression for the magnetic field induced polarization variation:

$$\frac{P(H)-P(0)}{P(0)} \propto \frac{W(H)-W(0)}{W(0)} \quad (6.3)$$

To get more insight into this, TD Raman shift for the ($B_{2g}(1)$) (the Raman mode attributed to displacements of Pr sublattices) and $A_g(7)$ Raman mode by applying magnetic field was plotted in figure-6.7 (c&d) respectively. It can be seen from figure-(c) that Δw (the difference between Raman shifts with and without magnetic field) decreases systematically with temperature and at RT it almost vanishes, suggesting a strong magneto-dielectric coupling at low temperatures. Also, no significant changes have been observed in the Raman shift corresponding to Fe vibrations ($A_g(7)$) with the application of magnetic field, which suggests that the Fe atoms do not contribute significantly to the field-induced polar order even at low temperatures. Thus, the softening of the low wavenumber Raman modes with magnetic-field in the $\text{PrFe}_{0.5}\text{Cr}_{0.5}\text{O}_3$ demonstrates the magnetic-field-induced electric polarization by stress-mediated magneto-dielectric coupling[55], which is consistent with the variation of Δw and $\Delta \epsilon$ (estimated from TD dielectric measurements) as shown in figure-6.7 (e). These results are excellent agreement with the results published by Rajeswaran *et al.* [19], where polarization is changing systematically with the strength of the applied magnetic field. Hence, it can be concluded that at low temperatures, the Pr atomic delocalization has a significant contribution to the observed polar order, whereas at RT, SPC as well as Pr atoms delocalization seems to be responsible for the natural and field-induced polar orders.

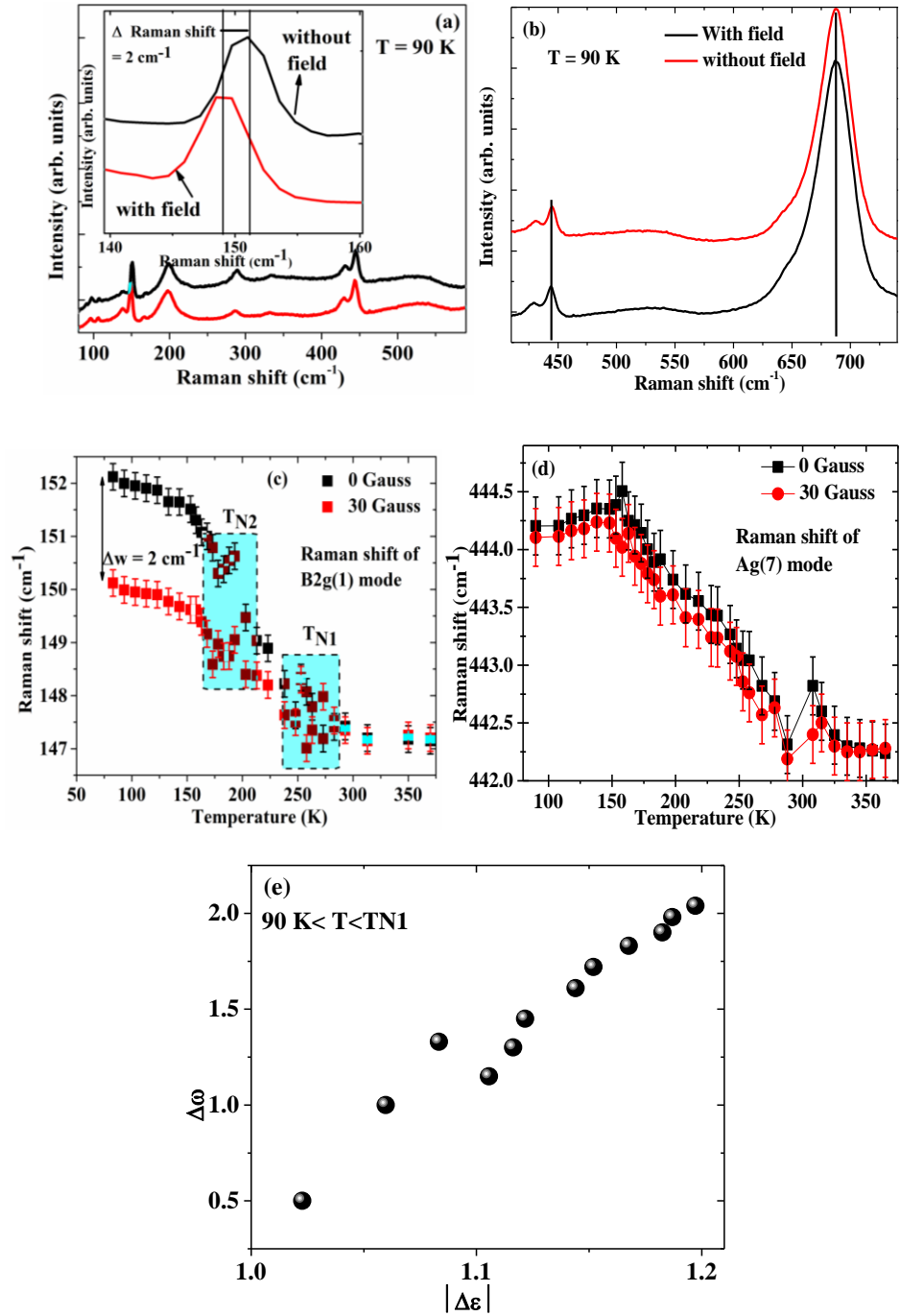
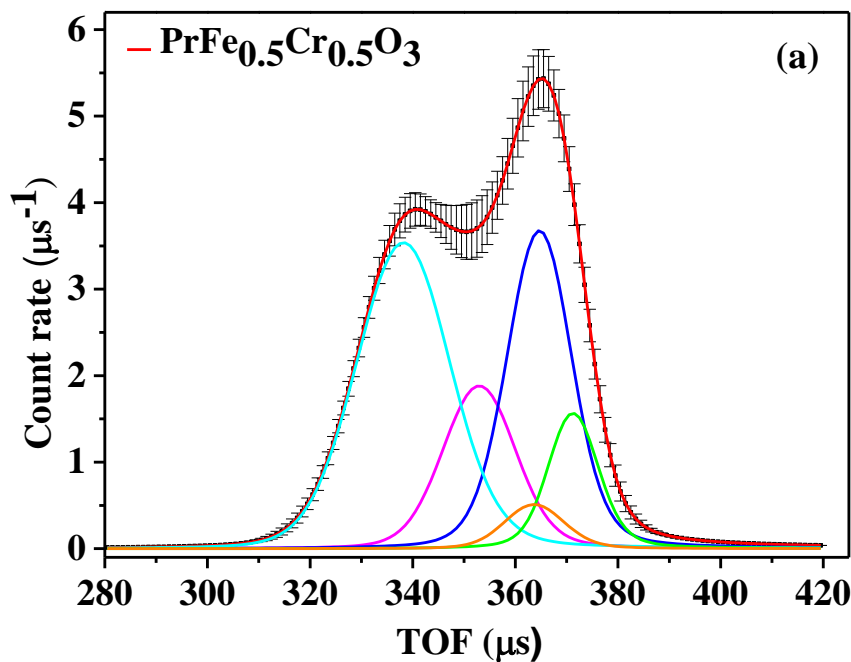


Figure-6.7: The low temperature Raman spectra (90 K) related to Pr atomic vibrations (a) and Fe atomic vibrations (b) By applying very small magnetic field (30 Gauss). Figure-(c&d): The variation of Raman shift as a function of temperature for B2g (1) and Ag (7) modes respectively with the application of magnetic field for $PrFe_{0.5}Cr_{0.5}O_3$. Figure-(e): The variation of Δw (variation in Raman shift with the application of magnetic field) vs $\Delta \epsilon$ (variation in dielectric constant due to the presence of hyperfine interactions).

6.3.7 Inelastic and deep inelastic (Compton) neutron scattering experiments

To shed more light on the delocalization of the Pr^{3+} ions, isotopic mass-resolved neutron Compton scattering as well as inelastic neutron scattering experiments were performed on $\text{PrFe}_{0.5}\text{Cr}_{0.5}\text{O}_3$ and PrFeO_3 sample. An example of a mass-resolved NCS spectrum recorded in the TOF domain for $\text{PrFe}_{0.5}\text{Cr}_{0.5}\text{O}_3$ and PrFeO_3 at $T=10\text{K}$ is shown in Figure 6.8 (a&b), respectively. As routinely applied for the analysis of the NCS spectra of samples composed off heavyweight nuclei[237], the total neutronic responses of both samples were fitted with underlying Gaussian nuclear momentum distributions convolved with the isotopic mass-dependent resolution functions. As mentioned in Section 2.2. (f), the technique of ‘stoichiometric fixing’ [43] was applied in fitting NCS spectra, which allowed for reliable fitting of the widths of the recoil peaks despite their partial overlapping in the signals recorded in the TOF domain (see Figure 6.8 (a&b)). Following the rule of thumb on the inverted-geometry NCS spectrometers, the recoil peaks appear centered at increasing values of the time of flight for the increasing masses of individual nuclear species.



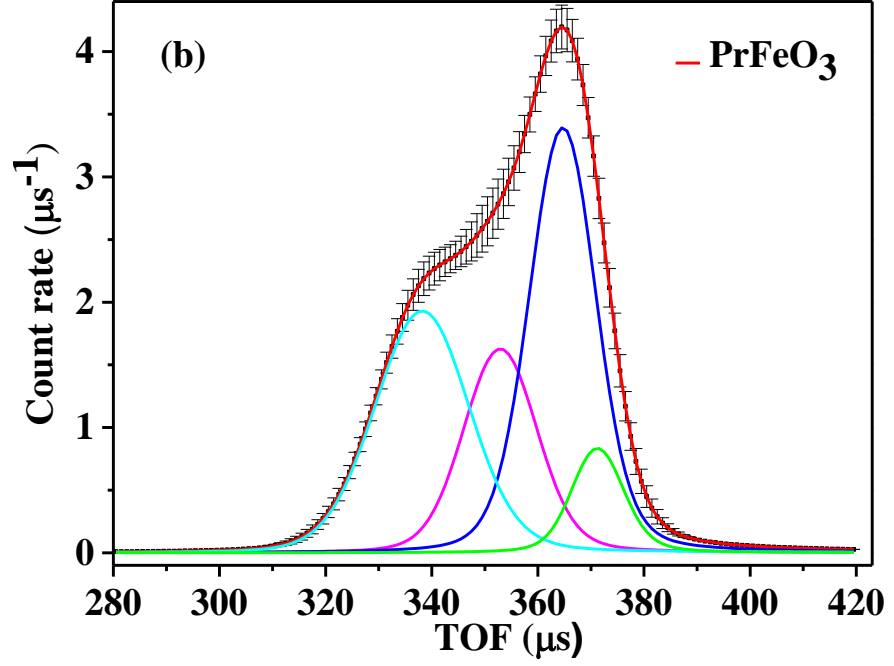


Figure 6.8: Neutron Compton scattering spectrum for Cr- substituted PrFeO_3 (a) and PrFeO_3 (b), both recorded at 10K. Black points show the sum (over all backward scattering detectors) of the recorded data. Solid red curve indicated the sum (over all backward scattering detectors) of the fits of the recorded data. The sum of the fits is dissected into sums (over all backward detectors) of fits to individual recoil lines of Pr (solid green line), Fe (solid navy blue line), Cr (solid orange line), aluminum sample container (magenta), and O (solid blue line).

In Figure 6.8 (a), these are the recoil peak of the oxygen, aluminum sample container, chromium (absent for PrFeO_3 – see Figure 6.8 (b)) iron and praseodymium, all Doppler-broadened by their respective nuclear momentum distributions. The widths (standard deviations), σ , of the Gaussian nuclear momentum distributions underlying the Doppler-broadened recoil peaks of individual nuclear species present in $\text{PrFe}_{0.5}\text{Cr}_{0.5}\text{O}_3$ and PrFeO_3 are listed in Table 6.1.

Sample	σ (Pr) [\AA^{-1}]	σ (Fe) [\AA^{-1}]	σ (Cr) [\AA^{-1}]	σ (O) [\AA^{-1}]
$\text{PrFe}_{0.5}\text{Cr}_{0.5}\text{O}_3$	8.8 ± 1.3	15.4 ± 1.7	11.1 ± 1.7	9.2 ± 0.5
T=10K				

PrFe _{0.5} Cr _{0.5} O ₃	32.5 ± 1.4	21.2 ± 1.5	21.2 ± 1.1	11.0±0.6
T=300K				
PrFeO ₃	8.1 ± 1.1	15.5 ± 1.3		8.9 ± 0.9
T=10K				
PrFeO ₃	32.8 ± 0.8	21.7 ± 1.3		10.8 ± 0.6
T=300K				

Table 6.1. *The widths (standard deviations), σ , of the Gaussian nuclear momentum distributions underlying the Doppler-broadened recoil peaks of individual nuclear species present in PrFe_{0.5}Cr_{0.5}O₃ and PrFeO₃ (see text for details).*

As can be clearly seen in Table 6.1, the widths of momentum distributions of Pr, Fe, and O in PrFe_{0.5}Cr_{0.5}O₃ and PrFeO₃ are equal within the single-standard deviation error level. Let us start with the remark that, by virtue of the uncertainty principle, the narrower the momentum distribution the wider the position distribution, and thus the more a given species is delocalized in space[234–237]. Thus, at first glance the praseodymium ion does not seem to get more delocalized in space due to the presence of Cr, both at 10K and 300K. However, a more careful inspection reveals quite marked and important differences between the two compounds. Firstly, as a rule of thumb according to the classical limit of quantum mechanics, the heavier the nuclear species under consideration, the more ‘classical or localized in space’ it should be. Thus, an expected natural progression of the widths of nuclear momentum distributions at any given constant temperature should be such that the heavier the species the wider its momentum distribution gets. Conversely, the widths of nuclear momentum distributions should be approximately equal for two nuclear species of equal masses at the same temperature in the classical limit. As can be seen by inspection of the results listed for T=300K for both compounds, this trend is approximately fulfilled at 300K, where, as expected, the nuclear quantum effects for heavyweight nuclei start to cease and the momentum distributions become more and more similar to Maxwell-Boltzmann

distributions of classical non-interacting particles subject to no confinement of any local Born-Oppenheimer potential[234–237]. However, at T=10K, a completely different picture emerges. The Pr nuclei, whose mass is approximately three times higher than the mass of the Fe and Cr nuclei, have momentum distribution width that is roughly fifty per cent narrower and equal to the width of the momentum distribution of the approximately ten times lighter oxygen nucleus. In order to provide a degree of quantitation to these trends, a new observable, referred to as the quantum excess of the nuclear kinetic energy (QE) [234–237] has been introduced. The QE measures the ‘quantumness’ of a given nuclear species of mass M and is defined as $QE = \frac{E_{quant}}{E_{cl}}$. In this expression, E_{quant} is the nuclear kinetic energy, $E_{quant} = \frac{3\hbar^2 s^2}{2M}$ measured in an NCS experiment for a realistic system where the momentum distribution can be interpreted as a square of the modulus of the nuclear wave function in the momentum space subject to the local confining potential of the mean force[234–237]. Furthermore, E_{cl} is the nuclear kinetic energy of a classical nucleus subject to no confining potential (and thus given by the Maxwell-Boltzmann distribution), $E_{cl} = \frac{3}{2}kT$. The values of the QE calculated based for all nuclear species present in $\text{PrFe}_{0.5}\text{Cr}_{0.5}\text{O}_3$ and PrFeO_3 are listed in Table 6.2.

Sample	QE (Pr)	QE (Fe)	QE (Cr)	QE (O)
$\text{PrFe}_{0.5}\text{Cr}_{0.5}\text{O}_3$ T=10K	2.7 ± 0.06	20.53 ± 0.24	11.39 ± 0.26	25.67 ± 0.08
$\text{PrFe}_{0.5}\text{Cr}_{0.5}\text{O}_3$ T=300K	1.21 ± 0.01	1.34 ± 0.01	1.40 ± 0.01	1.22 ± 0.01
PrFeO_3 T=10K	2.23 ± 0.04	20.79 ± 0.14		24.27 ± 0.25

PrFeO ₃	1.23±	1.37± 0.01	1.17± 0.01
T=300K	0.01		

Table 6.2. The values of the QE variable measuring the ‘quantumness’ of individual nuclear species present in PrFe_{0.5}Cr_{0.5}O₃ and PrFeO₃ (see text for details).

As can be clearly seen from the inspection of the Table 6.2, whereas the value of the QE at T=300K is ca. ten times lower than its counterpart at T=10K for Fe, Cr and O, the value of the QE at T=10K is only ca. two times higher compared to the QE value at T=300K for the praseodymium in both compounds. This result signifies much more ‘classical’ character of the praseodymium in the entire temperature scale, whereby it resembles much more a nucleus which is unconfined/not subject to any local binding potential and thus more delocalised compared to the other heavier nuclei such as Fe and Cr. Moreover, the praseodymium seems to be much more classical in nature in the sense of the QE variable at T=10K than an almost ten times lighter oxygen nucleus.

The picture of the the delocalization of the Pr³⁺ ions in PrFe_{0.5}Cr_{0.5}O₃ and PrFeO₃ emerging from the careful analysis of the NCS data is further corroborated by the INS results on PrFe_{0.5}Cr_{0.5}O₃ and PrFeO₃ obtained at T=10K (see Figure 6.8 (c)). In order to understand this result, it is worth noting that the nuclear kinetic energy can be interpreted as Boltzmann-population factor-weighted partial density of vibrational states[234–237]. For a constant temperature experiment, this interpretation means that the nuclear kinetic energy of a nucleus is roughly given by the value of the center of the gravity of a region of a vibrational spectrum that is dominated by the partial (atom-projected) vibrational densities of states of this nucleus. Concretely, as can be seen in Figure 6.8 (c), the center of gravity of the low (<400 cm⁻¹) vibrational region of the INS spectrum of PrFeO₃, attributed the vibrations of the praseodymium, and thereby the nuclear kinetic energy of the praseodymium, is shifted to the low energy values. Moreover,

upon doping with chromium, the center of gravity of this part of the vibrational spectrum of $\text{PrFe}_{0.5}\text{Cr}_{0.5}\text{O}_3$ seems to shift even further towards lower values of the energy (a marked softening of the bands centered at 210 and 250 cm^{-1} can be seen), thereby signaling even lower value of the nuclear kinetic energy of the praseodymium in $\text{PrFe}_{0.5}\text{Cr}_{0.5}\text{O}_3$ at $T=10\text{K}$. The fact that this effect of increased classical (unbound) character of Pr upon doping of PrFeO_3 with chromium is not apparent from the NCS results may be due to the limited energy resolution of the NCS method for this relatively heavy nuclear species.

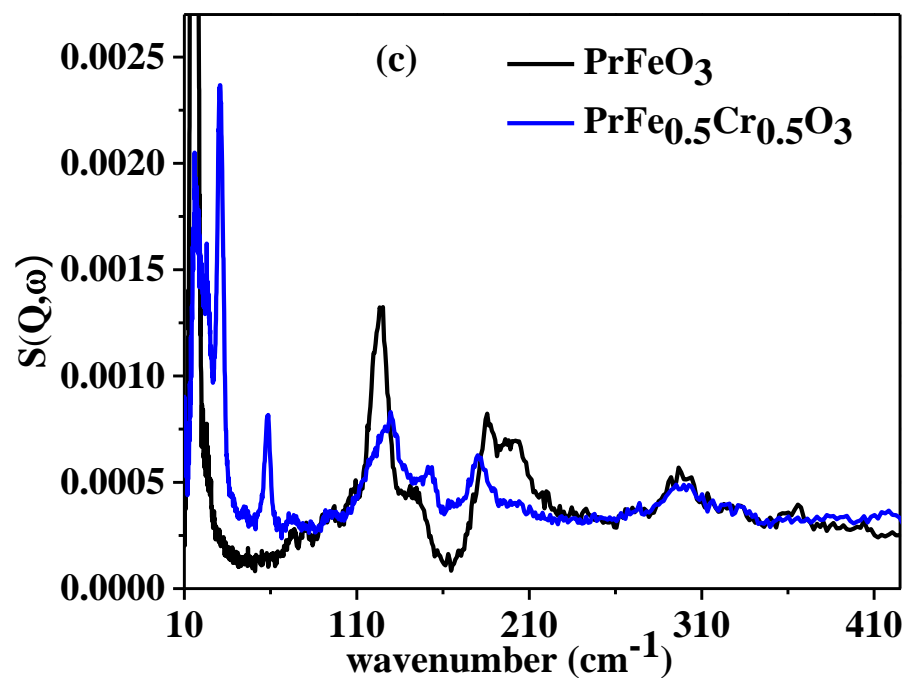


Figure 6.8 (c) Inelastic neutron scattering spectra of Cr-substituted PrFeO_3 (solid blue line) and PrFeO_3 (solid black line). The contribution from the sample aluminum container has been subtracted, and the resultant spectra were normalized/scaled in such a way that the integrated area in between 10 and 4000 cm^{-1} is equal to 1.

6.3.8 Temperature dependent dielectric measurements

The TD dielectric measurements have been performed to understand the presence of magneto-dielectric coupling and the corresponding results are depicted in figure-6.9 (a) at frequency 1MHz. It can be seen from the figure that around the magnetic ordering temperature, a clear anomaly has been observed in the permittivity data. Moreover, the first derivative of the (ϵ) versus T curve (as depicted in the inset of figure-6.9 (a)) confirms that the anomaly taking place at about 280 K. The dielectric anomaly in the form of cusp around the magnetic transition temperature reveals the possibility of observing magneto-dielectric effect very close to RT. The said cusp type characteristics were also observed earlier in GaFeO₃[249] and YMnO₃[250], which have been explained in terms of the presence of magneto-dielectric effect. Hence, the observed behavior is attributed to the antiferromagnetic ordering from the super-exchange interactions between the Fe³⁺/Cr³⁺ ions. It is worth noting here that in the absence of magnetic ordering; the dielectric constant varies similarly as in the high-temperature region (above 280 K). However, because of the presence of internal hyperfine magnetic field interactions below 280 K, the dielectric permittivity below this temperature cannot follow the same trend. Therefore, the variation of low temperature dielectric constant in the absence of zero hyperfine magnetic fields can be obtained by extrapolating the high-temperature window region. The difference $\Delta\epsilon$ between the ϵ_0 (zero field ϵ in low- temperature region) and ϵ (the experimental value of field ϵ in low temperature region) would only be the result of magnetic hyperfine interactions, and could be proportional to the square of magnetization[10] *i.e.* $\Delta\epsilon \sim M^2(T)$.

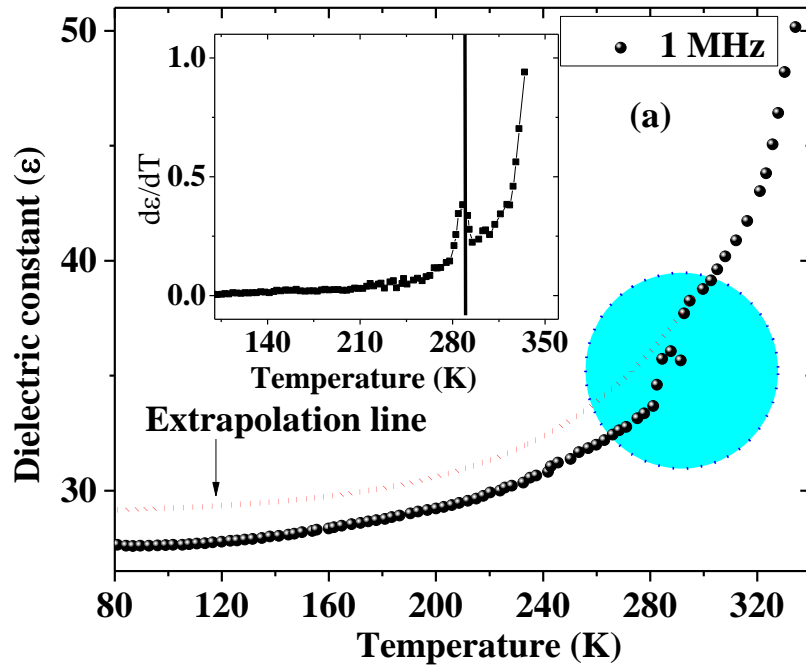


Figure-6.9 (a): The temperature dependence of dielectric constant variation at 1 MHz. Inset of the figure represents the first derivative of dielectric constant with temperature.

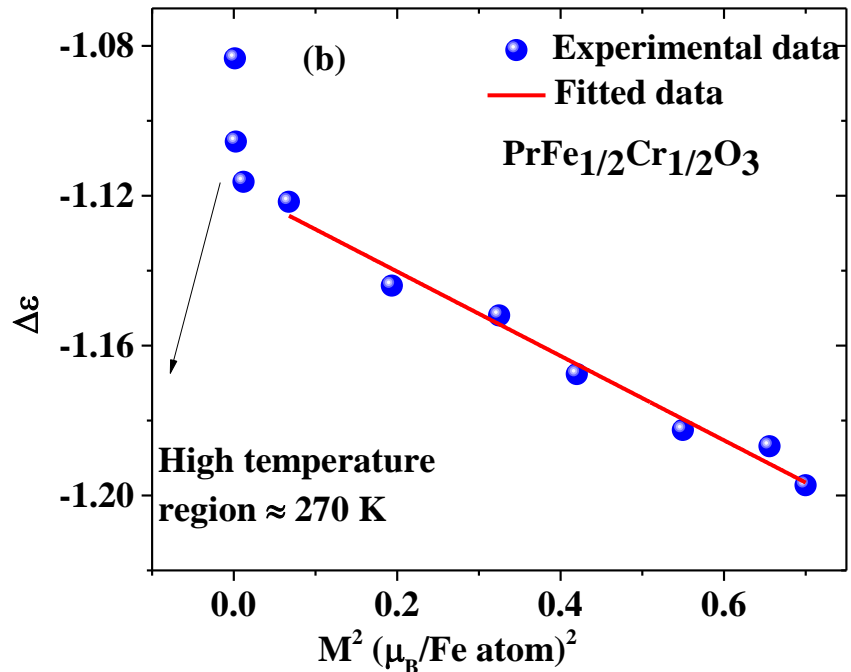


Figure-6.9 (b): The linear variation between the $\Delta\epsilon$ and $M^2(T)$.

Figure-6.9 (a) represents the variation of ϵ_0 estimated from extrapolating the high-temperature permittivity region as a function of temperature, whereas the variation of $\Delta\epsilon$ as a function of M^2 is depicted in figure-6.9 (b). The linear variation of M^2 in the temperature window 150-280 K can be seen from figure-6.9 (b), however this linear

dependence deviates around 280 K as a result of magneto-dielectric coupling. These results show excellent consistency with the magnetic field dependent Raman scattering experiments. Hence, it seems that the present results show a significant contribution in searching for new RT based magneto-dielectric materials.

6.4 Conclusion

In summary, the temperature dependence of dielectric, magnetic and vibration properties for $\text{PrFe}_{0.5}\text{Cr}_{0.5}\text{O}_3$ has been done in detail. The magnetic transition around 280 K has been identified by the magnetic susceptibility measurements, whereas the anomalies in the unit cell parameters, Raman shift and dielectric data confirm the presence of strong magneto-dielectric and spin-lattice coupling. Moreover, the signature of unusual negative thermal expansion has been observed below the spin reorientation temperature region, which could be attributed to the magneto-elastic effect due to repulsion between the magnetic moments of neighbor transition metal ions. The origin of natural and external magnetic field induced polar order seems to have a direct relationship with the displacements of Pr atoms and strong SPC, which is in excellent conformance with the result of neutron Compton scattering experiments. The origin of magneto-dielectric coupling has been explained in terms of rotation of spin coupled Fe-orbitals under the influence of magnetic field as clear from the magnetic field dependent Raman spectral analysis. As a final remark, the present study reveals that the intrinsic magneto-dielectric effect can be realized in strongly correlated compounds that contract/expands in response to an externally applied magnetic field and such materials could have immense potential applications in data storage devices.

Chapter-7

The Magneto-elastic and Optical Properties of Multiferroic GaFeO_{3-δ}

The most common feature observed in transition metal oxides is the charge neutral crystal field d-d transitions, which arises due to transition of an electron from t_{2g} to e_g orbitals. Present chapter deals with the possible origin of d-d transitions in the optical absorption spectra and its correlation with exciton lines shapes. It has been observed that the presence of peak due to d-d transition is associated with the annealing temperatures driven defects present in these samples. Apart from this, the variation of magneto-elastic coupling as a function of oxygen non-stoichiometry has been discussed in detail in this chapter. The results reported in this chapter have been published in literature.*

*Kumar *et al.* J. Magn. Magn. Mater. 514 (2020) 167210.
<https://doi.org/10.1016/j.jmmm.2020.167210>.

*Kumar *et al.* J. Phys. Chem. Solids. 130 (2019) 230-235.
<https://doi.org/10.1016/j.jpcs.2019.03.012>.

*Kumar *et al.* Journal of Physics and Chemistry of Solids. 135 (2019) 109102. <https://doi.org/10.1016/j.jpcs.2019.109102>.

7.1 Introduction

Multiferroic materials (MF) with ferroelectric and ferromagnetic properties offer possible applications for functional devices[24–27]. The prerequisite is a simultaneous presence of ferromagnetic and ferroelectric orders well above room temperature. There are certain number of materials in which ferromagnetism and ferroelectricity coexists, but the coupling between these two properties is not always large enough at room temperature (RT)[2]. For bulk ceramics, combining the different ferroic orders is a tricky problem as such properties are exclusive in most materials. Distinctly, the controlling of

magnetization (electric polarization) through external electric (magnetic) field *i.e.* the coupling between external magnetic (electric) field with electric dipoles (magnetization) is known as magneto-electric (ME) effect. Moreover, the magneto-electric effect is an independent phenomenon though it may coexist along with multi-ferroicity in specific compounds[2]. These materials exhibit coupling between electric and magnetic properties, which are emerging as one of the promising applications in spintronic devices, non-volatile memory devices, sensors, actuators *etc.*[6,25,148,251]. The fundamental challenge is to realize both the magnetic transition temperature (T_C) close to room temperature (RT) with strong magneto-electric coupling between the magnetic and electrical order parameters. So there are increasing activities in search of RT magneto-electric materials. Various approaches have been done earlier to understand the tuning of electrical, optical and magnetic properties in the perovskite oxides around room temperature[252–255]. With controlling the defect density and crystallite size, the tuning of aforementioned properties can be realized in these oxide systems[108,127,137].

GaFeO₃ (GFO) is one of the well-known multi-ferroic as well as magneto-electric material, which has been extensively studied because of its proposed applications and interesting physics[64,256–258]. GaFeO₃ is the one of the promising versatile ME material, which has large magneto-electric coupling constant (10^{-11} s/m at 4.2)[64]. The advantage of GaFeO₃ on other MF materials such as BiFeO₃, YbMnO₃, BiMnO₃, *etc.* is that its magnetic transition temperature can be tuned near to RT by varying Ga:Fe ratio, sintering temperature and method of preparation, which is not the case in earlier mentioned MF materials, where magnetic transition is either far above or very low from room temperature[257,259]. It is important here to note that for the practical applications high value of magneto-electric response is required which is observed to be maximum near (T_C)[228]. Hence, the tuning of magnetic transition temperature scales the possibility of ME coupling. Recently, Han *et al.*[260] studied the effect of grain size on the magnetic properties of GaFeO₃ samples and explained that T_C can be tuned by varying the

Fe-O-Fe bond parameters and hence strength of magnetic interactions. Sharma *et al*[261]. studied that the magnetic properties in GaFeO₃ are largely controlled by the site-disorder, which is very sensitive to the sintering temperature and method of sample preparation[261]. The presence of such kind of site-disorder may vary the strength of super-exchange interactions by varying the Fe-O-Fe bond parameters[261]. Thus, the possibility to tune T_C in wide limits can be achieved by changing the chemical composition and synthesis procedure.

GaFeO₃ has a non-centrosymmetric structure with four cationic sites Ga1, Ga2, Fe1 and Fe2 for Ga and Fe ions respectively[64,256]. The Ga1 ions make tetrahedral environment with oxygen atom whereas, Ga2, Fe1 and Fe2 ions occupy octahedral sites with the oxygen atom[64,256]. The distortions in the Ga2, Fe1 and Fe2 octahedra and non-centrosymmetric structure of Fe-ions, there is an existence of ferroelectric polarization along the b axis[64]. The beauty of the structure lies in the fact that Fe ions is surrounded by oxygen ligands and the local electric field due to oxygen leads to splitting of Fe *d*-levels into t_{2g}-e_g orbitals, which is known as crystal field splitting[70,108,127]. The crystal field *d-d* transitions contain crucial information related to electron-phonon couplings (EPC) and local electronic structure[117,127,215]. It is worth mentioning here that sintering temperature (T_S) is a crucial parameter, which strongly affects the electron-lattice and spin-lattice coupling[127,245]. It is now well accepted that Raman spectroscopy has the potential to probe the strength of these couplings[127,262,263]. The variation in the Raman shift as a function of temperature generally occurs due to spin-phonon coupling and effective lattice interaction contributions as a result of renormalization of the phonon frequency brought out by magnetic ordering changes alone. Further, the strength of the spin phonon coupling in these materials is associated to the colossal magneto-elastic, magneto-ferroelectricity, behavior, *etc*[228]. Therefore, it is of interest to study the strength of spin phonon coupling, EPC as a function of T_S and

get insight into the intriguing spin ordered coupling phenomena in GaFeO₃.

Keeping all these aspects in mind, OAS and Raman spectroscopy experiments were carried out on GaFeO₃ samples sintered at different temperatures. Using the phonon renormalization function(Δw), the coupling strengths for all series of samples are estimated and compared. The temperature-dependent ac susceptibility measurements were carried out to obtain the T_C and correlated with the Raman spectroscopic results. The present investigations suggest that for GaFeO₃ the oxygen non-stoichiometry is very suitable route to enhance the electron-lattice and spin-lattice coupling for practical applications.

7.2 Experimental detail

7.2.1 Sample preparation

Single-phase polycrystalline samples of GaFeO₃ were synthesized by wet chemical method[264,265]. To accomplish this, the stoichiometric amount of gallium metal was dissolved in dilute nitric acid (60%) in order to prepare gallium nitrate. The gallium nitrate and iron nitrate [Fe (NO₃)₃.H₂O (99.99%, Sigma Aldrich)] were mixed in an equimolar amount of citric acid and ethylene glycol. During this process, citric acid acts as a complexing agent and ethylene glycol acts as a fuel. The resulting solution was constantly stirred at 70 °C for formation of gel network and the prepared gel was calcined in a muffle furnace for 12h at 200 °C. The calcined gel was powdered and pelletized at the pressure of 10 tons to make the pellet. The final sintering of uniaxially compressed pellets was done at different sintering temperatures with heating rate 3°C/min and cooling rate of 1°C/minute for 12 hrs.

7.2.2 Structural characterization

Crystallinity and structural phase purity of GaFeO₃ were ensured using x-ray diffraction experiment with Bruker D8 diffractometer equipped with Cu target (Cu K α = 1.54 Å), in the angular range of 2 θ =

20°–80°. The obtained x-ray diffraction data were fitted by using the Fullprof_suit Rietveld refinement package[265,266].

7.2.3 Temperature-dependent ac susceptibility measurements

The variation of ferri-magnetic transition temperature as a function of T_S is confirmed by using temperature-dependent ac susceptibility measurements. The low-field (4 Oe) temperature-dependent ac-susceptibility measurements were carried out in the temperature range 150-300 K by using Physical Quantities Measurement System (PQMS) at frequency 1000 Hz and with temperature ramp rate 1 K/min.

7.2.4 Scanning Electron Microscopy (SEM)

To investigate the variation in surface morphology of the prepared samples, scanning electron microscopy (SEM) studies were carried out by using Supra-55 Zeiss scanning electron microscope.

7.2.5 Optical measurements

To investigate the effect of T_S on charge neutral *d-d* transitions and exciton line shapes, optical absorption spectroscopy (OAS) experiments were carried out in diffuse reflectance mode. These measurements have been performed in the 190–800 nm wavelength range using Cary-60 UV-VIZ-NIR spectrophotometer having Harrick Video-Barrelino diffuse reflectance probe[65,66,121].

7.2.6 X-ray absorption measurements

The presence of mixed oxidation states in the prepared samples have been confirmed by performing the x-ray absorption near edge spectroscopy (XANES) measurements at Fe K-edge in transmission mode and the DCM energy was calibrated using standard Fe foil at 7112 eV. All the XANES measurements were done at the BL-9 of Indus-2 synchrotron source at the RRCAT (Raja Ramanna Centre for Advanced Technology) Indore, India[253].

7.2.7 Raman experiments

The Raman experiments for prepared GaFeO₃ samples by using LABRAM HR dispersive spectrometer with laser source having

excitation wavelength 633 nm and CCD detector in backscattered mode[12]. For temperature-dependent Raman experiments THMS600 stage from Linkam with accuracy of the order of 0.1 K was used[262]

7.3 Results and discussion

7.3.1 X-ray diffraction (XRD)

Figure-7.1 represents the refined x-ray diffraction data by considering the space group $Pc2_1n$ for all series of samples. The one to one fit of experimental data with theoretical calculated data confirms the phase purity of prepared GaFeO_3 sample. In addition to this, the XRD peak slightly shifts towards lower 2θ side with increasing the sintering temperature, which is attributed to the systematic increase in the values of lattice parameters. The variations of unit cell parameters as a function of TS are listed in Table-7.1. From the Table it can be seen that Fe-O-Fe bond angle scales systematically, whereas minute changes in the Fe-O bond lengths has been observed as a function of T_s .

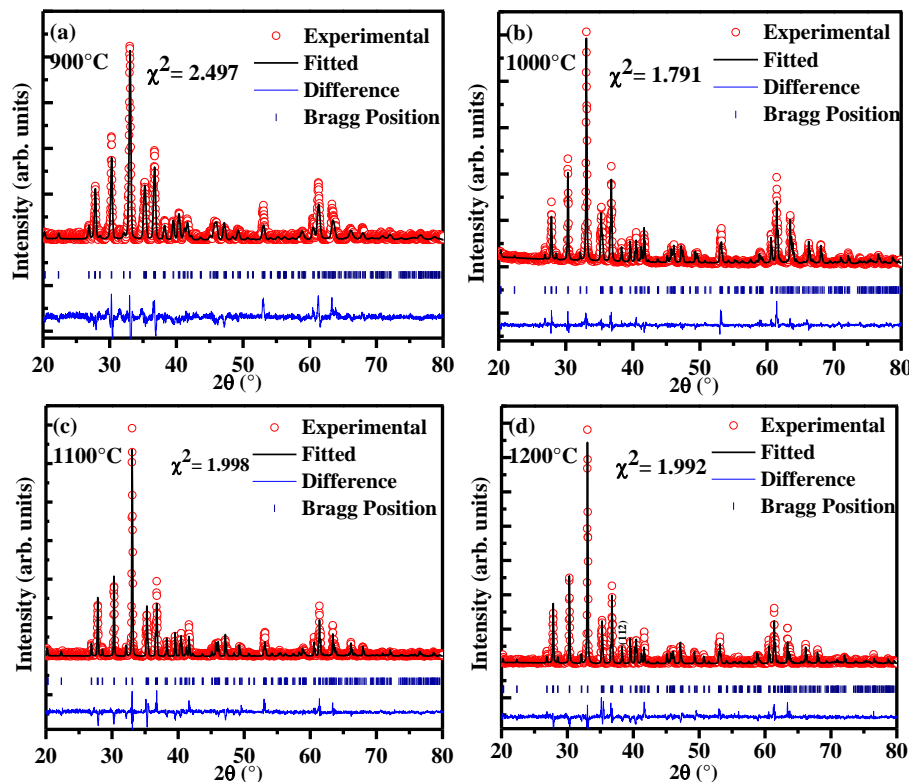


Figure-7.1: The refined x-ray diffraction for all prepared series of samples. The one to one fit of experimental data with calculated data confirms the structural phase purity of the sample.

Sintering temperature (°C)	900	1000	1100	1200
a (Å)	8.7386(4)	8.7408(2)	8.7418(3)	8.7435(7)
b (Å)	9.3823(8)	9.3885(3)	9.3897(5)	9.3937(8)
c (Å)	5.0758(3)	5.0799(6)	5.0802(4)	5.0827(6)
Fe1-O-Fe2(°)	131.22(5)	131.43(6)	132.15(5)	133.03 (4)
Fe1-O1(Å)	2.361(3)	2.361(1)	2.362(3)	2.362(7)
Fe1-O1(Å)	2.112(2)	2.111(3)	2.112(7)	2.113(5)
Fe1-O2(Å)	2.080(3)	2.080(5)	2.080(6)	2.081(7)
Fe1-O3(Å)	1.900(5)	1.901(1)	1.901(3)	1.902(8)
Fe1-O5(Å)	1.901(2)	1.901(5)	1.902(4)	1.901(6)
Fe1-O5(Å)	1.972(5)	1.972(2)	1.973(1)	1.973(9)
Fe2-O1(Å)	2.340(1)	2.341(3)	2.341(3)	2.341(5)
Fe2-O2(Å)	2.052(3)	2.053(4)	2.052(3)	2.053(7)
Fe2-O3(Å)	1.933(4)	1.934(4)	1.934(9)	1.935(2)
Fe2-O4(Å)	2.115(6)	2.115(2)	2.115(4)	2.116(8)
Fe2-O5(Å)	1.872(3)	1.872(7)	1.872(8)	1.872(7)
Fe2-O6(Å)	1.982(1)	1.982(6)	1.982(5)	1.983(2)

Table-7.1: The variation of unit cell parameters as a function of sintering temperature. The numbers in open bracket indicates the last digit error bar.

It is important here to note that the structural distortion arises due to T_S affects the strength of super-exchange interactions as explained by Goodenough-Kanamori (GK) rule[245] in terms of interactions between two adjacent transition metal ions with virtual charge transfer. To understand this in detail, magnetic measurements were carried out and detailed analysis will be elaborated in the following sections.

7.3.2 Temperature-dependent magnetic measurements

The variation of T_C as a function of T_S is further checked by using temperature-dependent ac susceptibility measurements. It can be seen from figure-7.2 that T_C scales directly with increasing the sintering temperature. The observed changes in the T_C is attributed to the enhancement in the super exchange interaction between neighboring Fe^{3+} ions, which has a strong dependency on Fe-O-Fe bond angles. The interesting feature in the form of cusp (see figure-7.2) at ferrimagnetic transition temperature could be attributed to magnetic anisotropy[267]. At this point, it should be noted that $GaFeO_3$ is highly anisotropic material[267] and all the cation sites are not magnetically identical. In the case of $GaFeO_3$, Fe ions occupied on Fe1, Fe2 sites, and Ga2 octahedral sites have strong local anisotropy, but Fe ions on tetrahedral site interact weakly with the other cations[268]. It is well known that Fe ions on octahedral sites have the property of hard magnetic phase, whereas the tetrahedral site Fe ion has the soft magnetic property[268]. Therefore, Fe ions in $GaFeO_3$ have different magnetic anisotropy energies at each cation site. Fe ions on the Ga1 site behave differently from those on Fe1, Fe2, and Ga2 sites. This leads to the magnetic anisotropy in the samples under investigations. Apart from this, the magnetic crystalline anisotropy depends on the angle between the components of a sub-lattice's magnetization[269] and increase in Fe-O-Fe bond angles scales the strength of antiferromagnetic super exchange interactions, which might be another contributing factor for the sharp cusp in higher sintered sample. Accordingly, it is expected that with the variation in the oxygen content of $GaFeO_3$ nanoparticles results to disorder in the occupation of cation sites, especially for octahedral sites, leads to a local deformation of the lattice and is consistent with the

variation in the angle between the components of a sub-lattice's magnetization. Hence, it might be expected that with the variation of sintering temperature, there are significant changes in the cationic distribution and magnetic properties.

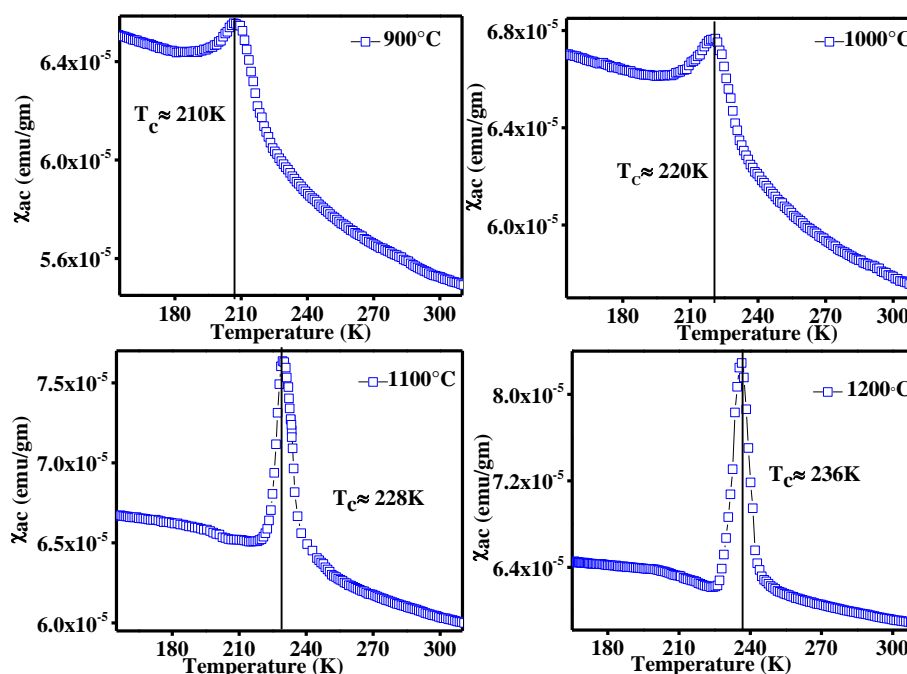


Figure-7.2: Temperature dependence of ac-susceptibility measurement results for prepared series of samples. The scaling of ferrimagnetic transition temperature and magnetic anisotropy can be clearly seen from with increasing the sintering temperature.

7.3.3 Scanning Electron Microscopy (SEM)

The surface morphology and microstructure of the prepared samples has been investigated by the scanning electron microscopy (SEM) studies carried out for the GaFeO_3 samples are shown in figure-7.3. It is seen from the figure that the sample sintered at the lowest temperature (900°C) possesses the small grain size, whereas increase in T_s results to increment in grain size. The observed variation is attributed to the grain growth at higher T_s , which leads to the decrease in voids and porosity. The calculated average grain size calculated from Image-j software are 0.50 μm for GFO-900°C, 0.65 μm for GFO-1000°C, 1.33 μm for GFO-1100°C, 3.72 μm for GFO-1200°C respectively.

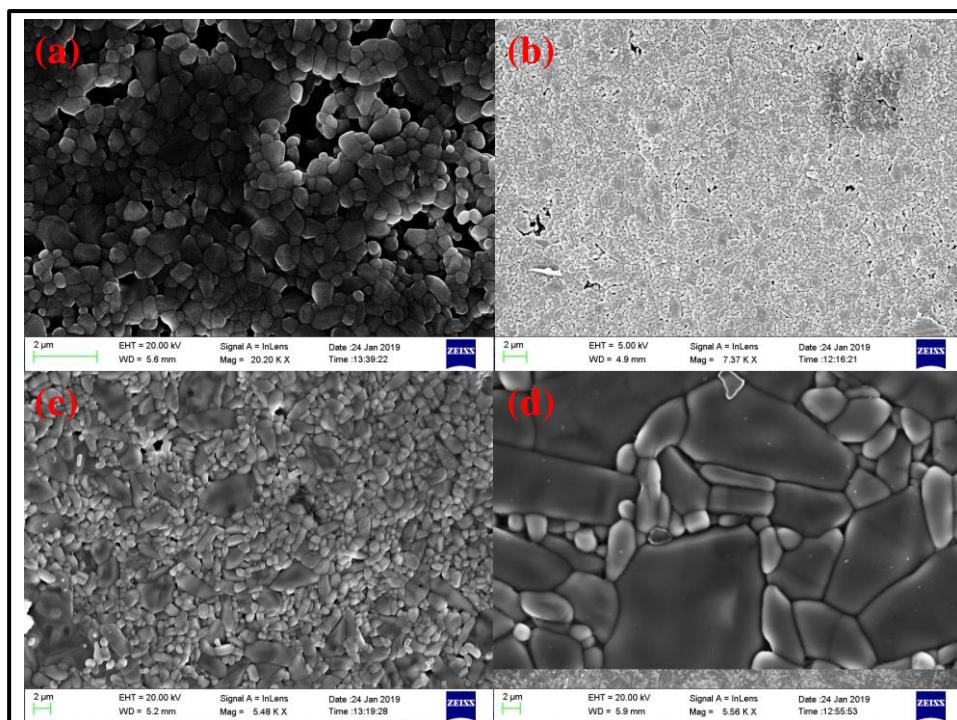


Figure-7.3: The scanning electron microscopy images for GaFeO_3 sintered at 900°C (a), 1000°C (b), 1100°C (c), 1200°C (d).

7.3.4 X-ray absorption at Fe K-edge

In order to investigate the oxidation state of Fe ions in GaFeO_3 , XANES measurements were carried out. Figure-7.4(a) represents the XANES data for all series of samples. The energies corresponding to the absorption edge of pure Fe foil (Fe^0), FeO (Fe^{2+}) and Fe_2O_3 (Fe^{3+}) were also measured and used as standard reference for energy calibrations[270–276]. The absorption edge of all prepared samples is found to be at lower energy as compared to that of standard Fe^{3+} (*i.e.* Fe_2O_3), which clearly indicates the coexistence of Fe in +2 and +3 oxidation states in the prepared samples. Further, to quantify the oxidation state of Fe, a polynomial equation has been fitted between the oxidation state and edge energy of the standard samples[151,152] as depicted in figure-7.4(b). Thus, the value of oxidation state of Fe for samples sintered at 900°C , 1000°C , 1100°C , and 1200°C is found to be 3 ± 0.005 , 2.99 ± 0.005 , 2.97 ± 0.005 , 2.96 ± 0.005 respectively. Hence, it can be concluded that there is a significant effect of sintering temperatures

on the oxidation state of Fe ions and oxygen stoichiometry in higher sintered samples, which result to red shift in x-ray absorption edge.

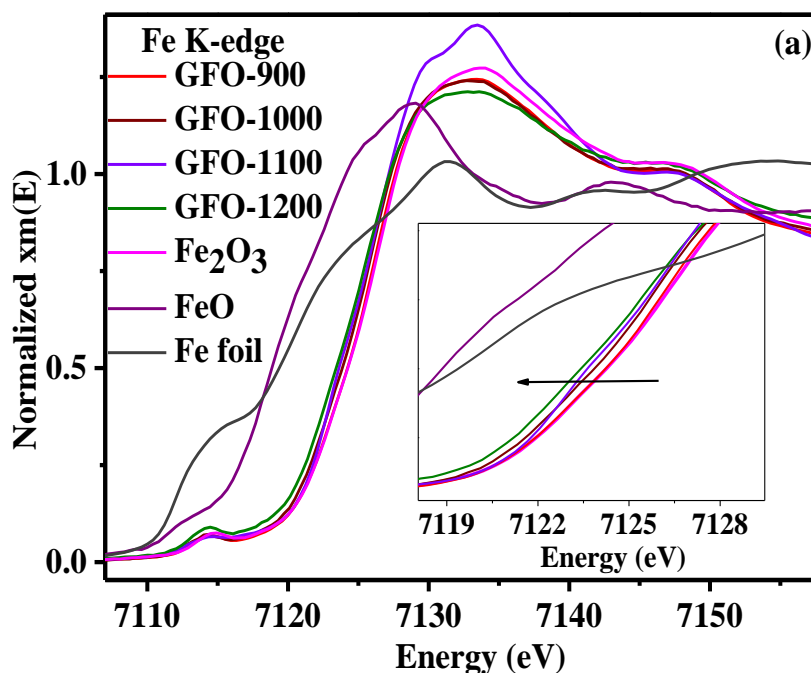


Figure-7.4(a): The x-ray absorption spectra at Fe K-edge for GaFeO_3 samples sintered at different temperatures.

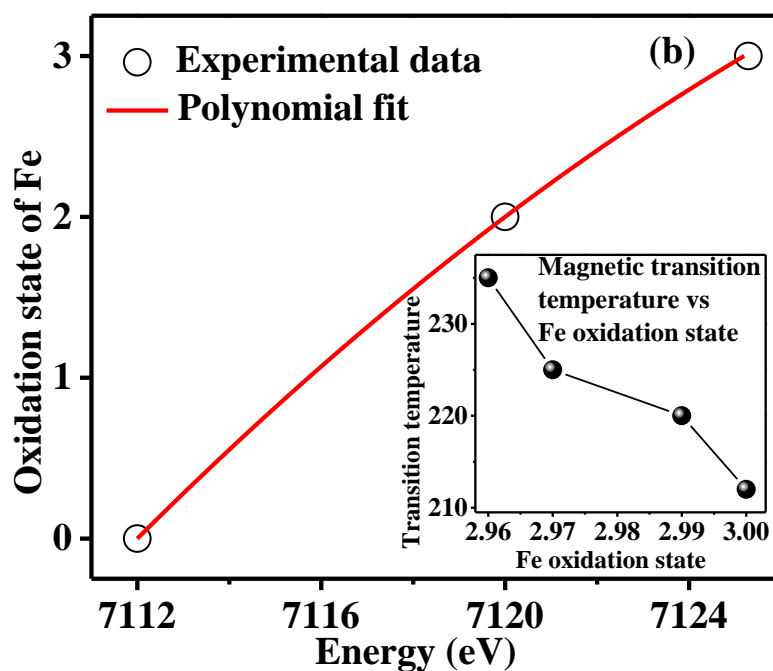


Figure-7.4 (b): The polynomial fitted plot of Fe oxidation state vs Fe K-edge energy for the standard samples. Inset represents the effect of oxygen defects on Fe oxidation state and magnetic transition temperature.

Apart from this, a pre-edge feature arising around 7115 eV has been observed, which arises due to quadrupolar allowed transitions and its intensity has a direct connection with the non-centrosymmetry around Fe octahedra[150]. The systematic increase in the intensity of pre-edge feature for higher sintered samples suggests the reduction in inversion symmetry around the transition metal atom[150]. Moreover, it has been reported earlier that pre-K-edge features in these perovskite oxides arise due to the strong mixing of $3d$ states of neighboring transition metal atoms *via* strong hybridization with $2p$ states of intermediate oxygen, which further causes the local distortions in the octahedra and may lead to the reduction in inversion symmetry[150].

7.3.5 Diffuse reflectance spectroscopy (DRS)

To understand the optical properties of prepared GaFeO_3 samples as a function of T_S , OAS experiments in diffuse reflectance mode were carried out[141,215,232,277,278]. The optical absorption spectra as a function of T_S are depicted in figure-7.5 (a). The variation in optical spectra with T_S is attributed to the competing effects due to micro-strain, oxygen defects and onsite columbic interactions[137]. The importance of the present work lies in the detailed investigations of the intensity feature centered around 1.7eV, which results to increase in the double exchange mediated charge transfer and magnetic interactions as a function of T_S . In the case of ferrites, this intensity feature arises due to transition of electron from t_{2g} (triply degenerate) level to e_g (doubly degenerate) level of same or near neighbor Fe atom[74,135,136]. The Fe atoms in GaFeO_3 are surrounded by the oxygen ligands, which exerts an electrostatic force (internal stark effect) on Fe- $3d$ orbitals and results to crystal field splitting of Fe orbitals[127,279,280]. The scaling in the intensity of the crystal field $d(t_{2g})-d(e_g)$ transitions with T_S is clear from the figure-7.5 (a) and can be realized in terms of oxygen non-stoichiometry induced variation in oxidation state of Fe atoms.

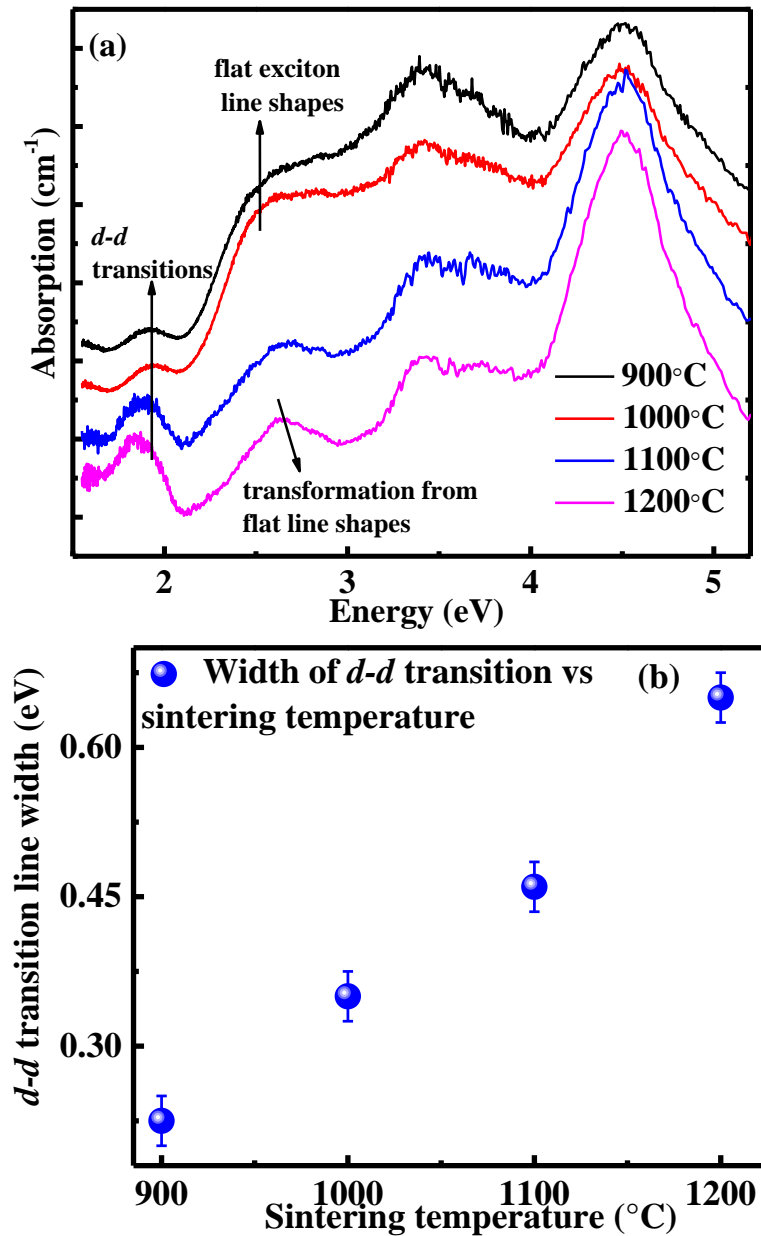


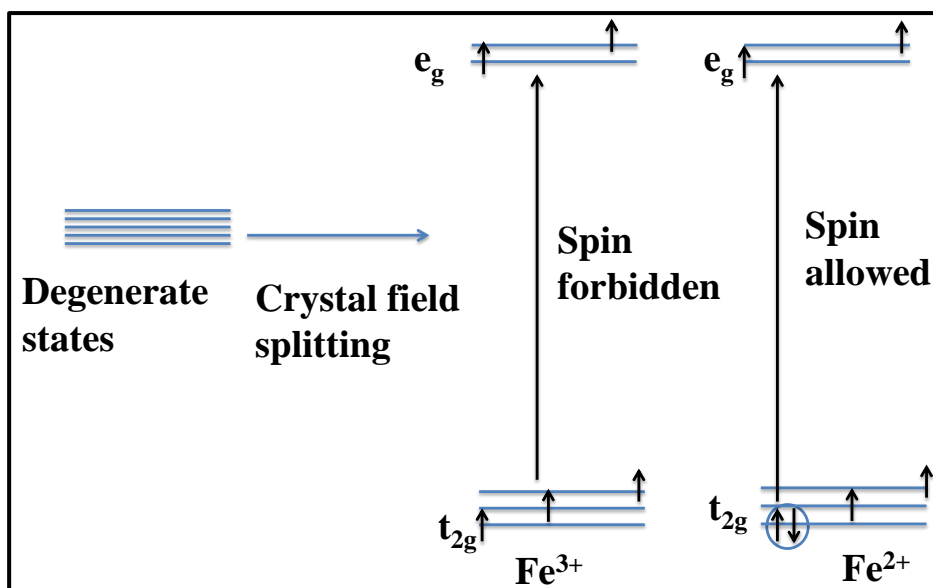
Figure-7.5 (a): The optical absorption spectra for GaFeO₃ at various sintering temperatures. Figure suggests the systematic scaling in the intensity and red shift in d-d transitions. The variation of d-d transitions width as a function of sintering temperatures is depicted in figure-(b).

In stoichiometric GaFeO₃, Fe is having d^5 electronic configuration and such transitions is expected to be *spin* forbidden[6], whereas, the samples sintered at high temperatures generally show deviation from exact oxygen stoichiometry, which leads to variation in

oxidation state of Fe (*i.e.* Fe to be present in +2 or +4 oxidation state)[127]. Fe^{+2} and Fe^{+4} have d^4 and d^6 electronic configuration respectively[108,127,137] and electron can be easily transported to the (e_g) level of same or near neighbor Fe atom[74,135,136]. The formation of Fe^{+2} ions with T_S scales the intensity of crystal field $d-d$ transitions, since the probability of electron transfer is maximum for the samples having large deviation from oxygen stoichiometry. The schematic illustration of spin allowed and forbidden transitions are given in schematic-1. At this juncture, it should be noted that the presence of spin-orbit coupling may relax the *spin selection rule*, however, the intensity of spin prohibited transitions are very less than spin permitted transitions[72,135]. In the present case, the intensity of such transitions is much higher; which strongly suggests the possibility of spin permitted transitions[59]. Thus, from this discussion, it is clear that the change in the oxygen stoichiometry in higher sintered samples would results to the intensity of $d-d$ transition. Another interesting and important aspect of OAS data is the red shifting of $d-d$ transitions as a function of T_S . This phenomenon has been realized by invoking the Tanabe-Sugano (T-S) diagrams[281,282]. T-S diagrams theoretically predicted the position of such transitions for samples having d^6 , d^5 , d^4 electronic configurations for Fe^{2+} , Fe^{3+} , and Fe^{4+} ions respectively. The Fe^{3+} ions does not show spin allowed transitions, whereas the predicted position for Fe^{4+} (d^4) and Fe^{2+} (d^6) is around $13,900 \text{ cm}^{-1}$ ($\sim 1.73 \text{ eV}$) and $10,300 \text{ cm}^{-1}$ ($\sim 1.28 \text{ eV}$) respectively[108,127,281]. In the present investigations, the red shift of $d-d$ transitions signifies the formation of Fe^{2+} ions or oxygen vacancies in high sintered samples. This red shift in $d-d$ transitions is in good agreement with the results published by Mocherela *et al*[280]. In addition to this, the tuning of position of $d-d$ transitions would be useful to realize the oxygen vacancies, which can be a new and unorthodox approach to understand the oxygen non-stoichiometry. Further, the width of these transitions scales systematically with increasing the T_S as depicted in figure-7.5 (b). To estimate the width of these transitions, the experimental data arising around 1.7 eV has been fitted by using Lorentzian function. As mentioned earlier, the width of such transitions

contain important information about electron-lattice coupling[70,71,127]. Thus, it seems that with T_S , EPC changes significantly due to oxygen vacancies, which changes the density of states (DOS) near to energy of $d-d$ transitions[70,72,127]. The detailed analysis of EPC as a function of T_S will be elaborated in next sections.

The intriguing feature around 2.6 eV is assigned as the transition from 6A_1 to 4A_1 states, which determines the strength of mixing of the 3d-states with the dipolar allowed charge transfer transitions[283]. Therefore, the feature around 2.6 eV can be assigned as a exciton line shape, which arises due to electric-dipole allowed charge transfer transition from 6A_1 to 4A_1 . From the deeper analysis of figure-7.5 (a), changes in exciton line shapes towards Gaussian one can be clearly seen, which could be very interesting to realize the one to one relation between the width of $d-d$ transitions, excitonic band and EPC. As discussed by Vella *et al*[284]., the excitonic bands provide important information related to EPC and mobility of the excitons. For pure GaFeO₃, this band is not clear, however for high temperature sintered samples, these lines shape transform towards the Gaussian side, which suggests the localization of excitons for higher sintered samples. From the model given by Vella *et al*.[284], the shape of excitonic peak is decided by the competition between EPC and mobility of the excitons. For Gaussian-like band, EPC prevails over mobility factor (B)[284]. Hence, it seems that the formation of excitonic peak towards Gaussian one shows the domination of EPC over B[117,127], which further could be attributed to the presence of oxygen defects/structural disorder in high temperature sintered samples. Hence, it can be concluded from here that the width of crystal field $d-d$ transitions and changes in the excitonic band towards Gaussian one signifies the scaling of the EPC with T_S . These results are strongly supported by the earlier reported literature[70,71,127].



Schematic-1: Represents the illustration of spin allowed and forbidden transitions.

7.3.6 Raman scattering results

Raman is a microscopic probe to investigate the subtle changes in the structure, EPC, spin-phonon coupling, presence of defects, structural disorders *etc.*[12,127,262]. The Raman spectrum for GaFeO₃ is dominated by the modes related to both tetrahedral and octahedral vibrations[64]. The orthorhombic primitive cell of GaFeO₃ has 8 formula units and has total 117 Raman active non-degenerate optical phonon modes, which decompose into $T_{\text{optical}} = 29 A_1 + 30A_2 + 29 B_1 + 29B_2$ Raman modes[64,257]. As discussed in earlier sections, the structure of GaFeO₃ comprises of Ga1–O tetrahedral, whose corner shared with the octahedra formed around Fe1–O, Ga2–O, and Fe2–O octahedron units, whereas the cations with octahedral arrangement have edge shared networks[64,285]. The octahedral environment units are loosely bound, whereas, the tetrahedral formed by Ga1-O atoms are comparatively strongly bound[64]. Hence, the Raman modes involving the tetrahedral vibrations could be observed in the high-frequency region, whereas, spectra corresponding to octahedral vibrations can be seen in low-frequency region[64]. The Raman modes positioned around 650-850 cm⁻¹ arise due to the symmetric stretching (SS) vibrational

modes of tetrahedral units, whereas the symmetric stretching vibrational modes corresponding to octahedral units come around 600-650 cm^{-1} [64]. The bending vibrations of polyhedral units are dominated in the region around 400 and 500 cm^{-1} . The Raman active rigid rotational modes for the octahedral and tetrahedral units are generally observed in the low-frequency region with wave number range[64,256,262] 80-390 cm^{-1} . The Raman spectra for the prepared GaFeO_3 samples are displayed in figure-7.6. The number of Raman modes is same for all samples, suggesting no change in structure or symmetry irrespective of T_S , which is in good conformance with the x-ray diffraction results. At this point, it should be noted that Raman scattering has a potential to probe the presence of compressive/tensile strain in the sample. The presence of compressive or tensile strain would result to shift in the position of Raman mode towards higher wave number side (blue shift) and lower wave number side (red shift) respectively. In the present study, a clear blue shift has been observed with increase in T_S , suggesting the enhancement in the bond strengths for high temperature sintered samples.

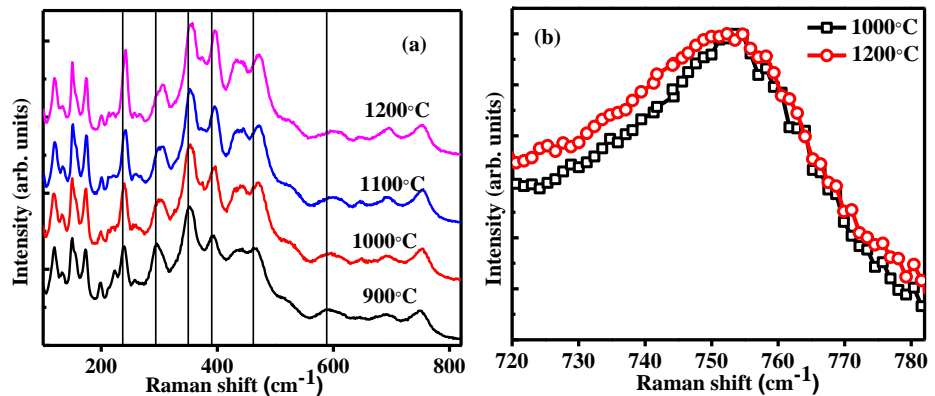


Figure-7.6: Room temperature Raman spectrum for the prepared series of samples (a). Figure-(b) represents the deviation from normal Lorentzian Raman line shapes or asymmetry observed in higher sintered samples on the same scale. The observed behavior is attributed to interaction of electron with the phonons at room temperature.

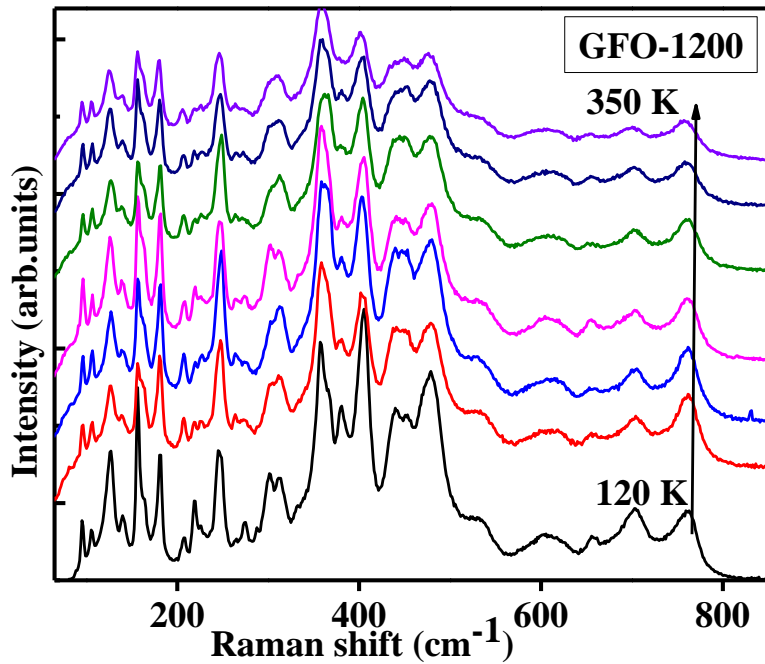


Figure-7.7: *The representative's temperature dependent Raman spectrum for GaFeO₃ sintered at 1200°C.*

Further, Raman spectral analysis provides crucial information related to electron-phonon interactions and the presence of such interactions would result in deviation from generally observed Lorentzian Raman line shapes[127]. The extent of EPC can be estimated from the variation of asymmetry parameter in Raman line shapes. It should be noted here that GaFeO₃ is a dielectric material and EPC is not supposed to be the dominating factor in Raman line shapes. However, the evaluation of results strongly infers that the samples sintered at higher temperatures contains more asymmetry than the sintered at low temperatures as represented in figure-7.6 (b). Apart from this, asymmetry has a direct dependency with the carrier density in semiconductors[127] and presence of extent of disorder[92,93]. Hence, it seems that the formation of oxygen vacancies would lead to phononic disorder and enhancement in the charge carriers, which could be the contributing factor for the scaling of EPC. The systematic increase in the asymmetry of phonon modes are in good conformance with the width of crystal field *d-d* transitions.

Further, to realize the effect of T_S on magneto-elastic properties, temperature-dependent Raman spectroscopy was used and corresponding Raman spectra for GFO-1200 is shown in figure-7.7. It is well accepted that Raman spectroscopy has the potential to probe the structural changes as a function of temperature[64,261]. The non-disappearance of any Raman mode strongly suggests the absence of any structural phase transition in the given temperature range, which is in good conformance with the earlier studies by neutron diffraction experiments[286]. Moreover, the changes in Raman spectra as a function of temperature are generally a consequence of various factors as ascribed below[63]:

$$w(T) - w(0) = \Delta w_{lattice} + \Delta w_{renormalization} + \Delta w_{sp-ph} + \Delta w_{anharmonic} \quad (7.1)$$

where, $w(0)$ is the Raman shift corresponds to 0 K, $\Delta w_{lattice}$ signifies the lattice volume contribution due to thermal excitations of atoms, $\Delta w_{renormalization}$ is the involvement from the renormalization of electronic states near magnetic transition temperature, Δw_{sp-ph} is the contribution of spin-phonon coupling and $\Delta w_{anharmonic}$ corresponds to the contribution of anharmonic terms respectively. The term $\Delta w_{lattice}$ represents the isotropic variation in volume and can be considered as negligible. Also, in the present case, no extra electrons/holes have been added by n/p type doping; Hence, the contribution due to renormalization of electronic states can be neglected because of low carrier concentration. Therefore, the observed changes in Raman modes with temperature are a consequence of higher-order terms contribution and spin-phonon coupling/ magneto-elastic coupling. Further, to estimate the contribution of anharmonic terms, the variation of Raman shift is fitted by Balkanski model expressed as[229,247]:

$$w(T) = w(0) - A \left[1 + \Sigma \frac{1}{\exp\left(\frac{\hbar\omega_i}{2\pi kT}\right) - 1} \right] \quad (7.2)$$

where, the term $w(0)$ is the Raman shift at 0 K, A (anharmonic coefficient) is the contribution from higher order terms for three phonon

processes. It can be seen from Balkanski fittings in the figure-7.8 that the variation of Raman shift as a function of temperature does not follow the normal anharmonic behavior and show deviations around the magnetic transition temperature, which strongly suggest the domination of another factor than anharmonicity.

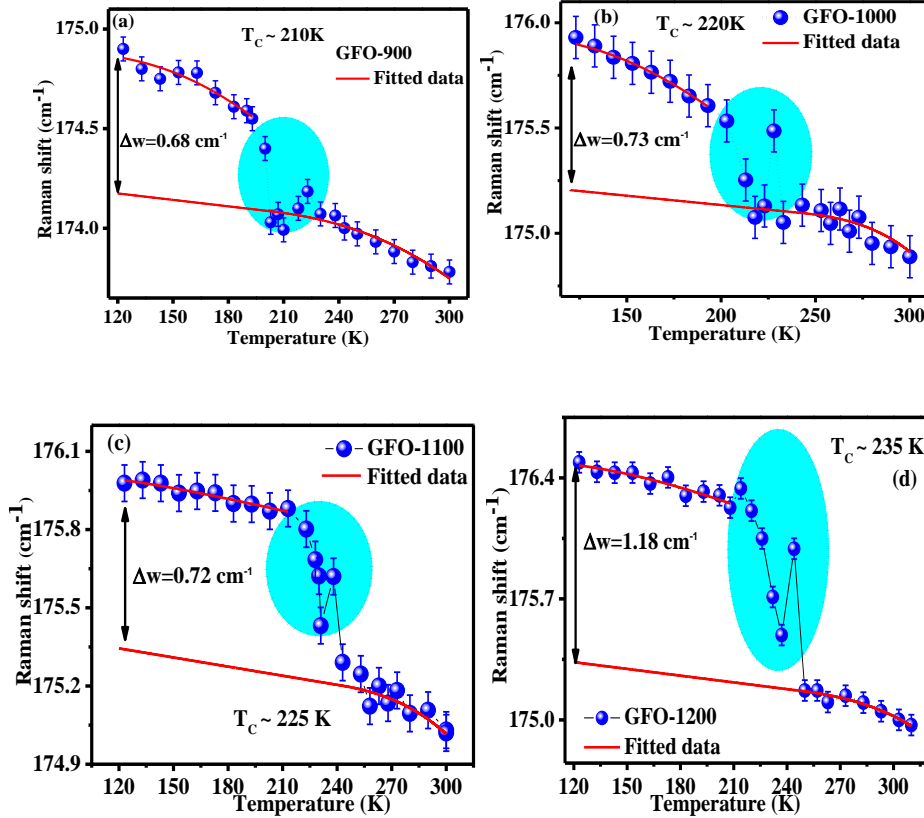


Figure-7.8: The variation of Raman modes corresponding to 175 cm^{-1} for GFO-900 (a), GFO-1000 (b), GFO-1100 (c), GFO-1200 (d) as a function of temperature.

Hence, it can be concluded that the key contributing factor for the anomalies observed in temperature-dependent Raman shift is the presence of strong magneto-elastic coupling. The anomalous behavior in the Raman shift around magnetic transition is related with the magnetic ordering induced renormalization of phonon modes and has a direct dependency on the spin-spin correlation function $\langle S_i \cdot S_j \rangle$ [63,64]. According to mean field theory, phonon renormalization function and magnetization is associated as follows[63,64]:

$$\Delta w(T) = w(T) - w_{anharmonic}(T) = \gamma \frac{M^2(T)}{M_{sat}^2(T)} \quad (7.3)$$

where, $M(T)$ is the temperature dependent magnetization per Fe-site ions, $M_{sat}(T)$ indicates the saturation magnetization and γ epitomizes the spin-phonon coupling strength. With invoking the Balkanski model, the experimental Raman shift has been fitted in the region before and after the magnetic transition temperature and the values of $\Delta w(T)$ has been estimated as depicted in figure-7.8. It can be seen from the figure that $\Delta w(T)$ grows from 0.68 cm^{-1} to 1.18 cm^{-1} with increasing T_S from $900 \text{ }^\circ\text{C}$ to $1200 \text{ }^\circ\text{C}$, suggesting the strong magneto-elastic coupling strength for higher sintered samples. The estimated values of $\Delta w(T)$ seems to decrease slightly for GFO-1100, however the change is so small and can be considered in the error bar range. Hence, it can be concluded that the larger $\Delta w(T)$ value for GFO-1200 sample could be attributed to stronger sensitivity of magnetic interactions to the atomic vibrations, which further could have a direct connection with the oxygen vacancies. In addition to increase in the strength of magneto-elastic coupling there is a systematic scaling in the T_C values with T_S as clear from figure-7.8. This behavior has been explained in terms of increase in the oxygen vacancies and Fe-O-Fe bond angles. The formation of oxygen non-stoichiometry in higher sintered samples enhances the exchange interactions and the mobility of e_g electrons, which strongly controls the strength of super-exchange interactions[287]. Apart from this, the conduction band consists of e_g electrons and magnetic properties are highly dictated by the band structure[288,289]. This seems meaningful due to the reason that ferromagnetic double exchange interactions is driven by the spin dependent transport of conduction electrons[59] which could be responsible for the determination of the magnetic ground state. At this point, it should be noted that the frequency of Raman mode is directly related to the force constant given by the formula, $\omega \approx \sqrt{k/M}$, where k is related to the bond strength and M is the reduced mass of the atoms. The blue shifting of Raman modes with increasing the T_S could be attributed to improvement in the strength

of bonds with increasing T_s . The important aspect that should be noted here is the potential of Raman spectroscopy to probe the subtle changes in the overlapping/hybridization between the metal-3d and O orbitals, which further increases the e_g electron bandwidth[288,289]. At this point, it is imperative to note that the superexchange interaction between neighboring Fe^{3+} ions in $GaFeO_3$ is strongly affected by the Fe-O-Fe bond parameters[290]. It is clear from the Table-1 that lattice parameters systematically scale with the T_s , which escalate the Fe-O-Fe bond angles and hence increases the strength of antiferromagnetic interactions. Also, the scaling in Fe-O-Fe bond parameters supports the Goodenough-Kanamori-Anderson coupling (GKA)[245]. The GKA coupling increases the magnetic interaction between the spins and hence increases the T_C values. The improvement in these exchange interactions is also consistent with the formation of Fe^{2+} ions, which enhances the Fe^{2+} -O- Fe^{3+} interactions and aggravate the mobility of e_g electrons, which might be responsible for the increasing trend in T_C with sintering temperature.

From this discussion, it is clear that sintering temperature is an important factor, which highly affects the structural, optical, magneto-elastic as well as ferri-magnetic interactions. Optical absorption spectroscopy experiments carried out on $GaFeO_3$ samples infers the variation in crystal field transitions and formation of exciton line shapes in high temperature sintered samples. The systematic scaling in the intensity and shifting of $d-d$ transitions to the lower energy suggest the formation of oxygen defects with T_s . The increase in oxygen vacancies for higher sintered samples would result in enhancement in double exchange interactions and hence affect the magnetic ground state. Room temperature Raman experiments infer the blue shift with increasing T_s , which suggests the improvement in the strength/overlapping of Fe-O bond with T_s . The increase in the overlapping affects the conduction of e_g electrons and hence variation in T_C has been observed as a function of T_s . The advantage of present investigations on $GaFeO_3$ is that the magnetic transition temperature T_C can be tuned by varying the sintering temperature, which is not the case in MF materials such as $BiFeO_3$,

YbMnO₃, BiMnO₃, where magnetic transition is either far above or very low from room temperature. Hence, the tuning the magnetic transition temperature scales the possibility of ME coupling and possibility of scheming near RT based novel MF devices.

7.3.7 Some concluding remarks on exciton line shapes

As discussed in the earlier sections that the description of the excitonic band gives evidence of localization or delocalization of excitons, depending on the shape of the band. The line shape of excitonic band in a system is basically decided by the rivalry between the tendencies of exciton to localize due to electron phonon coupling (EPC) and their mobile nature (B). The mobile nature of excitons is also measured by the F.W.H.M. of excitonic band, whereas, EPC is measured by root mean square amplitude (D) of the fluctuations of excitonic energy, which, is generally due to thermally activated vibrations of the lattice or structural disorders[77,117,291]. The beauty of this discussion lies in the fact that the line shape of excitonic band gives crucial information about the localization/delocalization of excitons. The absorption of excitonic band is given as[77,117,291,292]:

$$\alpha(E, T) = \alpha_0 [1 + (\frac{E - E_p^0 + \Delta_0(T)}{T_0(T)})^2]^{-1} \quad (7.4)$$

Vella[291] *et. al.* discussed in detail about the line shape of exciton for amorphous SiO₂ as a function of temperature. Further, in order to shed more light on the exciton localization or delocalization, PrFeO₃ sample has been irradiated with laser pulses. It is assumed that laser induced defects at different sites would results in systematic scaling of EPC, which may results to localization of the excitons. These results have been published in case of PrFeO₃ by Kumar *et al.* in literature[127]. The single phase purity of the PrFeO₃ and Cr-doped PrFeO₃ has already been discussed in chapter-2 (see figure-2.13 and 2.14).

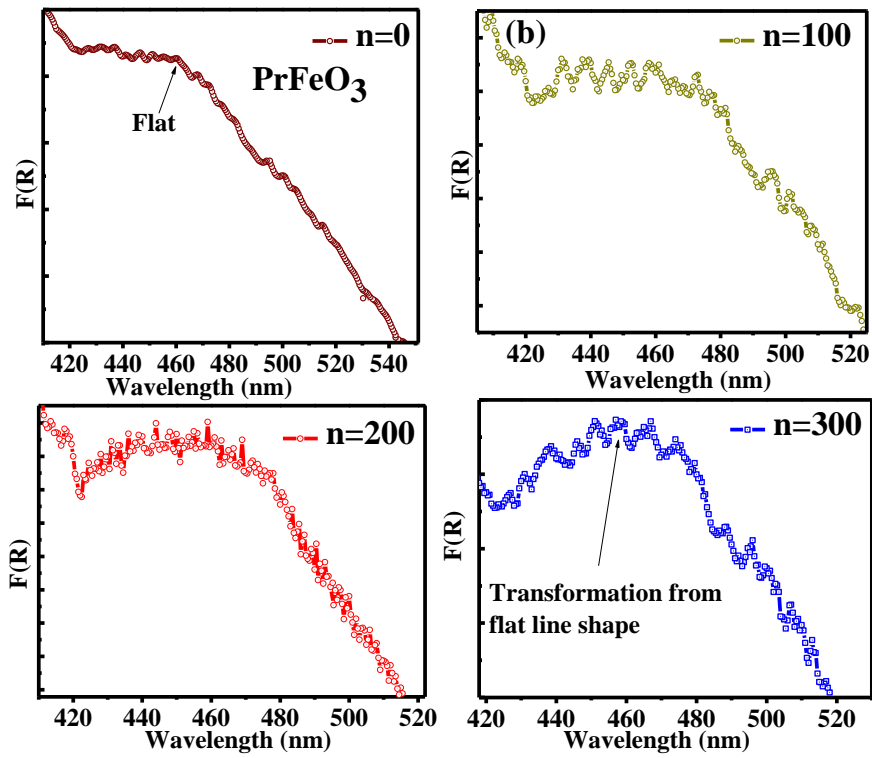
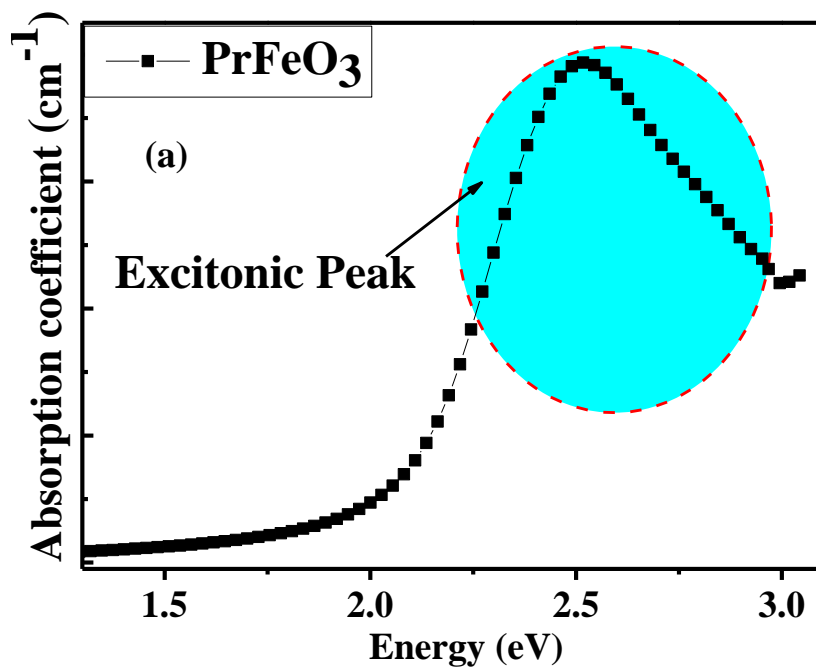


Figure-7.9: The defect induced localization of excitons due to increase in EPC with increasing the defects at different sites by laser irradiation.



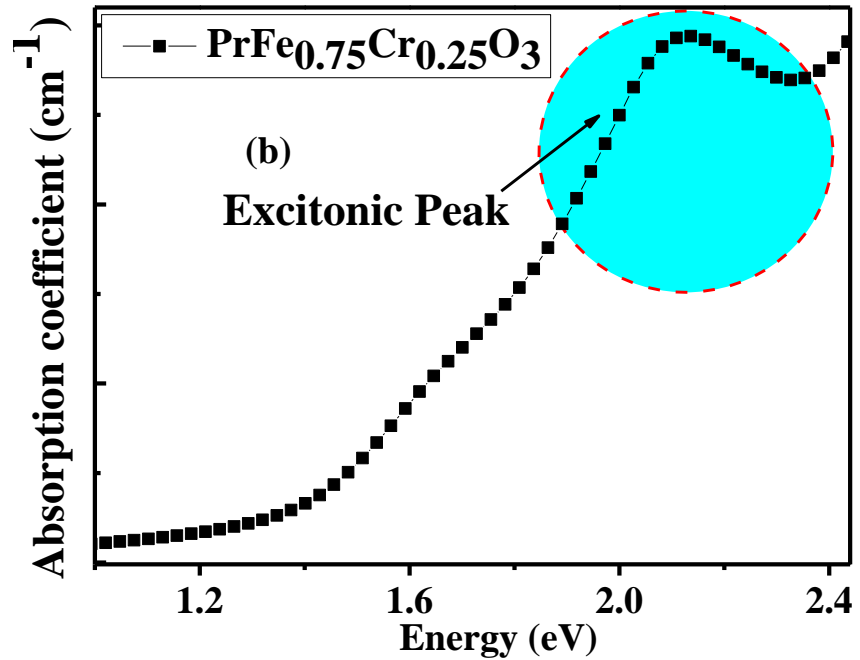


Figure-7.10(a): The simulated optical spectra for PrFeO_3 and Cr doped PrFeO_3 by using full-potential linearized augmented plane wave (FP-LAPW) method within the framework of density-functional theory.

Apart from this, First principle calculations have been carried out only for un-doped and 25% Cr doped samples. The theoretically simulated optical spectra for PrFeO_3 and 25% Cr doped PrFeO_3 signifies the transformation of excitonic peak from almost Gaussian to Lorentzian nature as shown in figure-7.9 (a) & (b). The F.W.H.M. of excitonic peak is given by cD^2/B and inversely scales with the mobility of electrons[117,291]. From simulated optical absorption data, it seems that width of 25% Cr doped (Lorentzian nature peak) samples is less than un-doped one, which might be due to increase in mobility of excitons.

Further, from the obtained band structure data we have estimated the quantity $1/(d^2E/dk^2)$ which is proportional to m^* (effective mass of electron/exciton) and inversely related to mobility factor (B) as illustrated in figure- 7.9(c). . It is observed that for Cr doped PrFeO_3 the value of m^* is small as compared to that of pure PrFeO_3 sample, which signifies the increase in the mobility (B) of the electron/exciton.

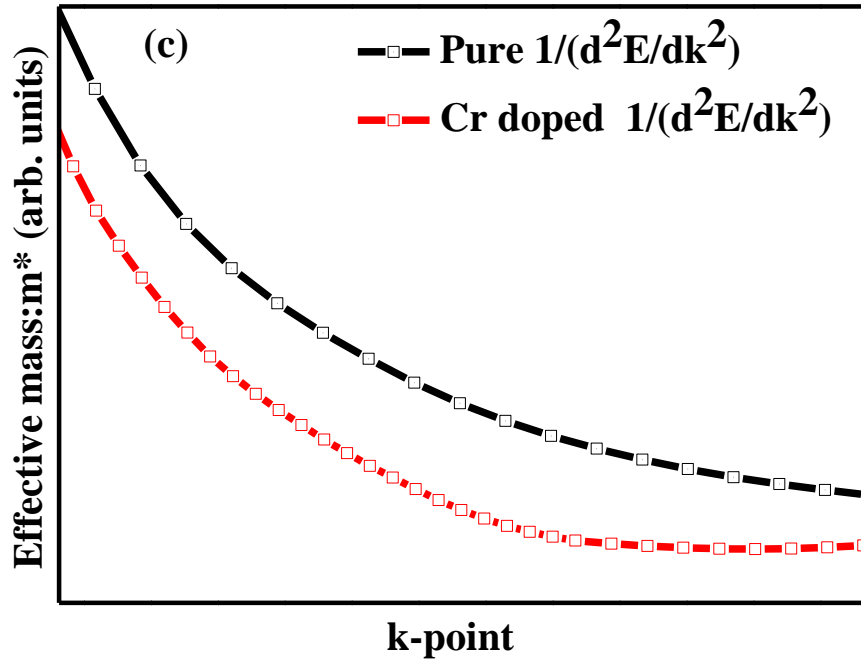


Figure-7.11(c): Variation of $1/d^2E/dk^2$ (a quantity proportional to effective mass) for pure and Cr doped PrFeO_3 between R and Γ k points (near band gap region).

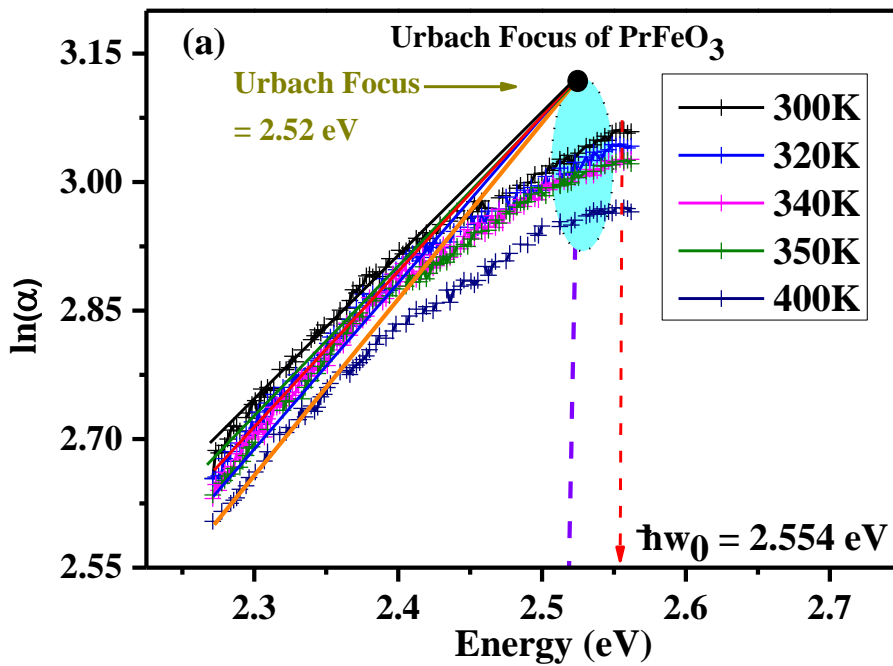


Figure-7.12(a): The estimated values of Urbach focus for pure PrFeO_3 .

Hence, it seems that the mobility factor (B) prevails over the energy fluctuations for Cr doped sample and for $D/B \gg 1$ for pure

PrFeO₃; possibly due to very high value of EPC or less mobility of exciton, which leads to localization or Gaussian line shape of exciton. On the other hand, less than one value of the ratio D/B is possibly due to decrease in EPC or increase in mobility of exciton for Cr doped system, which may leads to delocalization or Lorentzian line shape of exciton.

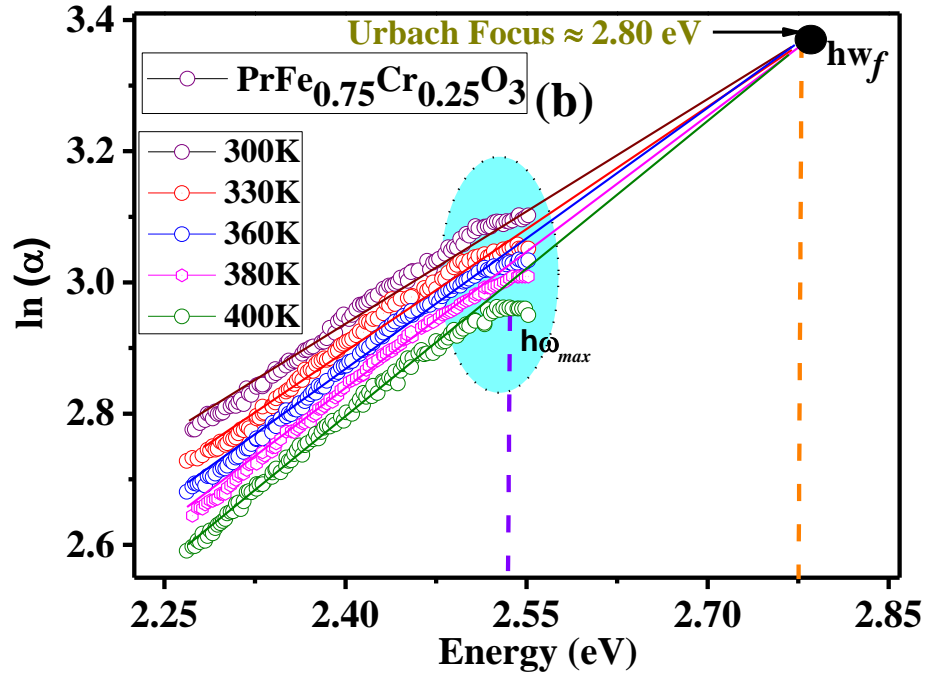


Figure-7.12: The estimated values of Urbach focus for pure PrFeO₃ (a) and 25% Cr doped PrFeO₃ (b). The relatively lower value of Urbach focus (hw_F) than that of hw_{max} is a signature of exciton localization (figure-2(a)) while vice-versa is true for delocalization (figure-7.12(b)).

Further, M.V. Kurik[98] have discussed a way to examine the signature for the exciton localization/delocalization by using optical absorption spectroscopy in terms of Urbach focus. As discussed by Kurik *et al.* [98] that the relatively higher value of Urbach focus (hw_F) than that of hw_{max} is a signature of exciton localization while vice-versa holds for exciton delocalization[98] (see figure-7.11).

Keeping this in view, we have estimated the value of Urbach focuses[99] for pure and Cr doped samples. The representative data for pure and 25% Cr doped PrFeO₃ is shown in figure-7.11 (a) &(b). The

estimated values of Urbach focus for pure and Cr doped PrFeO_3 is 2.52 eV and 2.80 eV respectively. It seems from the figure that in pure PrFeO_3 excitons are highly localized, whereas, in 25% Cr doped PrFeO_3 sample gives a signature of exciton delocalization. These results show the excellent consistency with the first principle calculation results and have been published in the literature[142].

7.4 Conclusion

A detailed investigations on the exciton line shapes, charge-neutral $d-d$ transitions, magneto-elastic properties and scaling of super-exchange interactions as a function of sintering temperature have been done. The deviation from expected anharmonic behavior in temperature-dependent Raman shift has been understood by invoking the Balkanski model for three phonon process. The evaluation of results suggest that the ferrimagnetic transition temperature has a strong dependency on sintering temperature, which has been realized in terms of systematic scaling in Fe-O-Fe bond angles and enhancement in the Goodenough-Kanamori-Anderson coupling with oxygen vacancies. The improvement in these exchange interactions is also consistent with the formation of Fe^{2+} ions, which may enhances the Fe^{2+} -O- Fe^{3+} interactions. The formation of near Gaussian exciton line shapes in high temperature sintered samples has been understood in terms of enhancement in the electron-phonon coupling/EPC, which is in good agreement with the increase in the width of crystal field $d-d$ transitions and asymmetry observed in Raman line shapes. Present investigations suggest that in case of GaFeO_3 the oxygen non-stoichiometry is very suitable route to enhance the electron-lattice and spin-lattice coupling for applications.

Chapter 8

Conclusions and future perspectives

This chapter summarizes the results of the present research work with concluding remarks. The possible future scope of present study has also been discussed.

8.1 Conclusion

❖ The detailed analysis of structural, optical and electronic properties have been studied for $\text{PrFe}_{1-x}\text{Cr}_x\text{O}_3$ system. The optical properties such as optical band gap and electronic disorder term (Urbach energy) of prepared series of samples have been examined in detail. Further, OAS has been used to probe the origin of dielectric loss in prepared series of samples. The detailed analysis of density of states and band structure is also provided using WIEN 2K code.

❖ A systematic correlation between crystallographic strain, Raman line width, disordered parameter (σ) and Urbach energy have been studied in detail. The systematic correlation between the aforementioned parameters have been observed, which implies that structural disorder affects phonons as well as electronic states of the system.

❖ Further, the possible origin of orbital facilitated Raman modes in orthorhombic perovskite $\text{PrFe}_{1-x}\text{Cr}_x\text{O}_3$ has been investigated using resonance Raman spectroscopy and first principle DFT calculations. These results establish $\text{PrFe}_{1-x}\text{Cr}_x\text{O}_3$ as a model compound for research on electron-phonon interactions in strongly correlated complex systems and show that Franck-Condon scattering in complex solids is not limited to Jahn-Teller active compounds.

❖ The origin of natural and external magnetic field induced polar order have been explained in terms of displacements of Pr atoms and strong SPC, which is in excellent conformance with the neutron gamma Dopplerimetry experiments. The origin of magneto-dielectric coupling

has been explained in terms of rotation of spin coupled Fe-orbitals under the influence of magnetic field as clear from the magnetic field dependent Raman spectral analysis. As a final remark, the present study strongly reveals that the intrinsic magneto-dielectric effect can be realized in strongly correlated compounds that contract/expands in response to an externally applied magnetic field and such materials could have immense potential applications in data storage devices.

❖ The reorientation of spin coupled Cr/Fe-orbitals under the influence of magnetic field was proposed as the mechanism responsible for the compression or expansion of material (*i.e.* magnetostriction) and ultimately for the observed intrinsic polar order at room temperature.

❖ The DRS (diffuse reflectance spectroscopy) has been used to probe the defect states in wide band gap materials.

❖ The evaluation of results suggest that the ferrimagnetic transition temperature has a strong dependency on sintering temperature, which has been realized in terms of systematic scaling in Fe-O-Fe bond angles and enhancement in the Goodenough-Kanamori-Anderson coupling with oxygen vacancies. These investigations suggest that in case of GaFeO₃, the oxygen non-stoichiometry is very suitable route to enhance the spin-lattice coupling for applications purpose.

Ultimately, magnetodielectric material (PrFe_{0.50}Cr_{0.50}O₃) has been synthesised which shows MD effect at room temperature, with a low or moderate magnetic field. The intrinsic MD effect has been evidenced in terms of magnetic field dependent red/blue shifting of Raman modes and the mechanism for observed MD phenomenon has been understood in terms of reorientation of spin-coupled transition metal orbitals. Our analysis reveals that MD effect can be realized in strongly correlated compounds that have scope to shrink/expand in response to an externally applied magnetic field.

8.2 Future Perspectives

- ❖ In this work, the structural, optical, dielectric, magneto-dielectric and vibrational properties of $\text{PrFe}_{1-x}\text{Cr}_x\text{O}_3$ and GaFeO_3 have been studied. This opens the possibilities of future research scope in these materials. Some of the experiments/studies that can be considered as steps of future research scope for these systems, are mentioned below.
- ❖ The intrinsic nature of observed MD effect can be further verified through magnetic field dependent non-electrical measurement techniques like XRD, XANES and DRS.
- ❖ The influence of defect on magneto-dielectric, magneto-elastic and magneto-optical properties still remain to be examined.
- ❖ As a future scope, the fundamental works such as temperature dependent spin dynamics, neutron diffraction studies can be done to understand the origin of magnetic phases exhibited by these materials should be explored.
- ❖ The effect of rare earth atoms delocalization on the natural and magnetic field induced polar order on $\text{RFe}_{0.50}\text{Cr}_{0.50}\text{O}_3$ samples is still remains to be examined.
- ❖ It would be interesting to grow thin films of these samples to explore their structural, electronic, optical, and magnetic properties and compare to results of this work such as presence high net magnetic moment, nature of $d-d$ transitions, magneto-elastic properties and variation of band gap as a function of doping.

References

- [1] N. Spaldin, Multiferroics beyond electric-field control of magnetism, *Proceedings of the Royal Society A: Mathematical, Physical and Engineering Sciences*. 476 (2020) 20190542. <https://doi.org/10.1098/rspa.2019.0542>.
- [2] W. Eerenstein, N.D. Mathur, J.F. Scott, Multiferroic and magnetoelectric materials, *Nature*. 442 (2006) 759–765. <https://doi.org/10.1038/nature05023>.
- [3] N.A. Spaldin, Multiferroics: Past, present, and future, *MRS Bulletin*. 42 (2017) 385–390. <https://doi.org/10.1557/mrs.2017.86>.
- [4] P. Yogi, S.K. Saxena, S. Mishra, H.M. Rai, R. Late, V. Kumar, B. Joshi, P.R. Sagdeo, R. Kumar, Interplay between phonon confinement and Fano effect on Raman line shape for semiconductor nanostructures: Analytical study, *Solid State Communications*. 230 (2016) 25–29. <https://doi.org/10.1016/j.ssc.2016.01.013>.
- [5] N.A. Hill, Why Are There so Few Magnetic Ferroelectrics?, *J. Phys. Chem. B*. 104 (2000) 6694–6709. <https://doi.org/10.1021/jp000114x>.
- [6] X.S. Xu, T.V. Brinzari, S. Lee, Y.H. Chu, L.W. Martin, A. Kumar, S. McGill, R.C. Rai, R. Ramesh, V. Gopalan, S.W. Cheong, J.L. Musfeldt, Optical properties and magnetochromism in multiferroic BiFeO₃, *Phys. Rev. B*. 79 (2009) 134425. <https://doi.org/10.1103/PhysRevB.79.134425>.
- [7] F. Mushtaq, H. Torlakcik, C. Steuer, M. Hoop, E. Siringil, X. Marti, G. Limburg, P. Stipp, B. Nelson, S. Pané, Magnetoelectrically Driven Catalytic Degradation of Organics, *Advanced Materials*. 31 (2019) 1901378. <https://doi.org/10.1002/adma.201901378>.
- [8] E. Mohammed, A. Assaj, P. Patil, Dr.Y. Chaudhari, P. Jagtap, S. Bendre, GMR Materials: A New Generation of Miniaturized Technology, *IOSR Journal of Applied Physics*. 5 (2013) 76–81. <https://doi.org/10.9790/4861-0517681>.
- [9] H.M. Rai, R. Late, S.K. Saxena, V. Mishra, R. Kumar, P.R. Sagdeo, Archana Sagdeo, Room temperature magnetodielectric studies on Mn-doped LaGaO₃, *Materials Research Express*. 2 (2015) 096105.
- [10] T. Kimura, S. Kawamoto, I. Yamada, M. Azuma, M. Takano, Y. Tokura, Magnetocapacitance effect in multiferroic BiMnO₃, *Phys. Rev. B*. 67 (2003) 180401. <https://doi.org/10.1103/PhysRevB.67.180401>.
- [11] I.A. Dekker, W.A.C. Nieuwveld, A capacitor memory for an analogue computer, *Applied Scientific Research, Section B*. 11 (1964) 247–254. <https://doi.org/10.1007/BF02922005>.
- [12] A. Kumar, S. Umrao, P.R. Sagdeo, Orbital facilitated charge transfer originated phonon mode in Cr-substituted PrFeO₃: A brief Raman study, *Journal of Raman Spectroscopy*. n/a (2020). <https://doi.org/10.1002/jrs.5894>.

- [13] X. Li, C. Tang, M. Ai, L. Dong, Z. Xu, Controllable Synthesis of Pure-Phase Rare-Earth Orthoferrites Hollow Spheres with a Porous Shell and Their Catalytic Performance for the CO + NO Reaction, *Chemistry of Materials*. 22 (2010) 4879–4889. <https://doi.org/10.1021/cm101419w>.
- [14] C.M. Kavanagh, R.J. Goff, A. Daoud-Aladine, P. Lightfoot, F.D. Morrison, Magnetically Driven Dielectric and Structural Behavior in Bi_{0.5}La_{0.5}FeO₃, *Chemistry of Materials*. 24 (2012) 4563–4571. <https://doi.org/10.1021/cm302513q>.
- [15] M. Sivakumar, A. Gedanken, D. Bhattacharya, I. Brukental, Y. Yeshurun, W. Zhong, Y.W. Du, I. Felner, I. Nowik, Sonochemical Synthesis of Nanocrystalline Rare Earth Orthoferrites Using Fe(CO)₅ Precursor, *Chemistry of Materials*. 16 (2004) 3623–3632. <https://doi.org/10.1021/cm049345x>.
- [16] P. Vaqueiro, M.A. López-Quintela, Influence of Complexing Agents and pH on Yttrium–Iron Garnet Synthesized by the Sol–Gel Method, *Chemistry of Materials*. 9 (1997) 2836–2841. <https://doi.org/10.1021/cm970165f>.
- [17] S. Krohns, P. Lunkenheimer, S. Meissner, A. Reller, B. Gleich, A. Rathgeber, T. Gaugler, H.U. Buhl, D.C. Sinclair, A. Loidl, The route to resource-efficient novel materials, *Nature Materials*. 10 (2011) nmat3180. <https://doi.org/10.1038/nmat3180>.
- [18] A. Sagdeo, K. Gautam, P.R. Sagdeo, M.N. Singh, S.M. Gupta, A.K. Nigam, R. Rawat, A.K. Sinha, H. Ghosh, T. Ganguli, A. Chakrabarti, Large dielectric permittivity and possible correlation between magnetic and dielectric properties in bulk BaFeO_{3-δ}, *Appl. Phys. Lett.* 105 (2014) 042906. <https://doi.org/10.1063/1.4892064>.
- [19] P.R. Sagdeo, S. Anwar, N.P. Lalla, Strain induced coexistence of monoclinic and charge ordered phases in La_{1-x}CaxMnO₃, *Phys. Rev. B*. 74 (2006) 214118. <https://doi.org/10.1103/PhysRevB.74.214118>.
- [20] H. Mohan Rai, S. K. Saxena, V. Mishra, A. Sagdeo, P. Rajput, R. Kumar, P. R. Sagdeo, Observation of room temperature magnetodielectric effect in Mn-doped lanthanum gallate and study of its magnetic properties, *Journal of Materials Chemistry C*. 4 (2016) 10876–10886. <https://doi.org/10.1039/C6TC03641D>.
- [21] M.K. Warshi, A. Kumar, P.R. Sagdeo, Design and development of a fully automated experimental setup for in-situ temperature dependent magneto-dielectric measurements, *Measurement Science and Technology*. (2019). <http://iopscience.iop.org/10.1088/1361-6501/ab387e>.
- [22] D. Khomskii, Classifying Multiferroics: Mechanisms and Effects, *Physics*. 2 (2009). <https://doi.org/10.1103/Physics.2.20>.
- [23] G. Yuan, S. Or, Multiferroicity in polarized single-phase Bi_{0.875}Sm_{0.125}FeO₃ ceramics, *Journal of Applied Physics*. 100 (2006) 024109–024109. <https://doi.org/10.1063/1.2220642>.
- [24] H. Niu, M.J. Pitcher, A.J. Corkett, S. Ling, P. Mandal, M. Zanella, K. Dawson, P. Stamenov, D. Batuk, A.M. Abakumov, C.L. Bull, R.I. Smith, C.A. Murray, S.J. Day, B. Slater, F. Cora, J.B.

- Claridge, M.J. Rosseinsky, Room Temperature Magnetically Ordered Polar Corundum GaFeO₃ Displaying Magnetoelectric Coupling, *J. Am. Chem. Soc.* 139 (2017) 1520–1531. <https://doi.org/10.1021/jacs.6b11128>.
- [25] T. Katayama, S. Yasui, T. Osakabe, Y. Hamasaki, M. Itoh, Ferrimagnetism and Ferroelectricity in Cr-Substituted GaFeO₃ Epitaxial Films, *Chem. Mater.* 30 (2018) 1436–1441. <https://doi.org/10.1021/acs.chemmater.8b00144>.
- [26] S. Basu, R. Singh, A. Das, T. Roy, A. Chakrabarti, A.K. Nigam, S.N. Jha, D. Bhattacharyya, Temperature Dependent EXAFS Study of Chromium-Doped GaFeO₃ at Gallium and Iron Edges, *J. Phys. Chem. C.* 119 (2015) 2029–2037. <https://doi.org/10.1021/jp508103x>.
- [27] C. Lefevre, F. Roulland, A. Thomasson, C. Meny, F. Porcher, G. André, N. Viart, Magnetic and Polar Properties' Optimization in the Magnetoelectric Ga_{2-x}Fe_xO₃ Compounds, *J. Phys. Chem. C.* 117 (2013) 14832–14839. <https://doi.org/10.1021/jp403733b>.
- [28] M. Fiebig, T. Lottermoser, D. Meier, M. Trassin, The evolution of multiferroics, *Nature Reviews Materials.* 1 (2016) 16046. <https://doi.org/10.1038/natrevmats.2016.46>.
- [29] A.B. Harris, T. Yildirim, A. Aharony, O. Entin-Wohlman, Towards a microscopic model of magnetoelectric interactions in Ni₃V₂O₈, *Phys. Rev. B.* 73 (2006) 184433. <https://doi.org/10.1103/PhysRevB.73.184433>.
- [30] C. Wang, G.-C. Guo, L. He, Ferroelectricity Driven by the Noncentrosymmetric Magnetic Ordering in Multiferroic TbMn₂O₅: A First-Principles Study, *Phys. Rev. Lett.* 99 (2007) 177202. <https://doi.org/10.1103/PhysRevLett.99.177202>.
- [31] N. Hu, C. Lu, Z. Xia, R. Xiong, P. Fang, J. Shi, J.-M. Liu, Multiferroicity and Magnetoelectric Coupling in TbMnO₃ Thin Films, *ACS Appl. Mater. Interfaces.* 7 (2015) 26603–26607. <https://doi.org/10.1021/acsami.5b08091>.
- [32] W. Eerenstein, N.D. Mathur, J.F. Scott, Multiferroic and magnetoelectric materials, *Nature.* 442 (2006) 759–765. <https://doi.org/10.1038/nature05023>.
- [33] U. Chowdhury, S. Goswami, A. Roy, S. Rajput, A.K. Mall, R. Gupta, S.D. Kaushik, V. Siruguri, S. Saravanakumar, S. Israel, R. Saravanan, A. Senyshyn, T. Chatterji, J.F. Scott, A. Garg, D. Bhattacharya, Origin of ferroelectricity in orthorhombic LuFeO₃, *Phys. Rev. B.* 100 (2019) 195116. <https://doi.org/10.1103/PhysRevB.100.195116>.
- [34] Y. Yamasaki, S. Miyasaka, Y. Kaneko, J.-P. He, T. Arima, Y. Tokura, Magnetic Reversal of the Ferroelectric Polarization in a Multiferroic Spinel Oxide, *Phys. Rev. Lett.* 96 (2006) 207204. <https://doi.org/10.1103/PhysRevLett.96.207204>.
- [35] G. Lawes, A.B. Harris, T. Kimura, N. Rogado, R.J. Cava, A. Aharony, O. Entin-Wohlman, T. Yildirim, M. Kenzelmann, C. Broholm, A.P. Ramirez, Magnetically Driven Ferroelectric Order in Ni₃V₂O₈, *Phys. Rev. Lett.* 95 (2005) 087205. <https://doi.org/10.1103/PhysRevLett.95.087205>.

- [36] J.-H. Lee, Y.K. Jeong, J.H. Park, M.-A. Oak, H.M. Jang, J.Y. Son, J.F. Scott, Spin-Canting-Induced Improper Ferroelectricity and Spontaneous Magnetization Reversal in SmFeO_3 , *Phys. Rev. Lett.* 107 (2011) 117201. <https://doi.org/10.1103/PhysRevLett.107.117201>.
- [37] V.S. Bhadram, B. Rajeswaran, A. Sundaresan, C. Narayana, Spin-phonon coupling in multiferroic RCrO_3 (R=Y, Lu, Gd, Eu, Sm): A Raman study, *EPL*. 101 (2013) 17008. <https://doi.org/10.1209/0295-5075/101/17008>.
- [38] K. Dey, A. Indra, S. Mukherjee, S. Majumdar, J. Stremper, O. Fabelo, E. Mossou, T. Chatterji, S. Giri, Natural ferroelectric order near ambient temperature in the orthoferrite HoFeO_3 , *Phys. Rev. B*. 100 (2019) 214432. <https://doi.org/10.1103/PhysRevB.100.214432>.
- [39] J.Y. Yang, X.D. Shen, V. Pomjakushin, L. Keller, E. Pomjakushina, Y.W. Long, M. Kenzelmann, Characterization of magnetic symmetry and electric polarization of $\text{YCr}_0.5\text{Fe}_0.5\text{O}_3$, *Phys. Rev. B*. 101 (2020) 014415. <https://doi.org/10.1103/PhysRevB.101.014415>.
- [40] B. Rajeswaran, D.I. Khomskii, A.K. Zvezdin, C.N.R. Rao, A. Sundaresan, Field-induced polar order at the Néel temperature of chromium in rare-earth orthochromites: Interplay of rare-earth and Cr magnetism, *Phys. Rev. B*. 86 (2012) 214409. <https://doi.org/10.1103/PhysRevB.86.214409>.
- [41] S.N. Ruddlesden, P. Popper, The compound $\text{Sr}_2\text{Ti}_2\text{O}_7$ and its structure, *Acta Crystallographica*. 11 (1958) 54–55. <https://doi.org/10.1107/S0365110X58000128>.
- [42] A.R. Chakhmouradian, P.M. Woodward, Celebrating 175 years of perovskite research: a tribute to Roger H. Mitchell, *Physics and Chemistry of Minerals*. 41 (2014) 387–391. <https://doi.org/10.1007/s00269-014-0678-9>.
- [43] V.M. Goldschmidt, *Die Gesetze der Krystallochemie, Naturwissenschaften*. 14 (1926) 477–485. <https://doi.org/10.1007/BF01507527>.
- [44] A. Kumar, V. Mishra, M. Warshi, A. Sati, A. Sagdeo, R. Kumar, P. R. Sagdeo, Strain Induced Disordered Phonon Modes in Cr doped PrFeO_3 , 2019. <https://doi.org/10.1088/1361-648X/ab1195>.
- [45] M.C. Weber, M. Guennou, H.J. Zhao, J. Íñiguez, R. Vilarinho, A. Almeida, J.A. Moreira, J. Kreisel, Raman spectroscopy of rare-earth orthoferrites RFeO_3 (R=La, Sm, Eu, Gd, Tb, Dy), *Phys. Rev. B*. 94 (2016) 214103. <https://doi.org/10.1103/PhysRevB.94.214103>.
- [46] W. Chen, M. Mizumaki, H. Seki, M.S. Senn, T. Saito, D. Kan, J.P. Attfield, Y. Shimakawa, A half-metallic A- and B-site-ordered quadruple perovskite oxide $\text{CaCu}_3\text{Fe}_2\text{Re}_2\text{O}_{12}$ with large magnetization and a high transition temperature, *Nature Communications*. 5 (2014) 3909. <https://doi.org/10.1038/ncomms4909>.
- [47] Z. Zhou, L. Guo, H. Yang, Q. Liu, F. Ye, Hydrothermal synthesis and magnetic properties of multiferroic rare-earth orthoferrites,

- Journal of Alloys and Compounds. 583 (2014) 21–31. <https://doi.org/10.1016/j.jallcom.2013.08.129>.
- [48] B.V. Prasad, G.N. Rao, J.W. Chen, D.S. Babu, Colossal dielectric constant in PrFeO₃ semiconductor ceramics, *Solid State Sciences*. 14 (2012) 225–228. <https://doi.org/10.1016/j.solidstatesciences.2011.11.016>.
- [49] A.V. Kimel, A. Kirilyuk, P.A. Usachev, R.V. Pisarev, A.M. Balbashov, T. Rasing, Ultrafast non-thermal control of magnetization by instantaneous photomagnetic pulses, *Nature*. 435 (2005) 655–657. <https://doi.org/10.1038/nature03564>.
- [50] R. Iida, T. Satoh, T. Shimura, K. Kuroda, B.A. Ivanov, Y. Tokunaga, Y. Tokura, Spectral dependence of photoinduced spin precession in DyFeO₃, *Phys. Rev. B*. 84 (2011) 064402. <https://doi.org/10.1103/PhysRevB.84.064402>.
- [51] Magnetic and structural properties of spin-reorientation transitions in orthoferrites, *Journal of Applied Physics*. 101 (2007) 123919. <https://doi.org/10.1063/1.2749404>.
- [52] Y.S. Didosyan, H. Hauser, G.A. Reider, W. Toriser, Fast latching type optical switch, *Journal of Applied Physics*. 95 (2004) 7339–7341. <https://doi.org/10.1063/1.1669350>.
- [53] V.V. Pavlov, A.R. Akbashev, A.M. Kalashnikova, V.A. Rusakov, A.R. Kaul, M. Bayer, R.V. Pisarev, Optical properties and electronic structure of multiferroic hexagonal orthoferrites RFeO₃ (R = Ho, Er, Lu), *Journal of Applied Physics*. 111 (2012) 056105. <https://doi.org/10.1063/1.3693588>.
- [54] S.M. Disseler, J.A. Borchers, C.M. Brooks, J.A. Mundy, J.A. Moyer, D.A. Hillsberry, E.L. Thies, D.A. Tenne, J. Heron, M.E. Holtz, J.D. Clarkson, G.M. Stiehl, P. Schiffer, D.A. Muller, D.G. Schlom, W.D. Ratcliff, Magnetic Structure and Ordering of Multiferroic Hexagonal LuFeO₃, *Phys. Rev. Lett*. 114 (2015) 217602. <https://doi.org/10.1103/PhysRevLett.114.217602>.
- [55] K. Fujita, T. Kawamoto, I. Yamada, O. Hernandez, N. Hayashi, H. Akamatsu, W. Lafargue-Dit-Hauret, X. Rocquefelte, M. Fukuzumi, P. Manuel, A.J. Studer, C.S. Knee, K. Tanaka, LiNbO₃-Type InFeO₃: Room-Temperature Polar Magnet without Second-Order Jahn–Teller Active Ions, *Chem. Mater*. 28 (2016) 6644–6655. <https://doi.org/10.1021/acs.chemmater.6b02783>.
- [56] I. Dzyaloshinsky, A thermodynamic theory of “weak” ferromagnetism of antiferromagnetics, *Journal of Physics and Chemistry of Solids*. 4 (1958) 241–255. [https://doi.org/10.1016/0022-3697\(58\)90076-3](https://doi.org/10.1016/0022-3697(58)90076-3).
- [57] M. Warshi, V. Mishra, V. Mishra, R. Kumar, P. Sagdeo, Possible Origin of Ferromagnetism in Antiferromagnetic Orthorhombic-YFeO₃ : A First-Principles Study, *Ceramics International*. (2018).
- [58] T. Moriya, Anisotropic Superexchange Interaction and Weak Ferromagnetism, *Phys. Rev.* 120 (1960) 91–98. <https://doi.org/10.1103/PhysRev.120.91>.
- [59] C. Zener, Interaction between the d-Shells in the Transition Metals. II. Ferromagnetic Compounds of Manganese with

- Perovskite Structure, *Phys. Rev.* 82 (1951) 403–405. <https://doi.org/10.1103/PhysRev.82.403>.
- [60] H.A. Kramers, L'interaction Entre les Atomes Magnétogènes dans un Cristal Paramagnétique, *Physica.* 1 (1934) 182–192. [https://doi.org/10.1016/S0031-8914\(34\)90023-9](https://doi.org/10.1016/S0031-8914(34)90023-9).
- [61] P.W. Anderson, Antiferromagnetism. Theory of Superexchange Interaction, *Phys. Rev.* 79 (1950) 350–356. <https://doi.org/10.1103/PhysRev.79.350>.
- [62] J.B. Goodenough, A.L. Loeb, Theory of Ionic Ordering, Crystal Distortion, and Magnetic Exchange Due to Covalent Forces in Spinels, *Phys. Rev.* 98 (1955) 391–408. <https://doi.org/10.1103/PhysRev.98.391>.
- [63] E. Granado, A. García, J.A. Sanjurjo, C. Rettori, I. Torriani, F. Prado, R.D. Sánchez, A. Caneiro, S.B. Oseroff, Magnetic ordering effects in the Raman spectra of $\text{La}_{1-x}\text{Mn}_x\text{O}_3$, *Phys. Rev. B.* 60 (1999) 11879–11882. <https://doi.org/10.1103/PhysRevB.60.11879>.
- [64] S. Dugu, K. Kara Mishra, D. Pradhan, S. Kumari, R. S. Katiyar, Coupled phonons and magnetic orderings in GaFeO_3 : Raman and magnetization studies, *Journal of Applied Physics.* 125 (2019) 064101. <https://doi.org/10.1063/1.5072766>.
- [65] A. Sati, A. Kumar, V. Mishra, K. Warshi, A. Sagdeo, S. Anwar, R. Kumar, P.R. Sagdeo, Direct correlation between the band gap and dielectric loss in Hf doped BaTiO_3 , *Journal of Materials Science: Materials in Electronics.* (2019). <https://doi.org/10.1007/s10854-019-01128-z>.
- [66] A. Sati, V. Mishra, A. Kumar, M.K. Warshi, A. Sagdeo, R. Kumar, P.R. Sagdeo, Effect of structural disorder on the electronic and phononic properties of Hf doped BaTiO_3 , *Journal of Materials Science: Materials in Electronics.* (2019). <https://doi.org/10.1007/s10854-019-01281-5>.
- [67] V. Mishra, A. Kumar, A. Sagdeo, P.R. Sagdeo, Comparative structural and optical studies on pellet and powder samples of BaTiO_3 near phase transition temperature, *Ceramics International.* 46 (2020) 3250–3256. <https://doi.org/10.1016/j.ceramint.2019.10.030>.
- [68] M.K. Warshi, A. Kumar, A. Sati, S. Thota, K. Mukherjee, A. Sagdeo, P.R. Sagdeo, Cluster Glass Behavior in Orthorhombic SmFeO_3 Perovskite: Interplay between Spin Ordering and Lattice Dynamics, *Chem. Mater.* (2020). <https://doi.org/10.1021/acs.chemmater.9b04703>.
- [69] S. Upasen, P. Batocchi, F. Mauvy, A. Slodczyk, P. Colomban, Chemical and structural stability of $\text{La}_{0.6}\text{Sr}_{0.4}\text{Co}_{0.2}\text{Fe}_{0.8}\text{O}_{3-\delta}$ ceramic vs. medium/high water vapor pressure, *Ceramics International.* 41 (2015) 14137–14147. <https://doi.org/10.1016/j.ceramint.2015.07.035>.
- [70] S. Huotari, L. Simonelli, C.J. Sahle, M.M. Sala, R. Verbeni, G. Monaco, Temperature dependence of crystal field excitations in CuO , *Journal of Physics: Condensed Matter.* 26 (2014) 165501. <https://doi.org/10.1088/0953-8984/26/16/165501>.

- [71] J.J. Lee, B. Moritz, W.S. Lee, M. Yi, C.J. Jia, A.P. Sorini, K. Kudo, Y. Koike, K.J. Zhou, C. Monney, V. Strocov, L. Patthey, T. Schmitt, T.P. Devereaux, Z.X. Shen, Charge-orbital-lattice coupling effects in the dd excitation profile of one-dimensional cuprates, *Phys. Rev. B.* 89 (2014) 041104. <https://doi.org/10.1103/PhysRevB.89.041104>.
- [72] A.S. Moskvina, A.A. Makhnev, L.V. Nomerovannaya, N.N. Loshkareva, A.M. Balbashov, Interplay of p-d and d-d charge transfer transitions in rare-earth perovskite manganites, *Phys. Rev. B.* 82 (2010) 035106. <https://doi.org/10.1103/PhysRevB.82.035106>.
- [73] Y.E. Perlin, S.I. Klokishner, V.N. Enakii, A.A. Kaminskii, H.S. Bagdasarov, G.A. Bogomolova, D.N. Vylegzhanin, Thermal broadening and shift of the energy levels of TR³⁺ Ions in Crystals, *Physica Status Solidi (a)*. 40 (1977) 643–653. <https://doi.org/10.1002/pssa.2210400232>.
- [74] R. Rückamp, E. Benckiser, M.W. Haverkort, H. Roth, T. Lorenz, A. Freimuth, L. Jongen, A. Möller, G. Meyer, P. Reutler, B. Büchner, A. Revcolevschi, S.-W. Cheong, C. Sekar, G. Krabbes, M. Grüniger, Optical study of orbital excitations in transition-metal oxides, *New J. Phys.* 7 (2005) 144. <https://doi.org/10.1088/1367-2630/7/1/144>.
- [75] C. Chen, X. Chen, H. Yu, Y. Shao, Q. Guo, B. Deng, S. Lee, C. Ma, K. Watanabe, T. Taniguchi, J.-G. Park, S. Huang, W. Yao, F. Xia, Symmetry-Controlled Electron–Phonon Interactions in van der Waals Heterostructures, *ACS Nano*. (2018). <https://doi.org/10.1021/acsnano.8b07290>.
- [76] H.-M. Cheng, K.-F. Lin, Hsu, C.-J. Lin, L.-J. Lin, W.-F. Hsieh, Enhanced Resonant Raman Scattering and Electron–Phonon Coupling from Self-Assembled Secondary ZnO Nanoparticles, *J. Phys. Chem. B.* 109 (2005) 18385–18390. <https://doi.org/10.1021/jp0533731>.
- [77] Y. Toyozawa, *Optical Processes in Solids*, Cambridge University Press, 2003.
- [78] D. Paramanik, S. Varma, Raman scattering characterization and electron phonon coupling strength for MeV implanted InP(111), *Journal of Applied Physics*. 101 (2007) 023528. <https://doi.org/10.1063/1.2426972>.
- [79] A.C. Ferrari, Raman spectroscopy of graphene and graphite: Disorder, electron–phonon coupling, doping and nonadiabatic effects, *Solid State Communications*. 143 (2007) 47–57. <https://doi.org/10.1016/j.ssc.2007.03.052>.
- [80] Y. Liao, *Practical Electron Microscopy and Database*: www.globalsino.com/EM/, 2013.
- [81] L. Martín-Carrón, A. de Andrés, Excitations of the orbital order in RMnO₃ manganites: light scattering experiments, *Phys. Rev. Lett.* 92 (2004) 175501. <https://doi.org/10.1103/PhysRevLett.92.175501>.

- [82] G. Kotnana, S. Jammalamadaka, Band gap tuning and orbital mediated electron–phonon coupling in $\text{HoFe}_{1-x}\text{Cr}_x\text{O}_3$ ($0 \leq x \leq 1$), 2015. <https://doi.org/10.1063/1.4931155>.
- [83] A.G. Souza Filho, J.L.B. Faria, I. Guedes, J.M. Sasaki, P.T.C. Freire, V.N. Freire, J. Mendes Filho, M.M. Xavier, F.A.O. Cabral, J.H. de Araújo, J.A.P. da Costa, Evidence of magnetic polaronic states in $\text{La}_{0.70}\text{Sr}_{0.30}\text{Mn}_{1-x}\text{Fe}_x\text{O}_3$ manganites, *Phys. Rev. B.* 67 (2003) 052405. <https://doi.org/10.1103/PhysRevB.67.052405>.
- [84] M. Osada, M. Kakihana, S. Wada, T. Noma, W.-S. Cho, Broken symmetry in low-temperature BaTiO_3 phases: Strain effects probed by Raman scattering, *Appl. Phys. Lett.* 75 (1999) 3393–3395. <https://doi.org/10.1063/1.125304>.
- [85] P.-Y. Chen, C.-S. Chen, C.-S. Tu, P.-H. Chen, J. Anthoniappen, Effects of texture on microstructure, Raman vibration, and ferroelectric properties in $92.5\%(\text{Bi}_{0.5}\text{Na}_{0.5})\text{TiO}_3-7.5\%\text{BaTiO}_3$ ceramics, *Journal of the European Ceramic Society.* 36 (2016) 1613–1622. <https://doi.org/10.1016/j.jeurceramsoc.2016.01.038>.
- [86] M. El Marssi, F. Le Marrec, I.A. Lukyanchuk, M.G. Karkut, Ferroelectric transition in an epitaxial barium titanate thin film: Raman spectroscopy and x-ray diffraction study, *Journal of Applied Physics.* 94 (2003) 3307–3312. <https://doi.org/10.1063/1.1596720>.
- [87] G. Gouadec, P. Colomban, Raman spectroscopy of nanostructures and nanosized materials, *Journal of Raman Spectroscopy.* 38 (2007) 598–603. <https://doi.org/10.1002/jrs.1749>.
- [88] R. Shuker, R.W. Gammon, Raman-Scattering Selection-Rule Breaking and the Density of States in Amorphous Materials, *Phys. Rev. Lett.* 25 (1970) 222–225. <https://doi.org/10.1103/PhysRevLett.25.222>.
- [89] N. Fukata, Impurity Doping in Silicon Nanowires, *Advanced Materials.* 21 (2009) 2829–2832. <https://doi.org/10.1002/adma.200900376>.
- [90] A.C. Ferrari, J. Robertson, Interpretation of Raman spectra of disordered and amorphous carbon, *Phys. Rev. B.* 61 (2000) 14095–14107. <https://doi.org/10.1103/PhysRevB.61.14095>.
- [91] A.C. Ferrari, Raman spectroscopy of graphene and graphite: Disorder, electron–phonon coupling, doping and nonadiabatic effects, *Solid State Communications.* 143 (2007) 47–57. <https://doi.org/10.1016/j.ssc.2007.03.052>.
- [92] A. Sergeev, M.Yu. Reizer, V. Mitin, Deformation Electron-Phonon Coupling in Disordered Semiconductors and Nanostructures, *Phys. Rev. Lett.* 94 (2005) 136602. <https://doi.org/10.1103/PhysRevLett.94.136602>.
- [93] J. Bhosale, A.K. Ramdas, A. Burger, A. Muñoz, A.H. Romero, M. Cardona, R. Lauck, R.K. Kremer, Temperature dependence of band gaps in semiconductors: Electron-phonon interaction, *Phys. Rev. B.* 86 (2012) 195208. <https://doi.org/10.1103/PhysRevB.86.195208>.
- [94] A. Bianconi, Ugo Fano and Shape Resonances, (2002). <https://doi.org/10.1063/1.1536357>.

- [95] J.D. Wiley, D. Thomas, E. Schönherr, A. Breitschwerdt, The absorption edges of GeS and Urbach's rule, *Journal of Physics and Chemistry of Solids*. 41 (1980) 801–807. [https://doi.org/10.1016/0022-3697\(80\)90091-8](https://doi.org/10.1016/0022-3697(80)90091-8).
- [96] I. Bonalde, E. Medina, M. Rodríguez, S.M. Wasim, G. Marín, C. Rincón, A. Rincón, C. Torres, Urbach tail, disorder, and localized modes in ternary semiconductors, *Phys. Rev. B*. 69 (2004) 195201. <https://doi.org/10.1103/PhysRevB.69.195201>.
- [97] F. Urbach, The Long-Wavelength Edge of Photographic Sensitivity and of the Electronic Absorption of Solids, *Phys. Rev.* 92 (1953) 1324–1324. <https://doi.org/10.1103/PhysRev.92.1324>.
- [98] M.V. Kurik, Urbach rule, *Physica Status Solidi Applied Research*. 8 (1971) 9–45. <https://doi.org/10.1002/pssa.2210080102>.
- [99] V. Mishra, A. Sagdeo, V. Kumar, M. Warshi, H.M. Rai, S. Saxena, D. Roy, V. Mishra, R. Kumar, P. Sagdeo, Electronic and optical properties of BaTiO₃ across tetragonal to cubic phase transition: An experimental and theoretical investigation, 2017. <https://doi.org/10.1063/1.4997939>.
- [100] G.D. Cody, T. Tiedje, B. Abeles, B. Brooks, Y. Goldstein, Disorder and the Optical-Absorption Edge of Hydrogenated Amorphous Silicon, *Phys. Rev. Lett.* 47 (1981) 1480–1483. <https://doi.org/10.1103/PhysRevLett.47.1480>.
- [101] A.V. Subashiev, O. Semyonov, Z. Chen, S. Luryi, Urbach tail studies by luminescence filtering in moderately doped bulk InP, *Appl. Phys. Lett.* 97 (2010) 181914. <https://doi.org/10.1063/1.3510470>.
- [102] A. Kumar, M.K. Warshi, V. Mishra, S.K. Saxena, R. Kumar, P.R. Sagdeo, Strain control of Urbach energy in Cr-doped PrFeO₃, *Appl. Phys. A*. 123 (2017) 576. <https://doi.org/10.1007/s00339-017-1186-9>.
- [103] I.A. Weinstein, A.F. Zatspein, Modified Urbach's rule and frozen phonons in glasses, *Physica Status Solidi (c)*. 1 (2004) 2916–2919. <https://doi.org/10.1002/pssc.200405416>.
- [104] K. Noba, Y. Kayanuma, Urbach tail for ferroelectric materials with an order-disorder-type phase transition, *Phys. Rev. B*. 60 (1999) 4418–4421. <https://doi.org/10.1103/PhysRevB.60.4418>.
- [105] P. Van Mieghem, Theory of band tails in heavily doped semiconductors, *Rev. Mod. Phys.* 64 (1992) 755–793. <https://doi.org/10.1103/RevModPhys.64.755>.
- [106] A.J. Millis, Lattice effects in magnetoresistive manganese perovskites, *Nature*. 392 (1998) 147–150. <https://doi.org/10.1038/32348>.
- [107] G. Burns, B.A. Scott, Lattice Modes in Ferroelectric Perovskites: PbTiO₃, *Phys. Rev. B*. 7 (1973) 3088–3101. <https://doi.org/10.1103/PhysRevB.7.3088>.
- [108] M.K. Warshi, A. Kumar, V. Mishra, A. Sati, A. Sagdeo, R. Kumar, P.R. Sagdeo, Effect of self-doping on the charge state of Fe ions and crystal field transitions in YFeO₃: Experiments and theory, *Journal of Applied Physics*. 125 (2019) 204101. <https://doi.org/10.1063/1.5092736>.

- [109] M.K. Warshi, A. Kumar, A. Sati, S. Thota, K. Mukherjee, A. Sagdeo, P.R. Sagdeo, Cluster Glass Behavior in Orthorhombic SmFeO₃ Perovskite: Interplay between Spin Ordering and Lattice Dynamics, *Chem. Mater.* 32 (2020) 1250–1260. <https://doi.org/10.1021/acs.chemmater.9b04703>.
- [110] M.K. Warshi, A. Kumar, P.R. Sagdeo, Design and development of a fully automated experimental setup for in situ temperature dependent magneto-dielectric measurements, *Meas. Sci. Technol.* 30 (2019) 125901. <https://doi.org/10.1088/1361-6501/ab387e>.
- [111] S. Manipatruni, D. Nikonov, C.-C. Lin, T. Gosavi, H. Liu, B. Prasad, Y. Lin Huang, E. Bonturim, R. Ramesh, I. Young, Scalable energy-efficient magnetoelectric spin–orbit logic, *Nature*. 565 (2019) 35–42. <https://doi.org/10.1038/s41586-018-0770-2>.
- [112] G. Kotnana, S. Jammalamadaka, Band gap tuning and orbital mediated electron–phonon coupling in HoFe_{1-x}Cr_xO₃ (0 ≤ x ≤ 1), *Journal of Applied Physics*. 118 (2015) 124101. <https://doi.org/10.1063/1.4931155>.
- [113] G. Kotnana, V.G. Sathe, S.N. Jammalamadaka, Spin–phonon coupling in HoCr_{1-x}Fe_xO₃ (x = 0 and 0.5) compounds, *Journal of Raman Spectroscopy*. 49 (2018) 764–770. <https://doi.org/10.1002/jrs.5332>.
- [114] J. Andreasson, J. Holmlund, C.S. Knee, M. Käll, L. Börjesson, S. Naler, J. Bäckström, M. Rübhausen, A.K. Azad, S.-G. Eriksson, Franck-Condon higher order lattice excitations in the LaFe_{1-x}Cr_xO₃ (x=0, 0.1, 0.5, 0.9, 1.0) perovskites due to Fe-Cr charge transfer effects, *Phys. Rev. B*. 75 (2007) 104302. <https://doi.org/10.1103/PhysRevB.75.104302>.
- [115] L.H. Yin, J. Yang, R.R. Zhang, J.M. Dai, W.H. Song, Y.P. Sun, Multiferroicity and magnetoelectric coupling enhanced large magnetocaloric effect in DyFe_{0.5}Cr_{0.5}O₃, *Appl. Phys. Lett.* 104 (2014) 032904. <https://doi.org/10.1063/1.4862665>.
- [116] J.F. Wager, Real- and reciprocal-space attributes of band tail states, *AIP Advances*. 7 (2017) 125321. <https://doi.org/10.1063/1.5008521>.
- [117] F. Messina, E. Vella, M. Cannas, R. Boscaino, Evidence of Delocalized Excitons in Amorphous Solids, *Phys. Rev. Lett.* 105 (2010) 116401. <https://doi.org/10.1103/PhysRevLett.105.116401>.
- [118] K. Nakamura, M. Kitajima, Real-time Raman measurements of graphite under Ar⁺ irradiation, *Applied Physics Letters*. 59 (1998) 1550. <https://doi.org/10.1063/1.106279>.
- [119] J. Huso, H. Che, D. Thapa, A. Canul, M.D. McCluskey, L. Bergman, Phonon dynamics and Urbach energy studies of MgZnO alloys, *Journal of Applied Physics*. 117 (2015) 125702. <https://doi.org/10.1063/1.4916096>.
- [120] A. Kumar, V. Mishra, M.K. Warshi, A. Sati, A. Sagdeo, R. Kumar, P.R. Sagdeo, Strain induced disordered phonon modes in Cr doped PrFeO₃, *Journal of Physics: Condensed Matter*. 31 (2019) 275602. <https://doi.org/10.1088/1361-648x/ab1195>.
- [121] A. Kumar, M.K. Warshi, V. Mishra, A. Sati, S. Banik, A. Sagdeo, R. Kumar, P.R. Sagdeo, Optical spectroscopy: An effective tool to

- probe the origin of dielectric loss in Cr doped PrFeO₃, *Ceramics International*. 45 (2019) 8585–8592. <https://doi.org/10.1016/j.ceramint.2019.01.177>.
- [122] J. Yuan, Z.-L. Hou, H.-J. Yang, Y. Li, Y.-Q. Kang, W.-L. Song, H.-B. Jin, X.-Y. Fang, M.-S. Cao, High dielectric loss and microwave absorption behavior of multiferroic BiFeO₃ ceramic, *Ceramics International*. 39 (2013) 7241–7246. <https://doi.org/10.1016/j.ceramint.2013.01.068>.
- [123] A. Sagdeo, A. Nagwanshi, P. Pokhriyal, A.K. Sinha, P. Rajput, V. Mishra, P.R. Sagdeo, Disappearance of dielectric anomaly in spite of presence of structural phase transition in reduced BaTiO₃: Effect of defect states within the bandgap, *Journal of Applied Physics*. 123 (2018) 161424. <https://doi.org/10.1063/1.5010870>.
- [124] A.K. Jonscher, Dielectric relaxation in solids, *J. Phys. D: Appl. Phys.* 32 (1999) R57. <https://doi.org/10.1088/0022-3727/32/14/201>.
- [125] C. Raptis, Evidence of temperature-defect-induced first-order Raman scattering in pure NaCl crystals, *Phys. Rev. B*. 33 (1986) 1350–1352. <https://doi.org/10.1103/PhysRevB.33.1350>.
- [126] R.T. Harley, J.B. Page, C.T. Walker, Raman Scattering as a Probe of Pure-Crystal Phonons in Tl^+ -Doped Potassium Halides, *Phys. Rev. Lett.* 23 (1969) 922–924. <https://doi.org/10.1103/PhysRevLett.23.922>.
- [127] A. Kumar, A. Sati, V. Mishra, M.K. Warshi, R. Kumar, P.R. Sagdeo, Charge neutral crystal field transitions: A measure of electron–phonon interaction, *Journal of Physics and Chemistry of Solids*. 135 (2019) 109102. <https://doi.org/10.1016/j.jpcs.2019.109102>.
- [128] F.A. Mir, M. Ikram, R. Kumar, Local symmetry breaking in PrFeO₃ thin films and other similar systems after Ni doping: A brief Raman study, *Vibrational Spectroscopy*. 55 (2011) 307–310. <https://doi.org/10.1016/j.vibspec.2010.10.007>.
- [129] J. Andreasson, J. Holmlund, C.S. Knee, M. Käll, L. Börjesson, S. Naler, J. Bäckström, M. Rübhausen, A.K. Azad, S.-G. Eriksson, Franck-Condon higher order lattice excitations in the LaFe_{1-x}Cr_xO₃ (x=0, 0.1, 0.5, 0.9, 1.0) perovskites due to Fe-Cr charge transfer effects, *Phys. Rev. B*. 75 (2007) 104302. <https://doi.org/10.1103/PhysRevB.75.104302>.
- [130] M. Kagaya, K. Yoshida, H. Zen, K. Hachiya, T. Sagawa, H. Ohgaki, Mode-selective phonon excitation in gallium nitride using mid-infrared free-electron laser, *Jpn. J. Appl. Phys.* 56 (2017) 022701. <https://doi.org/10.7567/JJAP.56.022701>.
- [131] A. Benyamini, A. Hamo, S.V. Kusminskiy, F. von Oppen, S. Ilani, Real-space tailoring of the electron–phonon coupling in ultraclean nanotube mechanical resonators, *Nature Physics*. 10 (2014) 151–156. <https://doi.org/10.1038/nphys2842>.
- [132] J.-H. Lee, Y.K. Jeong, J.H. Park, M.-A. Oak, H.M. Jang, J.Y. Son, J.F. Scott, Spin-Canting-Induced Improper Ferroelectricity and Spontaneous Magnetization Reversal in SmFeO₃, *Phys. Rev. Lett.*

<https://doi.org/10.1103/PhysRevLett.107.117201>.

- [133] N. Muniraju, T. Brueckel, Crystal and spin structure and their relation to physical properties in some geometrical and spin spiral multiferroics, in: 2012.
- [134] V. Srinu Bhadram, B. Rajeswaran, A. Sundaresan, C. Narayana, Spin-phonon coupling in multiferroic RCrO₃ (R-Y, Lu, Gd, Eu, Sm): A Raman study, *EPL (Europhysics Letters)*. 101 (2013) 17008. <https://doi.org/10.1209/0295-5075/101/17008>.
- [135] N. Hiraoka, H. Okamura, H. Ishii, I. Jarrige, K.D. Tsuei, Y.Q. Cai, Charge transfer and dd excitations in transition metal oxides, *The European Physical Journal B*. 70 (2009) 157–162. <https://doi.org/10.1140/epjb/e2009-00199-x>.
- [136] J.S. Lee, M.W. Kim, T.W. Noh, Optical excitations of transition-metal oxides under the orbital multiplicity effects, *New Journal of Physics*. 7 (2005) 147–147. <https://doi.org/10.1088/1367-2630/7/1/147>.
- [137] P.S.V. Mocherla, C. Karthik, R. Ubig, M.S. Ramachandra Rao, C. Sudakar, Tunable bandgap in BiFeO₃ nanoparticles: The role of microstrain and oxygen defects, *Appl. Phys. Lett.* 103 (2013) 022910. <https://doi.org/10.1063/1.4813539>.
- [138] A. Kumar, M.K. Warshi, M. Gupta, P.R. Sagdeo, The magneto-elastic and optical properties of multiferroic GaFeO_{3-δ}, *Journal of Magnetism and Magnetic Materials*. 514 (2020) 167210. <https://doi.org/10.1016/j.jmmm.2020.167210>.
- [139] A. Kumar, M.K. Warshi, V. Mishra, S.K. Saxena, R. Kumar, P.R. Sagdeo, Strain control of Urbach energy in Cr-doped PrFeO₃, *Applied Physics A*. 123 (2017) 576. <https://doi.org/10.1007/s00339-017-1186-9>.
- [140] B.D. Cullity, *Elements of X Ray Diffraction*, BiblioBazaar, 2011. <https://books.google.co.in/books?id=Z-98pwAACAAJ>.
- [141] V. Mishra, M.K. Warshi, A. Sati, A. Kumar, V. Mishra, A. Sagdeo, R. Kumar, P.R. Sagdeo, Diffuse reflectance spectroscopy: An effective tool to probe the defect states in wide band gap semiconducting materials, *Materials Science in Semiconductor Processing*. 86 (2018) 151–156. <https://doi.org/10.1016/j.mssp.2018.06.025>.
- [142] A. Kumar, V. Mishra, M.K. Warshi, A. Sati, A. Sagdeo, R. Kumar, P.R. Sagdeo, Possible evidence of delocalized excitons in Cr-doped PrFeO₃: An experimental and theoretical realization, *Journal of Physics and Chemistry of Solids*. 130 (2019) 230–235. <https://doi.org/10.1016/j.jpccs.2019.03.012>.
- [143] H.G. Hecht, The Interpretation of Diffuse Reflectance Spectra, *J Res Natl Bur Stand A Phys Chem*. 80A (1976) 567–583. <https://doi.org/10.6028/jres.080A.056>.
- [144] C.V. RAMAN, K.S. KRISHNAN, A New Type of Secondary Radiation, *Nature*. 121 (1928) 501–502. <https://doi.org/10.1038/121501c0>.

- [145] A.K. Jonscher, Dielectric relaxation in solids, *Journal of Physics D: Applied Physics*. 32 (1999) R57–R70. <https://doi.org/10.1088/0022-3727/32/14/201>.
- [146] D. Griffiths, *Introduction to Electrodynamics*, 2017. <https://doi.org/10.1017/9781108333511>.
- [147] A.K. Jonscher, REVIEW ARTICLE: Dielectric relaxation in solids, *Journal of Physics D Applied Physics*. 32 (1999) R57–R70. <https://doi.org/10.1088/0022-3727/32/14/201>.
- [148] M.K. Warshi, A. Kumar, P.R. Sagdeo, Design and development of a fully automated experimental setup for in situ temperature dependent magneto-dielectric measurements, *Measurement Science and Technology*. 30 (2019) 125901. <https://doi.org/10.1088/1361-6501/ab387e>.
- [149] L. Longobardi, Studies of quantum transitions of magnetic flux in a rf SQUID qubit, PhD Thesis, State University of New York at Stony Brook, 2009.
- [150] H.M. Rai, S.K. Saxena, R. Late, V. Mishra, P. Rajput, A. Sagdeo, R. Kumar, P.R. Sagdeo, Observation of large dielectric permittivity and dielectric relaxation phenomenon in Mn-doped lanthanum gallate, *RSC Adv*. 6 (2016) 26621–26629. <https://doi.org/10.1039/C5RA28074E>.
- [151] A. Sagdeo, K. Gautam, P.R. Sagdeo, M.N. Singh, S.M. Gupta, A.K. Nigam, R. Rawat, A.K. Sinha, H. Ghosh, T. Ganguli, A. Chakrabarti, Large dielectric permittivity and possible correlation between magnetic and dielectric properties in bulk BaFeO₃- δ , *Appl. Phys. Lett.* 105 (2014) 042906. <https://doi.org/10.1063/1.4892064>.
- [152] H.M. Rai, P. Singh, S.K. Saxena, V. Mishra, M.K. Warshi, R. Kumar, P. Rajput, A. Sagdeo, I. Choudhuri, B. Pathak, P.R. Sagdeo, Room-Temperature Magneto-dielectric Effect in LaGa_{0.7}Fe_{0.3}O₃+ γ ; Origin and Impact of Excess Oxygen, *Inorg. Chem*. 56 (2017) 3809–3819. <https://doi.org/10.1021/acs.inorgchem.6b02507>.
- [153] D.C. Koningsberger, R. Prins, *X-ray absorption: Principles, applications, techniques of EXAFS, SEXAFS and XANES*, John Wiley and Sons Inc., New York, NY, United States, 1987. <https://www.osti.gov/biblio/5927479>.
- [154] H. Wadati, A. Chikamatsu, R. Hashimoto, M. Takizawa, H. Kumigashira, A. Fujimori, M. Oshima, M. Lippmaa, M. Kawasaki, H. Koinuma, Temperature-Dependent Soft X-ray Photoemission and Absorption Studies of Charge Disproportionation in La_{1-x}Sr_xFeO₃, *Journal of The Physical Society of Japan - J PHYS SOC JPN*. 75 (2006). <https://doi.org/10.1143/JPSJ.75.054704>.
- [155] V. Komreddy, K. Ensz, H. Nguyen, D.P. Rillema, C.E. Moore, Design, synthesis, and photophysical properties of Re(I) tricarbonyl 1,10-phenanthroline complexes, *Journal of Molecular Structure*. 1223 (2021) 128739. <https://doi.org/10.1016/j.molstruc.2020.128739>.

- [156] P. Paufler, Introduction to XAFS. A Practical Guide to X-ray Absorption Fine Structure Spectroscopy. By Grant Bunker. Pp. viii + 260. Cambridge University Press, 2010. Price (hardback) GBP 40. ISBN-13: 978-0-521-76775-0., Journal of Synchrotron Radiation. 18 (2011) 818. <https://doi.org/10.1107/S0909049511023703>.
- [157] F. De Groot, Core level spectroscopy of solids. CRC Press, Boca Raton, (2008). <https://doi.org/10.1201/9781420008425>.
- [158] Nancy, B. Poojitha, R. Shukla, R. Dhaka, S. Dash, S. Sarkar, S.R. Barman, P.D. Babu, S.C. Sahoo, R.J. Choudhary, S. Saha, A.K. Patra, Spin-phonon coupling in Mn-Bi co-doped SmFeO₃: An experimental study, Journal of Magnetism and Magnetic Materials. 513 (2020) 167094. <https://doi.org/10.1016/j.jmmm.2020.167094>.
- [159] M.H. Kibel, X-Ray Photoelectron Spectroscopy, in: D.J. O'Connor, B.A. Sexton, R.St.C. Smart (Eds.), Surface Analysis Methods in Materials Science, Springer Berlin Heidelberg, Berlin, Heidelberg, 1992: pp. 165–186. https://doi.org/10.1007/978-3-662-02767-7_7.
- [160] A. Paul Blessington Selvadurai, V. Pazhanivelu, C. Jagadeeshwaran, R. Murugaraj, I. Panneer Muthuselvam, F.C. Chou, Influence of Cr substitution on structural, magnetic and electrical conductivity spectra of LaFeO₃, Journal of Alloys and Compounds. 646 (2015) 924–931. <https://doi.org/10.1016/j.jallcom.2015.05.213>.
- [161] J. Prado-Gonjal, Á.M. Arévalo-López, E. Morán, Microwave-assisted synthesis: A fast and efficient route to produce LaMO₃ (M=Al, Cr, Mn, Fe, Co) perovskite materials, Materials Research Bulletin. 2 (2011) 222–230. <https://doi.org/10.1016/j.materresbull.2010.11.010>.
- [162] S. Layek, S. Saha, H.C. Verma, Preparation, structural and magnetic studies on BiFe_{1-x}Cr_xO₃ (x = 0.0, 0.05 and 0.1) multiferroic nanoparticles, AIP Advances. 3 (2013) 032140. <https://doi.org/10.1063/1.4799063>.
- [163] S. Gupta, M.K. Mahapatra, P. Singh, Phase transformation, thermal expansion and electrical conductivity of lanthanum chromite, Materials Research Bulletin. 48 (2013) 3262–3267. <https://doi.org/10.1016/j.materresbull.2013.05.032>.
- [164] P. Kumar, R.K. Singh, A.S.K. Sinha, P. Singh, Effect of isovalent ion substitution on electrical and dielectric properties of LaCrO₃, Journal of Alloys and Compounds. 576 (2013) 154–160. <https://doi.org/10.1016/j.jallcom.2013.04.118>.
- [165] M. Bakr, Mohamed, H. Wang, H. Fuess, Dielectric relaxation and magnetic properties of Cr doped GaFeO₃, Journal of Physics D: Applied Physics. 43 (2010) 455409. <https://doi.org/10.1088/0022-3727/43/45/455409>.
- [166] P. Tirupathi, P. Justin, K. Prabahar, M. Poster, Broad temperature dependent magnetic and dielectric spectroscopy study of Dy(Fe_{0.5}Cr_{0.5})O₃ multiferroic ceramics, Journal of Alloys and

- Compounds. 731 (2018) 411–417.
<https://doi.org/10.1016/j.jallcom.2017.10.069>.
- [167] A. Ak, M. A, E. Sg, I. Sa, Y. Sm, L. F, S. G, M. R, Structural and magnetic properties of $\text{LaFe}_{0.5}\text{Cr}_{0.5}\text{O}_3$ studied by neutron diffraction, electron diffraction and magnetometry, *Mater. Res. Bull.* 40 (2005) 1633–1644.
- [168] L.H. Yin, J. Yang, R.R. Zhang, J.M. Dai, W.H. Song, Y.P. Sun, Multiferroicity and magnetoelectric coupling enhanced large magnetocaloric effect in $\text{DyFe}_{0.5}\text{Cr}_{0.5}\text{O}_3$, *Appl. Phys. Lett.* 104 (2014) 032904. <https://doi.org/10.1063/1.4862665>.
- [169] R.D. Shannon, Revised Effective Ionic Radii and Systematic Studies of Interatomic Distances in Halides and Chalcogenides, *Acta Crystallogr., Sect. A: Cryst. Phys., Diffr., Theor. Gen. Crystallogr.* 32 (1976) 751.
- [170] C. Kittel, *Introduction to Solid State Physics*, Wiley, 2004. <https://books.google.co.in/books?id=kym4QgAACAAJ>.
- [171] A. Kumar, M.K. Warshi, V. Mishra, A. Sati, S. Banik, A. Sagdeo, R. Kumar, P.R. Sagdeo, Optical spectroscopy: An effective tool to probe the origin of dielectric loss in Cr doped PrFeO_3 , *Ceramics International*. (2019). <https://doi.org/10.1016/j.ceramint.2019.01.177>.
- [172] M.K. Warshi, A. Kumar, V. Mishra, A. Sati, A. Sagdeo, R. Kumar, P.R. Sagdeo, Effect of self-doping on the charge state of Fe ions and crystal field transitions in YFeO_3 : Experiments and theory, *Journal of Applied Physics*. 125 (2019) 204101. <https://doi.org/10.1063/1.5092736>.
- [173] A. Kumar, V. Mishra, M.K. Warshi, A. Sati, A. Sagdeo, R. Kumar, P.R. Sagdeo, Possible evidence of delocalized excitons in Cr-doped PrFeO_3 : An experimental and theoretical realization, *Journal of Physics and Chemistry of Solids*. (2019). <https://doi.org/10.1016/j.jpics.2019.03.012>.
- [174] V. Mishra, A. Sagdeo, V. Kumar, M.K. Warshi, H.M. Rai, S.K. Saxena, D.R. Roy, V. Mishra, R. Kumar, P.R. Sagdeo, Electronic and optical properties of BaTiO_3 across tetragonal to cubic phase transition: An experimental and theoretical investigation, *Journal of Applied Physics*. 122 (2017) 065105. <https://doi.org/10.1063/1.4997939>.
- [175] S.M. Wasim, C. Rincón, G. Marín, P. Bocaranda, E. Hernández, I. Bonalde, E. Medina, Effect of structural disorder on the Urbach energy in Cu ternaries, *Phys. Rev. B*. 64 (2001) 195101. <https://doi.org/10.1103/PhysRevB.64.195101>.
- [176] H.M. Rai, S.K. Saxena, R. Late, V. Mishra, P. Rajput, A. Sagdeo, R. Kumar, P.R. Sagdeo, Observation of large dielectric permittivity and dielectric relaxation phenomenon in Mn-doped lanthanum gallate, *RSC Adv.* 6 (2016) 26621–26629. <https://doi.org/10.1039/C5RA28074E>.
- [177] A.K. Jonscher, Physical basis of dielectric loss, *Nature*. 253 (1975) 717.
- [178] A.K. Jonscher, Hopping losses in polarisable dielectric media, *Nature*. 250 (1974) 191.

- [179] P. Bräunlich, ed., *Thermally Stimulated Relaxation in Solids*, Springer Berlin Heidelberg, Berlin, Heidelberg, 1979. <https://doi.org/10.1007/3-540-09595-0>.
- [180] M. Kranjčec, I.P. Studenyak, Gy.S. Kovacs, I.D. Desnica Franković, V.V. Panko, P.P. Guranich, V.Y. Slivka, Electric conductivity and optical absorption edge of $\text{Cu}_6\text{P}(\text{SexS}_{1-x})_5\text{I}$ fast-ion conductors in the selenium-rich region, *Journal of Physics and Chemistry of Solids*. 62 (2001) 665–672. [https://doi.org/10.1016/S0022-3697\(00\)00187-6](https://doi.org/10.1016/S0022-3697(00)00187-6).
- [181] M. Kranjčec, D. I. Desnica, B. Čelustka, G. Sh. Kovacs, I. Studenyak, Fundamental optical absorption edge and compositional disorder in $\gamma\text{-}1\text{-(Ga}_x\text{In}_{1-x})_2\text{Se}_3$ single crystals, 1994. <https://doi.org/10.1002/pssa.2211440125>.
- [182] A. Sagdeo, K. Gautam, P.R. Sagdeo, M.N. Singh, S.M. Gupta, A.K. Nigam, R. Rawat, A.K. Sinha, H. Ghosh, T. Ganguli, A. Chakrabarti, Large dielectric permittivity and possible correlation between magnetic and dielectric properties in bulk $\text{BaFeO}_{3-\delta}$, *Appl. Phys. Lett.* 105 (2014) 042906. <https://doi.org/10.1063/1.4892064>.
- [183] M. Kamal Warshi, V. Mishra, A. Sagdeo, V. Mishra, R. Kumar, P.R. Sagdeo, Synthesis and characterization of RFeO_3 : experimental results and theoretical prediction, *Advances in Materials and Processing Technologies*. (2018) 1–15. <https://doi.org/10.1080/2374068X.2018.1483680>.
- [184] Y. Zhao, D.J. Weidner, J.B. Parise, D.E. Cox, Thermal expansion and structural distortion of perovskite data for NaMgF_3 perovskite. Part I, *Physics of the Earth and Planetary Interiors*. 76 (1993) 1–16. [https://doi.org/10.1016/0031-9201\(93\)90051-A](https://doi.org/10.1016/0031-9201(93)90051-A).
- [185] K. Sultan, M. Ikram, K. Asokan, Structural, optical and dielectric study of Mn doped PrFeO_3 ceramics, *Vacuum*. 99 (2014) 251–258. <https://doi.org/10.1016/j.vacuum.2013.06.014>.
- [186] M.C. Weber, M. Guennou, H.J. Zhao, J. Íñiguez, R. Vilarinho, A. Almeida, J.A. Moreira, J. Kreisel, Raman spectroscopy of rare-earth orthoferrites RFeO_3 ($\text{R}=\text{La, Sm, Eu, Gd, Tb, Dy}$), *Phys. Rev. B*. 94 (2016) 214103. <https://doi.org/10.1103/PhysRevB.94.214103>.
- [187] K. Nakamura, M. Kitajima, Ion-irradiation effects on the phonon correlation length of graphite studied by Raman spectroscopy, *Phys. Rev. B*. 45 (1992) 78–82. <https://doi.org/10.1103/PhysRevB.45.78>.
- [188] M. Kitajima, Defects in crystals studied by Raman scattering, *Critical Reviews in Solid State and Materials Sciences*. 22 (1997) 275–349. <https://doi.org/10.1080/10408439708241263>.
- [189] F.A. Mir, M. Ikram, R. Kumar, Local symmetry breaking in PrFeO_3 thin films and other similar systems after Ni doping: A brief Raman study, *Vibrational Spectroscopy*. 55 (2011) 307–310. <https://doi.org/10.1016/j.vibspec.2010.10.007>.
- [190] M. Popa, J. Frantti, M. Kakihana, Lanthanum ferrite LaFeO_3+d nanopowders obtained by the polymerizable complex method,

- Solid State Ionics. 154–155 (2002) 437–445. [https://doi.org/10.1016/S0167-2738\(02\)00480-0](https://doi.org/10.1016/S0167-2738(02)00480-0).
- [191] M. Romero, R.W. Gómez, V. Marquina, J.L. Pérez-Mazariego, R. Escamilla, Synthesis by molten salt method of the AFeO₃ system (A=La, Gd) and its structural, vibrational and internal hyperfine magnetic field characterization, *Physica B: Condensed Matter*. 443 (2014) 90–94. <https://doi.org/10.1016/j.physb.2014.03.024>.
- [192] A.H. Castro Neto, F. Guinea, Electron-phonon coupling and Raman spectroscopy in graphene, *Phys. Rev. B*. 75 (2007) 045404. <https://doi.org/10.1103/PhysRevB.75.045404>.
- [193] F.A. Mir, M. Ikram, R. Kumar, Symmetry breaking in Ni-doped PrFeO₃ thin films established by Raman study, *Phase Transitions*. 84 (2011) 167–178. <https://doi.org/10.1080/01411594.2010.529601>.
- [194] S.M. Wasim, Effect of structural disorder on the Urbach energy in Cu ternaries, *Phys. Rev. B*. 64 (2001). <https://doi.org/10.1103/PhysRevB.64.195101>.
- [195] S. Sorieul, J. Costantini, L. Gosmain, G. Calas, J.-J. Grob, L. Thomé, Study of Damage in ion-Irradiated α -SiC by Optical Spectroscopy, 2006. <https://doi.org/10.1088/0953-8984/18/37/008>.
- [196] P. Fedeli, F. Gazza, D. Calestani, P. Ferro, T. Besagni, A. Zappettini, G. Calestani, E. Marchi, P. Ceroni, R. Mosca, Influence of the Synthetic Procedures on the Structural and Optical Properties of Mixed-Halide (Br, I) Perovskite Films, *J. Phys. Chem. C*. 119 (2015) 21304–21313. <https://doi.org/10.1021/acs.jpcc.5b03923>.
- [197] Y. Stubrov, A. Nikolenko, V. Strelchuk, S. Nedilko, V. Chornii, Structural Modification of Single-Layer Graphene Under Laser Irradiation Featured by Micro-Raman Spectroscopy, *Nanoscale Research Letters*. 12 (2017) 297. <https://doi.org/10.1186/s11671-017-2089-6>.
- [198] Y. Stubrov, A. Nikolenko, V. Strelchuk, S. Nedilko, V. Chornii, Structural Modification of Single-Layer Graphene Under Laser Irradiation Featured by Micro-Raman Spectroscopy, *Nanoscale Research Letters*. 12 (2017) 297. <https://doi.org/10.1186/s11671-017-2089-6>.
- [199] L. Rodríguez-Martínez, J. Paul Attfield, Cation disorder and the metal-insulator transition temperature in manganese oxide perovskites, 1998. <https://doi.org/10.1103/PhysRevB.58.2426>.
- [200] S. Athinarayanan, A. Maignan, B. Raveau, Effect of A-site cation size mismatch on charge ordering and colossal magnetoresistance properties of perovskite manganites, 1997. <https://doi.org/10.1103/PhysRevB.56.5092>.
- [201] M. Balkanski, R.F. Wallis, E. Haro, Anharmonic effects in light scattering due to optical phonons in silicon, *Phys. Rev. B*. 28 (1983) 1928–1934. <https://doi.org/10.1103/PhysRevB.28.1928>.
- [202] Z. Dohčević-Mitrović, Z. Popovic, M. Scepanovic, Anharmonicity Effects in Nanocrystals Studied by Raman

Scattering Spectroscopy, 2009.
<https://doi.org/10.12693/APhysPolA.116.36>.

- [203] M.W. Khan, S. Husain, M.A.M. Khan, M. Gupta, R. Kumar, J.P. Srivastava, Small polaron hopping conduction mechanism in Ni-doped LaFeO₃, *Philosophical Magazine*. 90 (2010) 3069–3079. <https://doi.org/10.1080/14786431003781604>.
- [204] S.-H. Yoon, S.-J. Park, D.-J. Cha, B.-K. Min, C.S. Kim, Effects of Ga Substitution in LaFe_{1-x}Ga_xO₃ ($\chi = 0, 0.1, 0.3, 0.5, \text{ and } 0.7$), 2002. <https://doi.org/10.4283/JMAG.2002.7.2.040>.
- [205] K. Miura, K. Terakura, Electronic and magnetic properties of La₂FeCrO₆: Superexchange interaction for a d⁵-d³ system, 2001.
- [206] A. Ishikawa, J. Nohara, S. Sugai, Raman Study of the Orbital-Phonon Coupling in LCO₃, *Phys. Rev. Lett.* 93 (2004) 136401. <https://doi.org/10.1103/PhysRevLett.93.136401>.
- [207] A.G. Souza Filho, J.L.B. Faria, I. Guedes, J.M. Sasaki, P.T.C. Freire, V.N. Freire, J. Mendes Filho, M.M. Xavier, F.A.O. Cabral, J.H. de Araújo, J.A.P. da Costa, Evidence of magnetic polaronic states in La_{0.70}Sr_{0.30}Mn_{1-x}Fe_xO₃ manganites, *Phys. Rev. B.* 67 (2003) 052405. <https://doi.org/10.1103/PhysRevB.67.052405>.
- [208] J. Andreasson, J. Holmlund, C.S. Knee, M. Käll, L. Börjesson, S. Naler, J. Bäckström, M. Rübhausen, A.K. Azad, S.-G. Eriksson, Franck-Condon higher order lattice excitations in the LaFe_{1-x}Cr_xO₃ ($x=0, 0.1, 0.5, 0.9, 1.0$) perovskites due to Fe-Cr charge transfer effects, *Phys. Rev. B.* 75 (2007) 104302. <https://doi.org/10.1103/PhysRevB.75.104302>.
- [209] J. Andreasson, J. Holmlund, R. Rauer, M. Käll, L. Börjesson, C.S. Knee, A.K. Eriksson, S.-G. Eriksson, M. Rübhausen, R.P. Chaudhury, Electron-phonon interactions in perovskites containing Fe and Cr studied by Raman scattering using oxygen-isotope and cation substitution, *Phys. Rev. B.* 78 (2008) 235103. <https://doi.org/10.1103/PhysRevB.78.235103>.
- [210] M. Iliev, A. Litvinchuk, V. Hadjiev, Y.-Q. Wang, J. Cmaidalka, R.-L. Meng, Y. Sun, N. Kolev, M. Abrashev, Raman Spectroscopy of Low-Temperature (Pnma) and High-Temperature ($R\bar{3}c$) Phases of LaCrO₃, *Physical Review B.* 74 (2006) 214301. <https://doi.org/10.1103/PhysRevB.74.214301>.
- [211] A. Kumar, M.K. Warshi, V. Mishra, S.K. Saxena, R. Kumar, P.R. Sagdeo, Strain control of Urbach energy in Cr-doped PrFeO₃, *Appl. Phys. A.* 123 (2017) 576. <https://doi.org/10.1007/s00339-017-1186-9>.
- [212] V. Mishra, A. Kumar, A. Sagdeo, P.R. Sagdeo, Comparative structural and optical studies on pellet and powder samples of BaTiO₃ near phase transition temperature, *Ceramics International.* (2019). <https://doi.org/10.1016/j.ceramint.2019.10.030>.
- [213] V. Mishra, M.K. Warshi, A. Sati, A. Kumar, V. Mishra, R. Kumar, P.R. Sagdeo, Investigation of temperature-dependent optical properties of TiO₂ using diffuse reflectance spectroscopy, *SN Applied Sciences.* 1 (2019) 241. <https://doi.org/10.1007/s42452-019-0253-6>.

- [214] P. K. S. Blaha, K. Schwarz, G. Madsen, D. Kvasnicka, J. Luitz, WIEN2k: An Augmented Plane Wave plus Local Orbitals Program for Calculating Crystal Properties, 2001.
- [215] A. Kumar, V. Mishra, M.K. Warshi, A. Sati, A. Sagdeo, R. Kumar, P.R. Sagdeo, Possible evidence of delocalized excitons in Cr-doped PrFeO₃: An experimental and theoretical realization, *Journal of Physics and Chemistry of Solids*. (2019). <https://doi.org/10.1016/j.jpcs.2019.03.012>.
- [216] V. Mishra, M.K. Warshi, A. Sati, A. Kumar, V. Mishra, A. Sagdeo, R. Kumar, P.R. Sagdeo, Diffuse reflectance spectroscopy: An effective tool to probe the defect states in wide band gap semiconducting materials, *Materials Science in Semiconductor Processing*. 86 (2018) 151–156. <https://doi.org/10.1016/j.mssp.2018.06.025>.
- [217] J.B. Torrance, P. Lacorre, A.I. Nazzari, E.J. Ansaldo, Ch. Niedermayer, Systematic study of insulator-metal transitions in perovskites RNiO₃ (R=Pr,Nd,Sm,Eu) due to closing of charge-transfer gap, *Phys. Rev. B*. 45 (1992) 8209–8212. <https://doi.org/10.1103/PhysRevB.45.8209>.
- [218] M. Warshi, V. Mishra, V. Mishra, R. Kumar, P. Sagdeo, Possible Origin of Ferromagnetism in Antiferromagnetic Orthorhombic-YFeO₃: A First-Principles Study, *Ceramics International*. (2018).
- [219] J. Andreasson, J. Holmlund, S.G. Singer, C.S. Knee, R. Rauer, B. Schulz, M. Käll, M. Rübhausen, S.-G. Eriksson, L. Börjesson, A. Lichtenstein, Electron-lattice interactions in the perovskite LaFe_{0.5}Cr_{0.5}O₃ characterized by optical spectroscopy and LDA+U calculations, *Phys. Rev. B*. 80 (2009) 075103. <https://doi.org/10.1103/PhysRevB.80.075103>.
- [220] Y. Fujioka, J. Frantti, M. Kakihana, Franck–Condon Modes in Sr₂MnWO₆ Double Perovskite, *J. Phys. Chem. B*. 108 (2004) 17012–17014. <https://doi.org/10.1021/jp046178f>.
- [221] K. Thyagarajan, A. Ghatak, Introduction, in: K. Thyagarajan, A. Ghatak (Eds.), *Lasers: Fundamentals and Applications*, Springer US, Boston, MA, 2011: pp. 3–8. https://doi.org/10.1007/978-1-4419-6442-7_1.
- [222] *Applications and Principles of Electronic Materials* - Google Search, https://www.google.com/search?rlz=1C1CHBD_enIN754IN754&ei=qUFOXsGRN431kwWMZuICw&q=ApplicaDCAs&ua=ct=5 (accessed February 20, 2020).
- [223] R. Late, K.V. Wagaskar, P.B. Shelke, A. Sagdeo, P. Rajput, P.R. Sagdeo, Structural, optical, and dielectric investigations in bulk PrCrO₃, *Journal of Materials Science: Materials in Electronics*. (2020). <https://doi.org/10.1007/s10854-020-04189-7>.
- [224] R. Late, K. Wagaskar, S. Patil, P. Shelke, P. Sagdeo, Effect of bismuth doping on optical properties of polycrystalline PrCrO₃, 2020. <https://doi.org/10.1063/5.0002651>.
- [225] R. Late, H.M. Rai, S.K. Saxena, R. Kumar, A. Sagdeo, P.R. Sagdeo, Probing structural distortions in rare earth chromites using Indian synchrotron radiation source, *Indian Journal of*

- Physics. 90 (2016) 1347–1354. <https://doi.org/10.1007/s12648-016-0887-9>.
- [226] C.-Y. Kuo, Y. Drees, M.T. Fernández-Díaz, L. Zhao, L. Vasylechko, D. Sheptyakov, A.M.T. Bell, T.W. Pi, H.-J. Lin, M.-K. Wu, E. Pellegrin, S.M. Valvidares, Z.W. Li, P. Adler, A. Todorova, R. Kuchler, A. Steppke, L.H. Tjeng, Z. Hu, A.C. Komarek, *k=0* Magnetic Structure and Absence of Ferroelectricity in SmFeO_3 , *Phys. Rev. Lett.* 113 (2014) 217203. <https://doi.org/10.1103/PhysRevLett.113.217203>.
- [227] F. Pomiro, R.D. Sánchez, G. Cuello, A. Maignan, C. Martin, R.E. Carbonio, Spin reorientation, magnetization reversal, and negative thermal expansion observed in $\text{RFe}_0.5\text{Cr}_0.5\text{O}_3$ perovskites ($\text{R}=\text{Lu}, \text{Yb}, \text{Tm}$), *Phys. Rev. B.* 94 (2016) 134402. <https://doi.org/10.1103/PhysRevB.94.134402>.
- [228] G. Lawes, A.P. Ramirez, C.M. Varma, M.A. Subramanian, Magnetodielectric Effects from Spin Fluctuations in Isostructural Ferromagnetic and Antiferromagnetic Systems, *Phys. Rev. Lett.* 91 (2003) 257208. <https://doi.org/10.1103/PhysRevLett.91.257208>.
- [229] A. Kumar, V. Mishra, M.K. Warshi, A. Sati, A. Sagdeo, R. Kumar, P.R. Sagdeo, Strain induced disordered phonon modes in Cr doped PrFeO_3 , *J. Phys.: Condens. Matter.* 31 (2019) 275602. <https://doi.org/10.1088/1361-648X/ab1195>.
- [230] M.K. Warshi, A. Kumar, A. Sati, S. Thota, K. Mukherjee, A. Sagdeo, P.R. Sagdeo, Cluster Glass Behavior in Orthorhombic SmFeO_3 Perovskite: Interplay between Spin Ordering and Lattice Dynamics, *Chem. Mater.* 32 (2020) 1250–1260. <https://doi.org/10.1021/acs.chemmater.9b04703>.
- [231] A. Sati, A. Kumar, V. Mishra, K. Warshi, A. Sagdeo, S. Anwar, R. Kumar, P.R. Sagdeo, Direct correlation between the band gap and dielectric loss in Hf doped BaTiO_3 , *Journal of Materials Science: Materials in Electronics.* 30 (2019) 8064–8070. <https://doi.org/10.1007/s10854-019-01128-z>.
- [232] V. Mishra, M.K. Warshi, A. Sati, A. Kumar, V. Mishra, R. Kumar, P.R. Sagdeo, Investigation of temperature-dependent optical properties of TiO_2 using diffuse reflectance spectroscopy, *SN Applied Sciences.* 1 (2019) 241. <https://doi.org/10.1007/s42452-019-0253-6>.
- [233] A. Sati, A. Kumar, V. Mishra, K. Warshi, P. Pokhriyal, A. Sagdeo, P.R. Sagdeo, Temperature-dependent dielectric loss in BaTiO_3 : Competition between tunnelling probability and electron-phonon interaction, *Materials Chemistry and Physics.* 257 (2021) 123792. <https://doi.org/10.1016/j.matchemphys.2020.123792>.
- [234] M. Krzystyniak, G. Romanelli, M. Fabian, M. Gutmann, G. Festa, L. Arcidiacono, M. Gigg, K. Druzbicki, C. Andreani, R. Senesi, F. Fernandez-Alonso, VESUVIO+: The Current Testbed for a Next-generation Epithermal Neutron Spectrometer, *Journal of Physics: Conference Series.* 1021 (2018) 012026. <https://doi.org/10.1088/1742-6596/1021/1/012026>.

- [235] C. Andreani, M. Krzystyniak, G. Romanelli, R. Senesi, F. Fernandez-Alonso, Electron-volt neutron spectroscopy: beyond fundamental systems, *Advances in Physics*. 66 (2017) 1–73. <https://doi.org/10.1080/00018732.2017.1317963>.
- [236] G. Romanelli, M. Krzystyniak, R. Senesi, D. Raspino, J. Boxall, D. Pooley, S. Moorby, E. Schooneveld, N.J. Rhodes, C. Andreani, F. Fernandez-Alonso, Characterisation of the incident beam and current diffraction capabilities on the VESUVIO spectrometer, *Measurement Science and Technology*. 28 (2017) 095501. <https://doi.org/10.1088/1361-6501/aa7c2a>.
- [237] M. Krzystyniak, K. Druźbicki, S. Rudić, M. Fabian, Positional, isotopic mass and force constant disorder in molybdate glasses and their parent metal oxides as observed by neutron diffraction and Compton scattering, *Journal of Physics Communications*. 4 (2020) 095027. <https://doi.org/10.1088/2399-6528/abb8ee>.
- [238] R. Haworth, J.L. Shaw, A.C. Wright, R.N. Sinclair, K.S. Knight, J.W. Taylor, N. Vedishcheva, I. Polyakova, B.A. Shakhmatkin, S.A. Feller, D. Winslow, Superstructural units in vitreous and crystalline caesium borates, *Physics and Chemistry of Glasses - European Journal of Glass Science and Technology Part B*. 46 (2005) 477–482.
- [239] S.F. Parker, F. Fernandez-Alonso, A.J. Ramirez-Cuesta, J. Tomkinson, S. Rudic, R.S. Pinna, G. Gorini, J. Fernández Castañón, Recent and future developments on TOSCA at ISIS, *Journal of Physics: Conference Series*. 554 (2014) 012003. <https://doi.org/10.1088/1742-6596/554/1/012003>.
- [240] D. Colognesi, M. Celli, F. Cilloco, R. Newport, S.F. Parker, V. Rossi-Albertini, F. Sacchetti, J. Tomkinson, M. Zoppi, TOSCA neutron spectrometer: The final configuration, *Applied Physics A*. 74 (2002) s64–s66. <https://doi.org/10.1007/s003390101078>.
- [241] Z.A. Bowden, M. Celli, F. Cilloco, D. Colognesi, R.J. Newport, S.F. Parker, F.P. Ricci, V. Rossi-Albertini, F. Sacchetti, J. Tomkinson, M. Zoppi, The TOSCA incoherent inelastic neutron spectrometer: progress and results, *Physica B Condensed Matter*. 276 (2000) 98–99. [https://doi.org/10.1016/S0921-4526\(99\)01258-2](https://doi.org/10.1016/S0921-4526(99)01258-2).
- [242] S.F. Parker, C.J. Carlile, T. Pike, J. Tomkinson, R.J. Newport, C. Andreani, F.P. Ricci, F. Sacchetti, M. Zoppi, TOSCA: a world class inelastic neutron spectrometer, *Physica B: Condensed Matter*. 241–243 (1997) 154–156. [https://doi.org/10.1016/S0921-4526\(97\)00536-X](https://doi.org/10.1016/S0921-4526(97)00536-X).
- [243] R. Pinna, S. Rudić, S. Parker, J. Armstrong, M. Zanetti, G. Škoro, S. Waller, D. Zacek, C. Smith, M. Capstick, D. McPhail, D. Pooley, G. Howells, G. Gorini, F. Fernandez-Alonso, The neutron guide upgrade of the TOSCA spectrometer, *Nuclear Instruments and Methods in Physics Research Section A: Accelerators, Spectrometers, Detectors and Associated Equipment*. 896 (2018). <https://doi.org/10.1016/j.nima.2018.04.009>.

- [244] N.K.C. Muniraju, T. Brueckel, Crystal and spin structure and their relation to physical properties in some geometrical and spin spiral multiferroics, in: 2012.
- [245] J.B. Goodenough, Theory of the Role of Covalence in the Perovskite-Type Manganites LaMnO_3 , *Phys. Rev.* 100 (1955) 564–573. <https://doi.org/10.1103/PhysRev.100.564>.
- [246] T. Hashimoto, Magnetic Properties of the Solid Solutions between KMnF_3 , KCoF_3 and KNiF_3 , *J. Phys. Soc. Jpn.* 18 (1963) 1140–1147. <https://doi.org/10.1143/JPSJ.18.1140>.
- [247] M. Balkanski, R.F. Wallis, E. Haro, Anharmonic effects in light scattering due to optical phonons in silicon, *Phys. Rev. B.* 28 (1983) 1928–1934. <https://doi.org/10.1103/PhysRevB.28.1928>.
- [248] Z. Li, Y. Wang, Y. Lin, C. Nan, Evidence for stress-mediated magnetoelectric coupling in multiferroic bilayer films from magnetic-field-dependent Raman scattering, *Phys. Rev. B.* 79 (2009) 180406. <https://doi.org/10.1103/PhysRevB.79.180406>.
- [249] Z.H. Sun, B.L. Cheng, S. Dai, L.Z. Cao, Y.L. Zhou, K.J. Jin, Z.H. Chen, G.Z. Yang, Dielectric property studies of multiferroic GaFeO_3 , *Journal of Physics D: Applied Physics.* 39 (2006) 2481–2484. <https://doi.org/10.1088/0022-3727/39/12/001>.
- [250] Z.J. Huang, Y. Cao, Y.Y. Sun, Y.Y. Xue, C.W. Chu, Coupling between the ferroelectric and antiferromagnetic orders in YMnO_3 , *Phys. Rev. B.* 56 (1997) 2623–2626. <https://doi.org/10.1103/PhysRevB.56.2623>.
- [251] P. Ravindran, R. Vidya, A. Kjekshus, H. Fjellvåg, O. Eriksson, Theoretical Investigation of Magnetoelectric Behavior in BiFeO_3 , *Phys. Rev. B: Condens. Matter Mater. Phys.* 74 (2006) 224412.
- [252] H.M. Rai, P. Singh, S.K. Saxena, V. Mishra, M.K. Warshi, R. Kumar, P. Rajput, A. Sagdeo, I. Choudhuri, B. Pathak, P.R. Sagdeo, Room-Temperature Magneto-dielectric Effect in $\text{LaGa}_{0.7}\text{Fe}_{0.3}\text{O}_{3+\gamma}$; Origin and Impact of Excess Oxygen, *Inorg. Chem.* 56 (2017) 3809–3819. <https://doi.org/10.1021/acs.inorgchem.6b02507>.
- [253] H.M. Rai, R. Late, S.K. Saxena, V. Mishra, R. Kumar, P.R. Sagdeo, Archana Sagdeo, Room temperature magnetodielectric studies on Mn-doped LaGaO_3 , *Materials Research Express.* 2 (2015) 096105.
- [254] V.R. Palkar, D.C. Kundaliya, S.K. Malik, S. Bhattacharya, Magnetoelectricity at Room Temperature in the $\text{Bi}_{0.9-x}\text{Tb}_x\text{La}_{0.1}\text{FeO}_3$ System, *Phys. Rev. B: Condens. Matter Mater. Phys.* 69 (2004) 212102.
- [255] D. Lebeugle, D. Colson, A. Forget, M. Viret, Very Large Spontaneous Electric Polarization in BiFeO_3 Single Crystals at Room Temperature and Its Evolution under Cycling Fields, *Appl. Phys. Lett.* 91 (2007) 022907.
- [256] R. Arielly, W.M. Xu, E. Greenberg, G. Rozenberg, null Kh, M.P. Pasternak, G. Garbarino, S. Clark, R. Jeanloz, Intriguing Sequence of GaFeO_3 Structures and Electronic States to 70 GPa, *Phys. Rev. B: Condens. Matter Mater. Phys.* 84 (2011) 094109.

- [257] K. Sharma, V.R. Reddy, D. Kothari, A. Gupta, A. Banerjee, V.G. Sathe, Low temperature Raman and high field ^{57}Fe Mossbauer study of polycrystalline GaFeO_3 , *Journal of Physics: Condensed Matter*. 22 (2010) 146005. <https://doi.org/10.1088/0953-8984/22/14/146005>.
- [258] M. Bakr, Mohamed, H. Wang, H. Fuess, Dielectric relaxation and magnetic properties of Cr doped GaFeO_3 , *Journal of Physics D: Applied Physics*. 43 (2010) 455409. <https://doi.org/10.1088/0022-3727/43/45/455409>.
- [259] B. Kundys, F. Roulland, C. Lefèvre, C. Mény, A. Thomasson, N. Viart, Room temperature polarization in the ferrimagnetic $\text{Ga}_{2-x}\text{Fe}_x\text{O}_3$ ceramics, *Journal of the European Ceramic Society*. 35 (2015) 2277–2281. <https://doi.org/10.1016/j.jeurceramsoc.2015.02.029>.
- [260] T.C. Han, T.Y. Chen, Y.C. Lee, Grain size effect on site-disorder and magnetic properties of multiferroic GaFeO_3 nanoparticles, *Appl. Phys. Lett.* 103 (2013) 232405. <https://doi.org/10.1063/1.4838057>.
- [261] K. Sharma, V. Raghavendra Reddy, A. Gupta, A. Banerjee, A.M. Awasthi, Magnetic and ^{57}Fe Mössbauer study of magneto-electric GaFeO_3 prepared by the sol–gel route, *Journal of Physics: Condensed Matter*. 25 (2013) 076002. <https://doi.org/10.1088/0953-8984/25/7/076002>.
- [262] A. Kumar, vikash mishra, M.K. WARSHI, A. SATI, A. Sagdeo, R. Kumar, P.R. Sagdeo, Strain Induced Disordered Phonon Modes in Cr doped PrFeO_3 , *Journal of Physics: Condensed Matter*. (2019). <http://iopscience.iop.org/10.1088/1361-648X/ab1195>.
- [263] M.K. Warshi, A. Kumar, A. Sati, S. Thota, K. Mukherjee, A. Sagdeo, P.R. Sagdeo, Cluster Glass Behavior in Orthorhombic SmFeO_3 Perovskite: Interplay Between Spin Ordering and Lattice Dynamics, *Chem. Mater.* (2020). <https://doi.org/10.1021/acs.chemmater.9b04703>.
- [264] A. Kumar, M.K. Warshi, V. Mishra, S.K. Saxena, R. Kumar, P.R. Sagdeo, Strain control of Urbach energy in Cr-doped PrFeO_3 , *Appl. Phys. A*. 123 (2017) 576. <https://doi.org/10.1007/s00339-017-1186-9>.
- [265] A. Kumar, M.K. Warshi, V. Mishra, A. Sati, S. Banik, A. Sagdeo, R. Kumar, P.R. Sagdeo, Optical spectroscopy: An effective tool to probe the origin of dielectric loss in Cr doped PrFeO_3 , *Ceramics International*. (2019). <https://doi.org/10.1016/j.ceramint.2019.01.177>.
- [266] P.R. Sagdeo, S. Anwar, N.P. Lalla, Powder X-ray diffraction and Rietveld analysis of $\text{La}_{1-x}\text{Ca}_x\text{MnO}_3$ ($0 < x < 1$), *Powder Diffraction*. 21 (2006) 40–44. <https://doi.org/10.1154/1.2104536>.
- [267] W. Kim, J.H. We, S.J. Kim, C.S. Kim, Effects of cation distribution for AFeO_3 ($\text{A}=\text{Ga},\text{Al}$), *Journal of Applied Physics*. 101 (2007) 09M515. <https://doi.org/10.1063/1.2712819>.
- [268] J.-Y. Kim, T.Y. Koo, J.-H. Park, Orbital and Bonding Anisotropy in a Half-Filled GaFeO_3 Magnetoelectric Ferrimagnet, *Phys. Rev.*

- Lett. 96 (2006) 047205.
<https://doi.org/10.1103/PhysRevLett.96.047205>.
- [269] P.J. Besser, A.H. Morrish, C.W. Searle, Magnetocrystalline Anisotropy of Pure and Doped Hematite, *Phys. Rev.* 153 (1967) 632–640. <https://doi.org/10.1103/PhysRev.153.632>.
- [270] T. Leisegang, H. Stöcker, A.A. Levin, T. Weißbach, M. Zschornak, E. Gutmann, K. Rickers, S. Gemming, D.C. Meyer, Switching Ti Valence in SrTiO₃ by a dc Electric Field, *Phys. Rev. Lett.* 102 (2009) 087601. <https://doi.org/10.1103/PhysRevLett.102.087601>.
- [271] B.P. Andreasson, M. Janousch, U. Staub, G.I. Meijer, B. Delley, Resistive switching in Cr-doped SrTiO₃: An X-ray absorption spectroscopy study, *Materials Science and Engineering: B.* 144 (2007) 60–63. <https://doi.org/10.1016/j.mseb.2007.07.059>.
- [272] T.W. Capehart, J.F. Herbst, R.K. Mishra, F.E. Pinkerton, X-ray-absorption edge shifts in rare-earth–transition-metal compounds, *Phys. Rev. B.* 52 (1995) 7907–7914. <https://doi.org/10.1103/PhysRevB.52.7907>.
- [273] V.P.S. Awana, M. Karppinen, H. Yamauchi, M. Matvejeff, R.S. Liu, L.-Y. Jang, Oxygen Content and Valence of Ru in RuSr₂(Gd_{0.75}Ce_{0.25})₂Cu₂O_{10–δ} (Ru-1222) Magnetosuperconductor, *Journal of Low Temperature Physics.* 131 (2003) 1211–1216. <https://doi.org/10.1023/A:1023490202435>.
- [274] A. Sagdeo, K. Gautam, P.R. Sagdeo, M.N. Singh, S.M. Gupta, A.K. Nigam, R. Rawat, A.K. Sinha, H. Ghosh, T. Ganguli, A. Chakrabarti, Large dielectric permittivity and possible correlation between magnetic and dielectric properties in bulk BaFeO_{3–δ}, *Appl. Phys. Lett.* 105 (2014) 042906. <https://doi.org/10.1063/1.4892064>.
- [275] G. Sankar, P. Sarode, C.N.R. Rao, A XANES study of mixed-valence transition-metal oxides and rare-earth alloys, *Chemical Physics.* 76 (1983) 435–442.
- [276] G.A. (Stanford Univ. Waychunas CA (USA)), Synchrotron radiation XANES spectroscopy of Ti in minerals: Effects of Ti bonding distances, Ti valence, and site geometry on absorption edge structure, *American Mineralogist*; (USA). (n.d.). <https://www.osti.gov/servlets/purl/5152935>.
- [277] V. Mishra, M. Warshi, R. Kumar, P. Sagdeo, Design and development of in-situ temperature dependent diffuse reflectance spectroscopy setup, 2018. <https://doi.org/10.1088/1748-0221/13/11/T11003>.
- [278] V. Mishra, A. Kumar, A. Sagdeo, P.R. Sagdeo, Comparative structural and optical studies on pellet and powder samples of BaTiO₃ near phase transition temperature, *Ceramics International.* 46 (2020) 3250–3256. <https://doi.org/10.1016/j.ceramint.2019.10.030>.
- [279] S. Hussain, S.K. Hasanain, Chemical pressure induced red shift in band gap and d-d transition energies in Sr doped BiFeO₃, *Journal*

- of Alloys and Compounds. 688 (2016) 1151–1156. <https://doi.org/10.1016/j.jallcom.2016.07.158>.
- [280] P.S.V. Mocherla, C. Karthik, R. Ubig, M.S. Ramachandra Rao, C. Sudakar, Tunable bandgap in BiFeO₃ nanoparticles: The role of microstrain and oxygen defects, *Appl. Phys. Lett.* 103 (2013) 022910. <https://doi.org/10.1063/1.4813539>.
- [281] Y. Tanabe, S. Sugano, On the Absorption Spectra of Complex Ions II, *J. Phys. Soc. Jpn.* 9 (1954) 766–779. <https://doi.org/10.1143/JPSJ.9.766>.
- [282] Y. Tanabe, S. Sugano, On the Absorption Spectra of Complex Ions, III The Calculation of the Crystalline Field Strength, *J. Phys. Soc. Jpn.* 11 (1956) 864–877. <https://doi.org/10.1143/JPSJ.11.864>.
- [283] A.M. Kalashnikova, R.V. Pisarev, L.N. Bezmaternykh, V.L. Temerov, A. Kirilyuk, Th. Rasing, Optical and magneto-optical studies of a multiferroic GaFeO₃ with a high Curie temperature, *Journal of Experimental and Theoretical Physics Letters.* 81 (2005) 452–457. <https://doi.org/10.1134/1.1984028>.
- [284] E. Vella, F. Messina, M. Cannas, R. Boscaino, Unraveling exciton dynamics in amorphous silicon dioxide: Interpretation of the optical features from 8 to 11 eV, *Phys. Rev. B.* 83 (2011) 174201. <https://doi.org/10.1103/PhysRevB.83.174201>.
- [285] N. Sharma, A.K. Mall, R. Gupta, A. Garg, S. Kumar, Effect of sintering temperature on structure and properties of GaFeO₃, *Journal of Alloys and Compounds.* 737 (2018) 646–654. <https://doi.org/10.1016/j.jallcom.2017.12.122>.
- [286] S. Mukherjee, A. Garg, R. Gupta, Probing magnetoelastic coupling and structural changes in magnetoelectric gallium ferrite, *Journal of Physics: Condensed Matter.* 23 (2011) 445403. <https://doi.org/10.1088/0953-8984/23/44/445403>.
- [287] H. Chou, C.-W. Yen, C.-C. Yang, G.D. Dwivedi, K. Yang, C.P. Wu, K.C. Liu, W.-H. Li, Oxygen deficiency-induced anomalous enhancement of Neel temperature and magnetic coupling for Bi_{0.9}Ca_{0.1}FeO_{3-δ} and Bi_{0.9}Pb_{0.1}FeO_{3-δ}, *Acta Materialia.* 111 (2016) 297–304. <https://doi.org/10.1016/j.actamat.2016.03.071>.
- [288] A. Urushibara, Y. Moritomo, T. Arima, A. Asamitsu, G. Kido, Y. Tokura, Insulator-metal transition and giant magnetoresistance in La_{1-x}Sr_xMnO₃, *Phys. Rev. B.* 51 (1995) 14103–14109. <https://doi.org/10.1103/PhysRevB.51.14103>.
- [289] Y. Tomioka, A. Asamitsu, Y. Moritomo, H. Kuwahara, Y. Tokura, Collapse of a Charge-Ordered State under a Magnetic Field in Pr_{1/2}Sr_{1/2}MnO₃, *Phys. Rev. Lett.* 74 (1995) 5108–5111. <https://doi.org/10.1103/PhysRevLett.74.5108>.
- [290] T. Arima, D. Higashiyama, Y. Kaneko, J.P. He, T. Goto, S. Miyasaka, T. Kimura, K. Oikawa, T. Kamiyama, R. Kumai, Y. Tokura, Structural and magnetoelectric properties of Ga_{2-x}Fe_xO₃ single crystals grown by a floating-zone method, *Phys. Rev. B.* 70 (2004) 064426. <https://doi.org/10.1103/PhysRevB.70.064426>.
- [291] E. Vella, F. Messina, M. Cannas, R. Boscaino, Unraveling exciton dynamics in amorphous silicon dioxide: Interpretation of the

- optical features from 8 to 11 eV, *Phys. Rev. B.* 83 (2011) 174201.
<https://doi.org/10.1103/PhysRevB.83.174201>.
- [292] Y. Toyozawa, Optical spectra of exciton in the phonon field, *Journal of Luminescence.* 31–32 (1984) 50–55.
[https://doi.org/10.1016/0022-2313\(84\)90203-5](https://doi.org/10.1016/0022-2313(84)90203-5).